# Reinforcement Learning Guided Multi-Objective Optimization for Inverse Analysis

Yang Zhang, Ph.D.
University of Connecticut, 2024

Structural Health Monitoring (SHM) aims at assessing the integrity and engineering structures to ensure their safe and reliable operations. To achieve an early detection of damage, piezoelectric impedance-based active interrogation is increasingly recognized in SHM due to its self-sensing and actuation capability, operation in high-frequency range, and potential for model-based inverse identification of damage location and severity. Yet, a common issue in structural damage identification is the limited measurement information and complex baseline structural model, which renders the inverse analysis under-determined. Early-stage damage typically affects only small areas, allowing us to frame the problem as a multi-objective optimization that minimizes the difference between model predictions and physical measurements while enforcing sparsity in damaged locations. This setup often produces multiple solutions, a natural fit for structural damage identification. However, similar to human health diagnostics, an excess of solutions, especially redundant or non-sparse ones, can obscure accurate diagnosis. Therefore, an effective inverse problem-solving approach must balance underdetermination with sparsity to yield a small, diverse, and accurate set of solutions for reliable damage identification. Multimodality in the objective function and high-dimensional variables, due to the finite element model basis, challenge optimization algorithms, where entrapment in local solutions risks false positives and negatives.

In this dissertation, five interconnected approaches address these challenges. 1) A Sparsity-Aware Metaheuristic Algorithm is developed to handle the L0 norm directly, guiding the search toward sparse solutions that focus on limited areas for structural maintenance. 2) Enhanced Optimization with Local Search and Reinforcement Learning is achieved through various local search strategies and adaptive reinforcement learning techniques, such as Q-learning and learning automata, which improve optimization by leveraging search experiences and interactions with the environment. 3) Tunable Circuitry for Measurement Enrichment is integrated into the piezoelectric transducer system, tuning inductance values to enrich measurements and mitigate underdetermination by generating a family of datasets for each damage profile. 4) A Hierarchical Damage Identification Framework divides the structure into groups and applies group Lasso to achieve damage identification in stages: the first stage drives sparsity at the group level, while the second stage pinpoints the specific group with potential damage. 5) Model Order Reduction is implemented using Component Mode Synthesis to develop reduced-order models of the PZT-enhanced plate structure, allowing efficient forward analysis to approximate damage locations within substructures, followed by inverse model updating to determine damage location and severity. These approaches are validated using experimental piezoelectric impedance data, consistently deriving small, diverse solution sets that include the true damage scenarios.

In summary, this dissertation contributes to the field of structural health monitoring by introducing a combination of sparsity-aware framework, computational intelligence, mechatronics integration, machine learning and physical model order reduction. It offers a robust, accurate, and computationally efficient approach for damage detection and assessment in complex structural systems.

# Reinforcement Learning Guided Multi-Objective Optimization for Inverse Analysis

Yang Zhang

M.S., Beijing University of Technology, 2018

B.S., Wuhan University of Science and Technology, 2015

A Dissertation

Submitted in Partial Fulfillment of the

Requirements for the Degree of

Doctor of Philosophy

at the

University of Connecticut

2024

APROVAL PAGE

Doctor of Philosophy Dissertation

# Reinforcement Learning Guided Multi-Objective Optimization for Inverse Analysis

Presented by

Yang Zhang, M.S., B.S.

Approved by

Major Advisor:__________________________________________________

Dr. Jiong Tang

Associate Advisor:__________________________________________________

Dr. Chao Hu

Associate Advisor:__________________________________________________

Dr. Farhad Imani

Associate Advisor:__________________________________________________

Dr. Jeongho Kim

Associate Advisor:__________________________________________________

Dr. Julian Norato

Associate Advisor:__________________________________________________

Dr. Hongyi Xu

University of Connecticut
2024

*This work is dedicated to my beloved parents, my brother, sister-in-law and nephew for their love and endless support*

# Acknowledgment

First and foremost, I would like to express my deepest gratitude and respect to my major advisor, Prof. Jiong Tang, for his mentorship, support, and encouragement throughout my five years of graduate studies. His unwavering work ethics, profound wisdom, and passion for research have been a constant source of inspiration. From him, I have gained not only academic skills but also valuable perspectives on career and life. This has been a truly rewarding journey that I will cherish for the rest of my life.

I am also deeply thankful to my associated academic advisors: Prof. Chao Hu, Prof. Farhad Imani, Prof. Jeongho Kim, Prof. Julian Norato, Prof. Hongyi Xu, for their invaluable guidance throughout my studies and research. Special thanks go to Prof. Kai Zhou at PolyU, who has been both a collaborator and a mentor, offering wise advice in our academic collaborations, discussions, and research, as well as personal support. I am grateful to my lab members, especially Joshua Dupont and Ting Wang, with whom I shared many discussions and collaborative efforts in the field of smart structures and materials. I also extend my sincere thanks to my lab mates and alumni yet friends—Qianyu Zhou, Dong Xu, David Javadian, Eric Gillespie, and Christian Schirmer—for their support and assistance in the lab. My gratitude extends to the funding bodies that made my studies and research possible: NASA, DOT-TIDC, and NSF. Their support allowed me to focus fully on my studies and research at UCONN. I also appreciate the cooperation of my project colleagues, who contributed to our shared success.

I want to thank my parents, my brother, and my sister-in-law, along with extended family members for their unwavering support throughout this journey. In countless moments of homesickness, video calls with them provided solace and strength. I am also grateful for the joy brought by my new nephew and nieces, whose smiles, even from afar, lightened my heart. Special thanks to my aunt, Xin Yang, for her unconditional support, encouragement and help along the way. My friends—Yi Li, Yansong Pei, You Zhou, Han Xiao, …, filled my life with joy, whether on the badminton court, around the dinner table, or simply in daily life, making my time at UCONN unforgettable. There are too many people to thank, and words are never enough to express my gratitude. I am sincerely grateful to all who have touched my life along the way.

Time passes swiftly, carrying away countless beautiful moments and memories. As I write this acknowledgment, surrounded by autumn leaves and cool winds, I reflect on my five years at UCONN—a journey marked by seasons of growth. Last thanks said to myself in this journey with perseverance and dedication. “Diligence is the path to the mountain of knowledge, hard-working is the boat to the endless sea of learning.” Although this degree marks an important milestone, the journey of learning continues......

# Table of Contents

Chapter 1. Introduction ........ 1

1.1. Background and Problem Statement ........ 1
1.2. Review of State-of-the-art Approaches ........ 4
1.2.1. Casting inverse identification into optimization with sparsity ........ 4
1.2.2. Metaheuristics in damage identification and enhancements ........ 7
1.2.3. Mechatronics integration for damage identification ........ 8
1.2.4. Multi-stage/level damage identification and model order reduction ........ 9
1.3. Dissertation Outline ........ 12
Chapter 2. Piezoelectric Impedance-based High-accuracy Damage Identification Using Sparsity Conscious Multi-Objective Optimization Inverse Analysis ........ 15

2.1. Introduction ........ 16
2.2. Piezoelectric Impedance-based Damage Identification ........ 22
2.2.1. Finite element modeling of piezoelectric impedance ........ 22
2.2.2. Formulation of sparsity conscious multi-objective optimization for damage identification. 25
2.2.3. Multi-objective particle swarm optimization (MOPSO) procedure and challenges ........ 26
2.3. Solving Sparsity Conscious Multi-objective Particle Swarm Optimization ........ 28
2.3.1. Overall architecture of MOPSO guided by Q-learning ........ 28
2.3.2. Sparse population generation ........ 31
2.3.3. Q learning details and Q-table ........ 33
2.3.4. Action repository ........ 35
2.3.5. Solution procedure summary ........ 40
2.4. Damage Identification Implementation with Experimental Case Analyses ........ 40
2.4.1. Experimental setup and data acquisition ........ 40
2.4.2. Finite element modeling and updating ........ 42
2.4.3. Case study setup ........ 45
2.4.4. Effect of sparsity generation ........ 46
2.4.5. Examination of reinforcement learning guided local search ........ 49
2.4.6. Effect of Q-table guided action selection and computational cost analysis ........ 55
2.5. Conclusion ........ 58
Chapter 3. Harnessing Collaborative Learning Automata to Guide Multi-objective Optimization based Inverse Analysis for Structural Damage Identification ........ 60

3.1. Introduction ..... 61
3.2. Multi-objective Optimization Setup for Damage Identification ..... 66
3.3. Guiding Multi-objective Particle Swarm Optimization through Adaptive Learning Automata 68
3.3.1. General framework of particle swarm optimization ..... 68
3.3.2. Guidance to search with learning automata ..... 69
3.3.3. Learning automata guided MOPSO towards a diverse and small solution set ..... 71
3.3.4. Summary of the proposed optimization algorithm ..... 75
3.4. Demonstration and Validation through Case Investigations ..... 76
3.4.1. Benchmark test functions ..... 77
3.4.2. Insights into parametric settings and evaluation metrics ..... 78
3.4.3. Discussion on benchmark test case results ..... 79
3.5. Applying the LAMOPSO to Structural Damage Identification Practice ..... 83
3.5.1. Numerical case study ..... 84
3.5.2. Experimental case study ..... 87
3.5.3. Role of LA in enhancing MOPSO performance ..... 96
3.6. Conclusion and future work ..... 99
Chapter 4. Piezoelectric Impedance-based Structural Damage Identification Empowered with Tunable Circuitry Integration and Multi-objective Optimization based Inverse Analysis ..... 101
4.1. Introduction ..... 101
4.2. Piezoelectric Admittance based Active Interrogation with Enhancement ..... 106
4.2.1. Finite element modeling of piezoelectric admittance with tunable inductor integration ..... 106
4.2.2. Formulation of multi-objective optimization for damage identification ..... 110
4.3. Q-learning Enhanced Multi-objective Optimizer ..... 112
4.3.1. Framework of multi-objective particle swarm optimization (MOPSO) ..... 112
4.3.2. Action repository for exploration-exploitation balance ..... 114
4.3.3. Q-learning based enhancement ..... 117
4.4. Damage Identification Implementation with Enriched Piezoelectric Measurements ..... 119
4.4.1. Experimental setup and data acquisition ..... 119
4.4.2. Baseline model updating ..... 122
4.4.3. Damage identification using enriched experimental measurements ..... 127
4.4.4. Effects of data enrichment on identified results. ..... 132
4.5. Conclusion ..... 134

Chapter 5. High-frequency Active Interrogation for Structural Damage Identification Enabled by Intelligent Hierarchical Search ........ 136

5.1. Introduction ........ 136
5.2. Piezoelectric Admittance-based Damage Identification: Problem Formulation ........ 142
5.2.1. Modeling of piezoelectric admittance ........ 143
5.2.2. Casting damage identification into parametric optimization ........ 145
5.3. Group-wise Sparse Damage Detection Followed by Refined Identification ........ 146
5.3.1. Message passing ........ 148
5.3.2. A dual-resolution approach for damage identification ........ 150
5.3.3. Learning Automata guided swarm optimizer ........ 151
5.4. Structural Damage Identification Case Study and Discussion ........ 156
5.4.1. Experimental setup and data acquisition ........ 156
5.4.2. Finite element modeling and model updating ........ 158
5.4.3. Damage identification case setup employing the proposed hierarchical framework ........ 159
5.4.4. Damage identification results and discussion ........ 161
5.5. Conclusion ........ 169
Chapter 6. Precision Damage Identification in Structural Subsystems Using Reduced-Order Models and Piezoelectric Impedance Sensing ........ 171

6.1. Introduction ........ 172
6.2. Two-stage Damage Identification Via Piezoelectric Admittance Sensing ........ 176
6.2.1. Modeling of piezoelectric admittance ........ 176
6.2.2. Overview of two-stage damage identification approach ........ 178
6.3. Reduced-order Modeling for Piezoelectric Transducer-Structure System ........ 182
6.4. Structural Damage Identification Case Study and Discussion ........ 187
6.4.1. Problem setup of case investigation ........ 188
6.4.2. Order-reduced model establishment and performance validation ........ 191
6.4.3. Coarse-level damage localization ........ 193
6.4.4. Fine-level damage identification ........ 197
6.5. Conclusion ........ 200
Chapter 7. Concluding Remarks ........ 202

References 205

# List of Figures

Figure 1-1. Schematic illustration of direct and inverse problems. ........ 1

Figure 1-2. Illustration of piezoelectric impedance based active interrogation. ........ 2

Figure 2-1. Illustration of particle swarm. ........ 27

Figure 2-2. Illustration of the state transition process. ........ 30

Figure 2-3. Flowchart of sparsity conscious reinforcement-learning guided MOPSO. ........ 40

Figure 2-4. Schematic of experimental setup. ........ 41

Figure 2-5. Admittance measurement data under the healthy state and finite element prediction after model updating. ........ 42

Figure 2-6. Comparison of number of non-zero components in damage index vector vs iteration by different optimization algorithms (a) Case 1, (b) Case 2, (c) Case 3, and (d) Case 4. ........ 47

Figure 2-7. A representative solution from different algorithms after 100,000 iterations for Case 1 (a) NSGAII, (b) original MOPSO, (c) MOEA/D, and (d) Sparse-MOPSO. ........ 48

Figure 2-8. Case 1 identification results from various algorithms. ........ 50

Figure 2-9. Case 2 identification results from various algorithms. ........ 52

Figure 2-10. Case 3 identification results from various algorithms. ........ 53

Figure 2-11. Case 4 identification results from various algorithms. ........ 54

Figure 2-12. Number of selections of actions guided by Q-table (Case 1). ........ 56

Figure 2-13. Elapsed time comparison with and without integration of Q-learning. ........ 57

Figure 3-1. Flowchart of structural damage identification with bi-objective optimization. ........ 67

Figure 3-2. Illustration of learning automata (LA) scheme. ........ 70

Figure 3-3. Flowchart of the proposed LAMOPSO algorithm. ........ 76

Figure 3-4. Cantilever beam structure with 30 elements. ........ 85

Figure 3-5. Identified results for cantilever beam structure for Case 1 and Case 2. ........ 86

Figure 3-6. Experimental setup (a) testbed; (b) schematical illustration of data acquisition. ........ 88

Figure 3-7. Admittance curves from experiment and from finite element analysis after model updating..90

Figure 3-8. Illustration of segmentation and structural damage cases. ....................................................91

Figure 3-9. Inverse identification results of damage location/severity: Case 1. ........................................93

Figure 3-10. Inverse identification results of damage location/severity: Case 2. ......................................94

Figure 3-11. Inverse identification results of damage location/severity: Case 3. ......................................96

Figure 3-12. Probability distributions with 5 actions...................................................................................97

Figure 3-13. Probability distributions with 3 actions...................................................................................98

Figure 4-1. Schematic diagram of piezoelectric admittance-based damage identification system..........107

Figure 4-2. Illustration of the state transition process..............................................................................118

Figure 4-3. Experimental setup. (a) Schematic diagram of experimental setup, (b) Plate structure, (c) Agilent E3630A power supply for synthetic tunable inductor, (d) Dynamic Signal Analyzer (Agilent 35670A), and (e) Physical synthetic tunable inductor. .........................................................................................121

Figure 4-4. Tunable inductance circuit and physical tunable inductor....................................................121

Figure 4-5. Flowchart for model updating process. ..................................................................................124

Figure 4-6. Admittance curves from experiment and updated simulation. (a) Admittance curves without tunable inductor; (b) Admittance curves with tunable inductor; (c) Admittance comparison with and without inductance; and (d)Admittance curves with tunable inductor in different tuning values. ........................127

Figure 4-7. Case study setup. ....................................................................................................................129

Figure 4-8. Identified 4 solutions from (a) to (d) for Case 1....................................................................130

Figure 4-9. Identified 4 solutions from (a) to (d) for Case 2....................................................................131

Figure 4-10. Statistical illustration of number of identified solutions with respect to the number of inductance tunings, (a) Case1, and (b) Case 2. .........................................................................134

Figure 5-1. Flowchart of proposed two-stage damage identification framework. ...................................151

Figure 5-2. Illustration of learning automata scheme. Action corresponds to $a$. Stochastic environment means searching space. Response corresponds to $\beta$. ................................................................154

Figure 5-3. Experimental setup (a) testbed; (b) data acquisition. ............................................................157

Figure 5-4. Admittance curves from experiment and from finite element analysis after model updating. ............ 158

Figure 5-5. Group identification reliability analysis for Case 1, (a) LAMOPSO algorithm, (b) CMOQLMT algorithm and (c) MMOPSO algorithm. ............ 162

Figure 5-6. Multiple solutions from different algorithms for Case 1. ............ 163

Figure 5-7. Group identification reliability analysis for Case 2, (a) LAMOPSO algorithm, (b) CMOQLMT algorithm and (c) MMOPSO algorithm. ............ 164

Figure 5-8. Multiple solutions from different algorithms for Case 2. ............ 166

Figure 5-9. Group identification reliability analysis for Case 3, (a) LAMOPSO algorithm, (b) CMOQLMT algorithm and (c) MMOPSO algorithm. ............ 167

Figure 5-10. Multiple solutions from different algorithms for Case 3. ............ 168

Figure 6-1. Two-stage damage identification empowered by reduced order modeling. ............ 179

Figure 6-2. Structure-piezoelectric transducer system. ............ 183

Figure 6-3. Illustration of coupling matrix formulation. ............ 187

Figure 6-4. Layout and geometry of the electromechanical system investigated. ............ 190

Figure 6-5. Illutration of small-sized damage in the host strucure. ............ 190

Figure 6-6. Admittances of health and damage scenarios. (a) Magnitude curve over resonant frequency 5,374 Hz; (b) Phase curve over resonant frequency 5,374 Hz; (c) Magnitude curve over resonant frequency 8,484 Hz; (d) Phase curve over resonant frequency 8,484 Hz. ............ 191

Figure 6-7. Admittances of full-scale FE and order-reduced models. (a) Magnitude curve over resonant frequency 5,374 Hz; (b) Phase curve over resonant frequency 5,374 Hz; (c) Magnitude curve over resonant frequency 8,484 Hz; (d) Phase curve over resonant frequency 8,484 Hz. ............ 193

Figure 6-8. Segmentation for coarse-level damge localization. ............ 194

Figure 6-9. Envelope comparison among different damaged segments (red curve indicates the curve under actual damage). (a) Admittance under first segment with damage (5,374 Hz); (b) Admittance under second segment with damage (5,374 Hz); (c) Admittance under first segment with damage (8,484 Hz); (d) Admittance under second segment with damage (8,484 Hz). 194

Figure 6-10. Objective value distribution in original solution database and survived Pareto optimal set (denoted by red color). (a) Magnitude ($\left\|\Delta\mathbf{Y}_{(M)}\right\|_2$); (b) Phase ($\left\|\Delta\mathbf{Y}_{(\phi)}\right\|_2$); (c) $1\text{-MAC}(\mathbf{Y}_{(M)},\mathbf{Y}_{d(M)})$; (d) $1\text{-MAC}(\mathbf{Y}_{(\phi)},\mathbf{Y}_{d(\phi)})$. 196

Figure 6-11. Objective value trend with respect to the damage level of the second segment and 13 Pareto optimal solutions (denoted by red color). (a) Magnitude ($\left\|\Delta\mathbf{Y}_{(M)}\right\|_2$); (b) Phase ($\left\|\Delta\mathbf{Y}_{(\phi)}\right\|_2$); (c) $1\text{-MAC}(\mathbf{Y}_{(M)},\mathbf{Y}_{d(M)})$; (d) $1\text{-MAC}(\mathbf{Y}_{(\phi)},\mathbf{Y}_{d(\phi)})$. 197

Figure 6-12. Further division of the suspicious segment (i.e., second segment) for fine-level damage identification. 199

Figure 6-13. Pareto optimal solutions that represent the damge vectors identified. 200

# List of Tables

Table 2-1. Algorithm 1: Framework of Proposed Sparsity Conscious MOPSO. .......... 29

Table 2-2. Algorithm 2: Sparsity Population Generation. .......... 32

Table 2-3. Algorithm 3: Q-learning. .......... 34

Table 2-4. Algorithm 4: Action Selection. .......... 36

Table 2-5. Mathematical expressions of the actions. .......... 36

Table 2-6. Geometry and material properties of the piezoelectric transducer and the plate. .......... 42

Table 2-7. Computational cost/performance comparison between MOPSO and SRL-MOPSO. .......... 56

Table 3-1. Algorithm 1: Particle swarm optimization framework. .......... 69

Table 3-2. Algorithm 2: Learning Automata guided MOPSO. .......... 74

Table 3-3. Benchmark test functions. .......... 77

Table 3-4. *HV* results from 30 executions with two problem objectives. .......... 80

Table 3-5. *IGD* results from 30 executions with two problem objectives. .......... 82

Table 3-6. Geometry and material properties of the piezoelectric transducer and the plate. .......... 88

Table 4-1. Reward and penalty settings. .......... 116

Table 4-2. Geometry and material properties of the piezoelectric transducer and the plate. .......... 123

Table 5-1. Algorithm: Message Passing. .......... 148

Table 5-2. Damage case settings. .......... 160

Table 6-1. Finite element modeling details. .......... 190

Table 6-2. Operating parameter set-up of MOSA algorithm. .......... 199

Table 6-3. Pareto front (objective values of identified solutions). .......... 200

# Chapter 1. Introduction

## 1.1. Background and Problem Statement

An inverse problem is a type of problem in which the goal is to deduce he unknown parameters, inputs, or system characteristics from observed outputs or responses. This is the opposite of a direct problem, where known inputs are used to predict outputs through a well-defined model. Inverse problems are fundamental in science and engineering because they allow us to interpret and understand complex systems based on observable data, especially when direct measurements of the internal states or parameters are impractical or impossible. Mathematically, an inverse problem can be framed as finding an unknown variables $x$ from observation $y$, given a forward model $f$ that relates $x$ to $y$, as illustrated in Figure 1-1.

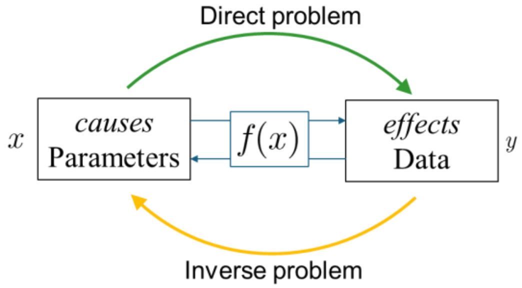

**Figure 1-1.** Schematic illustration of direct and inverse problems.

Typically, the forward model is represented as:

$$y = f(x) + \eta \tag{1.1}$$

where $y$ is the observed data, $f(x)$ represents the forward model (often a function or set of equations that describes how the system behaves), and $\eta$ is noise or error in the measurements. The objective of an inverse problem is to estimate $x$ such that $f(x) \approx y$, within acceptable error bounds, by solving:

$$x^* = \arg\min_x \left\| f(x) - y \right\| + \omega R(x) \tag{1.2}$$

Here, $\left\| f(x) - y \right\|$ represents the discrepancy between model prediction and observed data, often measured in a norm such as the $l_2$ norm (least squared), while $R(x)$ is a regularization term and $\omega$ is regularization weight. Regularization is commonly used in inverse problems to stabilize solutions and ensure uniqueness by penalizing specific properties of $x$ (e.g., enforcing smoothness or sparsity), addressing the challenges posed by the "ill-posed" nature of many inverse problems. The ill-posed problem means that it does not meet the three Hadamard criteria: 1) Solution existence, 2) Solution uniqueness, and 3) Solution stability (Hadamard, 1902). The wide applications of inverse problems are found in fields such as image processing (Bertero et al, 2021; Vogel, 2002), wavefield imaging (Gao et al, 2021), seismic inversion (Lin et al, 2023), structural design (Challapalli et al, 2021), structural health monitoring (Hou and Xia, 2021), to name a few. This dissertation focuses on an inverse problem within structural health monitoring (SHM). SHM is the practice of monitoring the integrity of structure in near-real time by analyzing its dynamic characteristics and conducting inverse analyses. The development of SHM techniques follows a sequence of increasingly complex stages: a) detecting the presence of damage, b) locating the damage, c) assessing the severity of the damage, and d) forecasting the progression of the damage. A major challenge in SHM is the early identification of minor damages, which is crucial for timely intervention and preventing severe consequences. Among the array of SHM techniques, piezoelectric impedance-based approaches are promising (Park et al, 2003; Wang and Tang, 2009; Shi et al, 2022; Min et al, 2012; Selva et al, 2013; Voutetaki et al, 2016; Ai et al, 2018 and 2022; Zhao et al, 2019; Ai and Zhang 2023). These methods utilize high-frequency interrogation to detect small incipient damage based on the two-way electromechanical coupling effect of piezoelectric transducer embedded in the host structure, as illustrated in Figure 1-2.

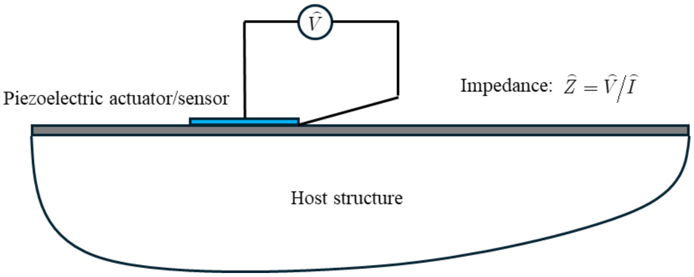

**Figure 1-2.** Illustration of piezoelectric impedance based active interrogation.

The piezoelectric transducer serves as the sensor and actuator simultaneously, which can excite the host structure by applying frequency-sweeping harmonic voltage while collecting frequency response measurements. The change of the piezoelectric impedance signature due to damage can be used as the damage indicator. By comparing the piezoelectric impedance measurements under structural damage with those obtained from a reliable baseline model under healthy status, the location and severity of damage can be identified through inverse analysis (Shuai et al, 2017; Cao et al, 2018a; Fan et al, 2019). Nevertheless, an intrinsic difficulty in damage identification is that the amount of useful information acquired from measurement is generally limited, oftentimes rendering the inverse analysis under-determined. For one thing, in finite element model-based damage identification, a structure is divided into a large number of segments. Each segment may be subject to damage which induces local property change, e.g., stiffness reduction. The inverse analysis usually aims at solving a damage index vector. The dimension of this vector is the number of segments, and each vector component represents possible stiffness reduction percentage in a segment owing to damage occurrence. Additionally, the piezoelectric impedance is only sensitive to damage around the measurement peaks. Simply increasing the number of measurement points (i.e., frequency points) does not necessarily increase the amount of information since there is no guarantee the additional measurements are mathematically independent. SHM is analogous to human healthcare in many ways, including that the diagnostics practice is oftentimes under-determined. Essentially, when the measurement information is limited, one would be satisfied if the inverse analysis can produce a small set of solutions, i.e., possible damage scenarios, that encompass the true damage scenario. If all these solutions point to insignificant damage, continuing operation of the structure can be recommended. Otherwise, additional measurements using different sensing techniques including human inspection can be dispatched to further investigate this small set of possible damage scenarios.

On the other hand, damage usually affects a limited number of areas within a structure, or expressed in mathematical terms, structural damage manifests sparsely. Thus, the regularization is typically utilized by adding a $l_0$ or $l_1$ norm to the above residual formulation with a regularization weight in Equation (1.2). Although advancements have been made, single-objective optimization yields a single solution which may be contaminated by model mismatch and measurement noise, and the inclusion of regularization in these approaches requires the selection of weighting constants that are challenging to determine *a priori*. Alternatively, structural damage identification can be formulated as a multi-objective optimization problem that minimizes concurrently a) the difference between measurements and model prediction in damage parametric space; and b) the $l_0$ norm of the damage index vector. This has multiple advantages intuitively. It avoids the *ad hoc* selection of weights between individual objectives employed in single-objective optimization. Moreover, this formulation yields multiple solutions, which fits the nature of structural damage identification. Yet, the objective function in this context often exhibits multimodality, involving high-dimensional variables due to the reliance on finite element models for damage identification. This complexity can lead to local optima, which, if the optimization process gets trapped, may result in false identifications, or missed damages, posing significant challenges for the optimization algorithms used in structural damage identification. Like human health diagnostics, an excess of solutions, especially redundant or non-sparse ones, can obscure accurate diagnosis. Thus, the goal is to seek a small, sparse, yet diverse solution set that can capture the ground truth.

## 1.2. Review of State-of-the-art Approaches

### 1.2.1. Casting inverse identification into optimization with sparsity

Inverse analysis can be conducted indirectly through optimization-based approaches that minimize the difference between measurement and model prediction in the damage parametric space. To tackle the issue of under-determinedness in damage identification, several investigations have resorted to imposing a physically sensible condition, i.e., the number of segments that are subject to damage is small. This is usually the case for real-world SHM especially when the damage is at its beginning stage with small-size and thus affects only a small region. Mathematically speaking the aforementioned damage index vector should be a sparse vector in which the majority of its components are zero, i.e., the damage index vector has small $l_0$ norm. One way of imposing this condition into a conventional single-objective optimization is through regularization with $l_0$ or $l_1$ norms of the damage index vector. The $l_1$ norm can be used as a convex relaxation of the $l_0$ norm, i.e., as a smooth approximation of the non-differentiable $l_0$ norm (Davenport et al, 2012). Fan et al (2019) employed the spectral projected gradient method in piezoelectric impedance sensing, where the objective function is a residual term added with $l_1$ regularization. Subsequently it has been recognized that population-based metaheuristic algorithms are suitable to solving such problems. For example, Ding et al (2020; 2022) utilized the Jaya algorithm to conduct damage identification, where the $l_{0.5}$ norm which is closer to the $l_0$ norm, was used. Similar effort using sparse representation for damage identification was carried out by Chen and Sun (2021). Although promising results have been obtained, in these single-objective optimization approaches the incorporation of the sparsity regularization involves the selection of weighting constants that are difficult to determine. It is also possible that the single solution identified may still miss the true damage scenario.

Meanwhile, enabling optimization solution with sparsity has been explored in various applications, including feature selection, sparse regression, critical node detection in networking, and neural network training etc. Feature selection aims to identify a subset of relevant features for a given target concept (Dash and Liu, 1997). Xue et al (2012) extended the particle swarm optimization by incorporating nondominated sorting, mutation, crowding distance, and dominance to solve a bi-objective feature selection problem. Sparse regression seeks a sparse approximation solution to the regression problem, with the solution vector containing only a few non-zero elements. Qian et al (2015) proposed a Pareto optimization for subset selection that simultaneously optimizes mean square error and subset size. Ventresca et al (2018) formulated a bi-objective critical node detection problem in networking to maximize the number of connected components and minimize the variance of their cardinalities. Three well-known multi-objective indicators, i.e., additive epsilon, hypervolume, and spacing, are used to measure the quality, and spread of solutions on the approximation front. They demonstrated that the NSGA-II algorithm may outperform other approaches on benchmark problems. Tian et al (2019a) developed a sparse evolutionary algorithm to optimize the weight parameters involved in neural network training. While their method inherits the fundamental ideas from the NSGA-II algorithm, they specifically designed techniques to initialize the population and generate offspring to ensure sparsity.

Under the umbrella of optimization-based inverse analysis, there is a different school of thought being explored, i.e., utilizing multi-objective optimization. From a computational standpoint, a multi-objective optimization naturally avoids the ad hoc selection of weightings between different objectives used in a single-objective optimization. Multi-objective optimization formulation has been employed in parametric identification with heterogeneous measurements for various reasons. For example, Jin et al (2014) developed a model updating formulation in which matching natural frequencies and matching mode shapes are treated as two separate objectives. To find feasible solutions under limited input information, Cha and Buyukozturk (2015) explored utilizing multiple modal strain energy (MSE) expressions as optimization objectives to seek multiple solutions. Pereira et al (2022) investigated the optimal positioning of sensors for SHM. A bi-objective problem is analyzed that minimizes the modal response difference as well as the number of sensors. Cao et al (2018a) specifically looked into incorporating sparsity of the damage index vector, the $l_0$ norm, as a separate objective in addition to the original objective of matching the response measurements, into damage identification.

A major difference between single objective optimization and multi-objective optimization is that the latter may yield multiple solutions. When the inverse analysis is under-determined, multiple solutions are expected mathematically. Seeking a small set of solutions that include the true damage scenario (accuracy) is especially relevant for piezoelectric impedance based active interrogation. On one hand, the high-frequency nature and harmonic responses lead to the possibility of model-based identification of small-size damage. On the other hand, high-frequency analysis using finite elements requires high mesh density and high dimensionality of the model, leading to an even more challenging inverse analysis problem. It is worth noting that the aforementioned investigation by Cao et al (2018a) appears to be the first attempt of multi-objective optimization for damage identification directly integrated with sparsity objective. In that effort, the multi-objective dividing rectangles (DIRECT) algorithm was employed, where a sigmoid transformation similar to that used in machine learning algorithms was utilized to reduce the search space. While a certain level of success has been demonstrated, the DIRECT algorithm is deterministic in nature and can only handle low dimension problems, thus having limited room for tailoring toward improvement. In particular, in the context of sparsity-oriented damage identification, our goal is to find a set of possible solutions that are sufficiently diverse in order to include the true damage scenario. The quality of the solution set in terms of diversity has not been explicitly addressed in related investigations concerning the sparsity of damage index vector.

### 1.2.2. Metaheuristics in damage identification and enhancements

In the realm of optimization, population based intelligent algorithms such as evolutionary algorithm (Alkayem et al, 2018), simulated annealing (Yao et al, 2017), genetic algorithm (Tiachacht et al, 2018), Jaya algorithm (Ding et al, 2019), and particle swarm (Minh et al, 2021) etc. have attracted considerable recent attention, as a variety of metaheuristics have been synthesized to tackle issues ranging from computational efficiency to various application-specific requirements. It is known that damage identification through inverse optimization is subject to many local extremes in the parametric space. How to enhance searching in the optimization to escape from local extremes becomes one focal point. For example, a hybridization of the K-clustering-based Jaya algorithm and Trees Seeds algorithm was proposed to achieve robust searching (Ding et al, 2020). Similarly, it was demonstrated that the Jaya algorithm combined with Hooke–Jeeves pattern search can improve the search performance (Ding et al, 2022). Genetic Algorithm (GA) was integrated with a Modified Cornwell Indicator (MCI) and then applied to damage identification for frame structure (Tiachacht et al, 2018). Minh et al (2021) developed an enhanced particle swarm optimization, where parameters can be adjusted online to control the convergence rate in each movement of a particle and to seek global optimum. Zheng et al (2022) improved empirical learning based on the idea of motivating solution candidates to move to better positions around their own initial positions through leveraging the experience of other candidates. A known challenge in optimization-based inverse identification is that, as the number of unknowns increases, the response surface generally becomes more complicated. As such, significant research opportunities exist for evolution- or population-based optimizations designed for such applications. In particular, most of the aforementioned algorithmic advancements are based on single-objective formulation. Enhancing the solution quality in multi-objective optimization tailored for damage identification application remains to be explored systematically.

### 1.2.3. Mechatronics integration for damage identification

To solve for a small solution set, one can resort to data enrichment. This is like human healthcare. When more information is obtained, one will have a narrow diagnose spectrum, or the small solution set in context of structural health monitoring.  Once that is achieved, the maintenance would only need to concentrate on these specific, small solution sets, greatly reducing maintenance costs. Toward this goal, the enrichment of measurement data is essential. It is worth noting that one unique feature of piezoelectric-based sensing setup allows for the seamless integration with circuitry elements, such as tunable inductor shunted with the piezoelectric transducer, to improve the dynamic measurement. The circuitry introduces additional degrees of freedom, and the dynamics of the electromechanical sensor-structure system can be successively altered upon tuning the inductor to different values. For the same structural damage, a larger set of measurements can be acquired, substantially increasing both the amount and variety of system response changes. This effectively mitigates the underdetermined challenge in the inverse analysis for damage identification. In earlier efforts, Jiang et al (2006, 2007, 2008) developed a tunable inductor based piezoelectric LC-oscillator that can alter the baseline resonant frequencies of the integrated system, thereby enriching the frequency-shift information employed for damage detection. Moreover, through properly tuned inductance, a strong interaction between the mechanical structure and electrical circuit can be achieved, leading to a significant increase in sensitivity for detecting damage. This tunable inductance technique can also lead to more robust damage detection in the presence of uncertainties (Zhao et al, 2008). Subsequently, Wang and Tang (2010a, 2010b) started to implement the tunable inductance concept into high-frequency impedance/admittance measurements that are promising for high-accuracy damage identification. Not only can LC resonance amplify the impedance measurements and the damage features but can substantially enrich the available measurement information. Similarly, Kim and Wang (2014) and Kim et al (2015) developed a method to enhance impedance measurements by integrating structures with an additional transducer and adaptive piezoelectric circuitry, effectively altering the integrated dynamics of the system. This approach, validated through spectral element method and experiments on a fixed-fixed beam structure, proved effective in accurately identifying damage in terms of location and severity. Furthering this, Kim and Wang (2019) expanded the technique to include bifurcation phenomena via bistable circuitry networks, improving damage-induced impedance measurement accuracy and noise resistance. These enhancements were substantiated through numerical and experimental studies on fixed-fixed beam structures. Recently, Zhang et al (2022a) explored the integration of tunable inductors into piezoelectric transducer circuits, enriching datasets for 1D CNN-based structural damage identification. This method, practiced on a beam structure with numerical simulation, demonstrated increased discrimination between damage types, including bolt loosening and mass changes, and achieved higher accuracy in damage classification compared to non-enriched methods. However, a gap remains in fully leveraging the potential of tunable circuitry integration within multi-objective optimization frameworks for model-based damage identification.

### 1.2.4. Multi-stage/level damage identification and model order reduction

Another major challenge lies in how to handle the high-dimensional, multi-modal optimization problem to find a diverse yet small solution set that can capture the true damage scenario. Furthermore, the incorporation of the $l_0$ norm as the second objective requires the identification of the sparsest solutions, which involves evaluating an exponentially increasing number of possible combinations of non-zero entries. This in theory leads to an NP-hard problem, making it computationally prohibitive especially for structural damage identification with high-frequency interrogation. Here, NP stands for 'nondeterministic polynomial time,' a classification of problems for which a computer can verify a solution in a reasonable amount of time if one is provided. In contrast, NP-hard problems are those where finding a solution is extremely difficult, even though verifying a given solution might be easy. These problems are highly complex, requiring significant computational resources to solve (Foucart and Rauhut, 2013). To tackle the challenges in inverse analysis of high-frequency active interrogation through multi-objective optimization, we aim at addressing two issues, i.e., reducing the dimensionality of the problem to alleviate the difficulty of the search, and enhancing the search capability of the algorithm using local heuristics to ensure solution accuracy as reviewed in Section 1.2.2. In terms of dimensionality reduction, a hierarchical approach is intuitive: first evaluating the location of structural damage, and then assessing the location and severity of the damage. Du et al (2019) introduced a two-phase structure damage assessment method that initially detects potential damages through a modal strain energy index and then quantifies severity using the Jaya algorithm. Perera et al (2020) implemented a two-stage damage identification method for complex structures using the roaming damage method, which identifies damage ranging from large low-damage areas to severely damaged individual beams, enhanced by a multi-objective optimization based on power mode shapes for comprehensive damage detection. Barman et al (2021) applied a two-stage method where the first stage uses mode-shape curvature-based damage indices for rough estimation of damage location, and the second stage refines this using a mixed unified particle swarm algorithm for precise lengthwise and interface location determination in composite structures. The results indicate high accuracy in identifying single and multiple delaminations, showing potential under noisy conditions. In the context of multi-objective optimization problem setting of this study, we can employ expert knowledge to facilitate two-stage damage identification. This expert insight is that structural damage typically exhibits sparsity or damage is not uniformly distributed. This inspires us to group identification variables into limited subsets, where if damage occurs within one group, the other groups remain sparse, trending towards zero collectively. Thus, in the first layer, we utilize the Group Lasso method instead of directly incorporating the $l_0$ norm. Group Lasso works by applying a penalty that is proportional to the $l_2$ norm of the coefficients within each group and then summing these norms with an $l_1$ penalty across groups. This method allows us to enforce sparsity at the group level, effectively detecting which group the damage falls into. Next, we pass this information to the second step. In the second phase of optimization, we only focus on the damaged variable group, significantly simplifying the search.

It is worth noting that our two-stage damage identification process involves two main components: Group Lasso and the Technique for Order Preference by Similarity to Ideal Solution (TOPSIS). Group Lasso drives entire variable groups toward sparsity. This technique has been applied in related research. For example, Dimopoulos et al (2022) introduced two sparsity-based methods using low-frequency response functions for damage detection, leveraging complex Group Lasso strategies to localize multiple defects with a single sensor. Similarly, Zhang et al (2022b) applied Group Lasso to enhance moving force identification by grouping non-overlapping sparse coefficient vectors, which correspond to vehicle forces, and linking these groups with measurements to accurately reconstruct the moving forces. In our approach, TOPSIS is used to facilitate the transition between stages. As a multi-criteria decision-making method, TOPSIS ranks alternatives based on their proximity to an ideal solution (Greco et al, 2016). It is selected for its efficiency in translating complex optimization outcomes into actionable insights, effectively bridging the gap between stages by identifying the most promising solutions for further analysis.

All above is related to the efforts paid on tailoring the algorithm for a better search. On the other hand, we can also conduct multi-level damage identification in an efficient and accurate manner from the aspects of model order reduction. With advancements in FE analysis, model order reduction has become a critical topic in computational mechanics and dynamics. Over the past few decades, a variety of order-reduction techniques have been developed (Lin et al, 2009; Basselink et al, 2013; Panayirci et al, 2011). Among these, component mode synthesis (CMS) methods stand out as an important and representative branch, demonstrating potential in a wide range of applications (Zhou and Tang, 2016 and 2021a; Masson et al, 2006). Yu et al (2016) developed an element-by-element model updating approach using the component mode synthesis (CMS) method, which significantly enhances computational efficiency in large-scale structural analysis and facilitates accurate damage identification at the element level. Butland and Avitabile (2010) proposed a reduced-order CMS method that incorporates test data into system modeling. This approach combines reduced components to accurately capture dynamic characteristics, even in the presence of typical measurement contaminants. Sarsri and Azrar (2016) presented a stochastic dynamic analysis method for large structures with uncertain parameters, coupling CMS with a second-order perturbation approach to compute the statistical moments of dynamic response efficiently in high-dimensional finite element models. Zhou et al (2016) developed a CMS approach specifically for NURBS finite element models. They introduced an optimized interface construction that preserves geometry consistency during dynamic analysis. This method was validated using case studies on wind turbine blades. Wang et al (2020) proposed a model-updating approach based on CMS and perturbation analysis, enabling efficient reduction in computational cost for large-scale finite element models by capturing higher-order mode effects and applying the method to a wing structure and bolted plate. Additional insights are provided by Chen et al (2014), Wang et al (2018), and Weng et al (2020). However, it is important to note that current CMS methods are typically limited to pure mechanical analyses. In this study, the presence of a piezoelectric transducer embedded in the host structure requires an electromechanical finite element model to capture the coupling between mechanical and electrical domains. Therefore, it is essential to extend standard CMS methods to make them compatible with electromechanical finite element modeling.

## 1.3. Dissertation Outline

Building upon the review of state-of-the-art literature, in this dissertation we aim at the establishment of a new sparsity conscious multi-objective optimization framework that can fully unleash the capability of piezoelectric impedance measurement for damage identification. To obtain small, sparse yet diverse solution set for early damage identification, we conduct research work on several aspects as outlined below:

- Develop a novel inverse identification framework utilizing the intelligent swarm optimizer which possesses flexibility for enhancement. A sparsity enforcement is first embedded into the population generation of the optimizer, which yields a solution repository intrinsically possessing sparsity. Then, the reinforcement learning is applied so the agents can adaptively opt for local strategies with the aim of enriching the searching patterns to diversify the solutions. Through the incorporation of a Q-table, searching toward more promising directions will be rewarded. The case analyses employing experimental data indicate that this sparsity-conscious multi-objective particle swarm optimization technique can lead to a small solution set which generally encompasses the true damage scenario. This effectively solves the structural damage identification problem with piezoelectric impedance measurement.

- Propose a reinforcement learning based multi-swarm optimizer to tackle challenges in pursuit of a small yet diverse solution set that can capture the true damage scenario as one of the solutions. The proposed method leverages the flexibility of the particle swarm optimizer and incorporates novel strategies of metaheuristics to realize targeted improvement. To enable the particle swarm to adaptively select the appropriate search strategy based on the current environment, the learning automata technique is adopted, which sidesteps the need for reward strategy selection that is usually ad hoc at each step of the search. The integration harnesses the automatic learning and self-adaptation capabilities of learning automata, enabling the particles to navigate based on environmental signals. This leads to accumulated probabilities tied to advantageous movements, fostering an adaptive exploration of particles in the search space. The proposed approach is first validated through implementing into benchmark test cases with comparisons. It is then applied to structural damage identification with piezoelectric admittance experimental signals. The results highlight the capability of the algorithm to identify a small solution set with high accuracy to match the actual damage scenario.
- A new methodology of tunable sensing in conjunction with multi-objective optimization inverse analysis is established. Taking advantage of the two-way electromechanical coupling of piezoelectric transducers, tunable inductance is integrated into the measurement circuit. For the same damage scenario, by tuning the inductance to a series of values, a family of impedance measurements can be acquired. Meanwhile, the inverse analysis is cast into a multi-objective optimization problem, aiming at minimizing the difference between measurement and model prediction and achieving sparsity in damage index vector. The circuitry integration details as well as the algorithm enhancement are reported with systematic case investigations. It is validated that

the new methodology with enriched measurement can produce smaller solution set encompassing the true damage scenario, thereby providing vital information for diagnoses and prognosis.

- A hierarchical framework is synthesized that searches potential damage locations first and then delves into accurate characterization of damage. To address the high-dimensional and multimodal challenges intensified by high-frequency measurement towards high-precision identification, Group Lasso technique is adopted for sparsity induction, and utilize the Technique for Order Preference by Similarity to Ideal Solution to realize optimization phase transition, aiming at improving the computational efficiency as well as the accuracy. The validation of our approach through a piezoelectric admittance sensing testbed underscores its potential for structural health monitoring practices by providing a robust, accurate, and computationally efficient approach for early-stage damage identification and assessment.
- Leveraging reduced-order modeling, a two-stage damage identification scheme is developed aiming at decomposing the complex task into a sequence of manageable steps: coarse damage localization and fine damage identification. Component mode synthesis is firstly applied to develop a reduced-order model of the system. This significantly decreases computational demands while preserving essential dynamic characteristics. The reduced model enables efficient forward analysis to approximate the location of potential damage within specific substructures of the plate. Once the probable damaged substructures are identified, an inverse model updating technique is employed. This step precisely determines the damage location and quantifies its severity within the targeted substructure. By focusing computational resources on smaller regions, the method enhances both accuracy and efficiency. Systematic case studies validate the effectiveness of the proposed approach, demonstrating its capability to accurately identify small-sized damages with reduced computational effort

# Chapter 2. Piezoelectric Impedance-based High-accuracy Damage Identification Using Sparsity Conscious Multi-Objective Optimization Inverse Analysis

Two elements are essential in structural health monitoring utilizing dynamic responses: response measurement with high-frequency contents, i.e., small characteristic wavelengths, that can adequately reflect damage features, and effective inverse identification analysis that is however oftentimes under-determined. The advancement of smart structure integration has led to active interrogation through frequency-sweeping piezoelectric impedance measurement at high frequency range. In this research we develop a multi-objective optimization formulation for the identification of damage location and severity utilizing piezoelectric impedance. While one optimization objective is to match the response measurement with finite element model prediction in the damage parametric space, the other is the number of locations of damage, i.e., the sparsity of damage index as the solution vector, since damage usually occurs within a small number of locations. This multi-objective formulation fits well the under-determined nature of damage identification, as it naturally provides multiple solutions as basis for further elucidation. The challenge remaining is how to find a small solution set that can include the actual damage scenario. Here we develop a novel inverse identification framework utilizing the intelligent swarm optimizer which possesses flexibility for enhancement. We first embed a sparsity enforcement process into the population generation of the optimizer, which yields a solution repository intrinsically possessing sparsity. We then apply reinforcement learning so the agents can adaptively opt for local strategies with the aim of enriching the searching patterns to diversify the solutions. Through the incorporation of a Q-table, searching toward more promising directions will be rewarded. Our case analyses employing experimental data indicate that this sparsity-conscious multi-objective particle swarm optimization technique can lead to a small solution set which generally encompasses the true damage scenario. This effectively solves the structural damage identification problem with piezoelectric impedance measurement.

## 2.1. Introduction

In structural health monitoring (SHM), dynamic responses of a host structure are utilized to infer the occurrence of damage and/or to identify the damage. A well-designed SHM scheme can positively impact the reliability and durability of various mechanical, aerospace, marine, and infrastructure systems. It is known that two elements are essential in SHM, the acquisition of dynamic responses carrying high-frequency contents that can be effectively extracted, and the inverse analysis of response change for the detection and identification of damage. High-frequency responses correspond to smaller characteristic wavelengths that can reflect features of small-size damage. The advent of smart materials has led to measurement advancement. The multi-field coupling of many smart transducers can facilitate near real-time active interrogation of a host structure, i.e., inducing carefully designed dynamic responses and then sensing the change of such responses as damage occurs. One type of example is the piezoelectric transducers that are compact in size, possess excellent linearity and can be easily integrated to a host structure (Park et al, 2003; Wang and Tang, 2009; Shi et al, 2022). They have been employed in a number of damage detection and identification schemes to actuate and sense global vibration, wave propagation, and electro-mechanical impedance etc (Li et al, 2019; Zhu et al, 2021; Xu and Deng, 2022). In particular, the piezoelectric impedance approach, i.e., using the same piezoelectric transducer to carry out frequency-sweeping excitation and simultaneously sense the local oscillation which then yields the piezoelectric impedance information, has shown promising aspects. The piezoelectric impedance can be measured in high-frequency range, and the harmonic responses acquired may enable model-based damage identification (Kim and Wang, 2014; Shuai et al, 2017; Cao et al, 2018a; Fan et al, 2020).

Despite the progresses made in recent years, there is however still significant technological gaps in SHM especially in damage identification inverse analysis. Although in many cases the detection of damage occurrence is important, ultimately the identification of location and severity of damage can provide vital information toward operation and maintenance of the structure as well as its remaining useful life prediction. From the viewpoint of a structure being continuum, structural damage is characterized by continuous variables, exhibiting in theory infinitely many possible damage scenarios. As such, inverse analysis based on finite element modeling has an edge over classification type of approaches that typically rely on a relatively small size of damage profiles for training. Nevertheless, an intrinsic difficulty in damage identification is that the amount of useful information acquired from measurement is generally limited, oftentimes rendering the inverse analysis under-determined. In finite element model-based damage identification, a structure is divided into a large number of segments. Each segment may be subject to damage which induces local property change, e.g., stiffness reduction. The inverse analysis usually aims at solving a damage index vector. The dimension of this vector is the number of segments, and each vector component represents possible stiffness reduction percentage in a segment owing to damage occurrence. The piezoelectric impedance is only sensitive to damage around the measurement peaks. Simply increasing the number of measurement points (i.e., frequency points) does not necessarily increase the amount of information since there is no guarantee the additional measurements are mathematically independent. Indeed, how to utilize the limited measurement to solve for the damage index vector has become a major challenge in SHM. Obviously, direct matrix inversion based on finite element model with artificial constraints such as the least square may not yield true damage scenario.

Inverse analysis can be conducted indirectly through optimization-based approaches that minimize the difference between measurement and model prediction in the damage parametric space. To tackle the issue of under-determinedness in damage identification, several investigations have resorted to imposing a physically sensible condition, i.e., the number of segments that are subject to damage is small. This is usually the case for real-world SHM especially when the damage is at its beginning stage with small-size and thus affects only a small region. Mathematically speaking the aforementioned damage index vector should be a sparse vector in which the majority of its components are zero, i.e., the damage index vector has small $l_0$ norm. One way of imposing this condition into a conventional single-objective optimization is through regularization with $l_0$ or $l_1$ norms of the damage index vector. The $l_1$ norm can be used as a convex relaxation of the $l_0$ norm, i.e., as a smooth approximation of the non-differentiable $l_0$ norm (Davenport et al, 2012). Fan et al (2019) employed the spectral projected gradient method in piezoelectric impedance sensing, where the objective function is a residual term added with $l_1$ regularization. Subsequently it has been recognized that population-based metaheuristic algorithms are suitable to solving such problems. For example, Ding et al (2020; 2022) utilized the Jaya algorithm to conduct damage identification, where the $l_{0.5}$ norm which is closer to the $l_0$ norm, was used. Similar effort using sparse representation for damage identification was carried out by Chen and Sun (2021). Although promising results have been obtained, in these single-objective optimization approaches the incorporation of the sparsity regularization involves the selection of weighting constants that are difficult to determine. It is also possible that the single solution identified may still miss the true damage scenario.

Under the umbrella of optimization-based inverse analysis, there is a different school of thought being explored, i.e., utilizing multi-objective optimization. From a computational standpoint, a multi-objective optimization naturally avoids the *ad hoc* selection of weightings between different objectives used in a single-objective optimization. Multi-objective optimization formulation has been employed in parametric identification with heterogeneous measurements for various reasons. For example, Jin et al (2014) developed a model updating formulation in which matching natural frequencies and matching mode shapes are treated as two separate objectives. To find feasible solutions under limited input information, Cha and Buyukozturk (2015) explored utilizing multiple modal strain energy (MSE) expressions as optimization objectives to seek multiple solutions. Pereira et al (2022) investigated the optimal positioning of sensors for SHM. A bi-objective problem is analyzed that minimizes the modal response difference as well as the number of sensors. Cao et al (2018a) specifically looked into incorporating sparsity of the damage index vector, the $l_0$ norm, as a separate objective in addition to the original objective of matching the response measurements, into damage identification.

A major difference between single objective optimization and multi-objective optimization is that the latter may yield multiple solutions. When the inverse analysis is under-determined, multiple solutions are expected mathematically. Indeed, SHM is analogous to human healthcare in many ways, including that the diagnostics practice is oftentimes under-determined. Essentially, when the measurement information is limited, one would be satisfied if the inverse analysis can produce a small set of solutions, i.e., possible damage scenarios, that encompass the true damage scenario. If all these solutions point to insignificant damage, continuing operation of the structure can be recommended. Otherwise, additional measurements using different sensing techniques including human inspection can be dispatched to further investigate this small set of possible damage scenarios. Seeking a small set of solutions that include the true damage scenario is especially relevant for piezoelectric impedance based active interrogation. On one hand, the high-frequency nature and harmonic responses lead to the possibility of model-based identification of small-size damage. On the other hand, high-frequency analysis using finite element requires high mesh density and high dimensionality of the model, leading to an even more challenging inverse analysis problem. It is worth noting that the aforementioned investigation by Cao et al (2018a) appears to be the first attempt of multi-objective optimization for damage identification directly integrated with sparsity objective. In that effort, the multi-objective dividing rectangles (DIRECT) algorithm was employed, where a sigmoid transformation similar to that used in machine learning algorithms was utilized to reduce the search space. While certain level of success has been demonstrated, the DIRECT algorithm is deterministic in nature and can only handle low dimension problems, thus having limited room for tailoring toward improvement. In particular, in the context of sparsity-oriented damage identification, our goal is to find a set of possible solutions that are sufficiently diverse in order to include the true damage scenario. The quality of the solution set in terms of diversity has not been explicitly addressed in related investigations concerning the sparsity of damage index vector.

In the realm of optimization, population based intelligent algorithms such as evolutionary algorithm (Alkayem et al, 2018), simulated annealing (Yao et al, 2017), genetic algorithm (Tiachacht et al, 2018), Jaya algorithm (Ding et al, 2019), and particle swarm (Minh et al, 2021) etc have attracted considerable recent attention, as a variety of metaheuristics have been synthesized to tackle issues ranging from computational efficiency to various application-specific requirements. It is known that damage identification through inverse optimization is subject to many local extremes in the parametric space. How to enhance searching in the optimization to escape from local extremes becomes one focal point. For example, a hybridization of the K-clustering-based Jaya algorithm and Trees Seeds algorithm was proposed to achieve robust searching (Ding et al, 2020). Similarly, it was demonstrated that the Jaya algorithm combined with Hooke–Jeeves pattern search can improve the search performance (Ding et al, 2022). Genetic Algorithm (GA) was integrated with a Modified Cornwell Indicator (MCI) and then applied to damage identification for frame structure (Tiachacht et al, 2018). Minh et al (2021) developed an enhanced particle swarm optimization, where parameters can be adjusted online to control the convergence rate in each movement of a particle and to seek global optimum. Zheng et al (2022) improved empirical learning based on the idea of motivating solution candidates to move to better positions around their own initial positions through leveraging the experience of other candidates. A known challenge in optimization-based inverse identification is that, as the number of unknowns increases, the response surface generally becomes more complicated. As such, significant research opportunities exist for evolution- or population-based optimizations designed for such applications. In particular, most of the aforementioned algorithmic advancements are based on single-objective formulation. Enhancing the solution quality in multi-objective optimization tailored for damage identification application remains to be explored systematically.

Meanwhile, enabling optimization solution with sparsity has been explored in various applications, including feature selection, sparse regression, critical node detection in networking, and neural network training etc. Feature selection aims to identify a subset of relevant features for a given target concept (Dash and Liu, 1997). Xue et al (2012) extended the particle swarm optimization by incorporating nondominated sorting, mutation, crowding distance, and dominance to solve a bi-objective feature selection problem. Sparse regression seeks a sparse approximation solution to the regression problem, with the solution vector containing only a few non-zero elements. Qian et al (2015) proposed a Pareto optimization for subset selection that simultaneously optimizes mean square error and subset size. Ventresca et al (2018) formulated a bi-objective critical node detection problem in networking to maximize the number of connected components and minimize the variance of their cardinalities. Three well-known multi-objective indicators, i.e., additive epsilon, hypervolume, and spacing, are used to measure the quality, and spread of solutions on the approximation front. They demonstrated that the NSGA-II algorithm may outperform other approaches on benchmark problems. Tian et al (2019a) developed a sparse evolutionary algorithm to optimize the weight parameters involved in neural network training. While their method inherits the fundamental ideas from the NSGA-II algorithm, they specifically designed techniques to initialize the population and generate offspring to ensure sparsity.

Building upon previous investigations, in this research we aim at the establishment of a new sparsity conscious multi-objective optimization framework that can fully unleash the capability of piezoelectric impedance measurement for damage identification. We choose the multi-objective particle swarm optimization (MOPSO) as the basic approach, owing to its fast convergence and in particular the capability of obtaining a set of trade-off solutions in a single run which offers the potential for designing local search strategies to enrich the search patterns. We start from a sparse population generation technique that can yield the initial sparsity of the damage index vector and then iterate during the solution procedure. This can tackle the issue of high dimensionality in inverse identification. Moreover, we incorporate local searches with a time-varying inertia weight and two sets of acceleration coefficients. Both sets form two distinct coefficient-based local search strategies that can facilitate firstly exploration and subsequently exploitation. Additionally, we develop three mutation-based local search strategies to trigger a local particle movement to encourage exploration abilities, resulting in a diverse set of solutions. Indeed, imposing sparsity matches with the damage identification nature, and it can also impact the search process toward the optimal solutions. As such, it provides the opportunity to ensure that the parametric space is searched thoroughly to yield a small but diverse solution set. Here we integrate Q-Learning, which is a reinforcement learning policy that will find the next best action, given a current state, into MOPSO. It chooses the action based on the maximum Q-table value and aims to maximize the reward for the achievement, i.e., finding a better solution. With this reinforcement learning, each particle is considered as an agent and each agent will have multiple search methods (local searching strategies). Through Q-table, the agents can interact well with the search environment as well as other agents, thus enhancing the global search capability. All the strategies are not executed simultaneously. Instead, a promising one will be selected at the current iteration according to the

Q-learning algorithm. The combination of sparse population generation and reinforcement learning based strategies for solution exploration will yield a small solution set that includes the true damage scenario.

The rest of the paper is organized as follows. In Section 2.2, finite element modeling of piezoelectric impedance for structural health monitoring is outlined, followed by the problem formulation of damage identification emphasizing sparsity of damage index vector. Section 2.3 elaborates the multi-objective optimization solution procedure, which includes the sparse population generation and iteration, and the integration details of Q-learning with MOPSO. In Section 2.4, an experimental case utilizing the new algorithm is presented. The case setup with data acquisition from the physical testbed and the corresponding finite element analysis are described in detail, followed by inverse identification of damage using experimental data. The solution quality is demonstrated. Section 2.5 gives the concluding remarks.

## 2.2. Piezoelectric Impedance-based Damage Identification

In this section, we present the formulation of damage identification utilizing piezoelectric impedance measurement. As the identification is model based, we first outline the finite element modeling of piezoelectric impedance prediction/simulation. We then formulate a multi-objective optimization problem that will be used to identify the location and severity of damage in a structure.

### 2.2.1. Finite element modeling of piezoelectric impedance

When a piezoelectric transducer is integrated to a host structure, the coupled structure-transducer interaction is characterized by the following equations (Shuai et al, 2017; Cao et al, 2018a)

$$\mathbf{M}\ddot{\mathbf{q}} + \mathbf{C}\dot{\mathbf{q}} + \mathbf{K}\mathbf{q} + \mathbf{K}_{12}Q = \mathbf{0} \tag{2.1a}$$

$$R\dot{Q} + k_c Q + \mathbf{K}_{12}^T\mathbf{q} = V_{\text{in}} \tag{2.1b}$$

where $\mathbf{q}$ is the displacement vector, $k_c$ is the inverse of the capacitance of the piezoelectric transducer; $\mathbf{K}_{12}$ is the electromechanical coupling vector between the transducer and the structure, and $\mathbf{K}$, $\mathbf{C}$, and $\mathbf{M}$ are the stiffness, damping, and mass matrices, respectively. In this research, we use piezoelectric admittance which is the reciprocal of impedance as information carrier for damage identification. Specifically, we apply frequency-sweeping harmonic voltage excitation, denoted as $V_{\mathrm{in}}$, to the transducer. $Q$ is the electrical charge on the surface of the piezoelectric transducer, and $R$ is the resistance in the measurement circuitry. It is worth noting that in the experimental implementation, we measure the voltage drop across the resistor, which is denoted as $V_{\mathrm{out}}$, and subsequently obtain the current as $\dot{Q} = V_{\mathrm{out}} / R$. As such, here we include an additional term $R\dot{Q}$ in Equation (1b), compared with those presented in previous research (Shuai et al, 2017; Cao et al, 2018a). We let the excitation frequency be denoted as $\omega$, and use overbar hereafter to indicate magnitude of the corresponding response variable. The piezoelectric admittance of the healthy structure, which is the ratio of the current magnitude and the voltage magnitude, can be derived as

$$y_h(\omega) = \frac{\bar{\dot{Q}}}{\bar{V}_{\mathrm{in}}} = \frac{j\omega\bar{Q}}{\bar{V}_{\mathrm{in}}} = \frac{j\omega}{j\omega R + k_c - \mathbf{K}_{12}^T(\mathbf{K} + j\omega\mathbf{C} - \omega^2\mathbf{M})^{-1}\mathbf{K}_{12}} \tag{2.2}$$

where *j* is the imaginary unit.

In a finite element model for damage identification, the structure is generally divided into *n* segments to facilitate the identification of location and severity of damage. That is, each segment is susceptible of damage occurrence, and damage causes homogenized change of structural properties within a segment. In this research, without loss of generality, we assume damage causes stiffness reduction in one or multiple segments. As such, the stiffness matrix with structural damage occurrence, $\mathbf{K}_d$, can then be expressed as $\mathbf{K}_d = \sum_{i=1}^{n} \mathbf{K}_h^i (1 - \alpha_i)$, in which $\mathbf{K}_h^i$ is stiffness matrix of the *i*-th segment under the healthy status and the summation refers to the direct summation in finite element model assemblage. $\alpha_i \in [0,1]$ is the damage index indicating the possible stiffness loss of the *i*-th segment, which is to be identified. The piezoelectric admittance corresponding to the damaged structure can be written as

$$y_d(\omega) = \frac{j\omega}{j\omega R + k_c - \mathbf{K}_{12}^T(\mathbf{K}_d + j\omega\mathbf{C} - \omega^2\mathbf{M})^{-1}\mathbf{K}_{12}} \tag{2.3}$$

Mathematically, the change of admittance can be derived based on Equations (2.2) and (2.3). To increase the computational efficiency, based on the assumption of damage being small in size, we apply the Taylor series expansion to the expression of the change of admittance and ignore the higher-order terms, i.e.,

$$\Delta y(\omega) = \sum_{i=1}^{n} [j\omega(j\omega R + k_c - \mathbf{K}_{12}^T \mathbf{Z}^{-1} \mathbf{K}_{12})^{-2} \mathbf{K}_{12}^T \mathbf{Z}^{-1} (\mathbf{L}_i^T \mathbf{K}_h^i \mathbf{L}_i) \mathbf{Z}^{-1} \mathbf{K}_{12}]\, \alpha_i \tag{2.4}$$

where $\mathbf{Z} = \mathbf{K} - \mathbf{M}\omega^2 + j\omega\mathbf{C}$ represents the dynamic stiffness of the structure, and $\mathbf{L}$ is the Boolean matrix indicating how the segmental stiffness matrices are assembled into the global stiffness matrix. Once again, the term $j\omega R$ corresponds to the measurement resistance employed in experiment. This formulation is completely consistent with the actual experimental data acquisition procedure. In Equation (2.4), the change of admittance under excitation frequency $\omega$ is denoted as $\Delta y(\omega)$. In damage identification practice, we conduct frequency sweeping in the frequency range of interest, and acquire a series of admittance changes $\Delta y(\omega_1)$, $\cdots$, $\Delta y(\omega_m)$, under *m* different excitation frequencies $\omega_1$, $\cdots$, $\omega_m$. We introduce the following notations of excitation frequency vector, admittance change vector, and damage index vector,

$$\boldsymbol{\omega} = [\omega_1, \quad \cdots, \quad \omega_m]^T \tag{2.5a}$$

$$\Delta \mathbf{y}(\boldsymbol{\omega}) = \left[\Delta y(\omega_1), \quad \ldots, \quad \Delta y(\omega_m)\right]^T \tag{2.5b}$$

$$\boldsymbol{\alpha} = [\alpha_1, \quad \cdots, \quad \alpha_n]^T \tag{2.5c}$$

Based on Equation (2.4), we can then obtain the following relation,

$$\Delta \mathbf{y} = \begin{bmatrix} \Delta y(\omega_1) \\ \vdots \\ \Delta y(\omega_m) \end{bmatrix} = \mathbf{T}_{m\times n} \boldsymbol{\alpha}_{n\times 1} \tag{2.6}$$

where **T** is the finite element-based sensitivity matrix that links the admittance change vector with the damage index vector.

### 2.2.2. Formulation of sparsity conscious multi-objective optimization for damage identification

In actual practice of damage identification, we conduct model updating so the finite element model of the healthy structure can match the actual structure. We then conduct piezoelectric admittance measurement to obtain the admittance change vector $\Delta \mathbf{y}$ with respect to the healthy admittance. However, it is worth emphasizing that, while the damage index vector $\boldsymbol{\alpha}$ and the admittance change vector is related directly as shown in Equation (2.6), this equation for solving for the damage index vector is oftentimes under-determined. In the admittance versus frequency curve, the peaks correspond to structural resonances. Structural damage manifests itself only in the vicinity of the resonant peaks in the admittance measurements, which means the information for damage inference is generally limited. Although one can increase the number of sweep frequency points of admittance measurement, there is no guarantee that such an increase can lead to additional information. In other words, simply increasing the number of measurement points does not necessarily increase the row rank of the sensitivity matrix **T**. This is especially true for admittance measurements at high frequency range. In order to achieve high-precision identification of small size damage, the finite element mesh density is high, and the segment size is usually chosen to be relatively small, leading to large number of segments, $n$.

Aiming at tackling this issue, in this research we cast the inverse identification into a multi-objective optimization formulation. One objective is obvious, i.e., we need to minimize the difference between the measured admittance change, $\Delta \mathbf{y}$, and the model prediction in damage parametric space, $\mathbf{T}\boldsymbol{\alpha}$. In practical situation, damage usually occurs within a small region of the structure, especially when the damage is at its beginning stage with small size. Therefore, we introduce another objective function that the damage index vector $\boldsymbol{\alpha}$ is sparse with small $l_0$ norm. The optimization problem then takes the following formulation with two objective functions,

$$\text{Find: } \boldsymbol{\alpha} \in \mathbf{E}^n,\ \alpha_l \le \alpha_i \le \alpha_u,\ i = 1,\ldots,n \tag{2.7a}$$

$$\text{Minimize: } f_1 = \left\| \Delta \mathbf{y} - \mathbf{T}\boldsymbol{\alpha} \right\|_2 \text{ and } f_2 = \left\| \boldsymbol{\alpha} \right\|_0 \tag{2.7b}$$

where $\|\cdot\|_2$ and $\|\cdot\|_0$ denote, respectively, the $l_2$ norm and the $l_0$ norm. It is worth noting that conventional regularization methods for enforcing the sparsity in single-objective optimization use for example the $l_2$ and the $l_1$ norms. However, the former may spread out the error almost evenly among all variables and return a non-sparse vector. Researchers often opt for the $l_1$ norm regularization as a compromise between sparsity and computational efficiency, but the $l_1$ norm is only a relaxation approximation of the $l_0$ norm under certain conditions (Davenport et al, 2012; Cao et al, 2018a; Fan et al, 2019). The conditions required may not always hold. In contrast, in this research we use the $l_0$ norm to achieve true sparsity since the $l_0$ norm directly penalizes the number of non-zero components. As we cast the problem into the above multi-objective optimization, we avoid the difficulty in selecting weightings needed for single-objective optimization, and as illustrated in the subsequent section we can indeed solve for sparse damage index vector directly though minimizing the $l_0$ norm. Another major advantage of casting the inverse identification into a multi-objective optimization is that such a formulation naturally yields multiple solutions, which fits the nature of SHM. These multiple solutions correspond to possible damage scenarios. If all the results point to insignificant severity, continuing operation can be expected. If certain damage scenarios identified within the optimal solution set raise concern, we may either adopt proper maintenance decision or dispatch additional sensor measurements and human inspection.

### 2.2.3. Multi-objective particle swarm optimization (MOPSO) procedure and challenges

Our goal is to develop an effective algorithm to solve the multi-objective optimization problem formulated as Equations (2.7a) and (2.7b). In recent years, significant attention has been paid to integrating various metaheuristics into population based intelligent optimization algorithms tailored for various applications. Here we specifically choose the MOPSO as the basic approach, owing to its fast convergence and in particular, as will be shown in the subsequent sections, the capability of obtaining a set of trade-off solutions in a single run. This offers the opportunity to significantly improve the solution quality and diversity for damage identification inverse analysis with sparsity. Particle swarm is a stochastic technique originally developed by Kennedy and Eberhard (1995). It simulates the social behavior of animals such as insects, herds, birds, and fishes. These swarms conform a cooperative way, and each member in the swarm keeps changing the search pattern according to the learning experiences of its own and other members.

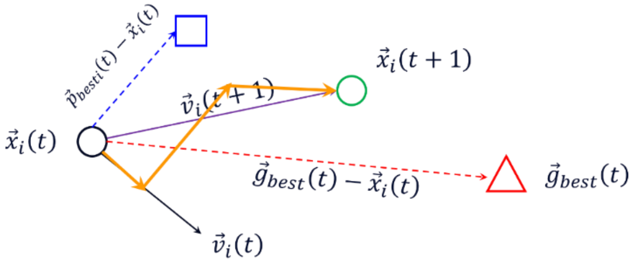

**Figure 2-1.** Illustration of particle swarm.

The working mechanism of particle swarm optimization is illustrated in Figure 2-1, in which each particle will fly toward the personal best in its memory and to the global best among all the particles. Thus, the new velocity and position can be expressed mathematically as

$$v_i(t+1) = zv_i(t) + c_1 r_1 (p_{\mathrm{best}\,i}(t) - x_i(t)) + c_2 r_2 (g_{\mathrm{best}}(t) - x_i(t)) \tag{2.8}$$

$$x_i(t+1) = x_i(t) + v_i(t+1) \tag{2.9}$$

where $v$ is the velocity of the particle, $x$ is the position of particle or the solution of the optimization problem, $r_1$ and $r_2$ are random numbers, *t* is the current iteration, $p_{\mathrm{best}}$ is the personal best, and $g_{\mathrm{best}}$ is the global best. In the above equations, coefficient $z$ is the inertia weight, $c_1$ is the coefficient of the cognitive component which indicates that each particle learns from its experience, and $c_2$ is the coefficient of the social component from which all particles learn. While having been used in various applications, conventional particle swam optimization may suffer from premature convergence and low exploration ability (Gad, 2022). The inverse analysis formulated as optimization problem shown in Equations (2.7a) and (2.7b) is challenging as the damage index vector generally has high dimension. How to embed sparsity into the optimization procedure and how to escape from local minima in such a problem are particularly challenging to deal with.

## 2.3. Solving Sparsity Conscious Multi-objective Particle Swarm Optimization

Particle swarm optimization employs a single search strategy in the search process to quickly converge to an optimal local region. During iterative calculation, particles tend to gather around the local extremes. In the absence of external interference, particles may become trapped in a valley with poor solution quality. On the other hand, while reinforcement learning allows for the selection of desired actions, the absence of a fitness function in these methods makes it difficult to determine how quickly the agent (i.e., particle) can control the system's state to achieve a set of goal states (Meerza et al, 2019). To address this, in this research we combine the features of reinforcement learning and the MOPSO process. This combination allows for action selection by incorporating the Q-Table into the fitness assessment of the MOPSO. As a result, agents can find the optimal path and learn the environment more efficiently with less complexity. Throughout the solution process, we embed a sparse population generation technique into the MOPSO, which enables the initialization and guidance of the solution sparsity of the damage index vector.

### 2.3.1. Overall architecture of MOPSO guided by Q-learning

In damage identification, the damage usually occurs in only a small number of segments, which corresponds to a sparse damage index vector. To improve upon the conventional particle swarm optimization, we start from a sparse population generation technique that can yield the initial sparsity of the damage index vector and then iterate during the solution procedure. Meanwhile, conventional MOPSO neglects the variability among particles of different generations and applies uniform and fixed parameters. Here we propose five local search strategies, aiming at emphasizing the exploration and exploitation capabilities through coefficient variations and increasing the solution diversity through mutations. To adaptively select appropriate strategies, we integrate Q-learning (Watkins and Dayan 1992) into MOPSO. Each particle selects the most suitable strategy for its own iteration and evolution based on the value of the Q-table. The entire optimization procedure interacting with Q-learning is shown in pseudo-code Algorithm 1 (Table 2-1). Motivated by the memetic algorithm (Samma et al, 2016), here we formulate a procedure to deal with multi-objective optimization problems with sparsity features. As detailed in Algorithm 1 (Table

2-1), after initializing the population using Algorithm 2 (Table 2-2) (to be elaborated in Section 2.3.2), the personal best, the global best, and the Q-table are initialized with all zeros for the entries corresponding to the states and their possible actions. The details of the Q-learning and Q-table will be given in Section 2.3.3. The current state is set as *Exploration* because the particle is expected to explore more searching space at the beginning of the algorithm. In the main iteration part, the particle (agent) will select the action which has the maximum value in the Q-table and execute the action. In a single optimization problem, the immediate reward can be obtained after executing the action if the condition $f(x_{new}) < f(x_{old})$ is satisfied. However, in multi-objective optimization, observing the fitness improvement of objectives one by one is not enough to get the reward since the objectives may conflict with each other. Therefore, the dominating algorithm is used to determine if the reward or a penalty is given after the action is executed. If the new solution dominates the old solution, then the agents receive a reward; otherwise, the agents get a penalty. The reward or penalty for executing an action is given in Section 2.3.4.

**Table 2-1.** Algorithm 1: Framework of Proposed Sparsity Conscious MOPSO.

**Algorithm 1:** Framework of Proposed Sparsity Conscious MOPSO

```
Randomly initialize each population using Algorithm 2
Initialize $p_{\text{best}}$ and $g_{\text{best}}$
Initialize Q table using Algorithm 3
Initialize current state $s_t$ as $s_{\text{Exploration}}$
for ii = 1 to MaxFEs do
    for jj = 1 to N do
        Select the best action for current state from Q table
        Enter action repository and execute corresponding action using Algorithm 4
        Obtain the immediate reward after executing the action
        Observe the new state $s' = \delta(a,s)$
        Update the Q table entry and current state using Algorithm 3
```

```
        Update external optimal solution repository
    End
End
```

---

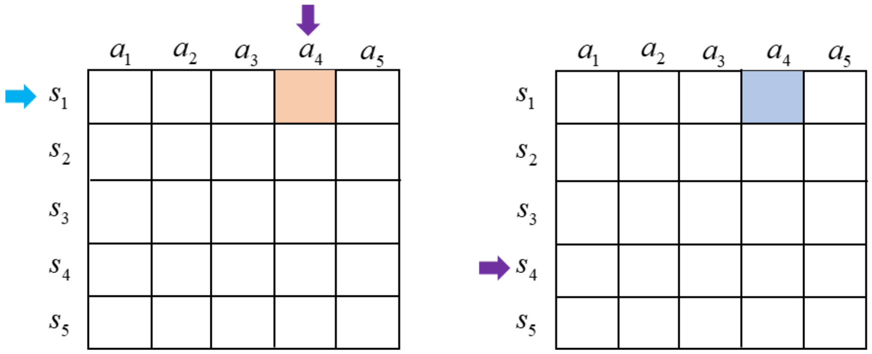

**Figure 2-2.** Illustration of the state transition process.

After the current action is executed, the agent can reach the new state using the observing function $\delta(s,a)$ which makes a transition from the current state to another. The transition here is that the index of the current action is the index of the next state. A diagram is drawn to show how to switch from the current state to the next state. As shown in Figure 2-2, the agent will select an action based on the maximum Q-table values given the current state as $S_1$. Let’s assume that action 4 ($a_4$) has a maximum value and then the next state will be set as $S_4$, which has the same index as the index of the current action $a_4$. By iterating this process, a dynamic selection and execution can be achieved between these states and actions.

After action 4 is executed, the rewards currently obtained can be used to update the entry for the current state and current action. Details about entry updating using rewards obtained will be given in Section 2.3.3. Then, the personal and global best are updated, and the external optimal repository will be updated accordingly. All the steps in the main loop will be performed until the maximum number of runs are reached.

### 2.3.2. Sparse population generation

In intelligent optimization, an initial population is created at the beginning as a set of candidate solutions. The population comprises individuals, each representing a possible solution. In our problem of damage identification, damage usually occurs in a small number of segments and the damage index vector expressed as Equation (2.5c) is thus sparse. If a specific component of the damage index vector is greater than 0, it indicates that the corresponding segment (i.e., the location) has non-zero stiffness reduction. It is worth noting that the occurrence of damage in a segment is a binary concept, described as either 0, no damage, or 1, with damage. We can utilize this to create a sparse population generation procedure so that not all unknowns will have non-zero values.

In this sub-algorithm of sparse population generation, we temporarily split the damage index information into two parts: (1) damage location, expressed as a damage location index and denoted as $\boldsymbol{\theta}_1 \in \{1, \cdots, n\}$; and (2) damage severity level, expressed as a percentage change in stiffness and denoted as $\boldsymbol{\theta}_2 \in \left[0,1\right]^T$. By using the element-wise product, we can then have $\boldsymbol{\alpha} = \boldsymbol{\theta}_1 \circ \boldsymbol{\theta}_2$. Here $\boldsymbol{\theta}_1$ is a binary vector with all elements being as 0 or 1 to indicate if there is damage or not at the corresponding segment, and $\boldsymbol{\theta}_2$ is a regular vector with continuous values to indicate the possible damage severity. Tian et al (2019a) proposed an evolutionary algorithm to deal with optimization in feature extraction and neural network training. In that research, a sparse population is generated during the initialization. This technique is adapted as shown in pseudo-code Algorithm 2 (Table 2-2) and implemented in our optimization framework.

Algorithm 2 (Table 2-2) mainly includes two parts: lines 1-6 acquire the rank (to be explained subsequently) using the non-dominated sorting (Deb et al 2000) for each damage location, and the remaining part generates a sparse population based on the rank obtained. In the first part, we randomly initialize a temporary full-rank severity matrix **S**, the size of which is *n* by *n*, with *n* as number of segments. Then we generate an *n* by *n* identity matrix for damage occurrence **B** and obtain a temporary population using the element-wise product. One feature of this temporary population is that only the elements on the diagonal have values. The purpose of this is to let each damage location make contribution to the fitness function independently. The fitness values are then passed into the Non-Dominated Sorting algorithm to return the ranks. So now each damage location gets one attribute called rank. In the remaining part, we re-initialize the severity matrix **S** with size of *N* by *n*. Here *N* is the number of populations. Different from the previous part, all entries of matrix **B** with size of *N* by *n* are set as zeros at this point. Then, two damage locations randomly selected are compared with each other using the ranks obtained in the previous part. The damage location with a smaller rank will be set as 1 in its **B** matrix component since smaller rank means the solution is closer to true damage scenario. By doing this for all the populations, we obtain a sparse population matrix with size of *N* by *n* using element-wise product. This returned population not only indicates the damage locations and severities but also has sparsity feature. This population will be passed to the main iteration loop for evolution.

**Table 2-2.** Algorithm 2: Sparsity Population Generation.

**Algorithm 2:** Sparsity Population Generation

```
Input: number of population N, number of variables n, lower bound of variable vMin, upper bound of variable vMax
Output: Population
Initialize a matrix randomly for severity $\mathbf{S} = rand_{n\times n}$
Initialize an identity matrix for occurrence of damage $\mathbf{B} = eye_{n\times n}$
for ii = 1 to length (S) do
    temp.Pop = $\mathbf{S} \circ \mathbf{B}$
    temp.Cost = CostFunction (temp.Pop)
End
Rank number $F \leftarrow$ NonDominatedSorting (temp)
Initialize variable matrix as $\mathbf{S} = (vMax - vMin) \times unifrnd(0,1,[N,n])$
Initialize a binary matrix as $\mathbf{B} = zeros(N,n)$
For jj =1 to N do
```

```
    $Ta = randperm(n, 2)$
    $a = Ta(1)$
    $b = Ta(2)$
    **If** $F_a < F_b$ **then**
        $\mathbf{B}(jj, a) \leftarrow 1$
    **else**
        $\mathbf{B}(jj, b) \leftarrow 1$
    **End**
**End**
Population = $\mathbf{S} \circ \mathbf{B}$
Return Population
```

### 2.3.3. Q learning details and Q-table

In Algorithm 1 (Table 2-1), which is the main algorithm, Q-learning is utilized to guide particles to adaptively choose the suitable local search strategy for its own iteration. Here in this sub-section, we elaborate on how Q-learning works and how particles interact with the environment using the Q-table. Q-learning falls under the class of reinforcement learning techniques (Watkins and Dayan, 1992). In reinforcement learning, the learner performs an action causing a state transition in the environment in which it resides and receives a reward or penalty for the action executed to reach a definite goal. The environment is the searching space of the particles. The states are current local searches. Two sets of acceleration coefficients, one prioritizing self-learning and the other prioritizing social-learning, are used with a time-varying inertia weight. These form distinct coefficient-based local search strategies that can facilitate firstly the exploration and subsequently the exploitation. Furthermore, three mutation-based local search strategies are formulated to encourage local particle movement. The first two randomly perturb a single dimension of either the personal best or the global best solution. The last strategy tunes each dimension of the personal best through mutation. To be concise, we name these five local search methods as *Exploration*, *Convergence*, *Elitist-based perturbation* (*EBP*), *Mutation*, and *Fine Tuning*. An action is the transition from one state to another. In the integrated algorithm, each particle of MOPSO is regarded as an agent. Updating of the Q-table occurs after each action is executed and ends when an episode is completed. The agent will not learn much after a single episode, but eventually, with sufficient exploring steps and episodes it will converge and learn the optimal Q values. The pseudo-code of the Q-learning is given in Algorithm 3 (Table 2-3).

**Table 2-3.** Algorithm 3: Q-learning.

**Algorithm 3:** Q-learning

```
For each state s and action, a
    Initialize $Q(s,a) \leftarrow 0$
    Initialize current state $s_t$
End
Repeat
    Select the best action $a_t$ for $s_t$ from the Q table and execute it
    Receive an immediate reward $r(s,a)$
    Observe the new state $s' = \delta(a,s)$
    Update the table entry using Equation (2.11)
    Update current state $s = s'$
Until MaxFEs is reached
```

There are 5 states and their corresponding actions. Therefore, we can create a Q-table with the size of 5 by 5 and initialize all the entries as zeros. We then reset all the values corresponding to different states in action *Fine Tuning* as -5, ensuring a higher priority for other actions to be executed. Usually, the current state is randomly chosen from the state repository. However, here we initialize the current state as *Exploration* since we demand the algorithm to start with exploring more searching space. Subsequently, the best action will be selected and executed based on the maximum Q-table value given the current state. This process can be written mathematically as

$$a_t = index\{\max(Q(s_t, actions))\} \tag{2.10}$$

Here, $a_t$ is the current action and $t = 1,\ldots,5$. After the action selected is executed, an immediate reward or penalty will be obtained. Reward or penalty is determined by the dominating algorithm, which will be discussed in the following sub-section. The agents observe the maximum future reward under the next state. The next state index is the same as the current action index, as depicted in Figure 2-2. The reward/penalty obtained will be passed into the updating function to update the Q-table entry $Q(s_t, a_t)$. The updating function is as

$$Q_{new}(s_t, a_t) = (1-b)Q(s_t, a_t) + b[r_{t+1} + \gamma \max_a Q(s_{t+1}, a_{all})] \tag{2.11}$$

where $b$ is called the learning rate which is defined as how much the new value is accepted, $\gamma$ is a discount factor used to balance immediate and future rewards, and *r* is the reward received for taking action $a_t$ at a given state $s_t$. In Equation (2.11), max is the operation of taking the maximum of the future reward from the new state $s_{t+1}$. Finally, the current state will be updated. By iterating this process, the optimal Q-table can be achieved.

### 2.3.4. Action repository

From the perspective of structural damage identification, the objective is to acquire a small but diverse solution set that covers the true damage scenarios. In addition to the sparse population generation algorithm presented in Section 2.3.2, the algorithms pursuing robust exploration capabilities are also sought. In this sub-section we present five local search strategies, including two coefficient variation-based strategies and three mutation-based strategies, which collectively aim at encouraging particle movement around local extremes and facilitating exploration for a diverse set of solutions. These strategies form an action repository so that each particle can select a proper one in each iteration. The pseudo-code for the action repository is shown in Algorithm 4 (Table 2-4).

**Table 2-4.** Algorithm 4: Action Selection.

```
Algorithm 4: Action Selection
Switch current action
    Case: 'Exploration'
        Update position and velocity of particle using Equations (2.8) and (2.9)
        Deal with bounds
        Update $p_{\text{best}}$ if $Dominates$ ($x_{\text{new}}$, $x_{\text{current}}$) is true; otherwise, do nothing
        $reward \leftarrow -1$ if $Dominates$ ($x_{\text{new}}$, $x_{\text{current}}$) is true; otherwise, $reward \leftarrow -2$
    Case: 'Convergence'
        Implement all steps same to case 'Exploration' only with different coefficients
    Case: 'EBP'
        Update position of personal best using equation in Table 1
        Deal with bounds
        Update $p_{\text{best}}$ if $Dominates$ ($x_{\text{new}}$, $x_{\text{current}}$) is true; otherwise, do nothing
        $reward \leftarrow -1$ if $Dominates$ ($x_{\text{new}}$, $x_{\text{current}}$) is true; otherwise, $reward \leftarrow -2$
    Case: 'Mutation'
        Mutate position of global best using equation in Table 1
        Deal with bounds
        Update $g_{\text{best}}$ if $Dominates$ ($x_{\text{new}}$, $x_{\text{current}}$) is true; otherwise, do nothing
        $reward \leftarrow -1$ if $Dominates$ ($x_{\text{new}}$, $x_{\text{current}}$) is true; otherwise, $reward \leftarrow -2$
    Case: 'Fine Tuning'
        Update $p_{\text{best}}$ using Equations (2.13)-(2.15)
        $reward \leftarrow -3$
End
```

**Table 2-5.** Mathematical expressions of the actions.

| Strategy Name | Particle dynamics | Coefficients |
|---|---|---|
| Exploration | $v_i(t+1) = \omega v_i(t) + c_1 r_1 (p_{\text{best}i}(t) - x_i(t)) + c_2 r_2 (g_{\text{best}}(t) - x_i(t))$<br>$x_i(t+1) = x_i(t) + v_i(t+1)$ | $\omega = \omega_{\max} - \frac{(\omega_{\max} - \omega_{\min}) it}{\text{maxIter}}$ $c_1 = 2.5$<br>$c_2 = 0.5$ |
| Convergence | $v_i(t+1) = \omega v_i(t) + c_1 r_1 (p_{\text{best}i}(t) - x_i(t)) + c_2 r_2 (g_{\text{best}}(t) - x_i(t))$ | $\omega = \omega_{\max} - \frac{(\omega_{\max} - \omega_{\min}) it}{\text{maxIter}}$ $c_1 = 0.5$ |

| | | |
|---|---|---|
| | $x_i(t+1) = x_i(t) + v_i(t+1)$ | $c_2 = 2.5$ |
| Elitist-based perturbation | $tempP_{\mathrm{Best}i,d} = \begin{cases} P_{Besti,d} + r_d \cdot (\text{vMax}_d\text{-vMin}_d) \\ \text{if rand} > 0.5 \\ P_{Besti,d} - r_d \cdot (\text{vMax}_d\text{-vMin}_d) \\ \text{if rand } \le 0.5 \end{cases}$<br>repeated for defined times | $N \sim (\mu, R^2)$<br>$R = R_{\max} - \frac{(R_{\max} - R_{\min}) \cdot it}{\text{maxIter}}$ |
| Mutation | $tempL_{Best,d} = L_{Best,d} + normrnd(\mu, R^2)$<br>repeated for defined times | $N \sim (\mu, R^2)$<br>$R = R_{\max} - \frac{(R_{\max} - R_{\min}) \cdot it}{\text{maxIter}}$ |
| Fine Tuning | $tempP_{Besti,d} = P_{Besti,d} + V_{i,d}$<br>repeated for all dimensions | —— |

The actions involved are described mathematically and summarized in Table 2-5. For the *Exploration*, we hope that the particle can explore more searching space and avoid premature convergence. Therefore, the coefficients in Equation (2.8) are set as $c_1 > c_2$. In the *Convergence* state, the algorithm will converge to the global best quickly. Therefore, the social part now is given a larger value, so $c_1 < c_2$. Since the inertial weight $z$ controls the balance between the global and local searches, it is set as a decay expression to search more space initially and at the end of the optimization will realize quick convergence. Here $z_{\max} = 0.9$ and $z_{\min} = 0.4$ are recommended (Kennedy and Eberhart, 1995). Whenever the action is selected and executed, the newly generated solution will be compared to the old one using the non-dominated sorting algorithm, and the immediate reward will be obtained as shown below

$$\text{if } x_{new} \prec x_{old},\ x_{old} = x_{new} \qquad \text{reward} \tag{2.12a}$$

$$\text{if } x_{new} \sim\prec x_{old},\ x_{old} = x_{old} \qquad \text{penalty} \tag{2.12b}$$

If the newly obtained solution dominates the old solution, a reward will be assigned to the corresponding action and the old solution will be replaced by the new one. Otherwise, the old solution remains, and a penalty will be given for the action selected. Here the reward is set as a negative number. Since we initialize the Q-table with all zero entries, if in the beginning the *Exploration* receives a reward, e.g., reward = 1, then the algorithm will be trapped there because we use the max Q-table value to select the action.

To alleviate the premature convergence issue, an elitist-based perturbation (*EBP*) strategy is adopted to perform perturbation on the personal best of the particle and provide extra diversity for it to jump out from the local optima (Lim and Isa, 2013). Here we establish a variable, *count*, to facilitate the repetition of the *EBP* strategy for a designated number of iterations, thereby enabling the activation of *EBP* when required. In this research, *count* = 10. In the *EBP* strategy, a randomly selected dimension in the personal best of the particle is perturbed using the expressions provided in Table 2-5. Here $P_{\mathrm{Besti,d}}$ means the *d*-th dimension of the personal best of the *i*-th population. $r_d$ is a random number obtained from the normal distribution of $N \sim (\mu, R^2)$ with $\mu = 0$ and standard deviation *R*. Here, $R_{\max} = 1$ and $R_{\min} = 0.1$ as suggested in literature (Lim and Isa, 2013) are the maximum and minimum perturbation ranges, respectively. *it* is the current number of iterations and *maxIter* is the maximum iteration of the algorithm. Still, the personal best will be replaced by a temporary personal best if the latter dominates the former and the immediate reward will be given as -1; otherwise, the personal best remains unchanged, and the reward will be -2 as a punishment.

In the action *Mutation*, emphasis is placed on the global best, facilitating local exploration and the possibility of identifying and transitioning to a superior position. Since the global best guiding all the particles in the MOPSO algorithm is like a leader, we use *L* to represent the global best. As shown in Table 2-5, $L_{\mathrm{Best,d}}$ indicates the *d*-th dimension of the global best. A random perturbation is generated based on the same norm distribution in strategy *EBP*. The decay standard deviation is used to achieve a high jump at the beginning and a low jump at the end of the algorithm. At this time, if the temporary global best dominates the current global best, it will replace the current one. The immediate reward is now given as 1. Since the global best plays a crucial role in guiding all the particles, a large reward is given to it when it gets improvement. Otherwise, the current global best remains the same and a penalty is given as -2.

In the *Fine Tuning* process, the action focuses on each dimension of the personal best instead of only one randomly selected dimension by updating its velocity. In other words, we expect the particles to move more in the direction favorable to improve the solution and, conversely, to move more slowly in the direction unfavorable to improve the solution. For each dimension, the tuning will be repeated *h* times to trigger the action. *h* cannot be too large since the optimization is dealing with the high-dimension problem and will take a long time to run for a large *h* value. Here we set *h* as 10. $V_{i,d}$ in the expression shown in Table 2-5 for action *Fine Tuning* means the velocity of the *d*-th dimension of the personal best of *i*-th population. Specific expressions of $V_{i,d}$ are given as (Ji et al, 2007; Samma et al, 2016)

$$V_{i,d} = \frac{o}{it^{p}} u + 2B_{i,d} \tag{2.13}$$

where *o* is the acceleration factor and set as 2, *p* is the descent parameter that controls the decay of the velocity and is set as 20, *u* is a uniformly distributed random number within [−0.5,0.5], and *it* is the current iteration number, and

$$B_{i,d} = \begin{cases} 2V_{i,d}, & \text{if } x_{new} \prec x_{old} \\ 0.5B_{i,d}, & \text{otherwise} \end{cases} \tag{2.14}$$

Then the personal best can be updated in the following manner,

$$tempP_{Besti,d} = \begin{cases} P_{\mathrm{Best}i,d} + V_{i,d}, & \text{if } x_{new} \prec x_{old} \\ P_{\mathrm{Best}i,d}, & \text{otherwise} \end{cases} \tag{2.15}$$

If the temporary personal best dominates the current one, it will replace the current personal best. Otherwise, the original personal best remains unchanged. In this action process, no matter if the solution gets improved or not, there is only punishment since it takes a long time to tune each dimension. Here the punishment is set as -3 so that it cannot be called frequently for the sake of computational efficiency.

### 2.3.5. Solution procedure summary

The overall solution procedure is now summarized in Figure 2-3. To achieve a small yet diverse set of solutions covering the true damage scenario, we first integrate sparse population generation into MOPSO. Moreover, we develop five local search strategies based on coefficient variation and mutation, which enhance the searching capability to obtain a diverse solution set. At the same time, Q-learning is introduced to help the particles adaptively choose the appropriate current iterative strategy for themselves. The efficacy of this new approach will be demonstrated in case studies that follow.

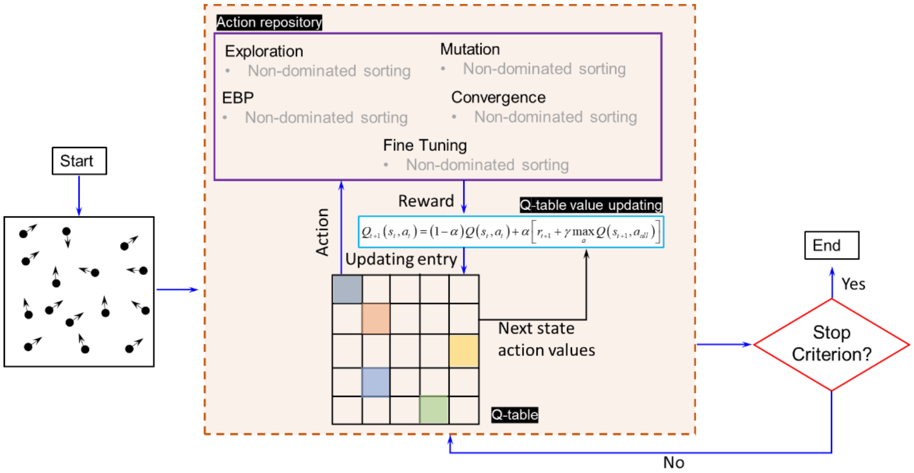

**Figure 2-3.** Flowchart of sparsity conscious reinforcement-learning guided MOPSO.

## 2.4. Damage Identification Implementation with Experimental Case Analyses

In this section, we conduct experimental case studies to verify the proposed approach. As derived in Section 2.2, the piezoelectric admittance change expression and sensitivity matrix are expressed in finite element forms. Here we first present the experimental setup and data acquisition, followed by finite element modeling. The numerical model and the experimental data are then employed for damage identification.

### 2.4.1. Experimental setup and data acquisition

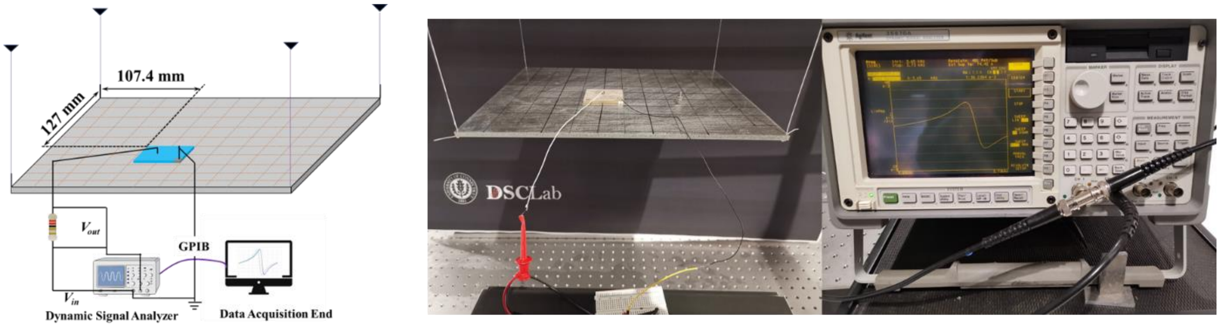

**Figure 2-4.** Schematic of experimental setup.

The experimental setup is shown in Figure 2-4. A piezoelectric transducer is bonded to the top surface of a plate using epoxy resin. To minimize the influence of the thickness of bonding layer, the resin layer is kept at smaller than 0.15 mm. The piezoelectric transducer is connected to an external resistor, as shown in Figure 2-4. By measuring the voltage across the resistor, we can obtain the current flowing through the circuit. Thus, the admittance measurement can be obtained as $Y(\omega) = V_{\text{out}} \,/\, R \big/ V_{\text{in}} = V_{\text{out}} \big/ R V_{\text{in}}$ where $Y$ is the admittance, $V_{\text{out}}$ denotes the voltage amplitude across the resistor, and $V_{\text{in}}$ indicates the amplitude of the input voltage. This simple yet effective measurement scheme is low-cost and can directly facilitate the model updating as every component of the numerical model can be measured directly. A dynamic signal analyzer (Agilent 35670A) is used to acquire the frequency response. Here 5 Volts (Vpk) harmonic voltage is applied to the transducer. For each excitation frequency, 25 cycles are used to reduce the noise effect.

In damage identification using admittance measurements, the damage effect is most prominent around the resonant peaks. In this research, acquire the admittance change information around two frequencies, 3,194.95 Hz (the 28th natural frequency) and 3,705.8 Hz (the 31st natural frequency). Theoretically, one may measure admittance in even higher frequency range for higher detection sensitivity. Employing admittance measurement in higher frequencies, on the other hand, necessitates a very high dimension of finite element mesh for the model to converge in such frequency range, resulting in increased computational cost., Therefore, there is a trade-off. To balance the computational cost and the choice of frequency band, without loss of generality, we choose the aforementioned frequency range, which will be used for demonstration of the proposed algorithm. Further investigations on the selection of frequency range will be conducted in future. The first frequency range for admittance measurement is from 3,150 Hz to 3,230 Hz and the second is from 3,650 Hz to 3,730 Hz. Each range has 401 frequency sweeping points. The admittance curves measured under the healthy baseline state are shown in Figure 2-5. It is worth noting that all the data acquisitions are completed under the room temperature of 20 degrees Celsius within 0.2-degree fluctuations. The numerical simulation results are obtained after model updating, which will be explained in detail in Section 2.4.2 next.

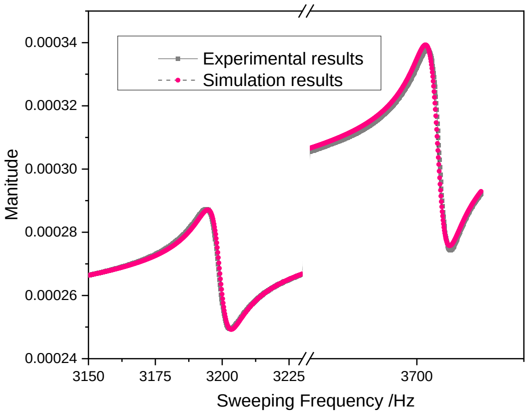

**Figure 2-5.** Admittance measurement data under the healthy state and finite element prediction after model updating.

### 2.4.2. Finite element modeling and updating

The geometry and material properties of the piezoelectric transducer and the plate are listed in Table 2-6. The plate is made of aluminum alloy. The piezoelectric transducer is the SM411 type from Steiner & Martins Inc. The piezoelectric transducer is placed at the following location: 107.4 mm from the left edge and 127 mm from the top edge of the plate.

**Table 2-6.** Geometry and material properties of the piezoelectric transducer and the plate.

| Structure | Parameters | Values |
|---|---|---|
| Plate | Length ($10^{-3}$ m) | 304.8 |
| | Width ($10^{-3}$ m) | 254 |

| | | |
|---|---|---|
| | Thickness ($10^{-3}$ m) | 3.874 |
| | Young's modulus ($10^3$ MPa) | 73 |
| | Density (kg/m$^3$) | 2769 |
| | Poisson's ratio | 0.3 |
| Piezo Transducer (SM411) | Length ($10^{-3}$ m) | 45 |
| | Width ($10^{-3}$ m) | 45 |
| | Thickness ($10^{-3}$ m) | 3.5 |
| | Young's modulus $E_{11}$ ($10^3$ MPa) | 74 |
| | Young's modulus $E_{33}$ ($10^3$ MPa) | 54 |
| | Density (kg/m$^3$) | 7800 |
| | Piezo constant $g_{31}$ ($10^{-3}$ m$^2$/C) | -10.4 |
| | Piezo constant $g_{33}$ ($10^{-3}$ m$^2$/C) | 24.2 |
| | Permittivity constant $\varepsilon_{33}$ ($10^{-8}$ F/m) | 1.348 |

In the numerical model, we employ the stress-voltage constitutive relation of the piezoelectric material. A finite element model is established based on an in-house MATLAB code. Both the transducer and the plate are meshed using the 20-node solid element. The total number of elements for the finite element analysis is determined as 13,766 after convergence analysis. Here the in-house MATLAB result is verified with ANSYS. In order to be consistent with the experimental setup, the admittance computed is also through the usage of a serially connected resistor with resistance 165 ohms. The stiffness and mass matrices obtained in finite element form are then substituted into the admittance expression derived in Section 2.2. The frequency sweeping points are the same as those used in experiment. In other words, the numerical simulation exactly matches with the experimental procedure.

It is worth noting that the material properties of the piezoelectric transducer given by the vendor are not always accurate. In addition, there are inevitable variations and uncertainties in experiment. Thus, to match the numerical results with experimental ones, model updating is conducted. For the plate structure, by measuring the total mass and volume, we can calculate its mass density. Hence there is one parameter of the plate to be updated, i.e., the Young's modulus $E_{\mathrm{plate}}$. For the piezoelectric transducer, the mass density of piezoelectric transducer can similarly be obtained by measuring its mass and volume. Furthermore, an LCR multimeter can gauge the piezoelectric capacitance ($C_p$) after the transducer is bonded to the plate. Subsequently, for this rectangular shaped transducer, the permittivity constant can be calculated as $\varepsilon_{33} = C_p \cdot d/A$, where $d$ and $A$ represent the thickness of the transducer and the area of electrode, respectively.

Before updating other parameters of the model, it is essential to understand the influence of each parameter on the admittance. We carry out sensitivity/perturbation analysis, and compare with experimental measurement to elucidate the boundary of parametric variation for the subsequent inverse analysis of model updating. Obviously, for a specific parameter, if the experimental data is properly encapsulated within the range of admittance prediction upon parametric perturbation, the corresponding variation percentage can be used as parametric boundary. Otherwise, we make adjustment to decide the parametric boundary. Moreover, the sensitivity analysis provides a quantifiable measure of the magnitude and direction of admittance changes in response to these parameter alterations. We recognize that variation of piezoelectric Young's modulus $E_{11}$ results in lateral shift in the admittance curve and magnitude changes. Besides, piezoelectric constants $g_{31}$ and $g_{33}$ variations predominantly lead to distinct variations in magnitudes in both real and imaginary parts. The variation of piezoelectric Young's modulus $E_{33}$, on the other hand, yields much less significant effect. This insight streamlines our optimization process, enabling a focus solely on influential parameters. i.e., $E_{11}$, $g_{31}$ and $g_{33}$. Finally, the intervals for parameter changes in model updating are decided as ±20% for plate Young's modulus $E_{\mathrm{plate}}$ and piezoelectric transducer Young's modulus $E_{11}$, and ±35% for piezoelectric constants $g_{31}$ and $g_{33}$. In model updating, our goal is to minimize the difference between the admittance from the experiment ($y_{\mathrm{h}}^{\exp}(\omega)$) and the admittance from the numerical model

($y_{\mathrm{h}}^{\mathrm{pred}}(\omega)$). Here, the subscript 'h' refers to the healthy state. The superscripts 'exp' and 'pred' refer to the data from experiment and from model prediction, respectively. The objective function for model updating is $obj = \left\| y_{\mathrm{h}}^{\exp}(\omega) - y_{\mathrm{h}}^{\mathrm{pred}}(\omega) \right\|_2$. There is a total of 172 iteration steps for minimizing the objective function in model updating by adopting single-objective particle swarm optimizer. Finally, the key parameters are updated as $E_{\mathrm{plate}} = 72.21\ \mathrm{GPa}$, $E_{11} = 81.4\ \mathrm{GPa}$, $g_{31} = -6.97 \times 10^{-3}\ \ \mathrm{m}^2 \big/ \mathrm{C}$, and $g_{33} = 24.2 \times 10^{-3}\ \ \mathrm{m}^2 \big/ \mathrm{C}$, as shown in Table 2-6.

The updated admittance curves are compared to experimental results, as shown in Figure 2-5. As can be observed, they match very well.

### 2.4.3. Case study setup

The plate structure to be monitored is divided into 120 segments, which means there are 120 variables to be identified in the damage index vector. It is worth emphasizing that, mathematically, the rows of the sensitivity matrix are not necessarily linearly independent, no matter how many sweep frequency points we choose and how these sweep frequency points. Therefore, the inverse problem shown in Equation (2.6) is generally under-determined. This is the fundamental reason we resort to a multi-objective optimization formulation to find the solution set. Four case studies are considered to verify systematically the proposed algorithm for damage identification. Without loss of generality, to avoid altering the boundary conditions throughout the experiment that may cause unwanted variations, damage scenarios are emulated by adding one or two small mass blocks to the plate. The added mass causes the shift of admittance curves, which is equivalent to stiffness reduction. In our experiment, after we introduce the added mass, we extract admittance curve in the frequency range of interest. We then adjust, in the numerical model, the stiffness (i.e., reducing the Young's modulus of the elements) in the specific segment to which the mass is added, such that the admittance curve calculated matches the experimental one (with added mass). The percentage of stiffness reduction in the damaged segment can then be obtained numerically.

- **Case 1**: a 1.0 g mass block is attached to the 75th segment, which causes an equivalent 14.8% stiffness reduction of that segment.
- **Case 2**: a 0.6 g mass block is attached to the 75th segment, which leads to an equivalent 11.0% stiffness reduction of that segment.
- **Case 3**: a 0.6 g mass block is attached to the 116th segment, which results in an equivalent 9.4% stiffness reduction.
- **Case 4**: a 0.12g and a 0.1g mass block are attached to the 49th and 65th segments respectively, which are equivalent to 0.734% and 0.899% stiffness reductions respectively.

These four cases are designed with damage locations chosen randomly. The first two cases have the same location but with different damage severities. Case 3 differs from Cases 1 and 2 in location and severity. Case 4 has multiple damage locations with smaller severities to emulate early damage occurrence. Such a case study setup can demonstrate the capability of the proposed algorithm to identify damage, regardless of the damage sizes and locations. To evaluate the algorithm performance, several well-established optimization algorithms, including the MOEA/D (Zhang and Li, 2007), the original MOPSO (Coello et al, 2004), and the NSGAII (Deb et al, 2000), are also employed and compared. Besides, the classical optimization solvers are selected here since they are still popular in the community of structural health monitoring (Lin et al, 2022; Xu et al, 2018; Lin et al, 2020; Gomes et al, 2018; Cha and Buyukozturk 2015; Tiachacht et al, 2018).

### 2.4.4. Effect of sparsity generation

As mentioned, damage usually occurs in a small number of segments especially at early stage, thus resulting in a sparse damage index vector. In this sub-section, the aforementioned four cases are analyzed to examine firstly the role that the sparsity generation algorithm plays. For this purpose, we implement the sparse population generation algorithm into MOPSO, and the resulted optimization algorithm is referred to as Sparse-MOPSO. It is worth noting that this Sparse-MOPSO is run without the reinforcement learning components, as we want to first focus on the benefit of sparsity generation. Three other optimization algorithms are employed for comparison. For a fair comparison, we set the maximum iterations as 20,000, 40,000, 60,000, 80,000, and 100,000, respectively, and investigate the results. In addition, for each algorithm, the population size is set to be 30. Each algorithm is run 10 times independently.

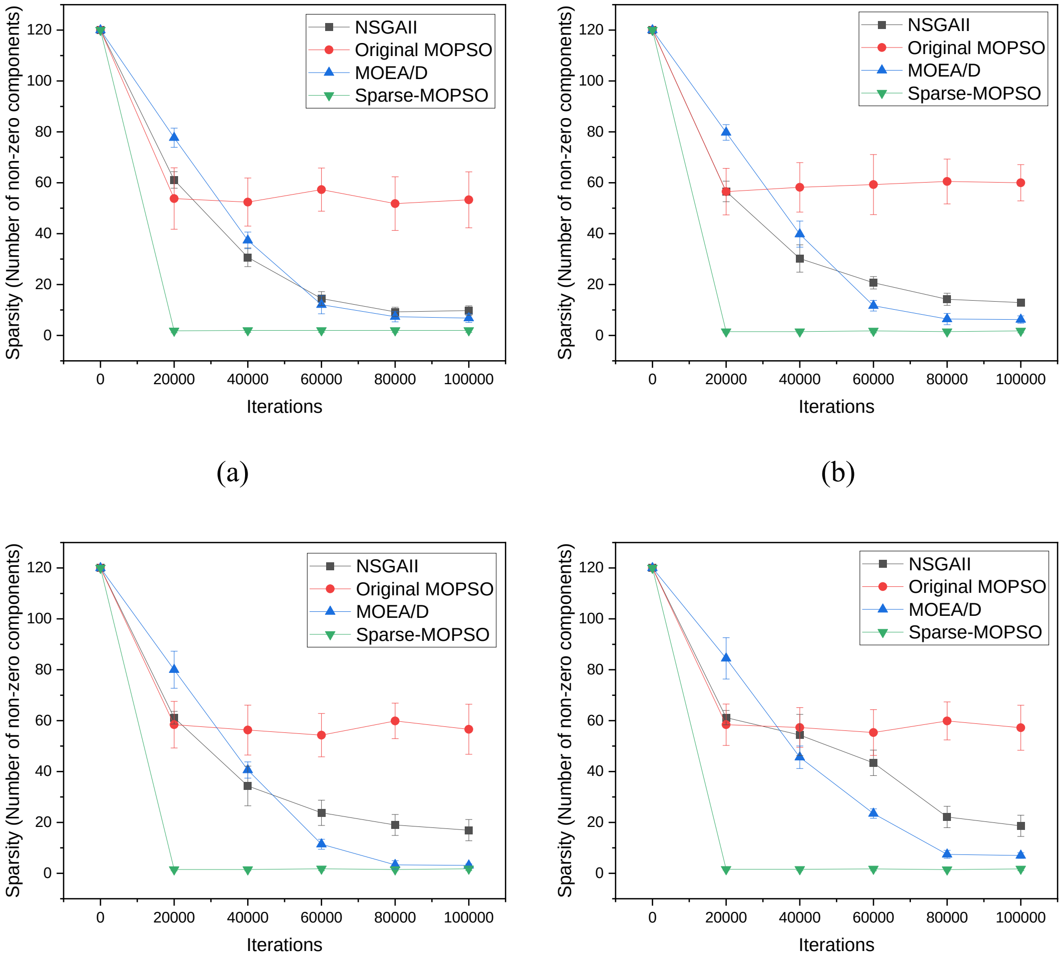

(a)

(b)

(c)

(d)

**Figure 2-6.** Comparison of number of non-zero components in damage index vector vs iteration by different optimization algorithms (a) Case 1, (b) Case 2, (c) Case 3, and (d) Case 4.

The comparison of sparsity (number of non-zero damage locations identified) versus iterations is provided in Figure 2-6 for the four cases mentioned. For each maximum iteration case, there are 10 independent runs. Therefore, the sparsity obtained is shown as average with error bar. All the algorithms reach convergence after 80,000 iterations, as the number of non-zero damage locations no longer change. Comparing the Sparse-MOPSO with the original MOPSO, we can observe that the sparsity generation algorithm employed in Sparse-MOPSO can achieve sparsity by controlling the number of non-zero damage index vector components to around 3 after convergence. The number of non-zero damage locations from the original MOPSO, on the other hand, is around 60 even after it reaches convergence. This indicates that the sparsity generation algorithm introduced indeed works well in dealing with the sparse characteristics in damage identification. By comparing the Sparse-MOPSO with the NSGAII and the MOEA/D, we can observe that the Sparse-MOPSO outperforms the other two by achieving sparsity more efficiently. For example, with the maximum iterations of 20,000, the Sparse-MOPSO achieves sparsity with about 3 non-zero damage locations while that number is greater than 60 for other algorithms.

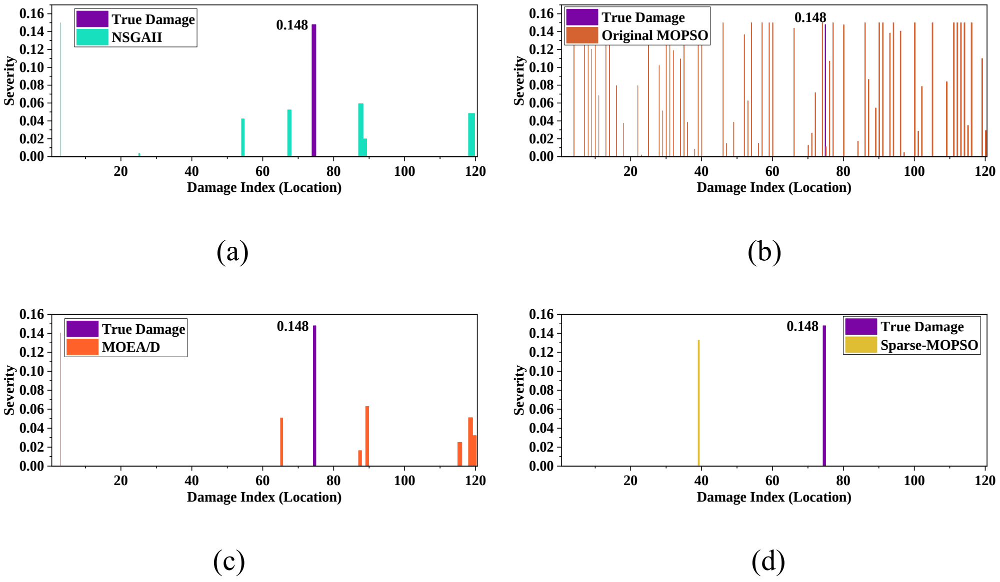

(a)

(b)

(c)

(d)

**Figure 2-7.** A representative solution from different algorithms after 100,000 iterations for Case 1 (a) NSGAII, (b) original MOPSO, (c) MOEA/D, and (d) Sparse-MOPSO.

In Figure 2-7, we compare one representative solution for Case 1 obtained by different algorithms after 100,000 iterations. The number of columns is the number of damage locations identified, and the height of a column represents the percentage of stiffness reduction at the specific damage location (i.e., the segment number). In this case, since the true damage scenario is located at only one segment, the expectation for all algorithms is that they can achieve the identification of one damage location after convergence. However, from the results, only the Sparse-MOPSO algorithm can find one damage location, although it does not identify the true location correctly. It is worth noting that at this point, we are more concerned about the performance of sparsity because only the sparsity generation is integrated into the Sparse-MOPSO. The solution correctness will be evaluated after we activate the reinforcement learning part of the MOPSO. For the NSGAII and the MOEA/D, the number of damage locations identified is around 7 after the respective convergence. For the original MOPSO, the identified damage locations are spread over almost the entire structure, thus it does not provide meaningful information for damage identification. It is thus evident that the sparsity generation algorithm proposed in this research works well in dealing with the sparse feature in damage identification.

### 2.4.5. Examination of reinforcement learning guided local search

In the preceding sub-section, the results indicate the necessity of the sparsity generation algorithm in handling sparse characteristics in damage identification. However, from the representative solution obtained, one can see that the solution from the Sparse-MOPSO, which yields the sparse solution set, does not capture the true damage scenario. The untrue solution represents a local minimum where the algorithm is trapped. To tackle this challenge, the local searching strategies combined with Q-learning developed in Section 2.3 are now activated. Hereafter, the proposed sparsity-conscious MOPSO guided by reinforcement-learning is referred to as SRL-MOPSO.

The four cases mentioned above are now thoroughly examined. For a truly fair comparison, we introduce the sparsity generation algorithm into all algorithms to be compared as well, including the NSGAII, the MOPSO, and the MOEA/D. The settings for all algorithms are consistent: maximum iterations 100,000 and population 30. Other related algorithmic parameters are provided in Section 2.3. The solutions obtained for Cases 1 to 4 are plotted in Figure 2-8 to Figure 2-11. Within the multi-objective optimization formulation for inverse analysis, multiple solutions are obtained for the under-determined damage identification problem. In these figures, each sub-plot represents one solution obtained from an individual algorithm. As explained, the number of columns in each subplot represents the damage locations identified, and the height of a column is the corresponding severity value. All the solutions are arranged, from left to right, with the increase of the number of identified damage locations.

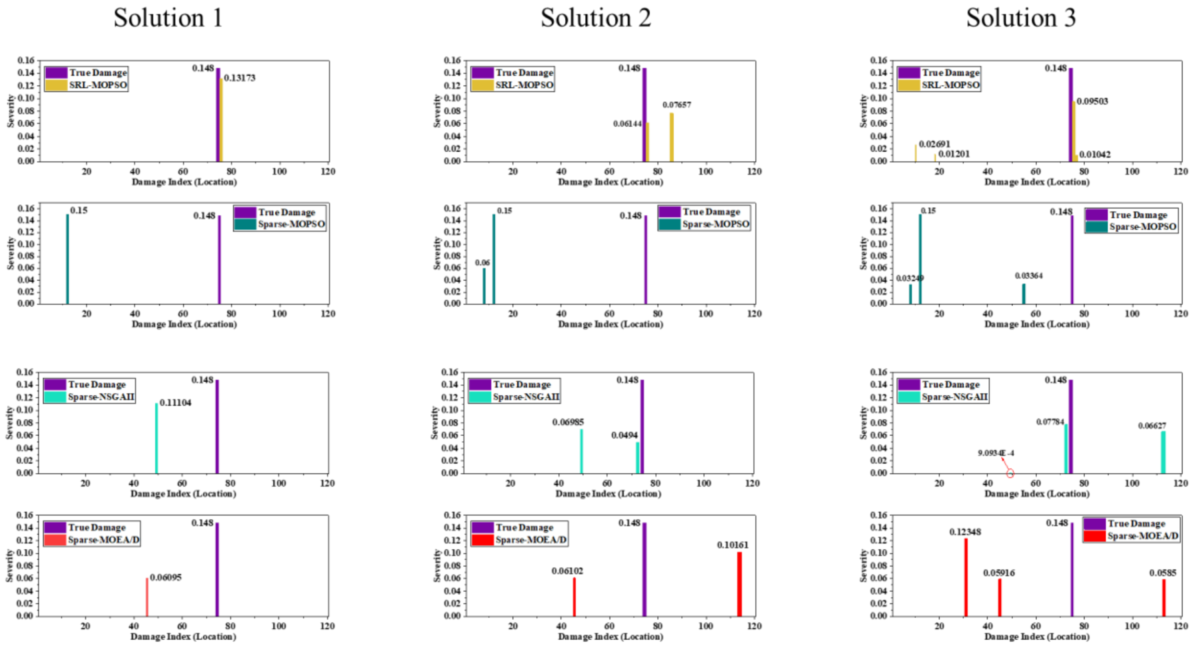

**Figure 2-8.** Case 1 identification results from various algorithms.

For Case 1, the solutions obtained from various algorithms are shown in Figure 2-8. Since the sparse generation is now introduced to all algorithms, we can observe that all solutions achieve a good sparsity. The maximum number of identified damage locations in Case 1 is 4, which is indeed small as compared to the total number of possible damage locations, i.e.,120. This indicates that the sparse population generation algorithm is a generic strategy that can enable the general optimization algorithms to improve their capabilities for damage identification. The difference between the SRL-MOPSO and the Sparse-MOPSO is that the former is integrated with local searches combined with Q-learning algorithm which aims at enhancing the global search capability toward finding the true damage scenario. By comparing the solutions obtained from the SRL-MOPSO and the Sparse-MOPSO (i.e., the first two rows in Figure 2-8), we can find that the 3 solutions generated by the SRL-MOPSO include 1, 2 and 4 damage locations, respectively, and all these solutions point to the same location, the 75th segment, that aligns with the true damage location. Indeed, the first solution from the SRL-MOPSO indicates one damage location at the 75th segment with stiffness reduction 13.173%, which matches well with the true damage scenario, i.e., the 75th segment with 14.8% stiffness reduction. Although the second and the third solutions from the SRL-MOPSO point to additional damage locations besides the true damage location, all the additional damage locations identified have quite small severity values. Collectively, these 3 solutions identified provide very consistent identification results that can be utilized in decision making in engineering practice. In contrast, the Sparse-MOPSO generally give solutions that are very different from the true damage scenario. Indeed, none of the 3 solutions from the Sparse-MOPSO points to the true damage location. Similarly, the solutions obtained from Sparse-NSGAII and the Sparse-MOEA/D all exhibit significant discrepancy with respect to the true damage scenario. This means that these algorithms may get trapped in local minima that are different from the true damage scenario.

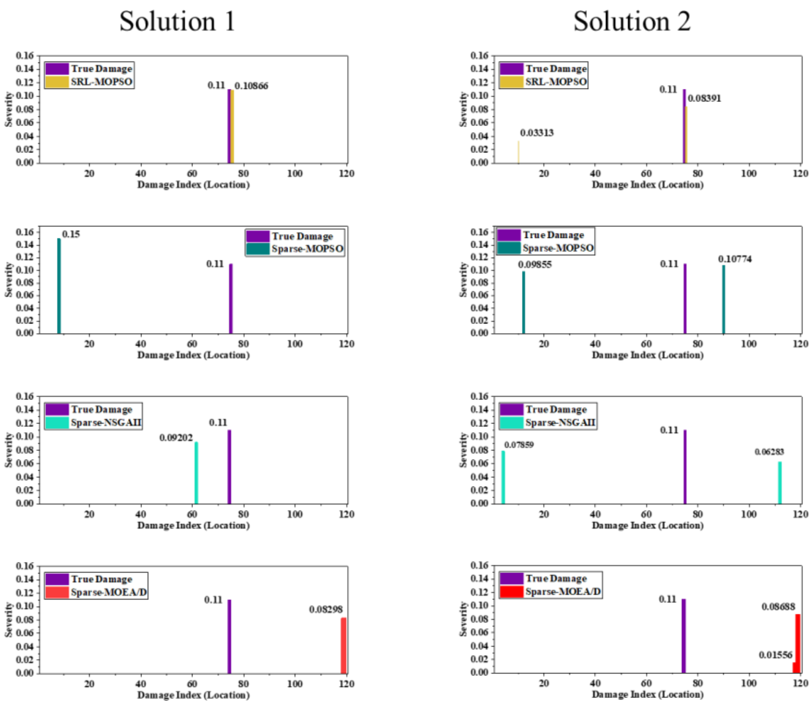

**Figure 2-9.** Case 2 identification results from various algorithms.

In Case 2, the true damage scenario has the same location at the 75th segment but different severity with respect to Case 1. The solutions obtained from various algorithms are plotted in Figure 2-9. In this case, the maximum number of non-zero damage locations identified by all algorithms is 2, after we integrate the sparse population generation. However, the Sparse-MOPSO, the Sparse-NSGAII and the Sparse-MOEA/D produce solutions that all deviate from the true damage scenarios. In comparison, the SRL-MOPSO is enhanced by the local search strategies which can help the particles to escape from the local optima and thus achieve a better global search. This leads to solutions that are much better matching with the true damage scenario. For the two solutions obtained from the SRL-MOPSO, we can see that the number of identified damage locations are 1 and 2, respectively, and both solutions point to the true damage location, i.e., the 75th segment. For solution 1 obtained from the SRL-MOPSO, the relative error between the true damage severity 11% stiffness reduction and the identified result 10.866% is only 1.22%, indicating excellent accuracy. For solution 2, the additional damage location identified has quite small severity level. Therefore, this second solution is only a minor deviation from the true damage scenario.

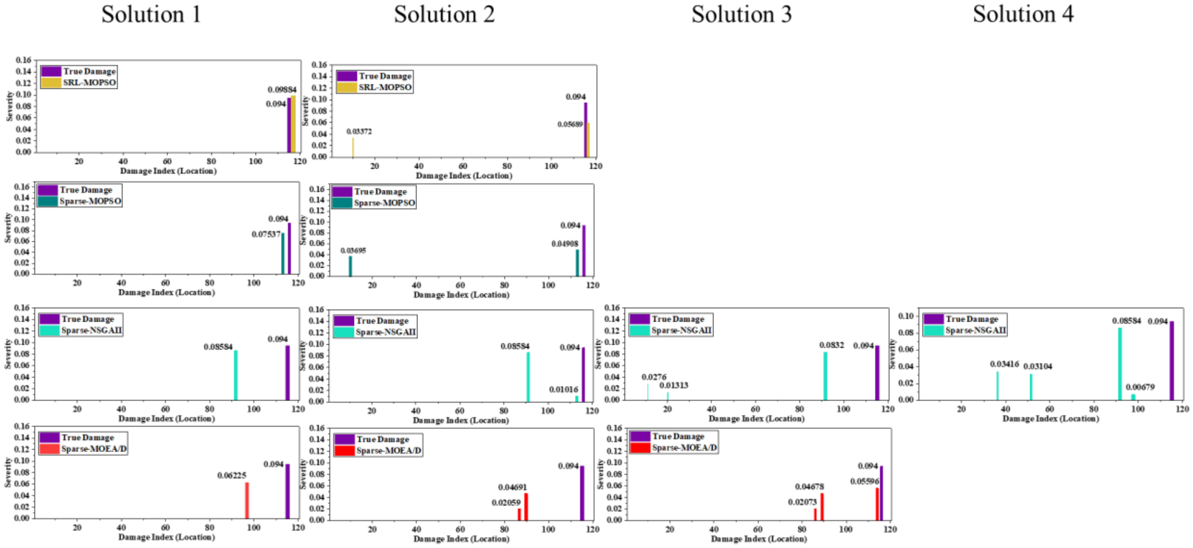

**Figure 2-10.** Case 3 identification results from various algorithms.

In Case 3, the damage occurs at the 116th segment, i.e., a different location than in Cases 1 and 2. The solutions obtained from various algorithms are shown in Figure 2-10. Owing to the integration of sparse population generation, the maximum number of non-zero damage locations identified is 4 by the Sparse-NSGAII. Both the SRL-MOPSO and the Sparse-MOPSO produce 2 solutions. Both solutions from the Sparse-MOPSO, however, point to incorrect damage locations. The other two algorithms, the Sparse-NSGAII and the Sparse-MOEA/D, identify 4 solutions and 3 solutions, respectively. Interestingly, none of these solutions points to the true damage location. The damage scenarios identified by all the other algorithms do not match with the true damage scenario. Once again, the SRL-MOPSO can identify the true damage scenario, shown as its solution 1. In its solution 2, although two damage locations are identified, the solution points to the 116th segment as a main location, which fits the true damage scenario. It is worth noting that modeling uncertainties and measurement noise inevitably exist. As such, it is expected that some solutions identified through the multi-objective formulation are different from the true damage scenarios. The SRL-MOPSO can identify a small solution set that includes the true damage scenario.

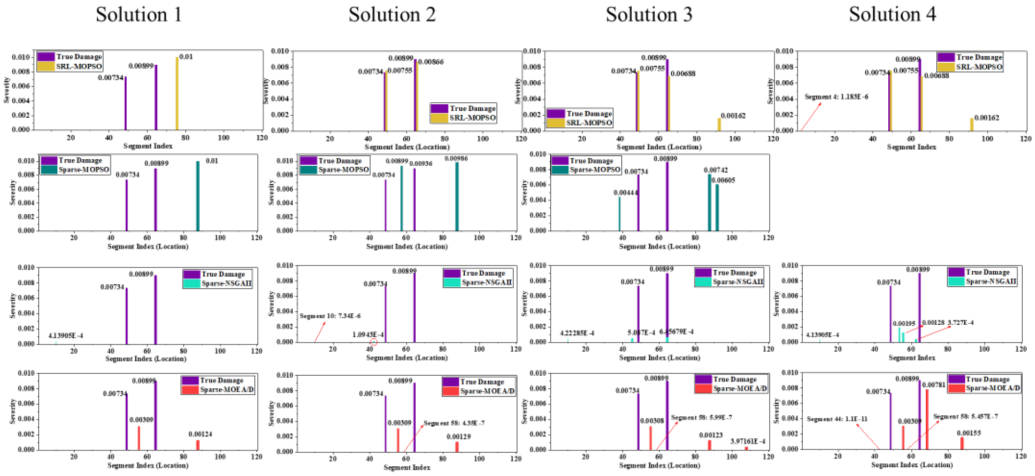

**Figure 2-11.** Case 4 identification results from various algorithms.

In Case 4, the damage is located at the 49th and the 65th segments with 0.734% and 0.899% stiffness reductions, respectively. This case setup aims at examining the capability of the algorithms when damage occurs at multiple locations. In this particular case, to challenge the algorithms, the damage severities are designed to be quite small. The solutions obtained from different algorithms are plotted in Figure 2-11. The number of solutions identified by the SRL-MOPSO, the Sparse-MOPSO, the Sparse-NSGAII and the Sparse-MOEA/D are, respectively, 4, 3, 4, and 4. Observing the first solution identified by the SRL-MOPSO, one can observe that it indicates a single damage, which does not match the true damage scenario with two damage locations. This is not a surprise, because one of the objective functions in the multi-objective optimization is the sparsity of the damage index vector, and the algorithm may indeed find a solution with single damage. Similarly, the first solutions identified by the other three algorithms do not match with the true damage scenario either. Meanwhile, comparing the first two rows of Figure 2-11, one can see that the SRL-MOPSO clearly outperforms the Sparse-MOPSO, as the former yields its solutions 2 to 4 that all are very close to the true damage scenarios. Amongst them, solution 2 with two damage locations basically matches with the true damage scenario in both location and severity. Although solutions 3 and 4 point to other damage locations in addition to the locations of the true damage scenario, those additional locations all have very small severities. Clearly, solutions 2 to 4 are quite consistent, and again can provide import information for decision making in engineering practice. In comparison, the Sparse NSGAII and the Spare-MOEA/D are unable to produce solutions that are close to the true damage scenario. This further highlights the importance of incorporating the strategies outlined in Section 2.3 for solution diversity and accuracy.

In summary, the case studies demonstrate the performance of the proposed approach. A small solution set that always includes the true damage scenario is obtained for each case. In actual practice, once multiple solutions are identified, there will subsequently be a decision-making process. If all these solutions point to insignificant damage, continuing operation of the structure can be recommended. If one or several solutions point to potentially severe consequence, additional measurements using different sensing techniques including human inspection can be dispatched to further investigate this small set of possible damage scenarios. On the other hand, if the solution set contained a very large number of solutions, then it would lose the essence of structural health monitoring because an operator would then need to examine too many possible damage scenarios afterwards. Obviously, the proposed SML-MOPSO can indeed fulfill the task of identifying a small solution set that always includes the true damage scenario.

### 2.4.6. Effect of Q-table guided action selection and computational cost analysis

In this sub-section, we analyze the effect of Q-learning by examining the interaction between the Q-table and action selection, and also discuss the computational cost and overhead.

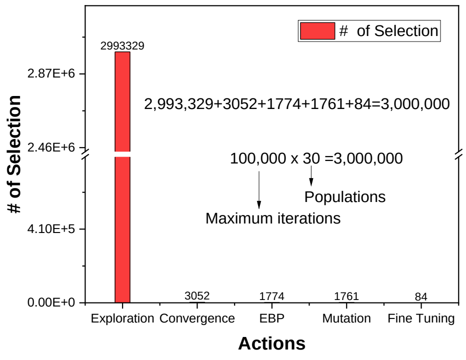

**Figure 2-12.** Number of selections of actions guided by Q-table (Case 1).

As stated in Section 2.3.3, an action is selected based on the maximum Q value in Q-table. Therefore, attention is paid to all the actions that are selected and executed after convergence. As shown in Figure 2-12, the histogram counts the number of times each local search strategy is executed after the algorithm converges. For those algorithms without local search, they tend to fall into local optima and thus reach premature convergence. This results in quite significant unexplored space in search in which the global optimum may reside. On the other hand, the proposed SRL-MOPSO takes most of the computational effort on the *Exploration* strategy to explore the entire parametric space. Of the four remaining local search strategies, the *Convergence* is executed nearly 3,000 times. This indicates that the particles are flying to the global optimum, i.e., reaching convergence, while exploring the unknown space. In comparison, both *EBP* and *Mutation* are executed nearly 1,700 times, indicating that they play an almost equal role. It is worth noting that the last strategy *Fine Tuning* is executed only 84 times. There are two possible reasons. One is that we only give a penalty to this strategy regardless of good or bad solution obtained after this strategy is executed since it takes up a particularly large amount of time when dealing with a high-dimensional damage index vector. Thus, it has a lower probability of being selected. The other reason is that when initializing the Q-table, we set Q-table value of -5 for the *Fine Tuning* and give priority for other local searches to be selected. The fact that the *Fine Tuning* strategy is executed such infrequently does not mean it is not needed. In fact, it is because of this strategy that other strategies have led to better performance. Without loss of generality, here we report the results based on Case 1 computation. Similar observations are obtained for other cases. The interaction between Q-table and action selection is animated as a gif file (Appendix).

**Table 2-7.** Computational cost/performance comparison between MOPSO and SRL-MOPSO.

| Metaheuristics | 20,000 iterations | | | 100,000 iterations | | |
|---|---|---|---|---|---|---|
| | Time (s) | sparsity | convergence | Time (s) | Sparsity | convergence |

|  |  |  |  |  |  |  |
|---|---|---|---|---|---|---|
| MOPSO | 179 | 56.7 | No | 893 | 53.3 | yes |
| SRL-MOPSO | 258 | 1.8 | Yes | 1091 | 1.8 | yes |

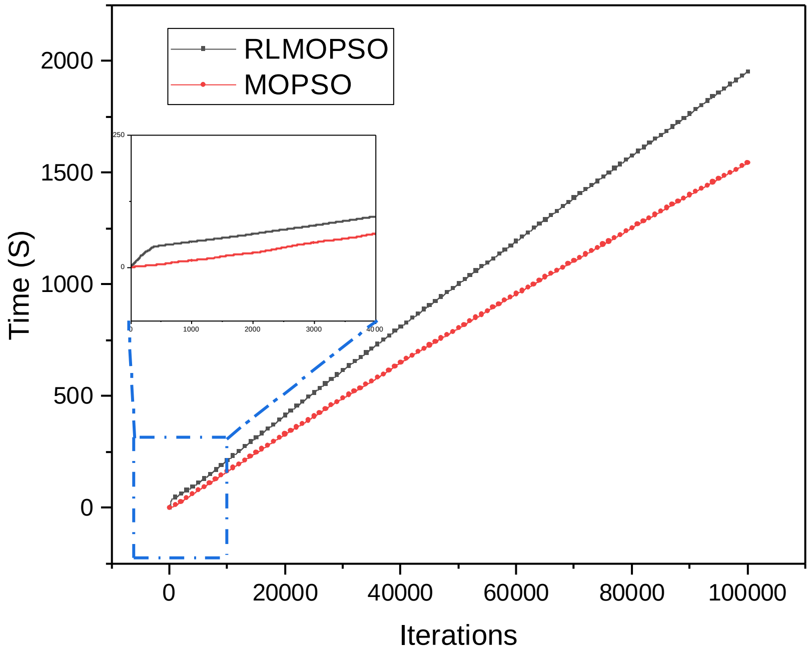

**Figure 2-13.** Elapsed time comparison with and without integration of Q-learning.

Finally, we analyze the computational cost with and without Q-learning. In what follows we present a comparison study. Throughout this research, damage identification inverse analysis is carried out on a regular Dell computer with Intel(R) Xeon(R) Silver 4210 CPU @ 2.20GHz (2 processors) a 128 GB RAM. Table 2-7 shows a comparative analysis between the MOPSO and the SRL-MOPSO algorithms, detailing their respective computational time, sparsity levels, and convergence statuses over two specific iteration counts: 20,000 and 100,000. Figure 2-13 illustrates the elapsed computational time for both algorithms across a broader range of iterations, highlighting the differences in time efficiency as the number of iterations increases. The proposed SRL-MOPSO, which incorporates Q-learning, understandably introduces a computational overhead. Specifically, for 20,000 iterations, the SRL-MOPSO takes 79 seconds longer than MOPSO, and for 100,000 iterations, it takes an additional 198 seconds. However, the benefits brought about by this integration far outweigh the time increase. Most notably, the sparsity improvement is drastic, dropping from 56.7 to 1.8 at 20,000 iterations and maintaining this enhanced sparsity at 100,000 iterations, as shown in Figure 2-6. Moreover, while the MOPSO fails to converge at 20,000 iterations, the SRL-MOPSO achieves this significant milestone, demonstrating its enhanced capability. In essence, the SRL-MOPSO's added computation time is only marginal, while leading to a reasonable trade-off for the pronounced advancements in performance.

## 2.5. Conclusion

In this research, a new sparsity conscious multi-objective optimization framework is developed to fully unleash the capability of piezoelectric admittance measurement measured in high-frequency range for structural damage identification. While promising, the measurement information of piezoelectric admittance change information is generally limited, oftentimes leading to an under-determined problem for damage identification. To tackle this challenge, multi-objective optimization inverse analysis is formulated. The multi-solution nature of such a formulation fits naturally the structural health monitoring practice. Specifically, we focus on the development of effective algorithm that can lead to a small solution set that includes the true damage scenario. We choose the multi-objective particle swarm optimization (MOPSO) as the basic platform and incorporate metaheuristics to enhance its capability toward damage identification. To obtain a small yet diverse solution set, a sparsity generation algorithm is integrated into MOPSO. Furthermore, a series of local search strategies through coefficient variation-based and mutation-based techniques are synthesized that form an action repository to enhance the global searching capability of MOPSO. To guide the particle to adaptively select the local search, Q-learning is integrated. Case studies utilizing physical experiment of piezoelectric active interrogation through piezoelectric admittance measurement and the associated finite element modeling are conducted. The importance of sparse population generation is first examined, followed by damage identification performance investigation. The proposed sparsity-conscious reinforcement learning guided MOPSO (SRL-MOPSO) is compared with benchmark algorithms including the NSGAII, the MOEA/D, and the original MOPSO. In all the cases examined utilizing experimental data, the SRL-MOPSO outperforms other algorithms, and shows excellent results in identifying a small solution set that includes the true damage scenario. This framework can potentially be extended to other model-based structural health monitoring approaches.

## Appendix

Visualization of Q-learning process is provided as an animation in gif format, where the heatmap shows how the action and state are selected and updated. https://github.com/yantzan/Animation-of-Q-table

# Chapter 3. Harnessing Collaborative Learning Automata to Guide Multi-objective Optimization based Inverse Analysis for Structural Damage Identification

Structural damage identification based on physical models is often transformed into an optimization problem that minimizes the difference between measurement information of structure being monitored and the model prediction in the parametric space. However, the objective function in this context often exhibits multimodality, involving high-dimensional variables due to the reliance on finite element models for damage identification. These features pose challenges to optimization algorithms, where entrapment in local solutions can lead to false positives and false negatives in damage identification. In this research, we propose a reinforcement learning based multi-swarm optimizer to tackle such challenges in pursuit of a small yet diverse solution set that can capture the true damage scenario as one of the solutions. The proposed method leverages the flexibility of the particle swarm optimizer and incorporates novel strategies of metaheuristics to realize targeted improvement. To enable the particle swarm to adaptively select the appropriate search strategy based on the current environment, we adopt the learning automata technique, which sidesteps the need for reward strategy selection that is usually *ad hoc* at each step of the search. The integration harnesses the automatic learning and self-adaptation capabilities of learning automata, enabling the particles to navigate based on environmental signals. This leads to accumulated probabilities tied to advantageous movements, fostering an adaptive exploration of particles in the search space. The proposed approach is first validated through implementing into benchmark test cases with comparisons. It is then applied to structural damage identification with piezoelectric admittance experimental signals. `The results highlight the capability of the algorithm to identify a small solution set with high accuracy to match the actual damage scenario.

## 3.1. Introduction

Structural Health Monitoring (SHM) encompasses techniques and processes aimed at assessing the integrity and performance of various structures in aerospace, marine, and manufacturing and transportation systems, highlighting its critical role in ensuring safety and longevity. The necessity of SHM stems from the ever-present risk of damage which can compromise structural functionality and safety. Damage identification within SHM is crucial, as it enables early detection and remediation, thereby mitigating risks and reducing maintenance costs. Typically, damage identification is reframed as an inverse optimization problem, where the goal lies in reconciling the real dynamic responses of the current structure, such as frequencies and mode shapes (Zhang and Sun 2021; Avci et al, 2021; Zhou and Tang 2021b; Ding et al, 2022), or piezoelectric impedance (Fan et al, 2019; Cao et al, 2023a; Zhang et al, 2024a), with predictions derived from finite element models. These responses are intrinsically linked to structural properties like mass, stiffness, and damping. This inverse problem can be addressed through meta-heuristic optimization algorithms. However, compared with the number of unknowns, the measurement information is quite limited. As such, structural damage identification is oftentimes an under-determined problem. Fortunately, expert knowledge can be used to tackle the underdetermination, i.e., damage usually affects a limited number of areas within a structure, or expressed in mathematical terms, structural damage manifests sparsely. Thus, the regularization is typically utilized by adding a $l_0$ or $l_1$ norm to the above residual formulation with a regularization weight. Although advancements have been made, single-objective optimization yields a single solution which may be contaminated by model mismatch and measurement noise, and the inclusion of regularization in these approaches requires the selection of weighting constants that are challenging to determine *a priori*. Alternatively, structural damage identification can be formulated as a multi-objective optimization problem that minimizes concurrently a) the difference between measurements and model prediction in damage parametric space; and b) the $l_0$ norm of the damage index vector. This has multiple advantages intuitively. It avoids the *ad hoc* selection of weights between individual objectives employed in single-objective optimization. Moreover, this formulation yields multiple solutions, which fits the nature of structural damage identification. Yet, the objective function in this context often exhibits multimodality, involving high-dimensional variables due to the reliance on finite element models for damage identification. This complexity can lead to local optima, which, if the optimization process gets trapped, may result in false identifications, or missed damages, posing significant challenges for the optimization algorithms used in structural damage identification.

Given the intricate nature of the optimization challenges outlined, it becomes imperative to explore tailored algorithmic solutions. In light of the "No Free Lunch" principle, which posits that no single algorithm can optimally solve all optimization problems, the customization of algorithms based on the specific settings and requirements of the optimization model becomes imperative. This necessitates tailoring algorithms to enhance their performance, making the choice and adaptation of algorithms a pivotal aspect of addressing the challenges inherent in structural damage identification. Typically, the improvement of algorithms is grounded on foundational evolutionary optimization techniques, such as genetic algorithms (Li et al, 2023), Jaya algorithm (Ding et al, 2022), and particle swarm optimization (Li et al, 2022; Zhang et al, 2024a), among others. Guided by a problem-oriented approach, the design of specific local search strategies or the integration of other local search algorithms is often employed to augment the performance of these foundational algorithms. For example, Livani et al (2018) improved flaw detection in two-dimensional structures by integrating the extended spectral finite element method (XSFEM) with a particle swarm optimization (PSO) algorithm, enhanced by a novel active/inactive flaw (AIF) strategy inspired by earthquake engineering, to efficiently locate cracks and holes while reducing computational costs. Ding et al (2022) enhanced Jaya algorithm for structural damage identification, integrating one-step K-means clustering, Hooke–Jeeves pattern search, and linear population reduction to tackle optimization challenges and uncertainties. Thanh et al (2022) improved the grey wolf optimizer by incorporating Lévy flight and new leadership dynamics, improving convergence and effectiveness in structural damage identification. Li et al (2023) proposed a novel method through the integration of an advanced surrogate modeling technique, specifically the sparse polynomial chaos expansion model, with a hybrid optimization strategy combining K-means clustering and genetic algorithm.

The improvements so far have predominantly focused on the application of a singular strategy to enhance algorithmic performance. However, the optimization problems in structural damage identification usually invite the development and incorporation of multiple local search strategies to balance the exploration and exploitation. This raises an intriguing question: how does one select the most appropriate strategy at each iteration to effectively navigate the search space? The selection process itself becomes a critical factor in the optimization journey, as the adaptability of algorithms to the shifting landscape of the problem at hand is key to their success. Recent explorations have seen the fusion of multiple local search strategies with machine learning techniques, like reinforcement learning, which can intelligently adjust their search adaptively based on the reinforcement signals. Among the efforts, Samma et al (2016) introduced multiple local strategies, namely, exploration, convergence, and various jump and tuning operations, within a particle swarm optimization framework, employing Q-learning for strategy selection, thereby enhancing algorithm performance on benchmark optimization problems. Ding et al (2023) developed a global vibration-based method utilizing an innovative Q-learning evolutionary algorithm, which combines K-means clustering, Jaya, and tree seeds algorithms, for the first time to accurately detect and quantify debonding in FRP strengthened structures through modal testing and model updating techniques, enhanced by $l_{0.5}$ regularization for sparse damage detection. Zhang et al (2024b) develops a novel Q-learning hybrid evolutionary algorithm (QHEA) that integrates Jaya algorithm, differential evolution, and Q-learning for structural damage identification. This approach enables response reconstruction and damage detection without input excitation, showcasing improved accuracy and robustness in identifying damage locations and severities.

The integration of foundational algorithms with reinforcement learning has shown promising results in optimization and structural damage identification. However, a critical issue in these hybrid models is the reward mechanism – where solutions surpassing previous ones are rewarded, and less optimal outcomes are penalized, directly influencing the optimization performance. In contrast, as an alternative reinforcement learning approach, Learning Automata (LA) offers a distinct approach by selecting appropriate local search strategies without the need for explicit rewards (Hashemi and Meybodi, 2011; Zhang et al, 2020). Instead, feedback is obtained through interaction with the environment, offering positive or negative signals. For instance, in structural damage identification, after executing a chosen strategy, the environment informs the agent whether it is closer to the actual damage location. A closer proximity results in a positive signal (represented as 0), while a move away triggers a negative signal (represented as 1), facilitating an intuitive feedback mechanism without the need for predefined reward policy. On the other hand, the studies abovementioned have seen most of advancements in single-objective optimization techniques, thus, there remains a critical gap in applying improvements to multi-objective optimization algorithms, particularly within our current optimization framework, which demands small yet diverse solutions for structural damage identification. Drawing from the preceding discussion, the research gap is identified as:

1) Single-objective optimization tends to yield a singular solution, potentially confined to a local extremum.
2) A notable challenge within physics-based structural damage identification emerges due to the high-dimensional variables involved and the multimodal objective function peppered with many local optima, underscoring the need for local search strategies.
3) To accurately capture true damage scenarios through a spectrum of solutions, there is a critical need for an approach that navigates this complexity without relying on a predefined reward policy.

These contexts set the stage for presenting our research work, which aims to address these challenges by developing novel strategies for effective and precise damage detection inspired by the success and flexibility of the respective techniques. In this research, we formulate the damage identification problem as a bi-objective optimization using different types of damage information carriers, such as modal information and piezoelectric admittance. The objective functions include Modal Assurance Criterion (MAC) (Greś et al, 2021) to incorporate modal responses in a simplistic problem with numerical simulation, and Root Mean Square Error (RMSE) to incorporate piezoelectric admittance measurements as well as the $l_0$ norm from a realistic SHM experimental setup. The $l_0$ norm is employed to minimize the number of identified damage locations, effectively promoting sparsity in the damage indices. This formulation is based on the fact that structural damage typically occurs sparsely, rather than uniformly throughout the structure. Subsequently, the multi-objective particle swarm optimization (MOPSO) as the basic platform for enhancement is selected, owing to its straightforward conceptualization, ease of implementation, computational efficiency, and small number of control parameters. Specifically, we implement time-varying coefficients and mutation-based local search strategies in PSO to form a spectrum of five distinct actions. These actions are facilitated through the design of Learning Automata (LA), where each particle is regarded as an individual LA. Each LA interacts with the environment so it can adaptively select the appropriate action according to its current position. Each time an action is performed, the environment gives feedback to inform the particle whether it is closer or further away from the optima. The particle will then update the probability of the action just performed based on this feedback. The more favorable the action, the higher the probability will be accumulated. It is worth noting that these local search strategies (actions) have their own characteristics and play different roles. The contributions of this study are fourfold:

1) A new inverse analysis approach through multi-objective optimization is synthesized to facilitate structural damage identification utilizing modal information and piezoelectric active interrogation.
2) An enhanced particle swarm optimizer is developed with particles intellectualized through learning automata, enabling a small yet diverse solution set.
3) The particles adaptively move towards optimal solutions based on environmental signals, validated through benchmark case comparison.
4) When implemented to numerical case and experimental data, the proposed approach effectively and accurately identifies structural damage.

The rest of the paper is organized as follows. Section 3.2 outlines the multi-objective optimization formulation for damage identification by using physical model prediction and experimental measurements. In Section 3.3, we first outline the necessary details of PSO. We then formulate time-varying coefficients and mutation-based local search strategies realized through LA. In Section 3.4, the proposed new algorithm is tested on benchmark cases to examine quantitatively the solution diversity and accuracy. Section 3.5 presents the implementation of the new algorithm to model-based damage identification using modal information and piezoelectric admittance measurements and highlights the performance. Section 3.6 summarizes the concluding remarks and future research directions.

## 3.2. Multi-objective Optimization Setup for Damage Identification

Physical model-based damage identification is an approach to structural health monitoring where the goal is to detect, localize, and quantify damage within a structure through comparison between experimental measurements and model predictions. This process typically involves gathering data from various types of structural responses such as frequencies, mode shapes, accelerations, or piezoelectric impedance, and then utilizing this data to inform a model of the current state of structure. In creating a generalized multi-objective optimization model for damage identification, we integrate both actual/experimental observations and theoretical model predictions. When utilizing modal information, we can establish a multi-objective optimization model with the MAC as the objective function. When employing piezoelectric impedance, we can develop a multi-objective optimization model that targets the Root Mean Square Error (RMSE or $l_2$ norm) and the $l_0$ norm as the objective functions. Here $l_0$ norm aims to enforce the sparsity of the damage representation, reflecting the assumption that actual damage is typically localized and affects a small portion of the structure. Mathematically, the model can be expressed as:

$$\text{Find: } \boldsymbol{\alpha} \in \mathbf{E}^n ,\ \alpha_l \leq \alpha_i \leq \alpha_u ,\ i = 1,...,n$$

$$\text{Minimize: } f_1 = \left\| Y_{meas} - Y_{pred}(\boldsymbol{\alpha}) \right\|_2 \text{ or } MAC(Y_{meas}, Y_{pred}(\boldsymbol{\alpha})) \tag{3.1a}$$

$$f_2 = \left\| \boldsymbol{\alpha} \right\|_0 \tag{3.1b}$$

where $\|\cdot\|_2$ and $\|\cdot\|_0$ denote the $l_2$ norm and the $l_0$ norm, respectively. $Y$ is a general variable representing different types of information carries employed for damage identification. $\boldsymbol{\alpha}$ is a damage index vector.

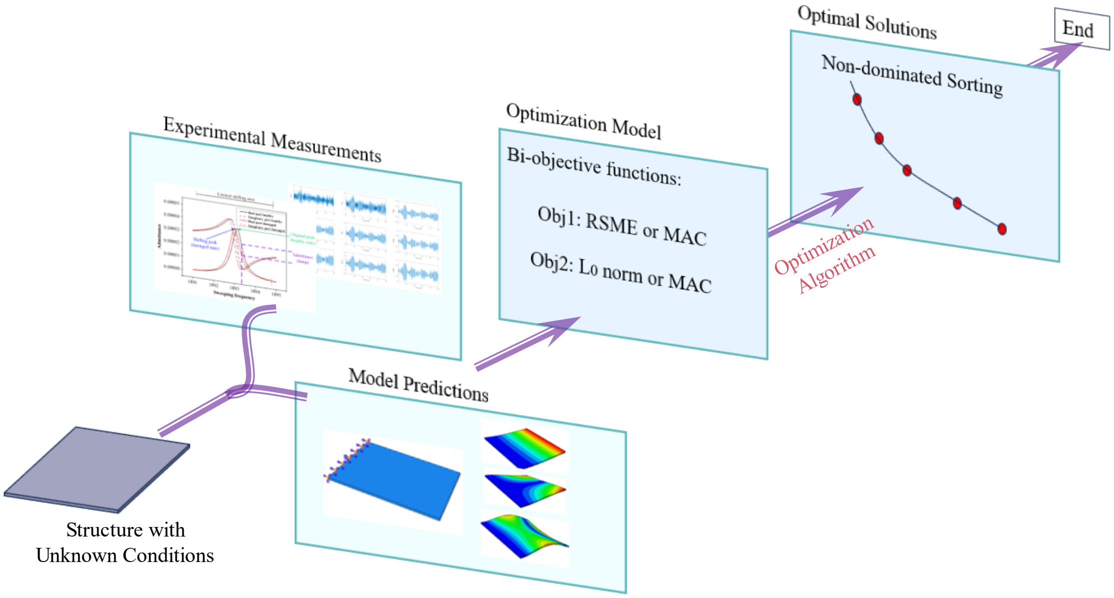

**Figure 3-1.** Flowchart of structural damage identification with bi-objective optimization.

The flowchart in Figure 3-1 depicts the basic steps of a physical model-based approach to damage identification in a structure with an unknown health state, utilizing both experimental data and model predictions. The two branches converge to evaluate differences, which are then fed into a bi-objective optimization process, ultimately yielding a set of solutions characterized by a Pareto front. This formulation of inverse analysis matches with the nature of structural damage identification. It will yield a solution set with multiple solutions that can be used for high level decision making. As stated, the challenge lies in how to handle this high-dimensional, multi-modal optimization problem to find a small yet diverse solution set that can capture the true damage scenario as one of the solutions. Thus, tailoring an algorithm to handle the challenges becomes necessary.

## 3.3. Guiding Multi-objective Particle Swarm Optimization through Adaptive Learning Automata

Solving the optimization model formulated for actual damage location and severity is mathematically challenging. On one hand, we pursue solution diversity such that the true damage scenario can be included in the solution set. On the other hand, the size of the solution set will need to be relatively small so it can provide useful insight into high-level decision-making. While a variety of optimizers can potentially be explored, in this research we choose multi-objective particle swarm optimization (MOPSO) as the basic platform for enhancement, owing to its straightforward conceptualization, ease of implementation, computational efficiency, and small number of control parameters. Furthermore, we resort to LA mechanism to develop novel strategies to tackle the issues in MOPSO to realize effective damage identification inverse analysis.

### 3.3.1. General framework of particle swarm optimization

Particle swarm optimization is a swarm inspired evolutionary algorithm originally proposed by Kennedy and Eberhart (1995). It is then extended to multi-objective optimization (Coello et al, 2004). PSO is essentially a population-based metaheuristic approach that starts with a randomly generated initial population representing the candidate solutions referred to as particles. The particle moves through a *D* dimensional space as follows,

$$x_i(t+1) = x_i(t) + v_i(t+1) \tag{3.2a}$$

$$v_i(t+1) = zv_i(t) + c_1 r_1 (p_{\text{best}i}(t) - x_i(t)) + c_2 r_2 (g_{\text{best}}(t) - x_i(t)) \tag{3.2b}$$

where $x_i(t)$ and $v_i(t)$ represent, respectively, the position and velocity of the *i*-th particle in the *t*-th iteration. $p_{\text{best}}$ is the best position visited by particle *i* till the *t*-th iteration, and $g_{\text{best}}$ is the global best position amongst all the positions visited by all the particles. *z* is the inertia weight that reflects the tendency of the particles to maintain their previous speed. $c_1$ and $c_2$ are acceleration coefficients. $c_1$ regulates how much the particle trusts its own experience, and $c_2$ represents the trend of particles approaching the best position of the entire swarm. $r_1$ and $r_2$ are two random numbers chosen from uniform distribution over the range (0, 1). In each iteration, each particle's velocity or position are constrained by the boundary conditions since the particles may exceed the allowed search space and produce invalid solution. The main steps of the PSO algorithm are given as the pseudo-code **Algorithm 1** (Table 3-1).

**Table 3-1.** Algorithm 1: Particle swarm optimization framework.

```
Algorithm 1: Particle swarm optimization framework
    (1) Initialize the position and velocity of the particles.
    (2) Calculate the fitness value $f(x_i)$ ($i = 1,\cdots,N$) using Equation (3.1)
    (3) For each particle $x_i$, compare its fitness value $f(x_i)$ with the personal best location that it has
        experienced. If $f(x_i) < p_{\text{best}}$, update it as the current local best position.
    (4) For each particle $x_i$, compare its personal best fitness value with the global best fitness value. If
        $f(x_i) < g_{\text{best}}$, update it as current global best position.
    (5) Adjust the velocity and position of the population according to Equation (3.2); perform boundary
        condition checking.
    (6) If the algorithm reaches the maximum number of iterations or the minimum values of the fitness
        function, stop and output the result; otherwise go to step (2).
```

### 3.3.2. Guidance to search with learning automata

Learning automata (LA) can be regarded as an abstract decision-making unit situated in a stochastic environment that determines the optimal scheme through a set of actions and by frequent interactions with the environment (Hashemi and Meybodi, 2011; Zhang et al, 2020). An automaton contains a finite number of actions, where an action is chosen based on a specific probability distribution and applied to the environment. The environment evaluates the impact of the applied action and then sends back a reinforcement signal to the automaton. The learning algorithm of the automaton utilizes this response to update the existing action probability distributions. By continuing this process, the automaton increases the chance of better actions which generate favorable responses from the environment.

Mathematically, LA are represented by the quadruple ( $a$ , $\beta$ , $p$, $T$), where $a = (a_1,\ldots,a_r)$ is a set of actions, $\beta = (\beta_1,\ldots,\beta_r)$ is a set of input, $p = (p_1,\ldots,p_r)$ is a probability vector regulating the output choices, and $T$ is the learning algorithm used to modify (update) $p$. The learning algorithm $T$ is a crucial factor affecting the performance of LA. The linear reward-penalty algorithm ($L_{\mathrm{rp}}$) is one of the commonly employed learning algorithms presented in literature (Hashemi and Meybodi, 2011). The learning model $T$ for $L_{\mathrm{rp}}$ scheme to update the state probability vector $p$ after receiving the reinforcement signal $\beta$ is given as follows,

$$p_j(k+1) = \begin{cases} p_j(k) + c(1 - p_j(k)) & \text{if } i = j \\ p_j(k)(1 - c) & \text{if } i \neq j \end{cases} \tag{3.3a}$$

$$p_j(k+1) = \begin{cases} p_j(k)(1 - b) & \text{if } i = j \\ \dfrac{b}{r-1} + p_j(k)(1 - b) & \text{if } i \neq j \end{cases} \tag{3.3b}$$

where $r$ is the number of actions defined in the automaton; parameters $c$ and $b$ represent reward and penalty step length, respectively. Equation (3.3a) corresponding to the case when $\beta = 0$ (favorable response), and Equation (3.3b) corresponds to the case when $\beta = 1$ (unfavorable response). $a_i$ is thus the action chosen at time $t$ as using the distribution $p(t)$. Figure 3-2 illustrates how LA interacts with the environment.

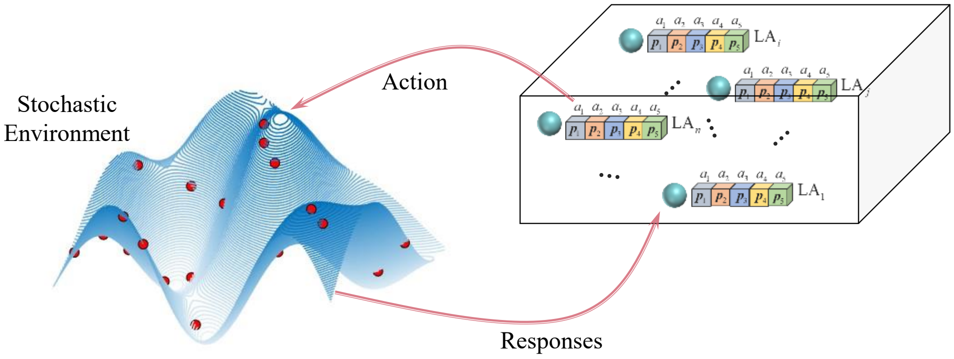

**Figure 3-2.** Illustration of learning automata (LA) scheme.

### 3.3.3. Learning automata guided MOPSO towards a diverse and small solution set

When solving the damage identification problem formulated in Equations (3.1a) and (3.1b), our objective is to obtain a small yet diverse set of solutions that encompasses the true damage scenario. We leverage multi-objective particle swarm optimization (MOPSO) to achieve this goal. The working mechanism of MOPSO, which involves updating particle positions based on individual and collective experiences, offers the potential to incorporate metaheuristics for performance enhancement. Specifically, we synthesize a series of local search strategies using time variation and mutation, treating them as actions. Subsequently, learning automata (LA) is utilized to select the most appropriate action at each iteration, based on feedback from the optimization process. The integration of MOPSO with LA is detailed as follows.

***Time varying inertia weight*** (TVIW): The TVIW was suggested by Shi and Eberhart (1999), which is conducive to early exploration and later exploitation. This can be expressed as $z^t = z_{\max} - t(z_{\max} - z_{\min}) / t_{\max}$, where $t_{\max}$ is the maximum number of iterations, $t$ is the current iteration, and $z_{\min}$ and $z_{\max}$ are the initial and final values of the inertia weight. Here $z_{\max} = 0.9$ and $z_{\min} = 0.4$ are recommended (Kennedy and Eberhart, 1995).

***Time varying acceleration coefficients*** (TVAC): The TVAC was proposed to enhance the global search ability during early stages as well as the convergence toward the global optima during the later stages (Ratnaweera et al, 2004). This is achieved by modifying two acceleration coefficients $c_1$ and $c_2$ in the following manner, $c_1^t = c_1^{\max} - (c_1^{\max} - c_1^{\min})t / t_{\max}$, $c_2^t = c_2^{\max} + (c_2^{\max} - c_2^{\min})t / t_{\max}$. Here, $c_1^{\min}$, $c_2^{\min}$ are the initial values of $c_1$, $c_2$; $c_1^{\max}$ and $c_2^{\max}$ are the final values of the $c_1$ and $c_2$, respectively. $t$ is the current iteration number, and $t_{\max}$ is the maximum number of allowable iterations. TVAC changes the cognitive component and the social component by reducing $c_1$ and increasing $c_2$ along with the iteration. It can make adjustment between social and cognitive experiences so as to mitigate premature convergence of the algorithm.

Recall Equations (3.2a) and (3.2b). Based on these time varying coefficients, we can define two actions as follows,

$$v_i(t+1) = z^t v_i(t) + c_1^t r_1(p_{\mathrm{best}i}(t) - x_i(t)) + c_2^{\min} r_2(g_{\mathrm{best}}(t) - x_i(t)) \tag{3.4a}$$

$$x_i(t+1) = x_i(t) + v_i(t+1) \tag{3.4b}$$

$$v_i(t+1) = z^t v_i(t) + c_1^{\min} r_1(p_{\mathrm{best}i}(t) - x_i(t)) + c_2^t r_2(g_{\mathrm{best}}(t) - x_i(t)) \tag{3.5a}$$

$$x_i(t+1) = x_i(t) + v_i(t+1) \tag{3.5b}$$

In both actions, we adopt time varying inertia weights. For Action 1, as shown in Equations (3.4a) and (3.4b), we use time varying acceleration coefficient $c_1$ and keep $c_2$ as constant. This can help particles to explore more space at the beginning of the optimization process. On the other hand, Action 2, as shown in Equations (3.5a) and (3.5b), takes $c_1$ as constant and uses a time varying acceleration $c_2$. Through this, the search process can achieve a convergence at the end of the optimization. The new position, which is the potential solution, will be updated using any action. Then the fitness values can be calculated and compared to the values from the old solution through dominant sorting algorithm. Positive feedback will be given as 0 if the new solution dominates the old one; otherwise, negative feedback will be given as 1 for the action selected at current iteration.

To help particles jump out of potential local extremes, an ***Elitist-based perturbation*** (EBP) strategy, Action 3, is adopted to perform perturbation on the personal best of the particle and provide extra diversity (Lim and Isa, 2013). To trigger the EBP strategy, we introduce a variable called *RT* that determines the number of times the EBP strategy is repeated. In the EBP strategy, a randomly selected dimension in the personal best of a particle is perturbed using following logic,

$$tempP_{\mathrm{best}i,d} = \begin{cases} p_{\mathrm{best}i,d} + r_d \cdot (\alpha_{\max,d} - \alpha_{\min,d}) & \text{if rand} > 0.5 \\ p_{\mathrm{best}i,d} - r_d \cdot (\alpha_{\max,d} - \alpha_{\min,d}) & \text{if rand} \leq 0.5 \end{cases} \tag{3.6}$$

Here $tempP_{\mathrm{best}i,d}$ is an intermediate variable that temporarily represents the personal best, $p_{\mathrm{best}i,d}$ denotes the *d*-th dimension of the personal best of the *i*-th population, $r_d$ is a random number obtained from the normal distribution of $N \sim (\mu, R^2)$ with $\mu = 0$ and standard deviation of $R$ where $R = R_{\max} - t(R_{\max} - R_{\min})\big/t_{\max}$ . $R_{\max} = 1$and $R_{\min} = 0.1$, as suggested by Lim and Isa (2013), are the maximum and minimum perturbation ranges, respectively. *t* is the current number of iterations, and $t_{\max}$ is the maximum iteration of the algorithm. $\alpha_{\min,d}$ and $\alpha_{\max,d}$ are the lower and upper bounds of the *d*-th dimension. The personal best will be replaced by the temporary personal best $tempP_{\text{best}i,d}$, if the latter dominates the former and the reinforcement signal will be given as 0 to indicate a favorable action. In other words, the personal best finds a new position which is closer to global solution or closer to true damage scenario in structural damage identification through EBP; otherwise, the personal best keeps unchanged, and the signal is 1 to show an unfavorable action, i.e., the action achieves nothing but costs computation time, so the penalty is necessary.

Another emphasis called ***Mutation*** (Action 4) aims at assisting the global best in examining its surroundings and determining whether it can break free from its current position and discover a more advantageous one. We use *L* to represent the global best, and have

$$tempL_{\text{best},d} = L_{\text{best},d} + norm(\mu, R^2) \tag{3.7}$$

where $tempL_{\text{best}i,d}$ is an intermediate variable that temporarily represents the global best. As shown above, $L_{\text{best},d}$ denotes the *d*-th dimension of the global best. A random perturbation is generated following the same normal distribution in strategy EBP. The decay standard deviation is used to attain a significant jump at the beginning and a smaller one at the end of the process. At this time, if the temporary global best dominates the global best, then it will replace the old one. The reinforcement signal is then given as 0 to show that ***Mutation*** is favorable. Otherwise, the signal is given as 1.

During the ***Fine-Tuning*** process (Action 5), the focus is on every dimension of the personal best through its velocity updating, rather than only one randomly selected dimension. This strategy aims to encourage particles to move more in the direction that enhances the solution and, conversely, to slow down in the direction that impedes solution improvement. To initiate the action, tuning is repeated *PT* times for each dimension. However, it is crucial to avoid setting *PT* to a high value because optimization deals with high-dimensional problems, and an excessively large *PT* value can prolong the runtime significantly. Here we set *PT* as 10. Let $V_{i,d}$ denote the velocity of the *d*-th dimension of the personal best of the *i*-th population in fine tuning. We employ the following in this research (Ji et al, 2007; Samma et al, 2016),

$$V_{i,d} = \frac{\varphi}{t^{\phi}} r + 2B_{i,d} \tag{3.8}$$

where $\varphi$ is the acceleration factor and set as 2, $\phi$ is the descent parameter that controls the decay of the velocity and is set as 20, *r* is a uniformly distributed random number within [−0.5,0.5], and *t* is the current iteration number. Moreover, we let

$$B_{i,d} = \begin{cases} 2V_{i,d}, & \text{if } x_{\text{new}} \prec x_{\text{old}} \\ 0.5B_{i,d}, & \text{otherwise} \end{cases} \tag{3.9}$$

Then the personal best can be updated based in the following manner,

$$tempP_{\text{best}i,d} = \begin{cases} p_{\text{best}i,d} + V_{i,d}, & \text{if } x_{\text{new}} \prec x_{\text{old}} \\ p_{\text{best}i,d}, & \text{otherwise} \end{cases} \tag{3.10}$$

The updated temporary best $tempP_{\text{best}i,d}$ will take replace of the personal best if it dominates the personal best. Otherwise, the original personal best remains unchanged. Subsequently, the positive signal 0 or negative signal 1 will be applied accordingly. The integration of the abovementioned strategies through LA into MOPSO is outlined as pseudo code shown in **Algorithm 2** (Table 3-2).

**Table 3-2.** Algorithm 2: Learning Automata guided MOPSO.

**Algorithm 2: Learning Automata guided MOPSO**

```
(1) Initialization: Randomly generate the positions and velocities of all particles, initialize the probability of selecting the global search strategy p as $p = 1 / o(a)$, where p represents the probability that the agent selects the global search strategy and $o(a)$ is the number of action. Randomly choose an action, Equations (3.4) -(3.8).
(2) Position and Velocity Updating:
```

```
    o  2.1 Update the velocity of current learning automaton using the selected action
    o  2.2 Update the position of current learning automaton using the selected action
    o  2.3 Deal with the bounds
    o  2.4 Calculate the fitness values
(3) Update the personal best using non-dominated sorting algorithms
(4) Update the global best using non-dominated sorting algorithms
(5) Delete the solutions if the number of solutions in Pareto front is reached.
(6) Update Probability: If updated solution dominates the old solution, update the probability using
    Equation (3.3a); otherwise, update the probability using Equation (3.3b)
(7) Terminal condition check: If any of pre-defined termination criteria is not satisfied, repeat from
    step 2. Otherwise, the algorithm terminates.
```

### 3.3.4. Summary of the proposed optimization algorithm

The proposed LA guided MOPSO algorithm, referred to as the LAMOPSO hereafter, is illustrated through the flowchart shown in Figure 3-3, in which the steps from top to bottom correspond to the steps in **Algorithm 2** (Table 3-2). After initialization, each population is regarded as a learning automaton (LA). Each LA has 5 actions, as described in the previous subsection. This LAMOPSO utilizes the ability of LA to learn and adaptively select a suitable strategy for the swarm in various search stages based on feedback received. Initially, LA randomly selects an action as all actions have an equal probability. As the search progresses, LA learns from feedback in each iteration and updates the selection probabilities of candidate actions. In later stages, after interacting with the environment, LA identifies the actions that yield positive results and accumulates the corresponding probabilities. It is noteworthy that the update of the selection probabilities of candidate strategies is not predetermined but learned from the evolution process via LA, which promotes the intelligence of the swarm.

The LAs are independent individuals since they have their own actions and corresponding probabilities. The advantage is that they can decide their next moves based on the current landscape. Meanwhile, they work in a collaborative way, as they update the same optimal solution repository. In order to obtain a small yet diverse set of solutions that accurately represent the true damage scenario, we have devised five search methods that rely on coefficient variation and mutation. These techniques augment the search process, thereby facilitating the acquisition of a diverse set of solutions. Furthermore, we have implemented Learning Automata to help the particles intelligently choose the appropriate strategy during each iteration.

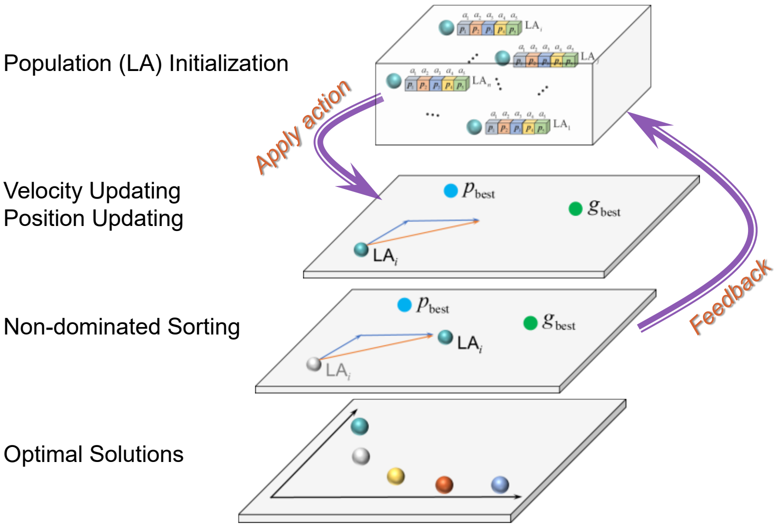

**Figure 3-3.** Flowchart of the proposed LAMOPSO algorithm.

## 3.4. Demonstration and Validation through Case Investigations

Our goal is to synthesize a new multi-objective optimization solver that can be effectively implemented to structural damage identification to tackle the peculiar challenges. Prior to examining the performance in structural damage identification, we first conduct case demonstration of the LAMOPSO developed in the preceding section on benchmark cases. This leads to, first and foremost, algorithmic implementation insights, and provides performance comparison with respect to representative optimization solvers to showcase the efficacy of the new approach.

### 3.4.1. Benchmark test functions

The topic of multi-objective optimization is quite broad, and a number of methods have been synthesized in recent years to tackle various challenges. In this section, without loss of generality, we conduct the performance comparison employing the following test functions: ZDT (Zitzler er al, 2000), CEC09 or UF (Zhang et al, 2008) and IMOP (Tian et al, 2019b). The proposed LAMOPSO is compared with multi-objective optimization solvers including NMPSO (Lin et al, 2018), MMOPSO (Lin et al, 2015), GPSOM (Noel, 2012), MO_Ring_PSO_SCD (Yue et al, 2018), MOEADDQN (Tian et al, 2023), CMOQLMT (Ming et al, 2023), MOCS (Du and Trung, 2023).

**Table 3-3.** Benchmark test functions.

| Problems | *M* | *D* | Population size | Descriptions |
|---|---|---|---|---|
| UF1 | 2 | 30 | 50 | Nonlinear decision space |
| UF2 | 2 | 30 | 50 | Nonlinear decision space |
| UF3 | 2 | 30 | 50 | Convex front |
| UF4 | 2 | 30 | 50 | Concave front |
| UF5 | 2 | 30 | 50 | Discrete points on a linear hyperplane |
| ZDT1 | 2 | 30 | 50 | Convex front |
| ZDT2 | 2 | 30 | 50 | Concave front |
| ZDT3 | 2 | 30 | 50 | Discontinuous front |
| ZDT4 | 2 | 30 | 50 | Convex front, many local optimal |
| ZDT6 | 2 | 30 | 50 | Concave front, non-uniform distribution |
| IMOP1 | 2 | 15 | 50 | Convex front with sharp tail |
| IMOP2 | 2 | 15 | 50 | Concave front with sharp tail |
| IMOP3 | 2 | 15 | 50 | Discontinuous front |

The algorithms selected for comparison exhibit a high degree of competitiveness. They are either variants of the PSO algorithm or variants of evolutionary algorithms and reinforcement learning techniques, such as Deep Q-Networks and Q-Learning, which all are the most directly related to current research. These algorithms have demonstrated promising performance in the domain of multi-objective optimization. Meanwhile, the test functions selected are frequently used in the past to evaluate the performance of metaheuristics. Especially, the IMOP test functions are designed in recent years, which have sharp Pareto front, thus posing challenges to the metaheuristics to converge to the true Pareto front. The test function details are listed in Table 3-3. These functions are employed to evaluate the convergence of the algorithms and the diversity of solutions generated by the algorithms.

### 3.4.2. Insights into parametric settings and evaluation metrics

In the benchmark testing, *D* is the dimension of each test problem and *M* is the number of objectives. Here, *M* is set as 2 for all testing instances. *D* is 30 for test functions ZDTs and UFs, and 15 for IMOPs. The true Pareto front of the IMOP test functions is quite sharp, which poses significant challenge. Thus, we use 15 for the IMOPs to mitigate the difficulty for all the algorithms to be evaluated. The variables in the IMOPs can be written as $\mathbf{x} = (x_1, \ldots, x_L, x_{L+1}, \ldots, x_D) \in [0,1]$. We apply three objective functions for the IMOPs, in which $y_1 = (1/L \sum_{l=1}^{L} x_l)^{a_1}$, $g = \sum_{l=L+1}^{D} (x_l - 0.5)^2$. Here, for the IMOPs, the two parameters involved are set as $a_1 = 0.05$ to control the mathematical difficulty in diversity preservation and $L = 5$ to control the length of variables used for calculations of $y_1$ and *g*. The specific expressions for all test functions are included in the appendix for reference. The total number of iterations for all test problems is set as 40,000 after convergence analysis based on two indicators as explained below.

In this research, we utilize the hypervolume (HV) and the inverted generational distance (IGD) to quantify the performance of the algorithms. The performance comparison is based on the Pareto set that is a set of solutions realizing the optimal trade-offs between the optimization objectives. The HV indicator defined below measures the convergence as well as the diversity (Friedrich et al, 2009),

$$HV\ \ X\ \ = \mathrm{VOL}(\underset{x\in X}{\mathrm{U}}(x,P)) \tag{3.11}$$

where $X$ is a solution set obtained by one algorithm, $\mathrm{VOL}(\cdot)$ is the Lebesgue measure, and $P$ is a set of reference points. The calculation of *HV* requires the normalized objective function values. Indeed, *HV* stands for the percentage covered by the Pareto front of the cuboid defined by the reference point *P* and the original point *x*. Here the reference point is set to be 1.1 times the upper bound of the normalized *PF*. The hypervolume metric can also assess both the convergence and diversity of the dominant solution set. A larger *HV* value indicates better diversity of solutions.

IGD is an indicator measuring the degree of convergence by computing the average of the minimum distance of points in the true Pareto to points in Pareto front obtained (Ishibuchi et al, 2018), i.e.,

$$IGD(PF,PF^*) = \frac{\sum\limits_{\mathbf{f}^*\in PF^*,\ i=1}^{|PF^*|}\sqrt{\min\limits_{\mathbf{f}\in PF}\left(\sum\limits_{m=1}^{M}(f_m^{*i} - f_m)^2\right)}}{|PF\ ^*|} \tag{3.12}$$

where *M* is the number of objectives, $PF^*$ is the true Pareto front for a specific test function; $|\ PF^*\ |$ is the cardinality of $PF^*$ and *PF* is the Pareto front obtained by one algorithm, $f_m^*$ and $f_m$ are the *m*-th objective values in true Pareto set and Pareto set calculated by one algorithm, respectively. The essence of Equation (3.12) is to calculate the Euclidean distance between the points on the true Pareto front and the points on the Pareto front obtained. Therefore, a smaller value of *IGD* means that the two fronts are closer to each other. In other words, a smaller value of *IGD* indicates a better convergence and completeness of the *PF* obtained.

### 3.4.3. Discussion on benchmark test case results

All algorithms are executed independently 30 times for each test problem on platform PlatEMO (Tian et al, 2017). The means and variances of the *HV* and *IGD* results obtained from 30 independent runs on UF, ZDT and IMPO are listed in Table 3-4 and Table 3-5, respectively. The best mean values of the *HV* index in each test function are highlighted with shade in the table. In each test case, the first-row values are the means, and the second-row parenthesized values are the variances.

**Table 3-4.** *HV* results from 30 executions with two problem objectives.

| Problems | Alg1 | Alg2 | Alg3 | Alg 4 | Alg 5 | Alg 6 | Alg 7 | Alg 8 |
|---|---|---|---|---|---|---|---|---|
| UF1 | 5.864e-1 | 6.082e-1 | 5.195e-1 | 4.841e-1 | 6.408e-1 | 6.630e-1 | 5.974e-1 | 5.872e-1 |
| | (1.02e-2) | (3.46e-2) | (6.93e-2) | (8.00e-3) | (3.83e-2) | (1.32e-2) | (1.28e-2) | (1.12e-2) |
| UF2 | 6.113e-1 | 6.716e-1 | 6.426e-1 | 3.768e-1 | 6.897e-1 | 6.857e-1 | 7.118e-1 | 7.122e-1 |
| | (2.17e-2) | (3.42e-3) | (1.12e-2) | (1.24e-2) | (5.67e-3) | (4.00e-3) | (1.33e-2) | (1.57e-2) |
| UF3 | 5.283e-1 | 4.277e-1 | 3.090e-1 | 1.551e-1 | 5.257e-1 | 5.691e-1 | 2.630e-1 | 4.436e-1 |
| | (7.02e-2) | (5.05e-2) | (3.35e-2) | (4.10e-3) | (1.03e-1) | (2.76e-2) | (1.79e-2) | (2.26e-2) |
| UF4 | 3.351e-1 | 3.686e-1 | 1.447e-1 | 2.516e-1 | 3.629e-1 | 3.795e-1 | 3.407e-1 | 3.880e-1 |
| | (2.08e-2) | (5.64e-3) | (3.17e-2) | (3.04e-3) | (6.88e-3) | (2.00e-3) | (1.83e-2) | (2.49e-3) |
| UF5 | 4.006e-2 | 4.082e-2 | 0.000e+0 | 0.000e+0 | 1.340e-1 | 2.633e-1 | 2.160e-1 | 2.762e-1 |
| | (5.06e-2) | (4.40e-2) | (0.00e+0) | (0.00e+0) | (7.21e-2) | (4.80e-2) | (8.17e-2) | (6.45e-2) |
| ZDT1 | 6.920e-1 | 7.133e-1 | 6.976e-1 | 2.308e-1 | 7.158e-1 | 7.154e-1 | 7.079e-1 | 7.163e-1 |
| | (7.45e-3) | (6.24e-4) | (2.31e-3) | (1.29e-2) | (9.74e-5) | (3.64e-4) | (1.43e-2) | (6.52e-4) |
| ZDT2 | 4.330e-1 | 4.384e-1 | 1.736e-1 | 0.000e+0 | 4.408e-1 | 4.398e-1 | 3.713e-1 | 4.418e-1 |
| | (2.66e-3) | (5.20e-4) | (0.00e+0) | (0.00e+0) | (8.33e-5) | (3.85e-4) | (1.55e-1) | (9.55e-3) |
| ZDT3 | 5.670e-1 | 5.972e-1 | 5.312e-1 | 3.940e-1 | 5.947e-1 | 5.977e-1 | 8.300e-1 | 8.399e-1 |
| | (3.33e-4) | (2.25e-4) | (3.63e-2) | (2.20e-2) | (2.86e-5) | (1.54e-4) | (9.39e-3) | (1.47e-2) |
| ZDT4 | 0.000e+0 | 5.975e-3 | 0.000e+0 | 0.000e+0 | 1.314e-1 | 0.000e+0 | 0.000e+0 | 7.176e-1 |
| | (0.00e+0) | (2.22e-2) | (0.00e+0) | (0.00e+0) | (1.86e-1) | (0.00e+0) | (0.00e+0) | (1.72e-3) |
| ZDT6 | 3.839e-1 | 3.832e-1 | 1.180e-1 | 0.000e+0 | 3.857e-1 | 3.776e-1 | 4.091e-1 | 4.247e-1 |
| | (7.71e-4) | (5.46e-4) | (3.49e-2) | (0.00e+0) | (2.59e-4) | (8.16e-3) | (1.20e-2) | (1.21e-4) |
| IMOP1 | 9.568e-1 | 9.856e-1 | 8.126e-1 | 2.982e-1 | 9.823e-1 | 9.863e-1 | 9.862e-1 | 9.880e-1 |

| | | | | | | | | |
|---|---|---|---|---|---|---|---|---|
| | (1.78e-2) | (6.26e-4) | (8.24e-2) | (2.17e-2) | (8.01e-5) | (2.20e-4) | (2.82e-3) | (3.71e-4) |
| IMOP2 | 2.186e-1 | 2.294e-1 | 1.326e-1 | 8.442e-2 | 2.271e-1 | 2.296e-1 | 2.018e-1 | 1.010e-1 |
| | (4.79e-3) | (3.49e-4) | (4.19e-2) | (7.81e-4) | (1.52e-3) | (2.77e-4) | (5.16e-2) | (2.03e-4) |
| IMOP3 | 5.912e-1 | 6.559e-1 | 2.319e-1 | 1.355e-1 | 6.540e-1 | 6.492e-1 | 3.790e-1 | 6.561e-1 |
| | (3.19e-2) | (5.94e-4) | (4.43e-2) | (6.29e-3) | (3.28e-4) | (1.08e-2) | (1.74e-2) | (3.43e-4) |

∗∗ Algorithms 1 to 8 in Table 3-4 are: NMPSO, MMOPSO, GPSOM, MO_Ring_PSO_SCD, MOEADDQN, CMOQLMT, MOCS and LAMOPSO.

As shown in Table 3-4, in terms of *HV* indicator, the proposed LAMOPSO outperforms the MOPSO variants such as NMPSO, MMOPSO, GPSOM, MO_Ring_PSO_SCD (the first 4 algorithms) and multi-objective cuckoo search (MOCS) (the 7th column) quite significantly. Especially, the variants GPSOM and MO_Ring_PSO_SCD have many *HV* of zeros on some test functions such as UF5 and ZDT2, 4, 6, indicating that the algorithm is trapped in local optima and unable to achieve diversity in the solution set. Moreover, the LAMOPSO outperforms all other algorithms on the UF and ZDT test sets. Interestingly, the two other algorithms, MOEADDQN and COMQLMT, are variants that incorporate reinforcement learning techniques. However, when pitted against our proposed LAMOPSO algorithm, they exhibit inferior overall performance. Across the majority of the test functions, these algorithms fail to match the capabilities of our LAMOPSO algorithm. The LAMOPSO leads to the largest mean *HV* values and entertains mostly smaller variances indicating more consistent results.

For the IMOP test functions, the LAMOPSO algorithm performs better on IMOP1. On the IMOP2 test function, CMOQLMT demonstrates superior performance, with MMOPSO emerging as its closest competitor, exhibiting only a marginally inferior result. For the IMOP3 test function, LAMOPSO takes a slight lead, while MMOPSO, MOEADDQN, and CMOQLMT algorithms put up a formidable competition, trailing closely behind. As mentioned earlier, the IMOP test functions have sharp Pareto fronts. IMOP2 has a concave front, and IMOP3 has a discontinuous front. The variants incorporating reinforcement learning techniques exhibit a general superiority compared to the variants of traditional algorithms. This observation suggests that reinforcement learning holds significant potential for enhancing and improving optimization algorithms. Overall, the proposed LAMOPSO yields the best performance of *HV* in 10 out of 13 test cases, which illustrates the outstanding performance in diversity and convergence.

Table 3-5 shows the *IGD* results comparison. Recall that smaller *IGD* values correspond to better convergence and completeness of the Pareto front obtained. It can be observed that the LAMOPSO outperforms other algorithms on most test sets, except for the UF1, 3, 4, IMOP2, and IMOP3 test functions which are won by the CMOQLMT and MMOPSO. It is noteworthy that the CMOQLMT algorithm, a variant that combines evolutionary algorithms with Q-learning, exhibits considerable competitiveness in terms of the IGD metric. This observation further reinforces the potential of reinforcement learning techniques in enhancing the performance of optimization algorithms. The learning automata employed in this work, being a form of reinforcement learning, is utilized to improve upon the traditional MOPSO algorithm, thereby manifesting this inherent potential. Overall, the LAMOPSO yields the best IGD results in 8 out of 13 test cases, and the results are consistent with generally small variances. This indicates that the LAMOPSO can converge well to the true Pareto front.

**Table 3-5.** *IGD* results from 30 executions with two problem objectives.

| Problems | Alg1 | Alg 2 | Alg 3 | Alg 4 | Alg 5 | Alg 6 | Alg 7 | Alg 8 |
|---|---|---|---|---|---|---|---|---|
| UF1 | 1.132e-1 | 7.836e-2 | 1.307e-1 | 1.626e-1 | 5.987e-2 | 4.255e-2 | 8.220e-2 | 9.121e-2 |
|  | (7.42e-3) | (2.28e-2) | (4.64e-2) | (7.95e-3) | (3.41e-2) | (1.04e-2) | (1.25e-3) | (9.97e-4) |
| UF2 | 8.232e-2 | 3.986e-2 | 6.586e-2 | 2.581e-1 | 2.753e-2 | 2.927e-2 | 1.144e-2 | 9.060e-3 |
|  | (1.46e-2) | (2.98e-3) | (8.54e-3) | (1.34e-2) | (6.19e-3) | (3.81e-3) | (4.17e-4) | (6.11e-4) |
| UF3 | 1.451e-1 | 2.127e-1 | 3.124e-1 | 5.603e-1 | 1.355e-1 | 1.131e-1 | 4.033e-1 | 2.338e-1 |
|  | (6.44e-2) | (3.49e-2) | (3.45e-2) | (7.23e-3) | (7.37e-2) | (2.86e-2) | (1.01e-3) | (2.12e-2) |
| UF4 | 7.956e-2 | 5.511e-2 | 2.125e-1 | 1.323e-1 | 6.069e-2 | 4.735e-2 | 7.674e-2 | 5.210e-2 |
|  | (1.59e-2) | (4.61e-3) | (3.21e-2) | (2.33e-3) | (5.67e-3) | (1.43e-3) | (2.21e-3) | (2.71e-2) |
| UF5 | 6.635e-1 | 6.824e-1 | 1.936e+0 | 2.244e+0 | 4.876e-1 | 2.422e-1 | 2.616e-1 | 2.294e-1 |
|  | (1.48e-1) | (1.65e-1) | (3.05e-1) | (1.39e-1) | (1.13e-1) | (4.55e-2) | (7.57e-2) | (1.52e-1) |

| | | | | | | | | |
|---|---|---|---|---|---|---|---|---|
| ZDT1 | 2.714e-2 | 1.015e-2 | 2.511e-2 | 4.312e-1 | 7.854e-3 | 8.120e-3 | 1.005e-2 | 5.950e-3 |
| | (7.00e-3) | (6.30e-4) | (1.06e-3) | (1.96e-2) | (8.48e-6) | (1.95e-4) | (7.29e-4) | (9.97e-4) |
| ZDT2 | 2.223e-2 | 1.064e-2 | 3.549e-1 | 9.335e-1 | 7.701e-3 | 8.137e-3 | 1.303e-1 | 6.120e-3 |
| | (4.29e-3) | (5.44e-4) | (1.69e-16) | (1.11e-1) | (6.03e-6) | (1.58e-4) | (2.53e-1) | (6.11e-4) |
| ZDT3 | 1.004e-1 | 1.176e-2 | 1.015e-1 | 3.282e-1 | 2.131e-2 | 1.009e-2 | 1.293e-2 | 7.100e-3 |
| | (1.03e-3) | (5.27e-4) | (3.00e-2) | (1.56e-2) | (3.03e-5) | (2.98e-4) | 1.81e-3 | (2.12e-2) |
| ZDT4 | 9.463e+0 | 1.834e+0 | 2.573e+2 | 2.744e+2 | 7.894e-1 | 1.994e+0 | 1.140e+1 | 5.210e-2 |
| | (5.50e+0) | (1.03e+0) | (1.29e+2) | (1.11e+1) | (4.41e-1) | (6.75e-1) | (2.04e+0) | (2.71e-2) |
| ZDT6 | 8.529e-3 | 8.938e-3 | 5.697e-1 | 5.066e+0 | 6.294e-3 | 1.067e-2 | 8.280e-3 | 4.986e-3 |
| | (9.55e-4) | (5.64e-4) | (1.25e-1) | (6.10e-2) | (5.45e-5) | (4.91e-3) | (4.32e-4) | (1.52e-1) |
| IMOP1 | 3.190e-1 | 1.230e-2 | 1.653e-1 | 6.070e-1 | 1.233e-1 | 1.149e-2 | 1.313e-2 | 1.136e-2 |
| | (4.74e-2) | (5.59e-4) | (2.30e-2) | (1.74e-2) | (1.43e-3) | (7.80e-4) | (8.06e-4) | (5.22e-4) |
| IMOP2 | 9.503e-2 | 1.591e-2 | 4.900e-1 | 6.579e-1 | 3.874e-2 | 2.095e-2 | 1.670e-1 | 2.066e-1 |
| | (2.69e-2) | (2.84e-3) | (1.32e-1) | (3.05e-2) | (1.87e-2) | (5.41e-3) | (3.26e-1) | (6.27e-3) |
| IMOP3 | 9.718e-2 | 9.915e-3 | 3.004e-1 | 5.847e-1 | 1.591e-2 | 1.880e-2 | 1.018e-2 | 9.530e-2 |
| | (2.02e-2) | (1.33e-3) | (2.47e-2) | (3.11e-2) | (8.99e-4) | (1.19e-2) | (1.14e-3) | (4.23e-4) |

∗∗ Algorithms 1 to 8 in Table 3-5 are: NMPSO, MMOPSO, GPSOM, MO_Ring_PSO_SCD, MOEADDQN, CMOQLMT, MOCS and LAMOPSO.

## 3.5. Applying the LAMOPSO to Structural Damage Identification Practice

As outlined in Section 3.2, the physical model-based damage identification can be cast into a multi-objective optimization problem utilizing different types of damage information carries. A unique challenge, however, lies in how to handle such a high-dimensional, multi-modal optimization problem to find a small yet diverse solution set that can capture the true damage scenario as one of the solutions. In this section, we conduct case studies to examine the proposed algorithm improvements using simulation modal responses and experimentally acquired piezoelectric admittance measurements.

### 3.5.1. Numerical case study

In this first case study, we apply the proposed algorithm to a simplistic SHM case study based on numerical simulation. This allows interested readers to quickly examine the algorithm details and gain insights.

#### 3.5.1.1. Damage identification with modal information

Vibration-based SHM relies on modal information obtained from dynamic analysis. By comparing measured and predicted natural frequencies and mode shapes, the locations and severities of damages can be identified. However, in practical engineering applications, the number of unknowns typically exceeds the number of useful measurements, rendering the structural identification an underdetermined problem. As stated in Section 3.2, in this research we adopt a bi-objective optimization approach to address the underdetermination. Here a correlation coefficient termed the modal assurance criterion (MAC) is utilized to compare two frequency change vectors, i.e., measured frequency change $\boldsymbol{\Delta\lambda}$ and predicted frequency change $\delta\boldsymbol{\lambda}$, as expressed below (Cao et al, 2018b),

$$\mathrm{MAC}(\boldsymbol{\lambda}, \boldsymbol{\alpha}) = \frac{\left\langle \Delta\boldsymbol{\lambda},\, \delta\boldsymbol{\lambda}(\boldsymbol{\alpha}) \right\rangle^2}{\left\langle \Delta\boldsymbol{\lambda},\, \Delta\boldsymbol{\lambda} \right\rangle \cdot \left\langle \delta\boldsymbol{\lambda}(\boldsymbol{\alpha}),\, \delta\boldsymbol{\lambda}(\boldsymbol{\alpha}) \right\rangle} \tag{3.13}$$

where $\left\langle *, * \right\rangle$ calculates the inner product of two vectors, and $\boldsymbol{\alpha}$ is the damage index vector. $\mathrm{MAC}(\boldsymbol{\lambda},\boldsymbol{\alpha}) \in [0,1]$ captures the similarity between $\boldsymbol{\Delta\lambda}$ and $\delta\boldsymbol{\lambda}$. The value of MAC equals to one means that two vectors compared are identical to each other in terms of direction. On the other hand, among the modal parameters of a structural system, the mode shape is obviously the only location-related parameter. Mode shape is more sensitive to local damage than modal frequency. It can provide more information about structural damage if we combine frequency change and mode shapes together. Thus, in order to take more local damage information into consideration, for the *j*-th mode shape, we can compare the measured change and predicted change using MAC in a similar manner,

$$\mathrm{MAC}(\phi, \boldsymbol{\alpha}) = \frac{\left\langle \{\Delta\phi_j\},\, \{\delta\phi_j(\boldsymbol{\alpha})\} \right\rangle^2}{\left\langle \{\Delta\phi_j\},\, \{\Delta\phi_j\} \right\rangle \cdot \left\langle \{\delta\phi_j(\boldsymbol{\alpha})\},\, \{\delta\phi_j(\boldsymbol{\alpha})\} \right\rangle} \tag{3.14}$$

Since both MACs are functions of $\boldsymbol{\alpha}$ and the measured data $\Delta\boldsymbol{\lambda}$ and $\{\Delta\phi_j\}$ are known, a multi-objective minimization problem can then be formulated as Equation (3.15). Here in the first objective function, we give the same weight for both MAC calculations from frequency and mode shape. The second objective function as mentioned is to regulate the undetermined problem since the measurement is usually limited.

$$\text{Find: } \boldsymbol{\alpha} \in \mathbf{E}^n\,,\ \alpha_l \le \alpha_i \le \alpha_u\,,\ i = 1,\ldots,n \tag{3.15a}$$

$$\text{Minimize: } f_1 = -0.5 \cdot \mathrm{MAC}(\boldsymbol{\lambda}) - 0.5 \cdot \mathrm{MAC}(\phi) \text{ and } f_2 = \left\|\boldsymbol{\alpha}\right\|_0 \tag{3.15b}$$

### 3.5.1.2. Damage identification results

We first conduct a test on a 30-element cantilever beam with a length of 10 mm per element, as shown in Figure 3-4. The beam has a Young's modulus of 69 GPa, a width of 50 mm, and a height of 20 mm for the cross-section. Without loss of generality, we utilize the first 6 natural frequencies and the 2nd mode shape as the simulated measurement data, obtained directly from the model in the numerical experiment. Two damage scenarios were considered: Case 1 with a single damage location at element 4 with a 24% stiffness reduction, and Case 2 with two damage locations at elements 4 and 15, with severities of 24% and 15%, respectively. It is noteworthy that the algorithm does not have prior knowledge of the number, locations, or severities of the damages. In this case study with 30 variables, we have set the maximum number of evaluations to 40,000, aligning with the standard used in benchmark test evaluations. As a result of the multi-objective optimization approach, we obtained a set of optimal solutions representing the trade-off between the objectives.

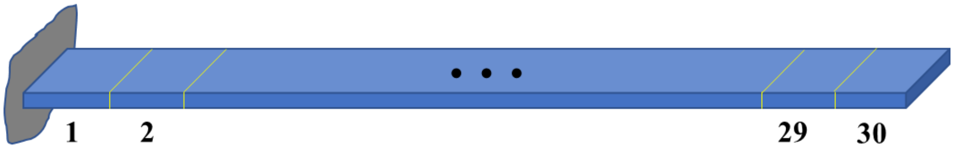

**Figure 3-4.** Cantilever beam structure with 30 elements.

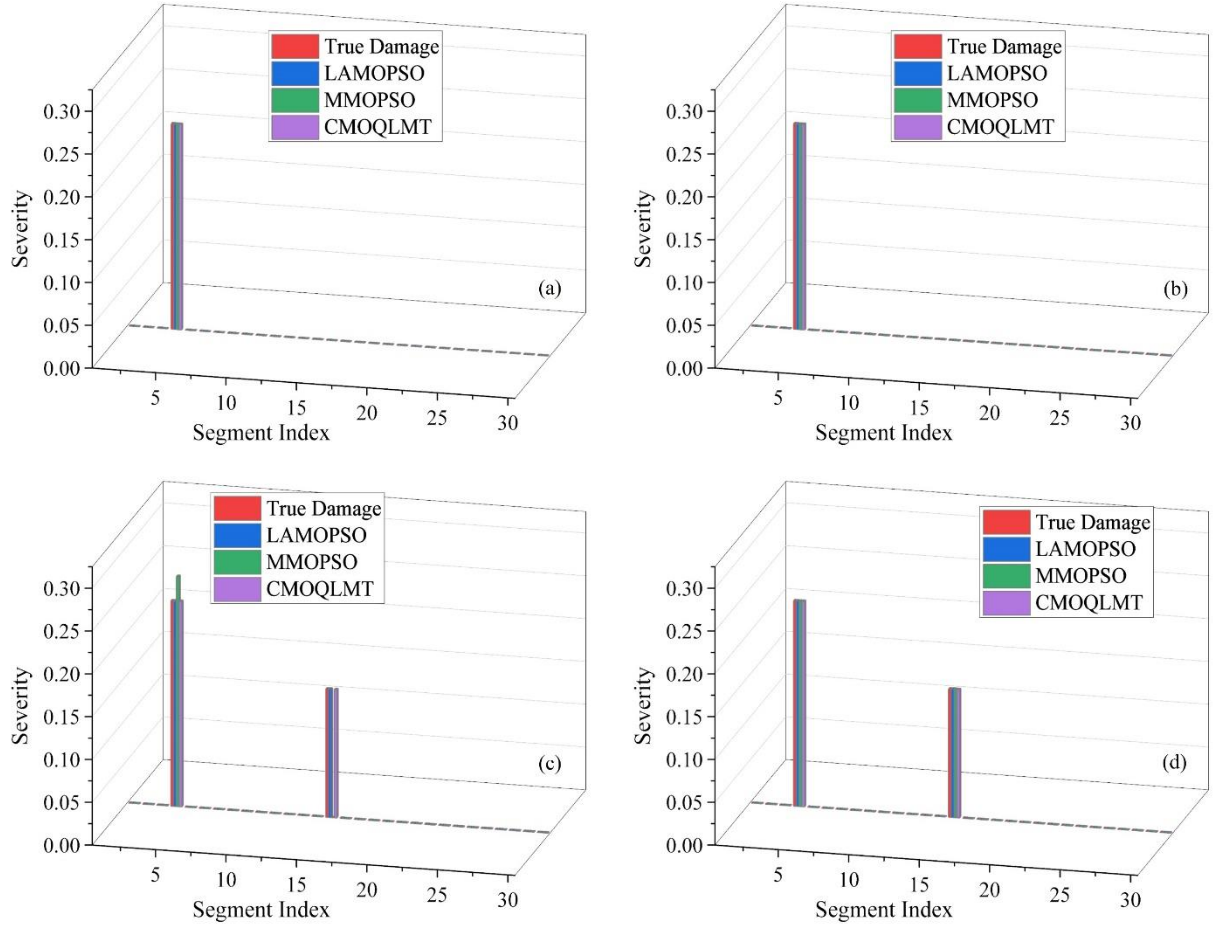

**Figure 3-5.** Identified results for cantilever beam structure for Case 1 and Case 2.

Figure 3-5 presents the damage identification results obtained by the proposed LAMOPSO algorithm. The top row displays two solutions corresponding to Case 1 (single damage location), while the bottom row shows two solutions for Case 2 (multiple damage locations). In previous benchmark tests, MMOPSO and CMOQLMT exhibited considerable competitiveness on certain test functions. Consequently, their performance was also evaluated on this engineering problem for comparison. As evident from the figure, two direct observations can be made: 1) a small solution set is obtained, which aligns with the expectation for underdetermined problem; 2) the obtained solutions show good sparsity due to the second objective function defined. Specifically, LAMOPSO and CMOQLMT algorithms accurately identify the true damage scenarios, regardless of the number of damage locations or varying damage severities. For MMOPSO algorithm, it behaves well in the case where the single damage happens, as shown in Figure 3-5(a) and Figure 3-5(b). While, in the second case with multiple damage, its first solution misses one true damage location, as shown in Figure 3-5(c). Overall, all the optimizers including the proposed LAMOPSO algorithm show good performance on this damage identification for beam structure.

### 3.5.2. Experimental case study

In this section, we present the application of the proposed algorithm to a realistic SHM experimental setup built upon piezoelectric active interrogation. The piezoelectric active interrogation typically employs a single piezoelectric transducer as actuator and sensor concurrently to collect the impedance or admittance information in near real-time (Fan et al, 2019; Ezzat et al, 2020). The impedance or admittance information can be collected in high-frequency range with smaller wavelengths, paving a way for high-accuracy damage identification when combined with a high-fidelity finite element model. Such high-fidelity finite element model, however, usually features high dimensionality, posing significant challenge to inverse identification.

#### 3.5.2.1. Experimental setup and physical modeling

Here we employ piezoelectric admittance-based active interrogation for structural damage identification on a real-world plate structure. For the sake of focused presentation of the current research, the detailed procedure for establishing the mathematical model of piezoelectric admittance-based damage identification, which can be found in literature (Shuai et al, 2017; Cao et al, 2023b), is outlined as shared data with link indicated in Appendix. Figure 3-6 illustrates the experimental setup, where a piezoelectric transducer is bonded to the top surface of a plate using epoxy resin. The parameters for the experimental setup are listed in Table 3-6. The plate is suspended by four thin strings at its corners to emulate free-free boundary conditions. A Dynamic Signal Analyzer (Agilent 35670A) measures the voltage across a 165 Ohm resistor to facilitate admittance measurement. A 5 Volts (Vpk) harmonic voltage with a good signal-to-noise ratio is applied to the transducer, and 25 cycles are used for each excitation frequency to reduce noise effects.

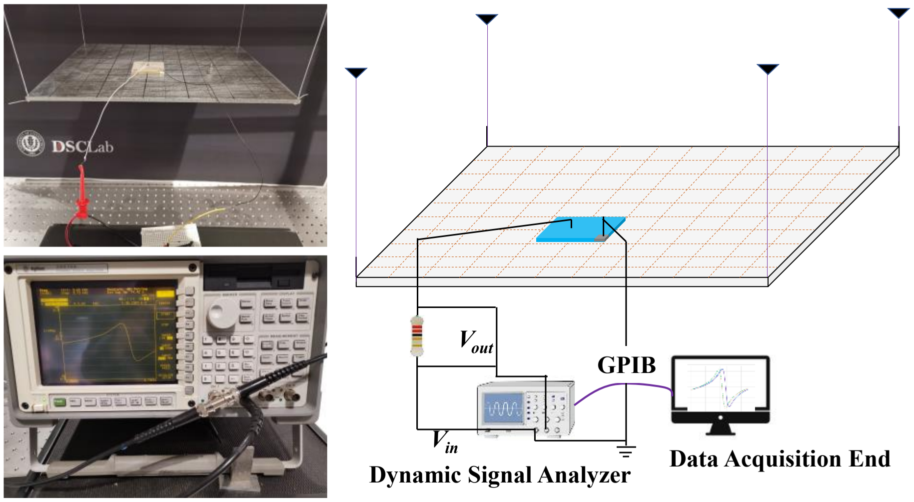

(a) (b)

**Figure 3-6.** Experimental setup (a) testbed; (b) schematical illustration of data acquisition.

**Table 3-6.** Geometry and material properties of the piezoelectric transducer and the plate.

| Structure | Parameters | Values |
|---|---|---|
| Plate | Length ($10^{-3}$ m) | 304.8 |
| | Width ($10^{-3}$ m) | 254 |
| | Thickness ($10^{-3}$ m) | 3.874 |
| | Young's modulus ($10^{3}$ MPa) | 72.21 |
| | Density (kg/m$^{3}$) | 2769 |
| | Poisson's ratio | 0.3 |
| Piezo Transducer (SM411) | Length ($10^{-3}$ m) | 45 |
| | Width ($10^{-3}$ m) | 45 |
| | Thickness ($10^{-3}$ m) | 3.5 |
| | Young's modulus $E_{11}$ ($10^{3}$ MPa) | 81.4 |
| | Young's modulus $E_{33}$ ($10^{3}$ MPa) | 54 |

| | |
|---|---|
| Density (kg/m$^3$) | 7800 |
| Piezo constant $g_{31}$ ($10^{-3}$ m$^2$/C) | -6.97 |
| Piezo constant $g_{33}$ ($10^{-3}$ m$^2$/C) | 24.2 |
| Permittivity constant $\varepsilon_{33}$ ($10^{-8}$ F/m) | 1.348 |

Concurrently, a finite element model is established using an in-house MATLAB code, verified with ANSYS. The plate and transducer are discretized using 20-node solid elements, resulting in the system comprising 13,776 elements and totaling 290,577 degrees of freedom. This is a very large scale problem, exemplifying the challenges in damage identification. The finite element model is then updated under the intact state based on experimental measurements, with result shown in Figure 3-7. To facilitate the identification process, the sensitivity approach by relating the admittance change to the damage index vector is adopted (Zhang et al, 2024a). Based on Section 3.2, we now have the damage identification model as:

$$\text{Find: } \boldsymbol{\alpha} \in \mathbf{E}^n,\ \alpha_l \le \alpha_i \le \alpha_u,\ i = 1,\ldots,n \tag{3.16a}$$

$$\text{Minimize: } f_1 = \left\|\Delta\mathbf{y} - \mathbf{T}\boldsymbol{\alpha}\right\|_2 \text{ and } f_2 = \left\|\boldsymbol{\alpha}\right\|_0 \tag{3.16b}$$

where $\Delta\mathbf{y}$ is admittance change from experimental measurements. $\mathbf{T}$ is sensitivity matrix calculated from the updated finite element model. $\boldsymbol{\alpha}$ is damage index vector. $\|\cdot\|_2$ and $\|\cdot\|_0$ denote, respectively, the $l_2$ norm and the $l_0$ norm. In this research we use the $l_0$ norm to achieve true sparsity since it directly penalizes the number of non-zero components.

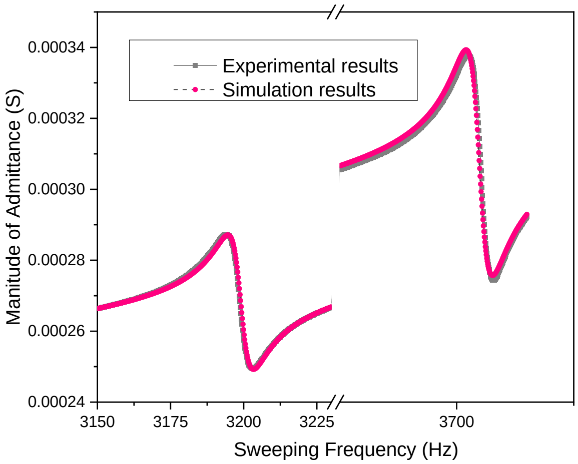

**Figure 3-7.** Admittance curves from experiment and from finite element analysis after model updating.

#### 3.5.2.2. Damage identification practice employing LAMOPSO

Without loss of generality, we acquire admittance measurements for damage identification within two frequency ranges: 3,150 Hz to 3,230 Hz (covering the 28th natural frequency at 3,194.95 Hz) and 3,650 Hz to 3,730 Hz (covering the 31st natural frequency at 3,705.8 Hz). Figure 3-7 displays the experimentally acquired admittance curves of the healthy plate structure as a baseline. In order to identify damage, the plate structure being monitored is divided into 120 (12 lengthwise, denoted as L, and 10 widthwise, denoted as W) segments. Damage identification is facilitated through identifying the stiffness reduction at specific damaged segment(s). Therefore, the damage index vector $\boldsymbol{\alpha}$ has 120 unknowns. To ensure the repeatability and to avoid the alteration of boundary conditions, the structural damage is emulated by applying small mass blocks at various locations of the plate. Three experimental cases are designed as illustrated in Figure 3-8, 11.0% stiffness reduction in the 75th segment (Case 1); 9.4% stiffness reduction in the 116th segment (Case 2); 0.734% stiffness reduction in the 49th segment and 0.899% stiffness reduction in the 65th segment (Case 3).

To illustrate the inverse identification performance through multi-objective optimization, the proposed LAMOPSO is compared with MMOPSO and CMOQLMT algorithms, which exhibit competitiveness with the proposed algorithm on benchmark instances. All algorithms are executed with a population size of 50 and a maximum iteration number of 100,000 due to the increased number of variables. The results for the three cases are shown in Figure 3-9 and Figure 3-10 with 3D bar plots, where each row shows the true damage scenario and the multiple solutions obtained from a specific algorithm. In each solution subplot, the location of a bar indicates the identified damage location, and the magnitude represents the calculated stiffness reduction.

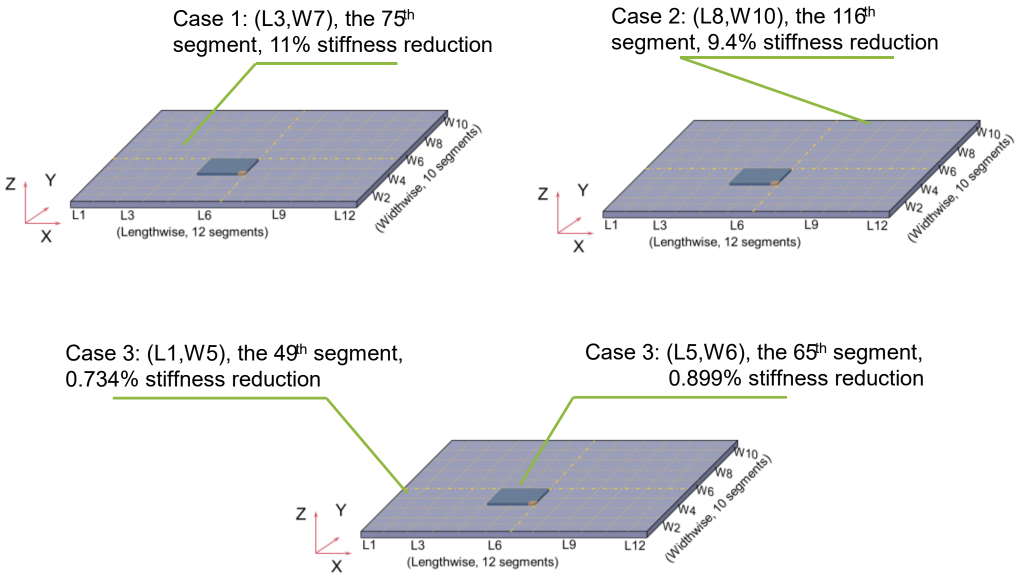

Case 1: (L3,W7), the 75th segment, 11% stiffness reduction

Case 2: (L8,W10), the 116th segment, 9.4% stiffness reduction

Case 3: (L1,W5), the 49th segment, 0.734% stiffness reduction

Case 3: (L5,W6), the 65th segment, 0.899% stiffness reduction

**Figure 3-8.** Illustration of segmentation and structural damage cases.

The results obtained for Case 1 are shown in Figure 3-9. The LAMOPSO, the MMOPSO, and the CMOQLMT find 2, 3, and 3 solutions, respectively. Through the multi-objective optimization formulation for inverse identification, we are able to obtain multiple solutions for an under-determined structural health monitoring problem, and the key is to find a small solution set. Apparently, all three algorithms are capable of achieving this in Case 1. Moreover, in each solution, only a small number of damage locations are identified. The maximum number of damage locations identified is 3 by the MMOPSO and CMOQLMT. Compared with the total number of segments 120, we can conclude that all three algorithms can produce sparse solutions. It is worth emphasizing that the sparsity of damage index vector reflects the nature of structural health monitoring where the number of damage locations is usually small especially during the early stage of damage occurrence.

The performance difference of these algorithms in Case 1 resides in solution accuracy and diversity. The LAMOPSO algorithm produces two solutions shown in the first row in Figure 3-9. The first solution effectively captures the true damage location, i.e., (L3, W7) or the 75th segment, with a damage severity of 10.27%, which is very close to the actual damage severity of 11.0% stiffness reduction. In the second solution, in addition to identifying the true damage location (the 75th segment) with severity 10.22%, the LAMOPSO identifies another damage location, the 10th segment with 0.24% stiffness reduction. As the severity in the 10th segment is very small compared with the true damage severity, we may deem it negligible. Essentially, these two solutions both point to the true damage scenario. The variant MMOPSO algorithm, in comparison, produces three solutions: 1) 12% stiffness reduction in the 95th segment; 2) 7.63% and 10.22% stiffness reductions in the 87th and the 95th segments, and 3) 7.58%, 10.15% and 0.12% stiffness reduction in the 87th, 95th, and 119th segments, respectively. None of these solutions points to the true damage scenario. Interestingly, the CMOQLMT algorithm produces three solutions with the solution 1 capturing the true damage scenario while the other two deviating from ground truth. The other two solutions obtained by the CMOQLMT algorithm identifies damage occurrence in the 10th segment and the 90th segment, and in the 10th, 63rd, as well as 90th segments, none of which points to the correct damage location. Overall, the proposed LAMOPSO algorithm outperforms the other two algorithms in terms of accuracy. It is worth noting that while the other two algorithms perform well in certain benchmark test cases as presented in Section 3.4.3, their performance in this structural damage identification problem with higher dimensionality becomes questionable.

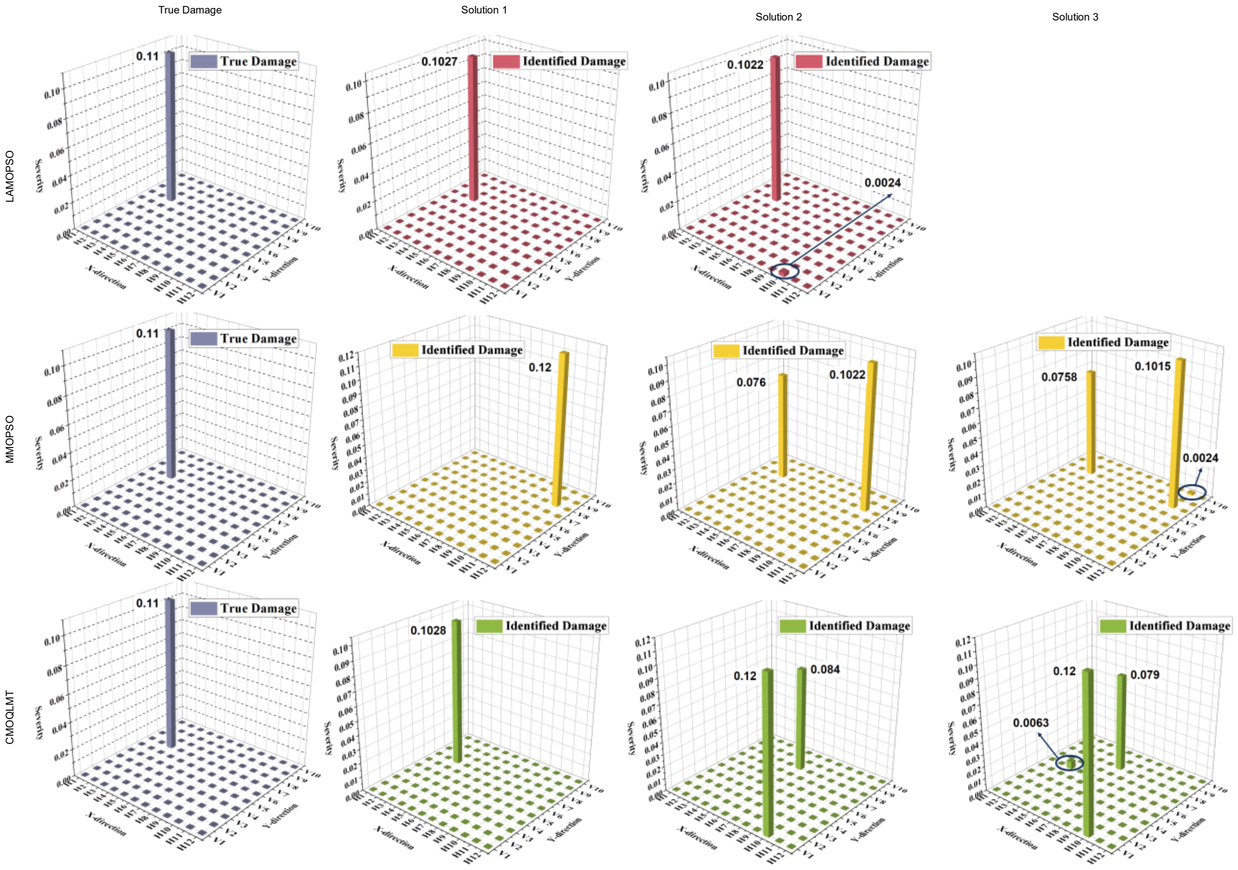

**Figure 3-9.** Inverse identification results of damage location/severity: Case 1.

In Case 2, the true damage location and severity are different from Case 1, and the solutions obtained from different algorithms are shown in Figure 3-10. All three algorithms produce 2 solutions. The solution set sizes are all small, which is good from structural health monitoring perspective. Each solution identified features sparsity, which is also good. Once again, the LAMOPSO algorithm produces two solutions shown in the first row in Figure 3-10. The first solution fits well the true damage location, i.e., (L8, W10) or the 116th segment, with a damage severity of 9.92%, which is close to the actual damage severity of 9.4% stiffness reduction. Similar to that in Case 1, in the second solution the LAMOPSO identifies two damage locations, with the first matching exactly the damage location (i.e., the 116th segment) with severity 8.96%, and the second in the 10th segment (L10, W1) with severity of 0.81%. In this solution, the second damage location has small severity, and this can be considered negligible when compared with the severity in the first location. Therefore, LAMOPSO can find two solutions that both point to the true damage scenario. The MMOPSO algorithm generates two solutions by none of them pinpointing the true damage location. Surprisingly, the CMOQLMT algorithm yields two solutions, and both capture the true damage scenario. The first solution points to the 116th segment with identified severity of 9.91% and the second solution identifies the 10th segment and the 116th segment with identified severity of 2.14% and 7.87% respectively. Overall, the proposed LAMOPSO and CMOQLMT algorithms achieve good performance on case 2. It is worth noting that both algorithms are improved with reinforcement learning, which means that the reinforcement learning shows promising potential in the optimizer enhancement.

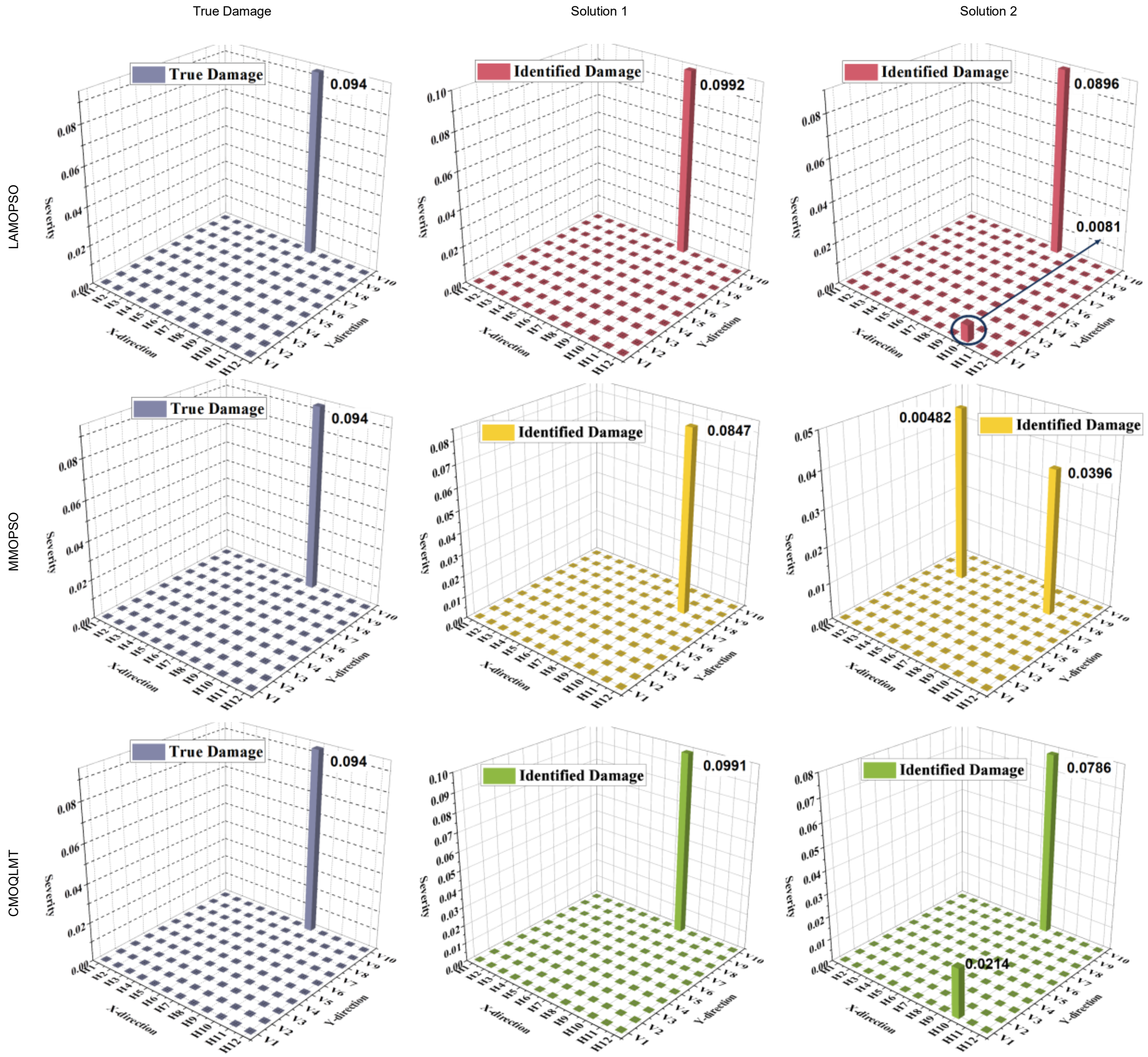

**Figure 3-10.** Inverse identification results of damage location/severity: Case 2.

Case 3 presents a more challenging problem with damage occurring in multiple locations with smaller severities. A well-performing algorithm would need to possess excellent global search capability. The results obtained from three algorithms are plotted in Figure 3-11. The maximum of solutions is 4 obtained by MMOPSO and CMOQLMT algorithms, while LAMOPSO yields 3 solutions. Although the true damage scenario has multiple damage locations in this case, it is not surprising for the algorithms to identify only one damage location as a possible solution because of the non-dominated sorting criterion involved in multi-objective optimization. The first solution by LAMOPSO does not match the true damage scenario. The second solution generated by the LAMOPSO algorithm captures the true damage scenario, pointing to the 49th segment with 0.73% stiffness reduction and the 65th segment with 0.907% stiffness reduction. The locations are correct, and the differences of damage severity with respect to true values, 0.734% and 0.899%, are extremely small. Furthermore, the third solution generated by the LAMOPSO is quite similar to the second solution, with additional damage location identified in the 105th segment with a severity of 9.8e-6 that is indeed negligible. As such, both the second and the third solutions essentially match the true damage scenario in this very challenging case setup. In comparison, as shown in Figure 3-11, neither the MMOPSO nor the CMOQLMT can produce solutions that match the true damage scenario. It is apparent that both algorithms are trapped in local optima, pointing to locations that are different from the true locations. Overall, the proposed LAMOPSO algorithm beats the other two benchmark optimizers when dealing with the challenging damage identification problem.

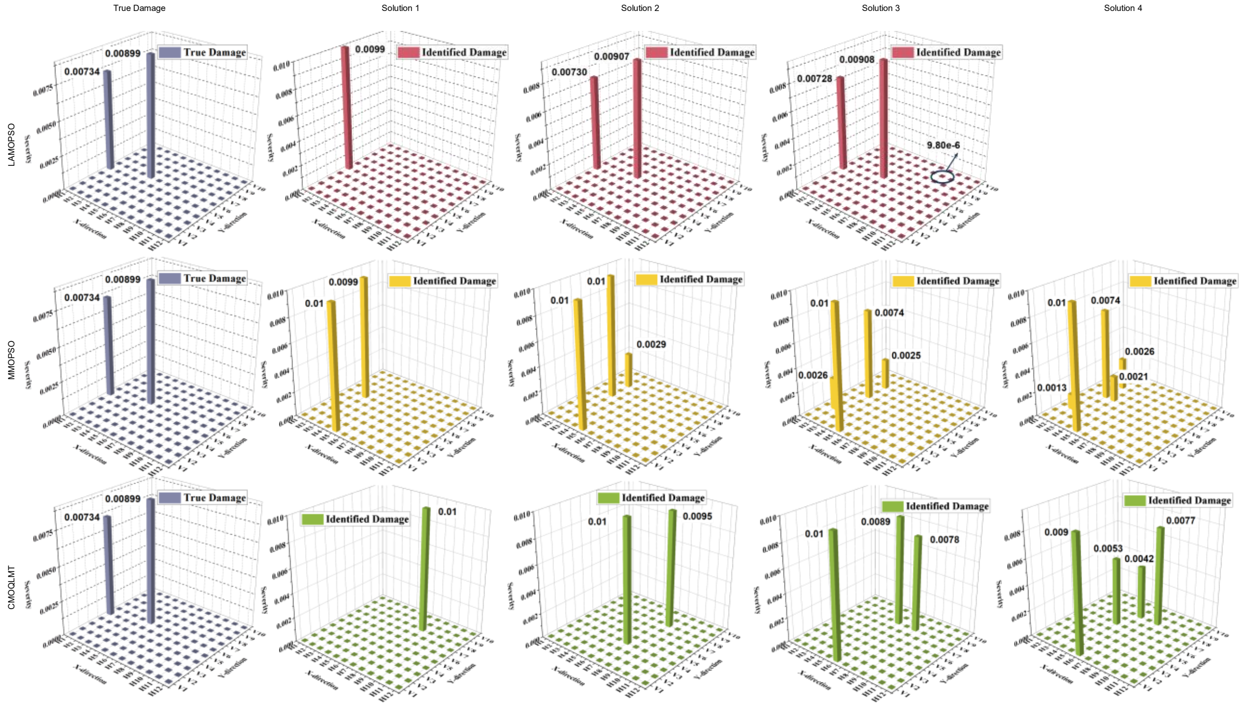

**Figure 3-11.** Inverse identification results of damage location/severity: Case 3.

### 3.5.3. Role of LA in enhancing MOPSO performance

The preceding subsection presents comprehensive case studies on the implementation of the proposed LAMOPSO algorithm to the challenging problem of structural damage identification using modal information or piezoelectric admittance measurement data. In these cases, the LAMOPSO performs better than the other two representative algorithms and leads to satisfying performance from the structural health monitoring perspective. Here we analyze the role of the learning automata (LA) in the proposed algorithm enhancement. In particular, as outlined in Section 3.3.3, 5 actions are implemented to guide the searching process. Their contributions are explicitly assessed in this subsection. In the proposed LAMOPSO algorithm, each particle is considered as a learning automaton. Each automaton has five selectable actions. Each action has a probability to indicate the likelihood that the action will be selected by the automaton. After the algorithm reaches convergence, we can visualize the final cumulative probability corresponding to each action for each learning automaton. To highlight the probability assessment in a repeatable manner with minimized influence of possible measurement noise and other uncertainties, here we use a numerical simulation case for illustration. We inject a damage with stiffness reduction of 3.4% to the 34th segment into the numerical model and conduct inverse identification employing simulation data. The population is set as 30 currently.

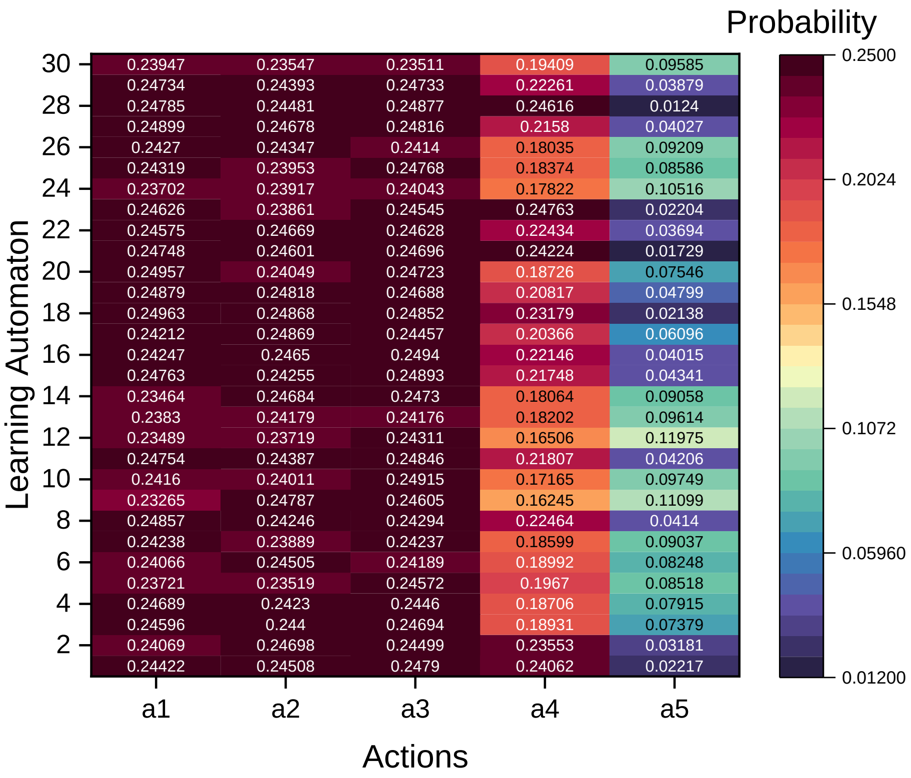

**Figure 3-12.** Probability distributions with 5 actions.

Shown in Figure 3-12 is the cumulative probability distribution plot. The horizontal axis corresponds to those 5 actions mentioned in Section 3.3.3, and the vertical axis corresponds to the 30 automatons (particles). In this figure, darker color indicates higher the probability of the corresponding action. We can observe that the final optimal actions are concentrated in the first three actions because they all possess a higher probability. Although the last two actions have cumulative probabilities, ultimately, they are not the optimal actions chosen by the learning automaton. As such, one question arises, i.e., why not remove the last two actions if they are not selected. To answer this question, we take a further look at the case where the last two actions are indeed removed. For that case, the cumulative probability distribution is shown in Figure 3-13. We can observe that the probability is nearly evenly distributed among 3 actions. However, the automatons still prefer the third action, as indicated by darker color. Therefore, we can conclude that the third action plays a very important role in updating the positions of particles and better solutions are obtained after executing this action. As formulated in Section 3.3, the third action is the mutation-based strategy for the personal best. This mutation strategy leads to diversity in the searching process.

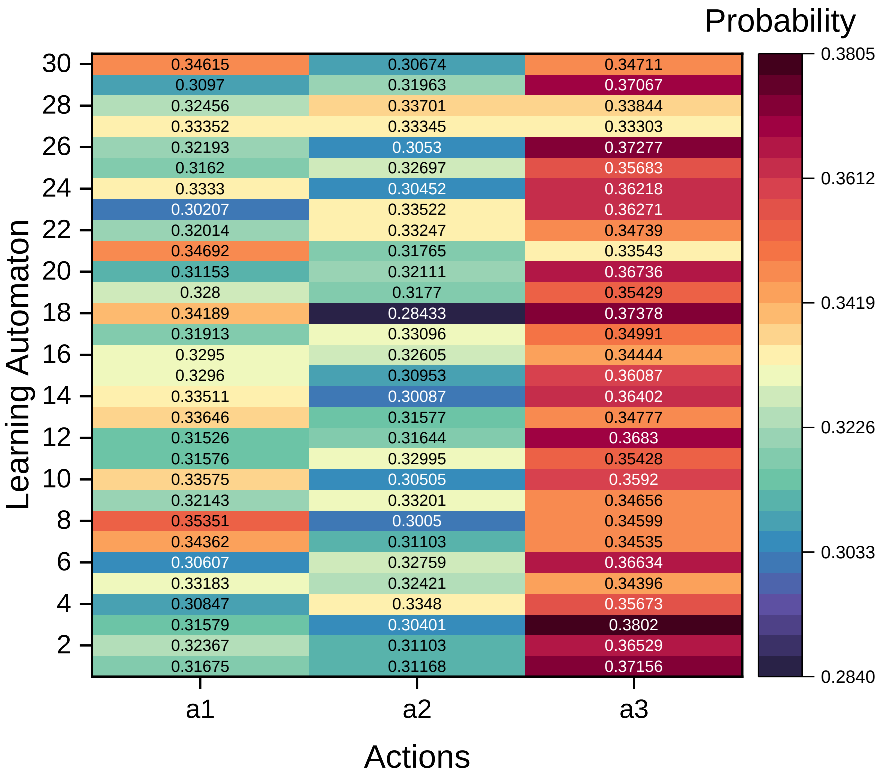

**Figure 3-13.** Probability distributions with 3 actions.

We can further examine how the last two actions are actually involved. We inspect the identification accuracy, i.e., the accuracy of stiffness reduction identified. Here we compare the true damage, the mean stiffness reduction corresponding to taking 5 actions and 3 actions respectively with 30 independent executions. To facilitate such comparison of damage involving location and severity, we define an *ad hoc* identification performance index. If the identification result points to a) the true damage location, and b) the stiffness reduction within 15% deviation from the true damage severity of 3.4%, then the result is considered *acceptable*. The identification performance index is defined as the ratio of the number of runs yielding acceptable result and the total number of runs (30). After 30 independent executions, the identification performance index is 93.33% with 5 actions, and 73.33% with 3 actions. Clearly, the last two actions play a very important role in ensuring the damage identification accuracy.

## 3.6. Conclusion and future work

This study presents a novel approach to structural damage identification through the development and implementation of a reinforcement learning-based multi-swarm optimizer. This optimizer is designed to address the complexities inherent in physical model-based damage identification, including the challenges posed by multimodality and high-dimensional variables. By integrating the particle swarm optimizer with metaheuristic strategies and leveraging the learning automata technique, we have successfully enabled an adaptive selection of search strategies that respond dynamically to the environmental context. This approach sidesteps the conventional need for ad hoc reward strategy selection, instead relying on the self-adaptation capabilities of learning automata to guide the particles' exploration of the search space effectively. The efficacy of proposed algorithm is underscored through rigorous validation against benchmark test cases and its application to real-world scenarios involving structural damage identification using modal information and piezoelectric admittance experimental signals. The results demonstrate the algorithm’s ability to accurately identify a small, diverse solution set that closely corresponds to the true damage scenarios.

This research not only marks a significant advancement in the field of structural health monitoring but also opens new avenues for the application of swarm intelligence and reinforcement learning in complex optimization problems. It offers promising prospects for future research and practical applications in structural engineering, including dynamic optimization, path planning, traffic prediction, neural network structure optimization, structural design, and beyond. Besides, more diverse local search strategies can be developed and the deep Q-network, or related neural network model can be used for actions section.

## Appendix

The multi-objective test functions and the piezoelectric admittance based damage identification method are posted online and can be accessed through this link: https://github.com/yantzan/PaperSubmissionSources/tree/c8c9ff1600dc0a794ad936eb25d7480138cb8b1d/ASC%20Resources

# Chapter 4. Piezoelectric Impedance-based Structural Damage Identification Empowered with Tunable Circuitry Integration and Multi-objective Optimization based Inverse Analysis

The piezoelectric impedance-based technique is increasingly recognized for its promise in structural health monitoring and damage identification. Built upon their self-sensing actuation capability, piezoelectric transducers can be integrated to host structures to acquire the system-level impedance information in high frequency range with small wavelength. Furthermore, the frequency-sweeping harmonic excitations in impedance measurements lead to the potential for model-based inverse identification of damage location and severity. A major challenge in damage identification, however, is that the inverse analysis is generally underdetermined, as the measurement information may not be adequate to yield a unique solution. In this research, a new methodology of tunable sensing in conjunction with multi-objective optimization inverse analysis is established. Taking advantage of the two-way electromechanical coupling of piezoelectric transducers, tunable inductance is integrated into the measurement circuit. For the same damage scenario, by tuning the inductance to a series of values, a family of impedance measurements can be acquired. Meanwhile, the inverse analysis is cast into a multi-objective optimization problem, aiming at minimizing the difference between measurement and model prediction and achieving sparsity in damage index vector. A Q-learning based multi-objective particle swarm optimization is synthesized to reach a small yet diverse solution set. We report the circuitry integration details as well as the algorithm enhancement with systematic case investigations. It is validated that the new methodology with enriched measurement can produce smaller solution set encompassing the true damage scenario, thereby providing vital information for diagnoses and prognosis.

## 4.1. Introduction

Structural Health Monitoring (SHM) refers to the process of near-real time detection and identification of structural faults by measuring the dynamic characteristics and conducting inverse analysis. Among the array of SHM techniques, piezoelectric impedance-based approaches are promising (Min et al, 2012; Selva et al, 2013; Voutetaki et al, 2016; Ai et al, 2018 and 2022; Zhao et al, 2019; Ai and Zhang 2023). These methods utilize high-frequency interrogation to detect small incipient damage based on the two-way electromechanical coupling effect of piezoelectric transducer embedded in the host structure. The piezoelectric transducer serves as the sensor and actuator simultaneously, which can excite the host structure by applying frequency-sweeping harmonic voltage while collecting frequency response measurements. The change of the piezoelectric impedance signature due to damage can be used as the damage indicator. It is worth mentioning that this technique utilizes frequency-sweeping harmonic excitation for piezoelectric impedance measurements, which inherently reduces susceptibility to transient noise effects. By comparing the piezoelectric impedance measurements under structural damage with those obtained from a reliable baseline model under healthy status, the location and severity of damage can be identified through inverse analysis (Shuai et al, 2017; Cao et al, 2018a; Fan et al, 2019). One major challenge is that, as impedance changes are most noticeable only around structural resonant peaks, the amount of impedance measurement data is generally limited. As a result, the inverse problem for damage identification is often underdetermined. Indeed, just as in human healthcare diagnostics, where an increase in testing leads to a broader evidence base and consequently narrows the diagnostic spectrum, so too does the accumulation of data refine the scope of structural damage identification. In such situations, the inverse analysis objective is to pursue a small solution set encompassing the actual damage scenario. Once that is achieved, the maintenance would only need to concentrate on these specific, small solution sets, greatly reducing maintenance costs. Toward this goal, the enrichment of measurement data is essential.

It is worth noting that one unique feature of piezoelectric-based sensing setup allows for the seamless integration with circuitry elements, such as tunable inductor shunted with the piezoelectric transducer, to improve the dynamic measurement. The circuitry introduces additional degrees of freedom, and the dynamics of the electromechanical sensor-structure system can be successively altered upon tuning the inductor to different values. For the same structural damage, a larger set of measurements can be acquired, substantially increasing both the amount and variety of system response changes. This effectively mitigates the underdetermined challenge in the inverse analysis for damage identification. In earlier efforts, Jiang et al (2006, 2007, 2008) developed a tunable inductor based piezoelectric LC-oscillator that can alter the baseline resonant frequencies of the integrated system, thereby enriching the frequency-shift information employed for damage detection. Moreover, through properly tuned inductance, a strong interaction between the mechanical structure and electrical circuit can be achieved, leading to a significant increase in sensitivity for detecting damage. This tunable inductance technique can also lead to more robust damage detection in the presence of uncertainties (Zhao et al, 2008). Subsequently, Wang and Tang (2010a, 2010b) started to implement the tunable inductance concept into high-frequency impedance/admittance measurements that are promising for high-accuracy damage identification. Not only can LC resonance amplify the impedance measurements and the damage features, but can substantially enrich the available measurement information. Similarly, Kim and Wang (2014) and Kim et al (2015) developed a method to enhance impedance measurements by integrating structures with an additional transducer and adaptive piezoelectric circuitry, effectively altering the integrated dynamics of the system. This approach, validated through spectral element method and experiments on a fixed-fixed beam structure, proved effective in accurately identifying damage in terms of location and severity. Furthering this, Kim and Wang (2019) expanded the technique to include bifurcation phenomena via bistable circuitry networks, improving damage-induced impedance measurement accuracy and noise resistance. These enhancements were substantiated through numerical and experimental studies on fixed-fixed beam structures. Recently, Zhang et al (2022) explored the integration of tunable inductors into piezoelectric transducer circuits, enriching datasets for 1D CNN-based structural damage identification. This method, practiced on a beam structure with numerical simulation, demonstrated increased discrimination between damage types, including bolt loosening and mass changes, and achieved higher accuracy in damage classification compared to non-enriched methods.

Overall, the integration of tunable inductance in structural damage detection as demonstrated in the above studies yields promising outcomes. Meanwhile, it is worth noting that the occurrence of damage in a structure generally exhibits sparsity, meaning that damage is not distributed across the entire structure, especially in its initial stages. Taking advantage of this feature, recent investigations have employed regularization techniques. Structural damage identification is treated as an optimization problem, aiming to minimize the difference between experimental measurements and model predictions in the parametric space. A regularization term can be added to the objective function, which steers the optimization towards sparse solutions. One way of imposing this condition into single-objective optimization is to regulate the damage index vector with $l_0$ or $l_1$ norm (Davenport et al, 2012). Notable applications include objective function with $l_1$ regularization (Fan et al, 2019), damage identification utilizing $l_{0.5}$ norm (Ding et al, 2020 and 2022), and sparse representation for damage identification (Chen and Sun 2021), etc. Despite achieving promising outcomes, the application of sparsity regularization by these single-objective optimization methods introduces complexities, especially in selecting appropriate weighting constants between different objective functions. There is also the possibility that the identified singular solution may not accurately represent the actual damage scenario as the optimizer may be trapped at local optima. To overcome these limitations, multi-objective optimization can be used to minimize the difference between measurement and model prediction while ensuring damage sparsity, which more accurately reflects the complexities of real-world scenarios. However, a gap remains in fully leveraging the potential of tunable circuitry integration within multi-objective optimization frameworks for model-based damage identification.

To bridge the existing gap, this research introduces a comprehensive method for structural damage identification using piezoelectric admittance, enhanced by tunable circuitry within a multi-objective optimization framework. This approach aims to enhance the sensitivity and accuracy of detecting damage while tackling the underdetermined nature of structural health monitoring. We close the loop by integrating physical models and experimental data into the optimization process, thereby establishing a robust and effective method for the accurate identification and assessment of structural damage. Mathematically speaking, the structural damage identification is converted into an optimization setup with bi-objective functions: one is to minimize the differences of admittance change between experimental measurements and model predictions in damage parametric space; another is to incorporate $l_0$ norm to address the sparsity. In practical scenarios, non-observable damage typically occurs within localized regions of the structure.

Multi-objective optimization is particularly well-suited for this inverse analysis. This setup can not only eliminate the need for selecting weights for objective functions, but it also generates multiple solutions, which align well with the nature of damage identification (Cao et al, 2023a). Importantly, these multiple solutions help mitigate the effects of noise and uncertainties. By providing a range of possible damage profiles, this approach reduces the risk of converging to incorrect local optima distorted by noise, a common issue in single-objective optimization methods.

We select the multi-objective particle swarm optimization (MOPSO) as the basic approach to solving the inverse analysis, owing to its fast convergence and its capability for obtaining a set of trade-off solutions in a single run, offering the potential for designing localization strategies to enrich the search patterns. Namely, local search strategies are devised using dynamic inertia weight and dual acceleration coefficient sets. These sets initiate two unique search mechanisms, promoting initial exploration and later exploitation. Furthermore, we develop three mutation-centric strategies for local search, aimed at stimulating particle movement and fostering exploration, resulting in a diverse set of solutions. To adaptively select the local search strategy, we have integrated Q-learning with MOPSO. This integration allows for selecting the most advantageous action based on the current state, guided by the maximum values in the Q-table to continuously seek better solutions. Each particle in the system, acting as an individual agent, is equipped with various local search strategies. These strategies enable the particles to effectively engage with both the search environment and other agents, thereby improving the overall search capability. Instead of executing all strategies at once, the approach involves strategically selecting the most promising one in each iteration as per the insights from the Q-Learning algorithm. Alongside refining the algorithm, a tunable synthetic inductor is synthesized to enrich the measurements by tuning it to different inductance values. The resulting circuit can attain a very broad range inductance values in compact form, making it ideal for electromechanical integration. Moreover, it has small damping in the electric circuit, yielding a strong resonance peak and sensitivity to damage detection. In summary, the contributions of this study are fourfold: (1) introducing a synthetic tunable inductor to enhance admittance measurements for damage identification; (2) transforming the inverse damage identification process into a multi-objective optimization to increase accuracy and address underdetermination; (3) hybridizing the metaheuristic algorithm with Q-learning to generate a small yet diverse set of solutions; (4) employing experimental measurements to validate the proposed effectiveness of the approach in real-world structural health assessments.

The rest of the paper is organized as follows. In Section 4.2, finite element modeling of piezoelectric admittance enriched by tunable inductance for structural health monitoring is outlined, followed by the problem formulation of damage identification emphasizing sparsity of damage index vector. Section 4.3 presents the hybrid optimizer to deal with the multimodal objective functions formulated. Specifically, the local search strategies are developed and combined with Q-learning algorithm to balance the exploration and exploitation. Section 4.4 elaborates the experiment process and the details of the synthetic inductor. Subsequently, the model updating for a high-fidelity physical model is detailed. Finally, case studies are conducted for the inverse damage identification using experimental data. The solution quality is demonstrated. Section 4.5 gives the concluding remarks.

## 4.2. Piezoelectric Admittance based Active Interrogation with Enhancement

In this section, we present the formulation of damage identification utilizing piezoelectric admittance measurement. As the identification is model based, we first outline the finite element modeling of piezoelectric admittance prediction/simulation with the integration of a tunable inductor. We then elaborate on how the tunable inductor can enrich the datasets for structural damage identification. Subsequently, we formulate a multi-objective optimization problem that will be used to identify the location and severity of damage in the host structure.

### 4.2.1. Finite element modeling of piezoelectric admittance with tunable inductor integration

When a host structure is integrated with a piezoelectric transducer shunted with an inductor, as show in Figure 4-1, the equations of motion can be derived as (Wang and Tang 2010a, 2010b),

$$\mathbf{M}\ddot{\mathbf{q}} + \mathbf{C}\dot{\mathbf{q}} + \mathbf{K}\mathbf{q} + \mathbf{K}_{12}Q = \mathbf{0} \tag{4.1a}$$

$$L\ddot{Q} + R\dot{Q} + k_c Q + \mathbf{K}_{12}^T \mathbf{q} = V_{\text{in}} \tag{4.1b}$$

where **q** is the displacement vector, $k_c$ is the inverse of the capacitance of the piezoelectric transducer; $\mathbf{K}_{12}$ is the electromechanical coupling vector between the transducer and the structure, and **K**, **C**, and **M** are the stiffness, damping, and mass matrices, respectively. *L* is a tunable inductance connected in series with the piezoelectric transducer, and *R* is a resistor employed to facilitate measurement. In this research, we use piezoelectric admittance which is the reciprocal of impedance as information carrier for damage identification. Specifically, we apply frequency-sweeping harmonic voltage excitation, denoted as $V_{\text{in}}$, to the transducer. *Q* is the electrical charge on the surface of the piezoelectric transducer. In implementation, we measure the voltage drop across the resistor *R*, which is denoted as $V_{\text{out}}$, and subsequently obtain the current as $\dot{Q} = V_{\text{out}} / R$.

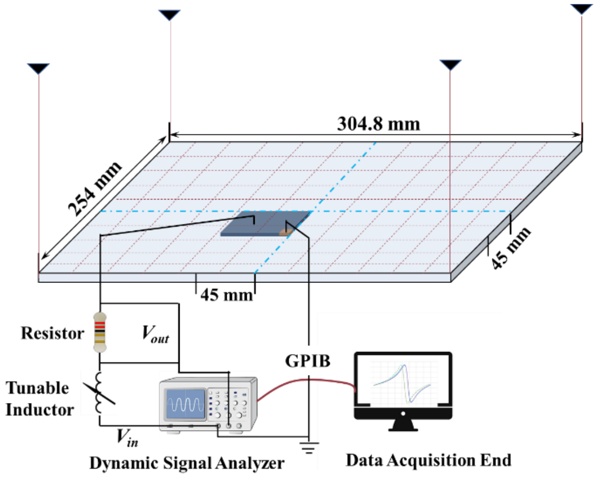

**Figure 4-1.** Schematic diagram of piezoelectric admittance-based damage identification system.

We let the excitation frequency be denoted as $\omega$, and use overbar hereafter to indicate magnitude of the corresponding response variable. The piezoelectric admittance of the healthy structure, which is the ratio of the current magnitude and the voltage magnitude, can be derived as

$$y_h(\omega) = \frac{\bar{\dot{Q}}}{\bar{V}_{\text{in}}} = \frac{j\omega}{-L\omega^2 + j\omega R + k_c - \mathbf{K}_{12}^T(\mathbf{K} + j\omega\mathbf{C} - \omega^2\mathbf{M})^{-1}\mathbf{K}_{12}} \tag{4.2}$$

where $j$ is the imaginary unit. The newly introduced concept is to integrate an inductive element with the piezoelectric shunt circuitry. Traditional impedance-based damage detection techniques do not have this element, and the piezoelectric admittance without the inductance is given as

$$y_h(\omega) = \frac{\dot{\bar{Q}}}{\bar{V}_{\text{in}}} = \frac{j\omega}{j\omega R + k_c - \mathbf{K}_{12}^T(\mathbf{K} + j\omega\mathbf{C} - \omega^2\mathbf{M})^{-1}\mathbf{K}_{12}} \tag{4.3}$$

One can find that Equation (4.2) corresponds to a fourth-order system with two resonances, while Equation (4.3) corresponds to essentially a second-order system with one resonance because, compared to $k_c$, $\omega R$ is very small. Obviously, Equation (4.2) with the integration of inductance differs significantly from Equation (4.3) in that the inductive circuitry introduces an additional degree of freedom (DOF), which results in a new resonance in the admittance curve.

In a finite element model for damage identification, the structure is generally divided into *n* segments to facilitate the identification of location and severity of damage. That is, each segment is susceptible of damage occurrence, and damage causes homogenized change of structural properties within a segment. In this research, without loss of generality, we assume damage causes stiffness reduction in one or multiple segments. As such, the stiffness matrix with structural damage occurrence, $\mathbf{K}_d$, can then be expressed as $\mathbf{K}_d = \sum_{i=1}^{n} \mathbf{K}_h^i (1 - \alpha_i)$, in which $\mathbf{K}_h^i$ is the stiffness matrix of the *i*-th segment under the healthy status and the summation sign refers to the direct summation in finite element model assemblage. $\alpha_i \in [0,1]$ is the damage index indicating the possible stiffness loss of the *i*-th segment, which is the quantity to be identified. The piezoelectric admittance corresponding to the damaged structure, when measured with the piezoelectric circuitry with the inductor, can be written as

$$y_d(\omega) = \frac{j\omega}{-L\omega^2 + j\omega R + k_c - \mathbf{K}_{12}^T(\mathbf{K}_d + j\omega\mathbf{C} - \omega^2\mathbf{M})^{-1}\mathbf{K}_{12}} \tag{4.4}$$

Mathematically, the change of admittance due to damage can be derived based on Equations (4.2) and (4.4). Since structural damage is generally small in size, we apply the Taylor series expansion to the expression of the change of admittance and ignore the higher-order terms, i.e.,

$$\Delta y(\omega) = \sum_{i=1}^{n} [j\omega(-L\omega^2 + j\omega R + k_c - \mathbf{K}_{12}^T \mathbf{Z}^{-1} \mathbf{K}_{12})^{-2} \mathbf{K}_{12}^T \mathbf{Z}^{-1} (\mathbf{L}_i^T \mathbf{K}_h^i \mathbf{L}_i) \mathbf{Z}^{-1} \mathbf{K}_{12}]\, \alpha_i \tag{4.5}$$

where $\mathbf{Z} = \mathbf{K} - \mathbf{M}\omega^2 + j\omega\mathbf{C}$ represents the dynamic stiffness of the structure, and $\mathbf{L}$ is the Boolean matrix indicating how the segmental stiffness matrices are assembled into the global stiffness matrix. In Equation (4.5), the change of admittance under excitation frequency $\omega$ is denoted as $\Delta y(\omega)$. In damage identification practice, we conduct frequency sweeping excitation in the frequency range of interest and acquire a series of admittance changes $\Delta y(\omega_1),\ldots,\Delta y(\omega_2)$ , under *m* different excitation frequencies $\omega_1,\ldots,\omega_m$ . We introduce the following notations of excitation frequency vector, admittance change vector, and damage index vector,

$$\boldsymbol{\omega} = [\omega_1, \ \cdots, \ \omega_m]^T \tag{4.6a}$$

$$\Delta\mathbf{y}(\boldsymbol{\omega}) = \left[\Delta y(\omega_1), \ \ldots, \ \Delta y(\omega_m)\right]^T \tag{4.6b}$$

$$\boldsymbol{\alpha} = [\alpha_1, \ \cdots, \ \alpha_n]^T \tag{4.6c}$$

The fundamental principle of impedance/admittance-based active interrogation systems is that structural damage results in changes in piezoelectric impedance or admittance, with these changes being most pronounced near the resonant peaks. In pursuit of more information, we can utilize the tunable inductor in the circuitry to enrich the measurements. Specifically, the integration of tunable inductor allows for the generation of diverse frequency response functions by utilizing different inductances. This significantly enriches the dataset useful for the identification and detection of damage. As we tune the inductor to a series of values $L_i$ ($i = 1,\ldots,k$), we can obtain a series of relations shown as Equation (4.5). Collectively, we obtain

$$\Delta \mathbf{y} = \begin{bmatrix} \Delta y(\omega_1, L_1) \\ \vdots \\ \Delta y(\omega_m, L_1) \\ \vdots \\ \Delta y(\omega_1, L_k) \\ \vdots \\ \Delta y(\omega_m, L_k) \end{bmatrix} = \mathbf{T}_{(k \cdot m) \times n} \boldsymbol{\alpha}_{n \times 1} \tag{4.7}$$

where **T** is the finite element-based sensitivity matrix that links the admittance change vector with the damage index vector. In Equation (4.7), *k* is the number of tuned inductances, and *m* is the number of sweeping frequency points in each frequency range. By tuning the inductor to various values, we can obtain a series of admittance curves. Thus, for the same damage scenario, we now have much more information to elucidate the damage location/severity. As such, we can constrain the solution within a very narrow range, thereby limiting the scope of structural repairs and maintenance to a smaller area. From the perspective of structural health monitoring, this smaller solution set is precisely what is expected. In comparison, when fixed circuitry is employed, the traditional piezoelectric impedance technique provides the following,

$$\Delta \mathbf{y} = \begin{bmatrix} \Delta y(\omega_1) \\ \vdots \\ \Delta y(\omega_m) \end{bmatrix} = \mathbf{T}_{m \times n} \boldsymbol{\alpha}_{n \times 1} \tag{4.8}$$

It is known that the integration of properly tuned inductance can lead to an order-of-magnitude amplification of the admittance change signature upon the occurrence of damage. Indeed, when the circuitry natural frequency is within the vicinity of a structural natural frequency, the sensitivity of admittance change with respect to damage is amplified (Wang and Tang, 2010b). This will be leveraged in the subsequent experimental investigation.

### 4.2.2. Formulation of multi-objective optimization for damage identification

By tuning the inductance values in the piezoelectric circuitry, as shown in Equation (4.7) we can obtain enriched measurement information. It is worth noting that, mathematically, we are still unable to guarantee that the additional information obtained is linearly independent. The inevitable measurement noise and model-experiment mismatch further compound the situation. Indeed, despite the measurement enrichment, the inverse problem is generally still not properly determined. To proceed, we cast the inverse problem into an optimization problem. Specifically, we formulate a multi-objective optimization problem as shown below,

$$\text{Find: } \boldsymbol{\alpha} \in \mathbf{E}^n,\ \alpha_l \leq \alpha_i \leq \alpha_u,\ i = 1,\ldots,n \tag{4.9a}$$

$$\text{Minimize: } f_1 = \left\| \Delta\mathbf{y} - \mathbf{T}\boldsymbol{\alpha} \right\|_2 \text{ and } f_2 = \left\| \boldsymbol{\alpha} \right\|_0 \tag{4.9b}$$

where $\|\cdot\|_2$ and $\|\cdot\|_0$ denote, respectively, the $l_2$ norm and the $l_0$ norm. In this formulation, the first objective is straightforward, i.e., to minimize the difference between the measured change in admittance, $\Delta\mathbf{y}$, and the model prediction in the parametric space, $\mathbf{T}\boldsymbol{\alpha}$. Meanwhile, it is worth noting that, typically, damage is localized within a small region of the structure, particularly when it is in its incipient stage with a small size. Therefore, we introduce the second objective function predicated on the sparsity of the damage index vector $\boldsymbol{\alpha}$, characterized by the $l_0$ norm, which means we expect the damage index vector to be sparse. Previous investigations often opt for the $l_1$ norm regularization as a compromise between sparsity and computational efficiency, but the $l_1$ norm is only a relaxation approximation of the $l_0$ norm under certain conditions (Davenport et al, 2012; Cao et al, 2018a; Fan et al, 2019). In contrast, we use the $l_0$ norm to achieve true sparsity since the it directly penalizes the number of non-zero components.

This multi-objective setup can avoid the difficulty in selecting weights for single-objective optimization. It generates multiple solutions, aligning with the nature of SHM. The solutions obtained correspond to various potential damage scenarios. If all outcomes suggest insignificant damage severity, the continuation of operations is warranted. Conversely, if any damage scenarios within the optimal solution are concerning, we may need to make maintenance decisions or conduct additional sensor measurements and inspections. Therefore, we'd expect a solution set that is small (i.e., with small number of individual solutions) and diverse.

## 4.3. Q-learning Enhanced Multi-objective Optimizer

Taking advantage of the tunable inductance with enriched measurement, the overarching goal of damage identification presented in this research is to leverage the multi-solution capability of multi-objective optimization to produce a diverse solution set. This is unique for SHM because we are indeed interested in getting multiple solutions. In this context, we select the multi-objective particle swarm optimization (MOPSO) as the main approach, owing to its efficiency in converging rapidly to a spectrum of balanced solutions. Nonetheless, the basic MOPSO in general is challenged by multimodal and high-dimensional setup, often converging prematurely to local optima. This can impede the attainment of diverse solutions. Fortunately, the inherent flexibility of the PSO algorithm allows for heuristic adaptations to fit various application scenarios. Specifically in this research, aiming at attaining a small yet diverse solution set, we implement dynamic inertia weight and dual acceleration coefficients to drive the initial exploration and the subsequent exploitation, along with mutation-based strategies for local perturbation to stimulate further movement and foster exploration. To adaptively select the local search strategy, we incorporate the Q-Learning into MOPSO. This combination enables the selection of the most beneficial actions according to the current state, utilizing the maximum values in the Q-table to consistently pursue improved solutions.

### 4.3.1. Framework of multi-objective particle swarm optimization (MOPSO)

Particle swarm optimization, a stochastic method initially devised by Kennedy and Eberhart (1995), emulates the collective behavior observed in animal groups, including insects, herds, birds, and fish. This technique involves cooperative interactions within the swarm, where each individual continuously adapts its search strategy based on both personal and communal learning experiences, i.e., the particles navigate towards its individual best position as well as the collective optimal position recognized by the swarm. The velocity and position updates of each particle are governed by a set of mathematical expressions as

$$v_i(t+1) = zv_i(t) + c_1 r_1 (p_{\mathrm{best}i}(t) - x_i(t)) + c_2 r_2 (g_{\mathrm{best}}(t) - x_i(t)) \tag{4.10}$$

$$x_i(t+1) = x_i(t) + v_i(t+1) \tag{4.11}$$

where *v* is the velocity of the particle, *x* is the position of particle or the solution of the optimization problem, $r_1$ and $r_2$ are random numbers, *t* is the current iteration, $p_{\text{best}}$ is the personal best, and $g_{\text{best}}$ is the global best. In the above equations, coefficient *z* is the inertia weight, $c_1$ is the coefficient of the cognitive component which indicates that each particle learns from its experience, and $c_2$ is the coefficient of the social component from which all particles learn.

Despite its widespread application, the standard particle swarm optimization is prone to premature convergence and might exhibit limited exploratory capabilities (Gad, 2022). The problem becomes more complex for the damage identification case formulated in Equations (4.9a) and (4.9b), which deals with a damage index vector that is high-dimensional. The challenge lies in devising strategies to avoid entrapment in local optima, which are significant obstacles in such complex problems. Some related work has been done by developing hybrid methods to improve search performance and escape local extremes. The hybridization means that the traditional optimizers, such as evolutionary algorithms (Alkayem et al, 2018), simulated annealing (Yao et al, 2017), genetic algorithms (Tiachacht et al, 2018), Jaya (Ding et al, 2019), and particle swarm optimization (Minh et al, 2021), are improved with other metaheuristics to enhance the performance of the optimizer when dealing with structural damage identification. The efforts achieving success in damage identification have been made such as hybridization of the K-clustering-based Jaya algorithm and Trees Seeds algorithm to achieve robust searching (Ding et al, 2020), Jaya algorithm combined with Hooke–Jeeves pattern search to improve the search performance (Ding et al, 2022), Genetic Algorithm (GA) integrated with a Modified Cornwell Indicator (MCI) (Tiachacht et al, 2018), and enhanced particle swarm optimization with online parameters adjustment to control the convergence rate (Minh et al, 2021) etc. However, the advancements mentioned above primarily focus on single-objective formulations, highlighting a need for systematic exploration in multi-objective optimization tailored to improve solutions specifically for damage identification applications. Therefore, in the sub-section that follows, we will hybridize the MOPSO algorithm with several local search strategies to enhance the performance.

### 4.3.2. Action repository for exploration-exploitation balance

Exploration and exploitation are essential strategies that drive the progress of evolutionary algorithms towards finding optimal solutions or achieving convergence (Črepinšek et al, 2013; Ding et al, 2023). Exploration pertains to the investigation of entirely new areas within the search space, whereas exploitation involves a thorough search in the vicinity of areas already visited within the search space. There is an inherent conflict between these two search patterns. Notably, an algorithm that prioritizes exploration can significantly impede its rate of convergence. Conversely, an algorithm that predominantly engages in exploitation is at risk of becoming confined to a local minimum. This conflict will be compounded in structural damage identification, in which the high dimensionality is involved, and the multi-modal objective function usually has many local extremes. To balance the exploration and exploitation for the sake of pursuing a small but diverse solution set, we present five local search strategies in this sub-section on the basis of MOPSO, including two coefficient variation-based strategies and three mutation-based strategies, which collectively aim at encouraging particle movement around local extremes and facilitating exploration for a diverse set of solutions. These strategies form an action repository so that each particle can select a proper one in each iteration. The five local search strategies are named *Exploration*, *Convergence*, *Elitist-based perturbation* (*EPB*), *Mutation* and *Fine Tuning*.

For the *Exploration*, the coefficients in Equation (4.10) are set as $c_1 > c_2$ with $c_1 = 2.5$ and $c_2 = 0.5$, which encourages the particle to explore more searching space and avoid premature convergence, as suggested by Samma et al (2016) . In the *Convergence* state, the social part is given a larger value with $c_1 = 0.5$ and $c_2 = 2.5$ to make the algorithm converge to the global best quickly. The inertial weight $z$ controls the balance between the global and local searches, therefore, it is set as a decay expression $z = z_{\max} - (z_{\max} - z_{\min}) it \big/ (\mathrm{maxIter})$ to search more space initially and will realize quick convergence at the end of the optimization. Here *it* is the current number of iterations, maxIter is the maximum iteration, and $z_{\max} = 0.9$ and $z_{\min} = 0.4$ are recommended (Kennedy and Eberhart, 1995). Whenever an action is selected and executed, the newly generated solution will be compared to the old one using the non-dominated sorting algorithm, i.e.,

$$\text{if } x_{\text{new}} \prec x_{\text{old}},\ x_{\text{old}} = x_{\text{new}} \qquad \text{reward} \tag{4.12a}$$

$$\text{if } x_{\text{new}} \sim\prec x_{\text{old}},\ x_{\text{old}} = x_{\text{old}} \qquad \text{penalty} \tag{4.12b}$$

In the above equations, the reward or penalty is determined as following: if the new solution is better than (i.e., dominates) the old one, it will replace the old solution and the action that produces it will receive a reward of -1; otherwise, the old solution stays, and the action gets a penalty of -2. The reward is set as a negative value. Since the Q-table starts with zeros (to be explained in the next sub-section), a reward at the start, e.g., reward = 1, could cause the algorithm to keep choosing the same action with the max Q-table value being utilized to decide the next action.

To mitigate the issue of premature convergence, an elitist-based perturbation (*EBP*) strategy is employed. This strategy introduces diversity by perturbing a randomly selected dimension of the personal best of the particle, thereby assisting in escaping from local optima: $tempP_{\text{best}i,d} = P_{\text{best}i,d} \pm r_d \cdot (l_{\text{upper},d} - l_{\text{lower},d})$. Here the sign assignment is probabilistic, i.e., positive for random numbers greater than or equal to 0.5, and negative otherwise. $P_{\text{best}i,d}$ refers to the *d*-th dimension of the personal best of the *i*-th population. $r_d$ is a random number obtained from the normal distribution of $N \sim (\mu, R^2)$ with $\mu = 0$ and standard deviation $R = R_{\max} - (R_{\max} - R_{\min}) it \big/ (\text{maxIter})$, where the maximum and minimum perturbation ranges are set as $R_{\max} = 1$ and $R_{\min} = 0.1$ as suggested in literature (Lim and Isa, 2013). $l_{\text{upper},d}$ and $l_{\text{lower},d}$ represent the upper and lower bounds for the *d*-th dimension of the *i*-th population, respectively. During the iterative process, if the temporary personal best $tempP_{\text{best}i,d}$ outperforms the current best, it is adopted, and an immediate reward of -1 is given; otherwise, the current solution persists, incurring a penalty of -2. Concurrently, the *Mutation* action is applied to the global best $g_{\text{best}} = g_{\text{best}} \pm r_d \cdot (l_{\text{upper},d} - l_{\text{lower},d})$, utilizing a similar random perturbation to enhance local exploration with the aim of identifying a more advantageous position. The perturbation is based on the same normal distribution used in the *EBP* strategy, with a decay standard deviation designed for extensive searching at the start of the algorithm and a more refined search towards the end. Should the temporary global best outperform the existing global best, it replaces it with a reward of 1 being granted; if not, it is maintained with a consequent penalty of -2. Here a larger reward is given to the action when it achieves improvement because the global best plays a crucial role in guiding all the particles. In the *Fine Tuning* process, attention is given to each dimension of the personal best by adjusting its velocity $v_{i,d}$. This means particles are expected to move more (positive) towards direction favorable to improve the solution and more slowly (negative) in less beneficial directions: $tempP_{\mathrm{best}i,d} = P_{\mathrm{best}i,d} \pm v_{i,d}$ (Ji et al, 2007; Samma et al, 2016). The current personal best will be replaced if the temporary personal best dominates it. Otherwise, the original personal best remains unchanged. It is worth mentioning that there is only a penalty in this action no matter if the solution gets improved or not, since it takes a long time to tune each dimension. Here the punishment is set as -3 so that it cannot be called frequently for the sake of computational efficiency.

In summary, the rewards for the first three actions are -1, and the penalties are -2. For *Mutation*, which operates on the global optimum, a higher reward of +1 is given if the action makes progress; otherwise, it is penalized with -2. *Fine tuning*, the other action, requires adjustments in each dimension. Since this process is time-consuming, it cannot be chosen too frequently. Therefore, this action has a penalty of -3. The reward and penalty settings are summarized in Table 4-1.

**Table 4-1.** Reward and penalty settings.

| **Actions** | **Reward/Penalty Settings** |
|---|---|
| Exploration | Reward: -1; Penalty: -2 |
| Convergence | Reward: -1; Penalty: -2 |
| EBP | Reward: -1; Penalty: -2 |
| Mutation | Reward: +1; Penalty: -2 |
| Fine Tuning | Reward: None; Penalty: -3 |

### 4.3.3. Q-learning based enhancement

As mentioned, five local search strategies are synthesized, aiming at emphasizing the exploration and exploitation capabilities through coefficient variations and increasing the solution diversity through mutations. These strategies are not selected and executed all at the same time for the particles. To adaptively select appropriate strategies, we integrate Q-learning (Watkins and Dayan 1992) into MOPSO. Each particle selects the most suitable strategy for its own iteration and evolution based on the value of the Q-table. Q-learning falls under the class of reinforcement learning techniques (Watkins and Dayan, 1992). In reinforcement learning, the learner performs an action causing a state transition in the environment in which it resides and receives a reward or penalty for the action executed to reach a definite goal. The environment is the searching space of the particles. The states are current local searches. An action is the transition from one state to another. In the integrated algorithm, each particle of MOPSO is regarded as an agent. Updating of the Q-table occurs after each action is executed and ends when an episode is completed. The agent will not learn much after a single episode, but eventually, with sufficient exploring steps and episodes it will converge and learn the optimal Q values.

There are 5 states and their corresponding actions. Therefore, we can create a Q-table with the size of 5 by 5 and initialize all the entries as zeros for actions 1 to 4 under all states, while setting the values for action 5 (*Fine Tuning*) under all states to -5, ensuring a higher priority for other actions to be executed. Usually, the current state is randomly chosen from the state repository. However, here we initialize the current state as *Exploration* since we demand the algorithm to start with exploring more searching space. Subsequently, the best action will be selected and executed based on the maximum Q-table value given the current state. This process can be written mathematically as $a_t = index\{\max(Q(s_t, actions))\}$. Here, $a_t$ is the current action and $t = 1,\ldots,5$. After the action selected is executed, an immediate reward or penalty will be obtained. Reward or penalty is determined by the dominating algorithm as described in previous sub-section. The agents observe the maximum future reward under the next state. The reward/penalty obtained will be passed into the updating function to update the Q-table entry $Q(s_t, a_t)$. The updating function is as follows:

$$Q_{new}(s_t, a_t) = (1-b)Q(s_t, a_t) + b[r_{t+1} + \gamma \max_a Q(s_{t+1}, a_{\text{all}})] \tag{4.13}$$

where *b* is called the learning rate which is defined as how much the new value is accepted, $\gamma$ is a discount factor used to balance immediate and future rewards, and *r* is the reward received for taking action $a_t$ at a given state $s_t$. In Equation (4.13), max is the operation of taking the maximum of the future reward among all actions $a_{\text{all}}$ from the new state $s_{t+1}$. Finally, the current state will be updated. By iterating this process, the optimal Q-table can be achieved.

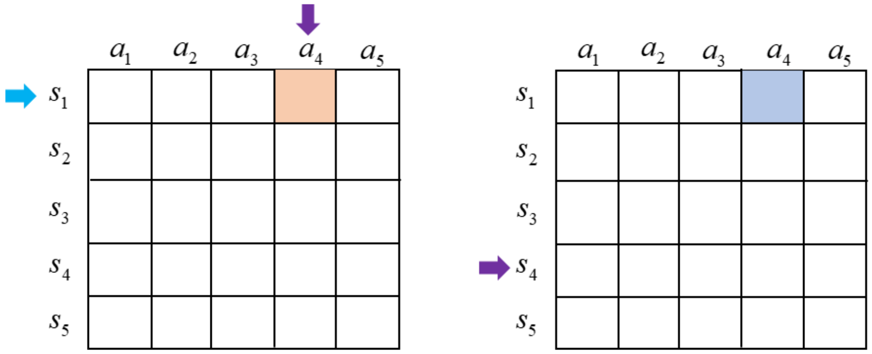

**Figure 4-2.** Illustration of the state transition process.

After the current action is executed, the agent can transition from the current state to another. The transition here is that the index of the current action is the index of the next state. A diagram is drawn to show how to switch from the current state to the next state, as shown in Figure 4-2, the agent will select an action based on the maximum Q-table values given the current state as $S_1$. Assume that action 4 ($a_4$) has a maximum value and then the next state will be set as $S_4$, which has the same index as the index of the current action $a_4$. By iterating this process, a dynamic selection and execution can be achieved between these states and actions. After action 4 is executed, the rewards currently obtained can be used to update the entry for the current state and current action. Then, the personal and global best are updated, and the external optimal repository will be updated accordingly. All the steps in the main loop will be performed until the maximum number of runs are reached.

## 4.4. Damage Identification Implementation with Enriched Piezoelectric Measurements

In this section, we start from presenting the physical testbed and the experimental procedures. We incorporate the synthetic inductor into the measurement circuitry to facilitate tunable inductance and illustrate its function in enriching the piezoelectric admittance measurements. As outlined in Section 4.2, the expressions for the change in piezoelectric admittance and the sensitivity matrix are formulated using finite element analysis. Subsequently, we present the model updating process to obtain a high-fidelity baseline model. As the main content of this section, we undertake experimental case studies to validate the approach proposed. Datasets augmented through inductance tunings are employed for damage identification in an actual structural plate. The Q-learning enhanced MOPSO algorithm is employed to facilitate the identification of fault location/severity solution set that is small and diverse. Furthermore, a discussion is presented at the conclusion of this section to deliberate on the impact of these augmented datasets on the solutions generated from the identification process.

### 4.4.1. Experimental setup and data acquisition

The experimental setup is shown in Figure 4-3. A piezoelectric transducer is bonded to the top surface of a plate using epoxy resin. To minimize the influence of the thickness of bonding layer, the resin layer is kept at smaller than 0.15 mm. The piezoelectric transducer is connected to an external resistor and a tunable inductor, as shown in Figure 4-3(a). By measuring the voltage drop across the resistor, we can obtain the current flowing through the circuit. Thus, the admittance measurement can be obtained as $Y(\omega) = V_{\text{out}} \big/ R V_{\text{in}}$ where $Y$ is the admittance, $V_{\text{out}}$ denotes the voltage amplitude across the resistor, and $V_{\text{in}}$ indicates the amplitude of the input voltage. This simple yet effective measurement scheme is low-cost and can directly facilitate the model updating as every component of the numerical model can be measured directly. A dynamic signal analyzer (Agilent 35670A) is used to acquire the frequency response. Here 100 mV (Vpk) harmonic voltage is applied to the transducer. The input voltage of 100 mV is selected to keep the currents small within the synthetic inductor so as to prevent the operational amplifiers, which have a maximum current capacity of 3 mA, from saturating during use. For each excitation frequency, 25 cycles are used to reduce the noise effect.

In damage identification using admittance measurements, the damage effect is most prominent around the resonant peaks. In this research, without loss of generality, we acquire the admittance change information around the 31st natural frequency of 3,703.9 Hz. Theoretically, one may measure admittance in an even higher frequency range for higher detection sensitivity. Employing admittance measurement in higher frequencies, on the other hand, necessitates a very high dimension of finite element mesh for the model to converge in such frequency range, resulting in increased computational cost. Therefore, there is a trade-off. To balance the computational cost and the choice of frequency band, without loss of generality, we choose the frequency range around aforementioned resonant frequency, which will be used to illustrate the performance enhancement due to circuitry integration in relatively high frequency range for damage identification. Further investigations into the selection of frequency range will be conducted in future. The frequency range is from 3,630 Hz to 3,790 Hz with 200 frequency sweeping points. It is worth noting that all the data acquisitions are completed under the room temperature of 20 degrees Celsius within 0.2-degree fluctuations. The numerical simulation results are obtained after updating of model parameters, which will be explained in detail in Section 4.4.2. In this research, 3 inductance tunings are applied, i.e., 223.5 mH, 225.5 mH, and 227.5 mH. Here the initial inductance is tuned to 225.5 mH, which essentially corresponds to matching the circuitry resonant frequency with the host structure's 31st resonant frequency. Upon this tuning, frequency veering occurs when the system exhibits a response where the resonance frequency appears to split or veer into two distinct peaks. This behavior can be indicative of a change in the dynamic properties of a system and is used in this study to enhance the sensitivity of damage detection methods by amplifying the changes in admittance that are associated with damage (Jiang et al, 2008). The inductance values of 223.5 mH and 227.5 mH are chosen around the central value of 225.5 mH to demonstrate the feasibility of the method. At 223.5 mH, the right peak is higher than the left, and at 227.5 mH, the opposite is observed, effectively showcasing the capability of the approach to obtain diverse information or measurements for damage identification. The focus on this research is twofold, demonstrating the benefit of tunable inductance and examining the effectiveness of the Q-learning enhanced MOPSO. Future research may look into more inductance tunings and data acquisitions around different frequency ranges.

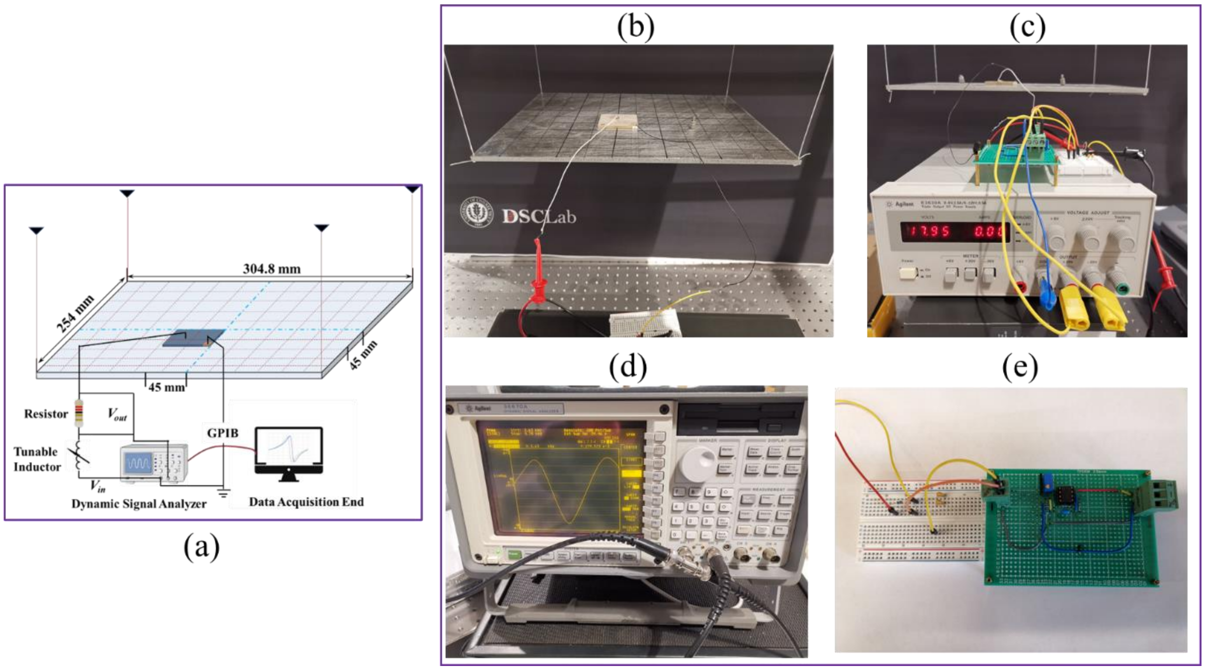

**Figure 4-3.** Experimental setup. (a) Schematic diagram of experimental setup, (b) Plate structure, (c) Agilent E3630A power supply for synthetic tunable inductor, (d) Dynamic Signal Analyzer (Agilent 35670A), and (e) Physical synthetic tunable inductor.

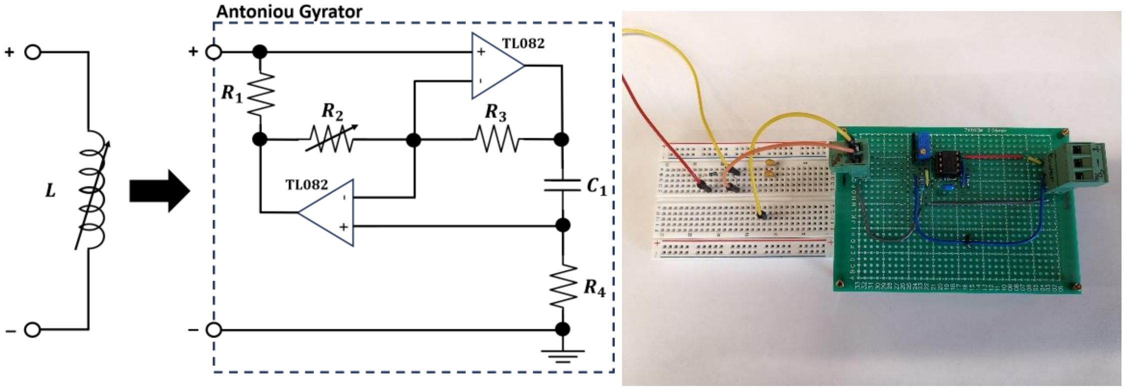

**Figure 4-4.** Tunable inductance circuit and physical tunable inductor.

To successfully implement the proposed method of damage identification, it is necessary to precisely match the electrical resonance of the shunt circuit to the natural frequency of the piezoelectric element. In this investigation, a tunable synthetic inductance dubbed the Antoniou Gyrator is used. By taking advantage of the voltage gain of operational amplifiers, the circuit in Figure 4-4 mimics the electrical impedance of an inductor according to Equation (4.14)

$$L = \frac{R_1 R_3 R_4}{R_2} C_1 \tag{4.14}$$

where $R_1$, $R_2$, $R_3$, $R_4$ and $C_1$ are resistances and capacitance values corresponding to the circuit elements in Figure 4-4. There are several advantages to this circuit compared to traditional coil inductors. For example, the equivalent inductance can be adjusted by replacing one of the resistors with a potentiometer, allowing the electric resonance to be precisely and continuously tuned. In the experiment $R_1$, $R_3$, $R_4$, and $C_1$ are chosen as $2.4\ \mathrm{k\Omega}$, $2.4\ \mathrm{k\Omega}$, $1.0\ \mathrm{k\Omega}$ and $68\ \mathrm{nF}$ respectively, while $R_2$ is replaced with a $5.0\ \mathrm{k\Omega}$ potentiometer. The resulting circuit can attain a very broad range inductance values in compact form, making it ideal for electromechanical integration. To ensure stable operation across a wide frequency range, high input impedance (~$10^{12}\Omega$) TL082 operational amplifiers are used. Another significant advantage of this configuration is that the equivalent impedance is entirely reactive under ideal assumptions. In other words, the DC resistance is substantially lower than equivalent coil inductors. This minimizes damping in the electric circuit, yielding a stronger a stronger resonance peak and greater sensitivity to damage detection.

### 4.4.2. Baseline model updating

The geometry and material properties of the piezoelectric transducer and the plate are listed in Table 4-2. The plate is made of aluminum alloy. The piezoelectric transducer is the SM411 type from Steiner & Martins Inc. The piezoelectric transducer is placed at the following location: 107.4 mm from the left edge and 127 mm from the top edge of the plate.

**Table 4-2.** Geometry and material properties of the piezoelectric transducer and the plate.

| Structure | Parameters | Values |
|---|---|---|
| Plate | Length ($10^{-3}$ m) | 304.8 |
|  | Width ($10^{-3}$ m) | 254 |
|  | Thickness ($10^{-3}$ m) | 3.874 |
|  | Young's modulus ($10^3$ MPa) | 73 |
|  | Density (kg/m$^3$) | 2769 |
|  | Poisson's ratio | 0.3 |
|  | Damping Ratio ( $\xi$ ) | 0.207% |
| Piezo Transducer (SM411) | Length ($10^{-3}$ m) | 45 |
|  | Width ($10^{-3}$ m) | 45 |
|  | Thickness ($10^{-3}$ m) | 3.5 |
|  | Young's modulus $E_{11}$ ($10^3$ MPa) | 74 |
|  | Young's modulus $E_{33}$ ($10^3$ MPa) | 54 |
|  | Density (kg/m$^3$) | 7800 |
|  | Piezo constant $g_{31}$ ($10^{-3}$ m$^2$/C) | -10.4 |
|  | Piezo constant $g_{33}$ ($10^{-3}$ m$^2$/C) | 24.2 |
|  | Permittivity constant $\varepsilon_{33}$ ($10^{-8}$ F/m) | 1.348 |

In the numerical procedure, we establish a finite element model utilizing a stress-voltage constitutive equation for the piezoelectric material. The transducer and the plate are discretized with a 20-node solid element mesh. The finite element analysis involves a total of 13,766 elements, reaching this mesh density upon convergence analysis verification against in-house MATLAB computations and cross-referenced with ANSYS outputs. The stiffness and mass matrices derived in finite element methodology are incorporated into the admittance expression from Section 4.2. The frequencies at which the system is swept for analysis are aligned with those utilized in the physical experiments, ensuring the simulation mirrors the experimental protocol.

It should be emphasized that the vendor-supplied material properties of the piezoelectric transducer may not be entirely precise. Moreover, experimental procedures are subject to inherent variations and uncertainties. As such, model updating is imperative, which involves adjusting the numerical outcomes to align with the experimental data. For the plate structure, we can measure the total mass and volume and then calculate its mass density. Hence there is one parameter of the plate to be updated, i.e., the Young's modulus $E_{\text{plate}}$. Similarly, for the piezoelectric transducer, its mass density can be calculated by assessing its mass and volume. An LCR multimeter is then used to measure the piezoelectric capacitance ($C_p$) once the transducer is affixed to the plate. Subsequently, for the transducer with a rectangular geometry, the permittivity constant, denoted as $\varepsilon_{33}$, is derived using $\varepsilon_{33} = C_p \cdot d/A$, where $d$ and $A$ represent the thickness of the transducer and the area of electrode, respectively.

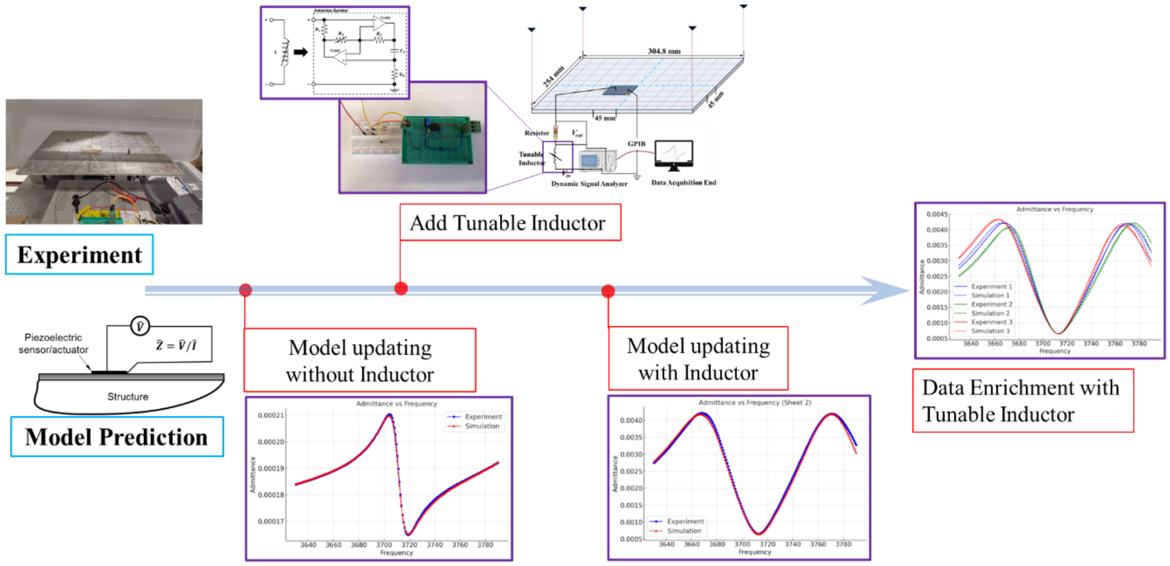

**Figure 4-5.** Flowchart for model updating process.

Prior to the updating of other parameters of the model, comprehending the effect of each on the admittance is critical. Sensitivity and perturbation analyses are performed and compared with experimental data to determine the parametric limits for the subsequent inverse analysis employed in model updating. For a given parameter, if the range of predicted admittance through parameter perturbation encompasses the experimental data, then the resultant variation percentage may be set as the parametric limit. Otherwise, we make adjustment to decide the parametric boundary. In addition, sensitivity analysis yields a measurable indication of the magnitude and direction of the changes in admittance due to parameter variations. Grounded in the parameter sensitivity analysis, we bifurcate the model updating process into two phases: before and after the introduction of the tunable inductance, as depicted in Figure 4-5. Prior to the inductance integration, the method adheres to the conventional admittance-based approach, hence the admittance curve exhibits a singular peak. At this stage, it is only necessary to update parameters associated with the piezoelectric material.

We recognize that the variation in the piezoelectric Young's modulus $E_{11}$ is correlated with lateral deviations in the admittance curve and its magnitude. Moreover, alterations in the piezoelectric constants $g_{31}$ and $g_{33}$ typically result in pronounced changes in both the real and imaginary components of magnitude. In contrast, changes in the piezoelectric Young's modulus $E_{33}$ tend to have a more subdued impact. This insight directs our optimization strategy to prioritize parameters with the most influence, specially $E_{11}$, $g_{31}$ and $g_{33}$. The range for the parameter modification during model updating is thus established at ±20% for the plate Young's modulus $E_{\mathrm{plate}}$ and ±35% for the piezoelectric constants $g_{31}$ and $g_{33}$. In the process of model updating, our objective is to minimize the difference between the admittance derived from experimental observations, denoted as $y_{\mathrm{h}}^{\mathrm{exp}}(\omega)$, and the admittance from the numerical model ( $y_{\mathrm{h}}^{\mathrm{pred}}(\omega)$ ). Here, the subscript 'h' refers to the healthy state. The superscripts 'exp' and 'pred' refer to the data from experiment and from model prediction, respectively. The objective function for model updating is $obj = \left\| y_h^{\mathrm{exp}}(\omega) - y_h^{\mathrm{pred}}(\omega) \right\|_2$. There is a total of 40 iteration steps for minimizing the objective function in model updating by adopting single-objective particle swarm optimizer. Finally, the key parameters are updated as $E_{\text{plate}} = 71.66\ \text{GPa}$, $E_{11} = 84.8\ \text{GPa}$, $g_{31} = -7.1 \times 10^{-3}\ \text{m}^2/\text{C}$, and $g_{33} = 24.2 \times 10^{-3}\ \text{m}^2/\text{C}$. It is worth mentioning that mechanical damping plays a crucial role in model updating. In this study, we determine the range of damping through sensitivity analysis. After updating, the damping ratio around the resonant frequency selected in this research is determined as $\xi = 0.207\%$ listed in Table 4-2. Following the model updating of the baseline finite element model of the structural component, we then add inductance to the model for further refinement, as shown in Figure 4-5. At this stage, only two circuitry parameters need consideration: the inductance value and the overall circuit resistance. The inductance values are measured experimentally as given in Section 4.4.1. The fixed resistance in the circuit is known, but the resistance of the tunable inductor may have frequency dependence. Therefore, the total circuit resistance is updated based on the impedance measurements. Ultimately, the resistance value for the entire circuit is updated from 100.3 ohms to 174.5 ohms.

The updated admittance curves are compared to experimental results, as shown in Figure 4-6. As can be observed, they match very well. Figure 4-6(a) shows admittance curves without tunable inductor; Figure 4-6(b) presents admittance curves with tunable inductor, and Figure 4-6(d) includes admittance curves with tunable inductor in different tuning values. It is worth noting that Figure 4-6(c) compares the admittance curve with and without inductance. Obviously, with the circuitry resonance effect and under the same level of voltage excitation, the magnitude of the admittance with inductance is significantly amplified. This amplification serves a dual purpose in mitigating noise effects: it directly increases the signal-to-noise ratio in measurement, enhancing the overall quality of data acquisition. Furthermore, it may even amplify the damage-induced admittance change, making subtle damage features more discernible and thereby improving the sensitivity and reliability of the damage detection process.

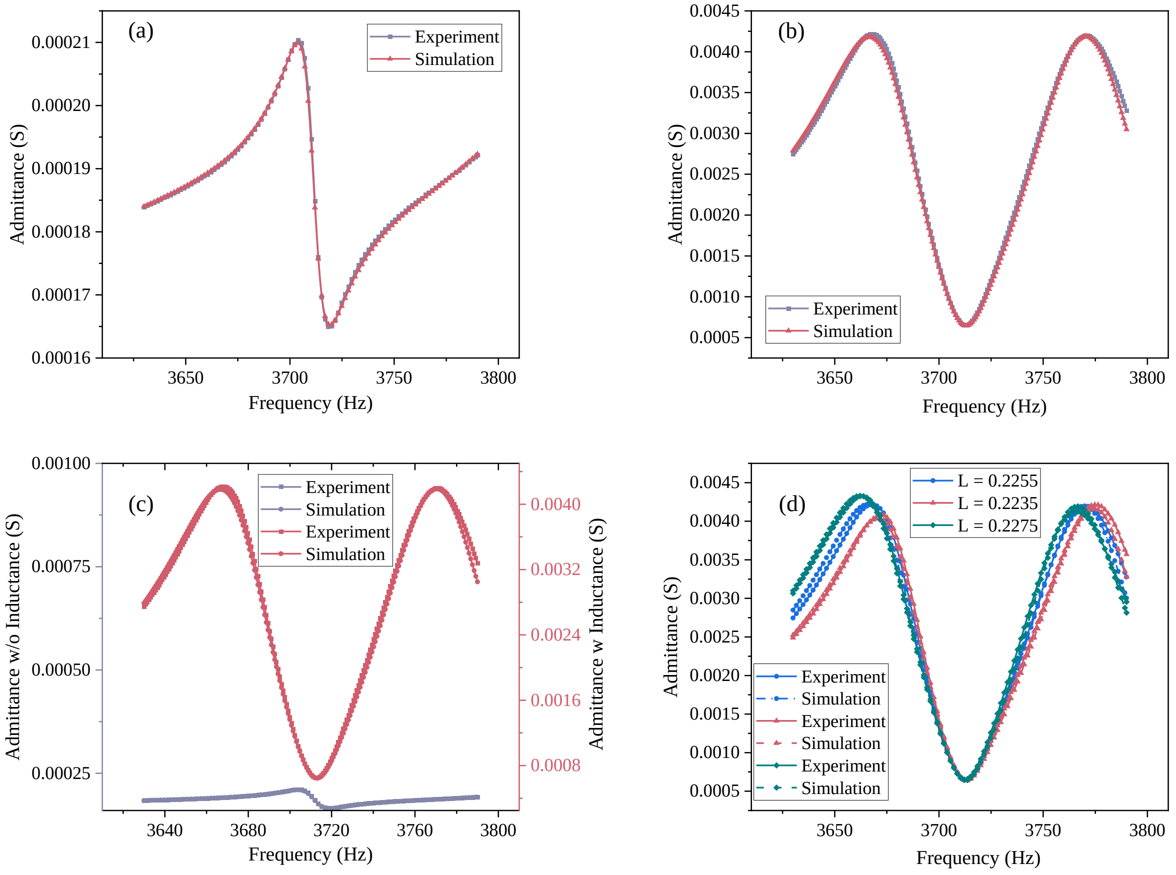

**Figure 4-6.** Admittance curves from experiment and updated simulation. (a) Admittance curves without tunable inductor; (b) Admittance curves with tunable inductor; (c) Admittance comparison with and without inductance; and (d)Admittance curves with tunable inductor in different tuning values.

### 4.4.3. Damage identification using enriched experimental measurements

In order to facilitate structural health monitoring and precise identification of damage location/severity, we divide the plate structure into 120 segments, i.e., $n = 120$ in Equations (4.5) and (4.6c), which correspond to 120 variables within the damage index vector that needs to be identified. Each segment contains many finite elements. This approach balances computational efficiency with practical damage detection resolution. Each segment's property change is homogenized into an equivalent stiffness change percentage, enabling accurate damage identification while keeping the problem computationally tractable. This segmentation avoids the impracticality and unnecessary complexity of identifying damage at the individual element level for all 13,766 elements. It is crucial to note that, from a mathematical perspective, the rows of sensitivity matrix may not exhibit linear independence, regardless of the number of frequency points selected for the sweep and the number of inductance tunings. Consequently, the inverse problem, as formulated in Equation (4.7), is typically underdetermined. This underdetermination is the primary rationale for employing a multi-objective optimization approach to ascertain a set of potential solutions. To systematically validate the proposed damage identification algorithm, two cases with single and multiple damage locations are considered.

For the sake of generality and to mitigate the introduction of extraneous variations that could arise from changes in boundary conditions during the experimental phase, damage scenarios are emulated by affixing one or two small mass blocks onto the plate. The added mass causes the shift of admittance curves, which is equivalent to stiffness reduction. In our experiment, after the mass addition, we capture the admittance curve within the targeted frequency range. The numerical model is then updated by altering the stiffness (specifically, decreasing the Young's modulus of the elements) at the precise segments where the mass is added. This is done until the calculated admittance curve aligns with the one observed experimentally (considering the added mass). Consequently, the extent of stiffness reduction in the affected segments can be ascertained numerically. These two cases are designed with damage locations chosen randomly. The first case has a single damage location. While the second case has two damage locations. The details for the case study setup are shown in Figure 4-7. Such a case study setup can demonstrate the capability of the proposed algorithm to identify damage, regardless of the damage sizes and locations. The optimization terminates upon reaching the maximum number of iterations, which was determined through a systematic analysis. We tested maximum iterations from 20,000 to 100,000 in 20,000 increments, observing the solutions produced in each scenario. Cases with 40,000 iterations and above yielded approximately the same results. For efficiency, we set the maximum iteration at 20,000 in this study.

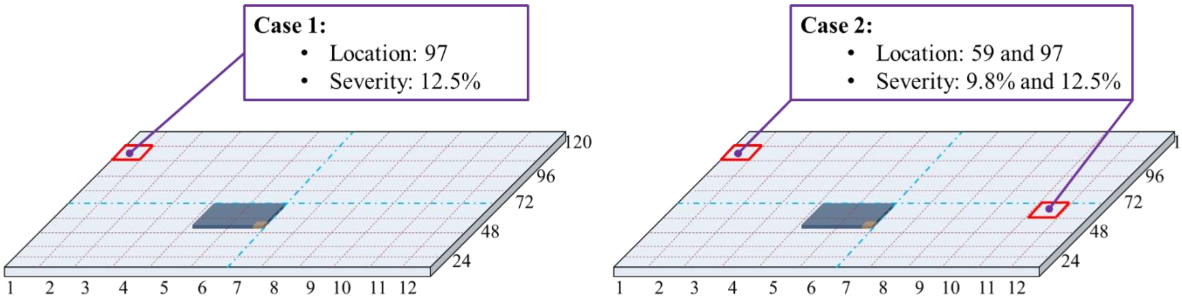

**Figure 4-7.** Case study setup.

For Case 1, the true damage is positioned at the 97th segment with a severity of 12.5%. The solutions obtained are shown in Figure 4-8. Three direct observations can be drawn from the plot. First, within the setting of multi-objective optimization, we have obtained a set of multiple solutions for the underdetermined problem. Second, the size of this solution set is generally small, which aligns with our objective. Third, each solution exhibits good sparsity, with the maximum number of identified damage locations being four, which is indeed a relatively small number in comparison to the potential 120 damage locations, indicating the effectiveness of our identification process. In Solution 1, the algorithm accurately identifies the damage location at segment 97 with a slight severity difference of 5E-5. Solution 2 also correctly identifies the damaged segment but with a lesser severity of 7.53%, and it indicates an additional damage presence at segment 69 with a severity of 13%. Solution 3 exhibits a similar pattern of correct damage localization at segment 97 with a severity of 6.011%, accompanied by two additional identified locations at segment 68 and segment 69, with severity of 13% and 8.804%, respectively. Lastly, Solution 4 shows the true damage at segment 97 with a severity of 6.006%, and three locations at segments 11, 68 and 69 with severities of 4.766E-8, 13% and 8.804%, respectively. Obviously, segment 11 with severity of 4.766E-8 is small that can be ignored compared to the true damage scenario with severity of 12.5%. Therefore, solution 4 is almost the same as solution 3. Although the solutions 2-4 from the proposed approach point to additional damage locations besides the true damage location, all the additional damage locations identified cannot be deemed incorrect. They are a characteristic outcome of the multi-objective optimization framework, adhering to criteria like non-dominated sorting algorithm. Collectively, these 3 solutions identified provide very consistent identification results that can be utilized in decision making in engineering practice. Most importantly, the proposed MOPSO enhanced with Q-learning can capture the actual damage scenario accurately (solution 1).

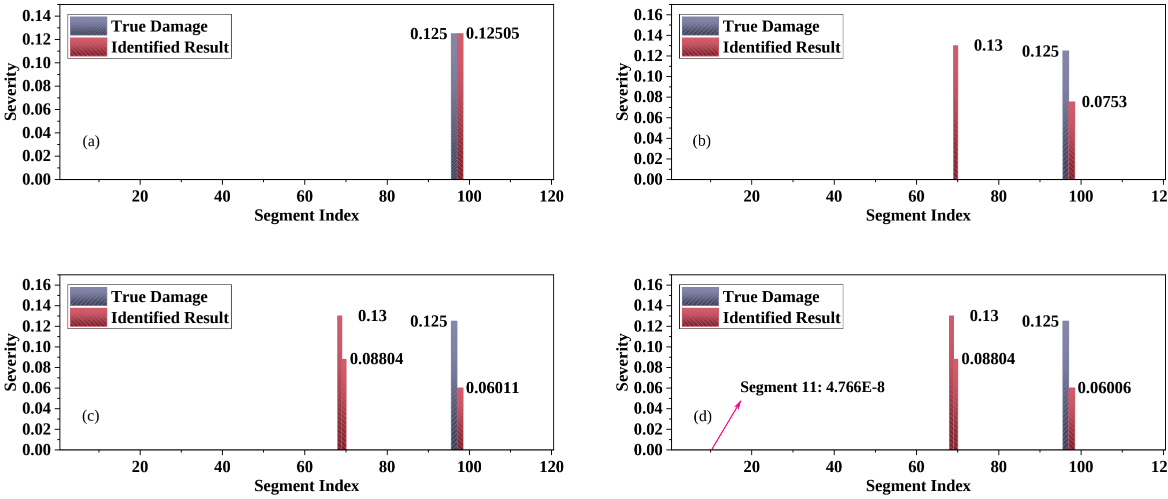

**Figure 4-8.** Identified 4 solutions from (a) to (d) for Case 1.

In Case 2, damage is present at segments 59 and 97, exhibiting stiffness reductions of 9.8% and 12.5% respectively. This scenario is designed to assess the effectiveness of the algorithm in identifying damages at multiple locations. The results from our proposed algorithm are depicted in Figure 4-9. Notably, the algorithm identifies a maximum of four solutions, a small number in comparison to the total of 120 segments being examined. The first solution from our algorithm reveals only one damage location, deviating from the actual scenario of two damaged locations. This is not a surprise, because one of the objective functions in the multi-objective optimization is the sparsity of the damage index vector, and the algorithm may indeed find a solution with single damage. Solution 2 identifies two damage locations, closely aligning with the actual damage scenario in terms of both location and severity. In Solution 3, in addition to accurately identifying the two real damage locations, an additional damage location at segment 69 is identified, with a severity of 13%. The distinction of Solution 4 compared to Solution 3 lies in its identification of an extra damage location at segment 68, exhibiting a severity level of 4.81%. Despite the identification of additional damage locations in the solutions, the solution set is notably small, consisting of only four options, all exhibiting good sparsity. From a practical engineering viewpoint, the further inspection or post-filtering methods can efficiently pinpoint the true damage locations with a minimal additional cost.

To summarize, the case studies underscore the efficacy of our proposed method. Each case yields a concise set of solutions that reliably encompasses the actual damage scenario. In real-world applications, following the identification of multiple solutions, a decision-making process ensues. If all solutions indicate negligible damage, it may be advisable to continue operating the structure. Conversely, if any solution suggests a risk of severe damage, additional assessments, including human inspections and alternate sensing techniques, should be undertaken to investigate these limited potential damage scenarios more closely. A large solution set would undermine the purpose of structural health monitoring by overwhelming the operator with too many possibilities to consider. Our algorithm successfully achieves the goal of pinpointing a small, yet comprehensive set of solutions that invariably includes the actual damage scenario.

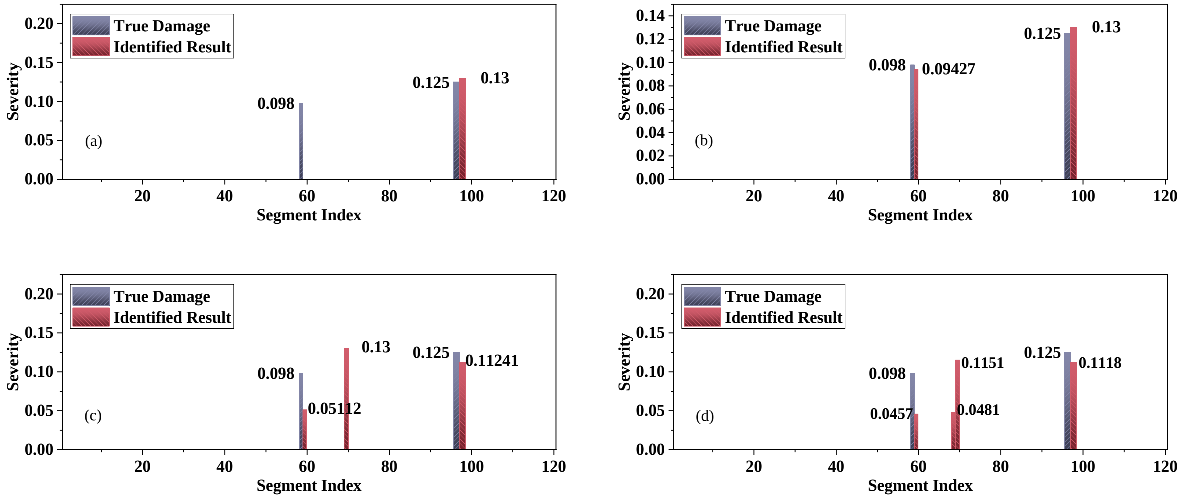

**Figure 4-9.** Identified 4 solutions from (a) to (d) for Case 2.

### 4.4.4. Effects of data enrichment on identified results.

In this section, we examine the effects of data enrichment. It should be emphasized that our goal is to obtain a small but diverse set of solutions by acquiring more information, aiming at capturing the actual damage scenarios. The plots in Figure 4-10 present the statistical relationship between the number of inductance tunings (shown on the *x*-axis) and the number of identified solutions (shown on the *y*-axis) for the aforementioned two damage identification cases. S1, S2 and S3 correspond to the cases with inductance values of 223.5 mH, 225.5 mH and 227.5 mH, respectively. In both plots, as the number of tunings increases from a single tuning (S1, S2, or S3) to combinations involving two or three tunings (S1+S2, S1+S3, S2+S3, or S1+S2+S3), the number of solutions generally decreases. This trend is exactly what we aim for. Additionally, we plot accuracy curves to illustrate how accuracy changes with the number of tunings.

The averaged number of solutions and accuracy are calculated as follows:

1) Multiple Runs for Each Tuning Combination: For each tuning or tuning combination case, we run the algorithm or optimization process 8 times. This is to account for any variability in the results and to ensure robustness.
2) Solution Set Generation: Each run produces a set of solutions generated by the proposed algorithm. These solutions represent potential damage scenarios identified by the method.
3) Accuracy Calculation: For each run, we check if the solution set obtained covers the true damage scenario. If the solution set includes the true damage scenario, we count it as a success.
4) Statistical Accuracy: If the solution sets from all 8 runs include the true damage scenario, the accuracy for that tuning combination is considered 100%. If fewer runs capture the true damage scenario, the accuracy is calculated as the percentage of successful runs out of 8.

Specifically, in Case 1, when using a single tuning, the average number of solutions exceeds 10. As the number of tunings increases, providing more input information, the number of solutions becomes fewer. As shown in Figure 4-10(a), with two tunings, the average number of solutions hovers around 5. With three tunings, the average number is around 2.5. Two points are worth noting here. First, with two tunings, the average number of solutions for the three combination types is not identical due to the stochastic optimization algorithm used. Since it relies on a non-dominated sorting algorithm, the number of solutions may vary across optimization runs. Second, although the number of solutions with three tunings is indeed fewer than with single or dual tunings, this is not always the case, which is illustrated in Case 2. Figure 4-10(b) shows the statistical distribution of the number of solutions for Case 2 under different tunings. An interesting observation is that with three tunings, the average number of solutions is not fewer than with two tunings. There are two possible reasons for this. First, as mentioned earlier, a stochastic optimization algorithm is used. Second, although we can obtain more information by more tuning, not all of it is guaranteed to be completely linearly independent. Thus, it is possible for the number of solutions in the three-tuning scenario may be slightly larger than that in the two-tuning scenario.

In terms of accuracy, for case 1, although we can obtain multiple solutions with one tuning, none of them can capture the actual damage according to the definition of accuracy. As the number of tunings increases to two, we observe a significant improvement in accuracy. Additionally, it is worth mentioning that our definition of accuracy is that there is at least one solution in the solution set that can capture the actual damage. Surprisingly, in the solution set identified by our algorithm, each solution captures the actual damage case. Therefore, the accuracy is almost 100%. As the number of tunings increases to three, we find that the accuracy of the identified solutions also reaches a high level. Similarly, for case 2, as the number of tunings increases, the accuracy of the solutions also reaches 100%.

Overall, we can observe that as the input information increases, the number of solutions shows a decreasing trend while the accuracy improves. In each case, the obtained solution set is small and accurate, effectively capturing the true damage scenarios. The results demonstrate both the advantage of inductance tuning and the effectiveness of Q-learning enhanced MOPSO inverse analysis.

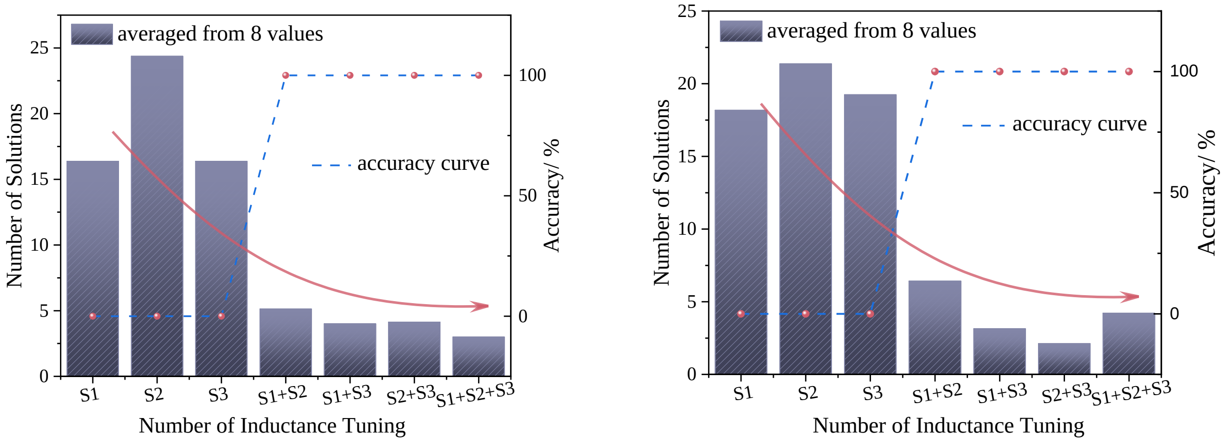

(a) (b)

**Figure 4-10.** Statistical illustration of number of identified solutions with respect to the number of inductance tunings, (a) Case1, and (b) Case 2.

## 4.5. Conclusion

In this research, we integrate a tunable inductance into the measurement circuit to improve the robustness and accuracy of the piezoelectric admittance-based active interrogation for identifying structural damage. By tuning the inductance to a series of values, we can collect a family of admittance measurements for a given damage scenario. As a result, the measurement method and the undetermined inverse problem for damage identification are fundamentally improved to provide more accurate damage identification results. While promising, it cannot be guaranteed that the measurement information of piezoelectric admittance change is linearly independent, the damage identification could still be an under-determined problem. To tackle this challenge, we formulate a multi-objective optimization inverse analysis, coupled with a hybrid optimizer that merges metaheuristics with reinforcement learning. This combination is developed to balance the exploration and exploitation in dealing with multimodal objective functions, which usually have many local extremes. We choose the multi-objective particle swarm optimization (MOPSO) as the basic platform and incorporate metaheuristics to enhance its capability toward damage identification. A series of local search strategies through coefficient variation-based and mutation-based techniques are synthesized that form an action repository to enhance the global searching capability of MOPSO. To guide the particle to adaptively select the local search, Q-learning is integrated. Through case studies involving physical experiments and finite element modeling, our approach has consistently identified a concise set of solutions that encapsulate the actual damage scenarios in all tested cases. We also discuss how varying the inductance affects the solution set, noting a trend of fewer solutions with more tunings. This method shows potential for broader application in model-based structural health monitoring.

While this study shows promising results in robust damage identification for practical situations by adopting harmonic excitation-based piezoelectric impedance measurement, multi-objective optimization, and tunable inductance amplification, challenges persist in quantitatively assessing noise impacts on measurements and inverse analysis results. Future research will focus on addressing these challenges to further enhance the method's reliability in real-world applications.

# Chapter 5. High-frequency Active Interrogation for Structural Damage Identification Enabled by Intelligent Hierarchical Search

A common issue in structural damage identification is the measurement information being limited while the baseline structural model is complex, which renders the inverse analysis under-determined. Leveraging that the damage in its early stage usually affects only small area(s), a multi-objective optimization can be formulated by minimizing the difference between model prediction and physical measurement and concurrently enforcing the sparsity in damage locations. The challenges, however, lie in handling the high-dimensional parametric space with multimodal objective functions as well as the computational cost brought by incorporating the $l_0$ norm minimization. In this research, we synthesize a hierarchical framework that searches potential damage locations first and then delves into accurate characterization of damage. In particular, to address the high-dimensional and multimodal challenges intensified by high-frequency measurement towards high-precision identification, we adopt the Group Lasso technique for sparsity induction, and utilize the Technique for Order Preference by Similarity to Ideal Solution to realize optimization phase transition, aiming at improving the computational efficiency as well as the accuracy. The validation of our approach through a piezoelectric admittance sensing testbed underscores its potential for structural health monitoring practices by providing a robust, accurate, and computationally efficient approach for early-stage damage identification and assessment.

## 5.1. Introduction

Structural damage identification is a key process in the field of structural health monitoring (SHM), essential for maintaining the integrity and safety of mechanical, civil, and aerospace systems. This process often involves the utilization of vibration information (Barman et al, 2021), Lamb wave signals (Kumar and Sunny, 2021), strain (Aller et al, 2022), flight data from multicopter (Dutta et al, 2022), and piezoelectric impedance (Cao et al, 2023a) among others, to identify structural property changes through inverse analysis or model updating (Sung et al, 2021). While a variety of techniques have been explored over the years, piezoelectric impedance-based approach has shown promising aspects (Park et al, 2003; Wang and Tang, 2009; Shi et al, 2022). In such an approach, a small and lightweight piezoelectric transducer is embedded into the host structure, serving as self-sensing actuator to collect the electromechanical impedance of the integrated system in high-frequency range. This is particularly appealing for aerospace structures, where compact packing and low weight/volume requirements are necessary, and the sensing mechanism has to be highly sensitive. Examples of exploration include adaptive structures (Inman and Grisso, 2007), rotary aerospace structures (Hoshyarmanesh and Abbasi, 2018), and aircraft wing composite structures (Boukabache et al, 2012; Liu and Chattopadhyay, 2013; Yuan et al, 2016; Fu et al, 2018). Traditionally, many of these studies rely on the comparison between baseline data and in-field measurements, using indicators such as root mean square error to damage detection purpose.

While the detection of damage occurrence is certainly important, structural diagnosis and prognosis will have to be built upon the thorough characterization of both damage location and severity, a process known as damage identification. In a piezoelectric impedance scheme for structural health monitoring through active interrogation, frequency-sweeping voltage is applied to the transducer to induce high-frequency local oscillation. Meanwhile, the system response can be extracted by measuring the current flow in the transducer circuity, which then yields the measurement of impedance (or its reciprocal, the admittance). This sensor-structure interaction can be modeled with finite element analysis. Since the impedance measurements are associated with harmonic responses, it appears feasible to conduct inverse analysis mathematically, based on the corresponding finite element model, to identify the change of the properties of the underlying structure such as the local stiffness and/or mass (Kim and Wang, 2014; Shuai et al, 2017; Cao et al, 2018a; Fan et al, 2020; Zhang et al, 2024a). There are, however, both opportunities and challenges in piezoelectric impedance-based damage identification. On one hand, piezoelectric transducers feature high bandwidth and very good linearity, which allows the measurement of impedance information in high-frequency range for inverse analysis of small-sized damage. On the other hand, to facilitate high-frequency model-based inverse analysis, the baseline finite element model will have to have high mesh density and high dimensionality of damage index to reflect the small-sized damage. The effect of structural damage to impedance/admittance versus excitation frequency relation is most pronounced around the peaks of the measurements. Compared with the number of unknowns, the measurement information is quite limited. As such, structural damage identification using high-frequency interrogation is generally an under-determined problem. For such problems, direct matrix inversion with artificial constraints may not yield realistic solution. Fortunately, there is a physically meaningful condition we can leverage, i.e., the sparsity of damage index. In damage identification inverse analysis, typically the host structure is divided into a large number of segments. While each segment may be subject to damage-induced property change which is referred to as the damage index, realistically damage in its early stage affects only small area(s). As such, the damage index vector is generally sparse.

Since direct matrix inversion may not be conducted in such an under-determined problem, it is natural to cast the inverse analysis of damage identification into an optimization problem to identify the damage index vector that matches the model prediction with respect to the measurement. A number of investigations have incorporated the sparsity requirement into the optimization formulation by augmenting the aforementioned objective function with a regularization term (Davenport et al, 2012; Fan et al, 2018; Chen and Sun, 2021; Ding et al, 2020 and 2022). It is worth noting that a single-objective optimization generally yields a single solution which may be easily contaminated by model mismatch and/or measurement noise, and the inclusion of regularization requires the selection of weighting constants that are difficult to determine *a priori*. Alternatively, the sparsity condition can be treated as a second objective function. Subsequently, one can form a multi-objective optimization problem that minimizes concurrently a) the difference between model prediction in the parametric space and the in-field measurement, and b) the $l_0$ norm of the damage index vector to facilitate sparsity. This setup leads to multiple solutions which fits the nature of structural diagnosis. From implementation standpoint it avoids the selection of *ad hoc* weightings between the different objectives. Major challenge, however, lies in how to handle such a high-dimensional, multi-modal optimization problem to find a diverse yet small solution set that can capture the true damage scenario. Furthermore, the incorporation of the $l_0$ norm as the second objective requires the identification of the sparsest solutions, which involves evaluating an exponentially increasing number of possible combinations of non-zero entries. This in theory leads to an NP-hard problem, making it computationally prohibitive especially for structural damage identification with high-frequency interrogation. Here, NP stands for 'nondeterministic polynomial time,' a classification of problems for which a computer can verify a solution in a reasonable amount of time if one is provided. In contrast, NP-hard problems are those where finding a solution is extremely difficult, even though verifying a given solution might be easy. These problems are considered to be highly complex, requiring significant computational resources to solve (Foucart and Rauhut, 2013). To tackle the aforementioned challenges in inverse analysis of high-frequency active interrogation through multi-objective optimization, we aim at addressing two issues, i.e., reducing the dimensionality of the problem to alleviate the difficulty of the search, and enhancing the search capability of the algorithm using local heuristics to ensure solution accuracy.

In terms of dimensionality reduction, a hierarchical approach is intuitive: first evaluating the location of structural damage, and then assessing the location and severity of the damage. Du et al (2019) introduced a two-phase structure damage assessment method that initially detects potential damages through a modal strain energy index and then quantifies severity using the Jaya algorithm. Perera et al (2020) implemented a two-stage damage identification method for complex structures using the roaming damage method, which identifies damage ranging from large low-damage areas to severely damaged individual beams, enhanced by a multi-objective optimization based on power mode shapes for comprehensive damage detection. Barman et al (2021) applied a two-stage method where the first stage uses mode-shape curvature-based damage indices for rough estimation of damage location, and the second stage refines this using a mixed unified particle swarm algorithm for precise lengthwise and interface location determination in composite structures. The results indicate high accuracy in identifying single and multiple delaminations, showing potential under noisy conditions.  In the context of multi-objective optimization problem setting of this study, we can employ expert knowledge to facilitate two-stage damage identification. This expert insight is that structural damage typically exhibits sparsity or damage is not uniformly distributed. This inspires us to group identification variables into limited subsets, where if damage occurs within one group, the other groups remain sparse, trending towards zero collectively. Thus, in the first layer, we utilize the Group Lasso method instead of directly incorporating the $l_0$ norm. Group Lasso works by applying a penalty that is proportional to the $l_2$ norm of the coefficients within each group and then summing these norms with an $l_1$ penalty across groups. This method allows us to enforce sparsity at the group level, effectively detecting which group the damage falls into. Next, we pass this information to the second step. In the second phase of optimization, we only focus on the damaged variable group, significantly simplifying the search.

It is worth noting that our two-stage damage identification process involves two main components: Group Lasso and the Technique for Order Preference by Similarity to Ideal Solution (TOPSIS). Group Lasso drives entire variable groups toward sparsity. This technique has been applied in related research. For example, Dimopoulos et al (2022) introduced two sparsity-based methods using low-frequency response functions for damage detection, leveraging complex Group Lasso strategies to localize multiple defects with a single sensor. Similarly, Zhang et al (2022b) applied Group Lasso to enhance moving force identification by grouping non-overlapping sparse coefficient vectors, which correspond to vehicle forces, and linking these groups with measurements to accurately reconstruct the moving forces. In our approach, TOPSIS is used to facilitate the transition between stages. As a multi-criteria decision-making method, TOPSIS ranks alternatives based on their proximity to an ideal solution (Greco et al, 2016). It is selected for its efficiency in translating complex optimization outcomes into actionable insights, effectively bridging the gap between stages by identifying the most promising solutions for further analysis.

Meanwhile, we can strengthen the search capability to handle the multimodal objective function with high dimensionality. In general, no single algorithm can solve all optimization problems. This necessitates problem-oriented tailoring of the algorithm to target at the specifics of the problem at hand. The idea lies in incorporating the development of specific local search techniques or existing local search algorithms into the foundational algorithms. For example, Tiachacht et al (2018) adapted the genetic algorithm with a modified Cornwell indicator to enable damage assessment, while Minh et al (2021) advanced particle swarm optimization with online parameter adjustments for optimal global search. Additionally, Ding et al (2022) augmented the Jaya algorithm with K-means clustering and Hooke–Jeeves pattern search, and Thanh et al (2022) improved the grey wolf optimizer by introducing Lévy flight and new leadership dynamics. Similarly, efforts by Livani et al (2018), Zheng et al (2022), and Li et al (2023) provide additional insights. Although various advancements have been made, these enhancements predominantly cater to single-objective optimization. A gap remains in multi-objective optimization for structural damage identification. Bridging this gap, our study adopts the particle swarm optimization (PSO) algorithm, selected for its straightforward concept, ease of implementation, computational efficiency, and minimal control parameters. It is known that PSO tends to fall into local optima, and its premature convergence presents significant challenges, particularly exacerbated by the high-dimensional nature of structural damage identification problems. Fortunately, its inherent flexibility allows for effective integration with local search strategies to enhance its performance. In this study, to tackle challenges in multi-objective optimization, we developed five categories of local search strategies aimed at ensuring a small, diverse, and accurate solution set while achieving convergence. This allows for precise and efficient identification of damage, similar to narrowing down a diagnosis in healthcare. The first two strategies are coefficient-based, designed to modulate parameter dynamics for effective early exploration and later convergence. The remaining strategies are mutation-based, designed to perturb personal and global bests to overcome potential local optima. Importantly, these strategies are not applied simultaneously; instead, the most suitable one is selected for each particle. We employ Learning Automata (LA), a type of reinforcement learning algorithm, to facilitate this selection process. LA operates as a form of stochastic optimization, utilizing adaptive rules to navigate and learn from the search space, as highlighted by Hashemi and Meybodi (2011) and Zhang et al (2020). Here, each particle functions as an individual LA, interacting with its environment to adaptively choose the best action based on its current position. Feedback from the environment after each action informs the particle whether it is moving closer to or further from the optimal solution, allowing it to adjust the probability of the chosen action accordingly. Actions that prove more effective receive a higher accumulated probability. A unique advantage of LA is its ability to obviate the need for a predefined reward strategy, common in traditional reinforcement learning, thus enabling self-adaptive learning.

The overarching goal of this research is to formulate a new hierarchical framework for the piezoelectric admittance-based damage identification: first detecting the potential damage location and then accurately identifying the damage location and severity. The enhanced multi-objective particle swarm optimization (MOPSO) algorithm is employed to solve the problem in pursuit of a small yet diverse solution set. The contributions of study are multi-fold: 1) It reformulates structural damage identification using piezoelectric admittance into a multi-objective optimization problem; 2) It introduces a hierarchical framework that employs Group Lasso and TOPSIS for inter-stage communication; 3) It presents a novel swarm optimizer that incorporates multiple local search strategies and is steered by learning automata; 4) It validates the efficacy of this new methodology using a piezoelectric admittance sensing testbed for damage identification. The rest of the paper is organized as follows. Section 5.2 outlines the piezoelectric admittance measurement concept and the finite element based mathematical modeling, followed by the multi-objective optimization formulation for damage identification. In Section 5.3, we first outline the hierarchical framework for structural damage identification. And then develop time-varying coefficients and mutation-based local search strategies for swarm optimizer, which is guided through LA. Section 5.4 presents the implementation of the new algorithm to piezoelectric admittance-based damage identification using measurement signals and highlights the performance. Section 5.5 provides the concluding remarks.

## 5.2. Piezoelectric Admittance-based Damage Identification: Problem Formulation

This section first briefly presents the technique of piezoelectric admittance-based damage identification as well as the finite element model of the integrated system that will serve as the baseline for model-based inverse analysis. We then formulate a multi-objective optimization problem that will be employed to facilitate damage identification inverse analysis.

### 5.2.1. Modeling of piezoelectric admittance

In damage identification, we employ the dynamic response of a structure as an information carrier to infer the damage occurrence. In piezoelectric admittance-based approach, we integrate a piezoelectric transducer into a host structure, and utilize the transducer as actuator and sensor concurrently. The equations of motion of the integrated system can be derived as (Shuai et al, 2017; Cao et al, 2018a)

$$\mathbf{M}\ddot{\mathbf{q}} + \mathbf{C}\dot{\mathbf{q}} + \mathbf{K}\mathbf{q} + \mathbf{K}_{12}Q = \mathbf{0} \tag{5.1a}$$

$$R\dot{Q} + k_c Q + \mathbf{K}_{12}^T \mathbf{q} = V_{\text{in}} \tag{5.1b}$$

where **q** is the displacement vector, $k_c$ is the inverse of the capacitance of the piezoelectric transducer; $\mathbf{K}_{12}$ is the electromechanical coupling vector due to the transducer, and **K**, **C**, **M** are the stiffness, damping and mass matrices, respectively. $V_{\text{in}}$ is a frequency-sweeping harmonic voltage excitation, and *Q* is the charge flow. To facilitate the measurement of charge flow, a small resistor *R* is connected in series with the piezoelectric transducer so the voltage across it can be measured. The details of the measurement system will be presented in Section 5.4. We let the excitation frequency be denoted as $\omega$, and use the overbar hereafter to indicate magnitude of the corresponding response variable. The piezoelectric admittance under the healthy structure status can be derived as

$$y_h(\omega) = \frac{\bar{\dot{Q}}}{\bar{V}_{\text{in}}} = \frac{j\omega}{j\omega R + k_c - \mathbf{K}_{12}^T(\mathbf{K} + j\omega\mathbf{C} - \omega^2\mathbf{M})^{-1}\mathbf{K}_{12}} \tag{5.2}$$

where *j* refers to the imaginary unit. Damage may occur in any part of a structure with arbitrary severity. In order to pinpoint damage, we divide the structure into *n* segments where *n* is a relatively large number in order to characterize damage at early stage with small size. Since we conduct damage identification based on the finite element modeling, we assume the damage causes homogenized change of structural properties within a segment. Without loss of generality, in this research we assume the damage results in stiffness reduction only. The stiffness matrix of the healthy structure is expressed as $\mathbf{K} = \sum_{i=1}^{n} \mathbf{K}_h^i$ , in which $\mathbf{K}_h^i$ is the stiffness matrix of the $i^{\text{th}}$ segment under the healthy status and the summation refers to the direct summation in finite element model assemblage. The stiffness of the structure with damage is then expressed as $\mathbf{K}_d = \sum_{i=1}^{n} \mathbf{K}_h^i (1 - \alpha_i)$, where $\alpha_i \in [0,1]$ is the damage index to be identified indicating the stiffness loss of the $i^{\text{th}}$ segment. When damage occurs, the piezoelectric admittance becomes

$$y_d(\omega) = \frac{\dot{\bar{Q}}}{\bar{V}_{\text{in}}} = \frac{j\omega}{j\omega R + k_c - \mathbf{K}_{12}^T (\mathbf{K}_d + j\omega \mathbf{C} - \omega^2 \mathbf{M})^{-1} \mathbf{K}_{12}} \tag{5.3}$$

Obviously, damage occurrence is reflected by the change of piezoelectric admittance. Based on Equations (5.2) and (5.3), utilizing the Taylor series expansion we can obtain the change of admittance as

$$\Delta y(\omega) = y_d(\omega) - y_h(\omega) = \sum_{i=1}^{n} [j\omega (j\omega R + k_c - \mathbf{K}_{12}^T \mathbf{Z}^{-1} \mathbf{K}_{12})^{-2} \mathbf{K}_{12}^T \mathbf{Z}^{-1} (\mathbf{L}_i^T \mathbf{K}_h^i \mathbf{L}_i) \mathbf{Z}^{-1} \mathbf{K}_{12}]\, \alpha_i \tag{5.4}$$

where $\mathbf{Z} = \mathbf{K} - \mathbf{M}\omega^2 + j\omega \mathbf{C}$ represents the dynamic stiffness of the structure, and $\mathbf{L}$ is the Boolean matrix indicating how the segmental stiffness matrices are assembled into the global stiffness matrix. In damage identification, we conduct frequency-sweeping measurement of admittances within the frequency range of interest at *m* frequency points. Let the measurement frequency points, and the corresponding admittance changes be $\boldsymbol{\omega} = [\omega_1, ..., \omega_m]^T$ and $\Delta \mathbf{y}(\boldsymbol{\omega}) = [\Delta y(\omega_1), ..., \Delta y(\omega_m)]^T$, respectively. The damage index vector is denoted as $\boldsymbol{\alpha} = [\alpha_1, ..., \alpha_n]^T$. Collecting all the measurement information, we obtain the following relation,

$$\Delta \mathbf{y}_{m\times 1} = \begin{bmatrix} \Delta y(\omega_1) \\ ... \\ \Delta y(\omega_m) \end{bmatrix} = \mathbf{S}_{m\times n} \boldsymbol{\alpha}_{n\times 1} \tag{5.5}$$

where $\mathbf{S}$ is referred to as the sensitivity matrix coming from Equation (5.4). In actual practice, model updating is usually conducted first to ensure that the finite element model matches well with the healthy structure. Subsequently, in damage identification throughout the structure's lifespan, admittance measurements are collected periodically to inversely identify damage location and severity expressed as $\boldsymbol{\alpha}$.

### 5.2.2. Casting damage identification into parametric optimization

It is worth emphasizing that, while the damage index vector $\boldsymbol{\alpha}$ and the admittance change vector is related directly as shown in Equation (5.5), this equation for solving for the damage index vector is generally under-determined. In the admittance versus frequency curve, the peaks correspond to structural resonances. Structural damage manifests itself only in the vicinity of the resonant peaks in the admittance measurements, which means the information for damage inference is limited. Although one can increase the number of sweeping frequency points of admittance measurement, there is no guarantee that the additional measurement would lead to linearly independent information. In other words, simply increasing the number of measurement points does not necessarily increase the row rank of the sensitivity matrix **S**. This issue is especially relevant for admittance measurements at high-frequency range. To achieve high-precision identification of small size damage, the finite element mesh density is high, and the segment size for characterizing potential damage is usually chosen to be small, leading to large number of segments, *n*.

Aiming at tackling this issue, in this research we cast the inverse identification into a multi-objective optimization formulation. One objective is obvious, i.e., we need to minimize the difference between the measured admittance change, $\Delta\mathbf{y}$, and the model prediction in damage parametric space, $\mathbf{S}\boldsymbol{\alpha}$. In practical situations, damage usually occurs within a small region of the structure, especially when the damage is at its beginning stage with small size. Therefore, we introduce another objective function that the damage index vector $\boldsymbol{\alpha}$ is sparse with small $l_0$ norm. The optimization problem then takes the following form with two objective functions, i.e.,

$$\text{Find: } \boldsymbol{\alpha} \in \mathbf{E}^n \text{, } \alpha_l \le \alpha_i \le \alpha_u \text{, } i = 1,\ldots,n$$

$$\text{Minimize: } f_1 = \left\| \Delta\mathbf{y} - \mathbf{S}\boldsymbol{\alpha} \right\|_2 \tag{5.6a}$$

$$\text{Minimize: } f_2 = \left\| \boldsymbol{\alpha} \right\|_0 \tag{5.6b}$$

where $\|\cdot\|_2$ and $\|\cdot\|_0$ denote, respectively, the $l_2$ norm and the $l_0$ norm. $\alpha_u$ and $\alpha_l$ represent the upper and lower bounds of $\alpha_i$ respectively. Here, $\alpha_l = 0$ indicates a healthy state, while $\alpha_u = 1$ represents a fully damaged state. In this research we use the $l_0$ norm to achieve true sparsity since it directly penalizes the number of non-zero components. As we cast the problem into the above multi-objective optimization, we avoid the difficulty in selecting weightings needed for single-objective optimization, and as illustrated in the subsequent section we can indeed solve for sparse damage index vector directly though minimizing the $l_0$ norm. Another major advantage of casting the inverse identification into a multi-objective optimization is that such a formulation naturally yields multiple solutions, which fits the nature of diagnosis and SHM. These multiple solutions correspond to possible damage scenarios that can be further assessed through additional measurements or empirical observations.

Addressing the structural damage identification problem directly through the aforementioned multi-objective optimization framework, however, presents significant challenges, primarily due to its non-convex nature and the combinatorial complexity from the sparsity requirement in the damage index vector $\boldsymbol{\alpha}$. To mitigate these, we propose a two-phase optimization strategy that initially employs Group Lasso (Dimopoulos et al, 2022; Zhang et al, 2022b) for a coarse damage localization followed by a focused optimization on identified regions. Group Lasso, an extension of Lasso for grouped variables, enables us to incorporate domain knowledge by dividing $\boldsymbol{\alpha}$ into groups, facilitating structured regularization. The domain knowledge is that the damage occurrence usually shows sparse features. This approach not only aids in variable selection across grouped predictors but also significantly reduces the dimensionality of the problem by identifying key groups likely to exhibit damage.

## 5.3. Group-wise Sparse Damage Detection Followed by Refined Identification

In the process of structural damage identification, damage usually occurs only in small, localized regions, whereas the majority of the structural segments remain intact or in the healthy state. This localized nature of damage suggests that, if the segments of the structure are divided into groups, there might be groups where all the segments are undamaged. This suggests that we may first attempt to determine which group contains damage. With this preliminary information, we may then use the optimization model established in the previous section for a targeted approach to damage identification. The key difference at this stage is that the damage index matrix within the optimization model will need to focus only on the segments within the specific group identified, rather than scanning the entire structure. This targeted approach significantly reduces the complexity and difficulty of the optimization. Group Lasso fits perfectly with this strategy (Dimopoulos et al, 2022; Zhang et al, 2022b). It provides a pathway that enables the incorporation of group-wise considerations into the regularization process. Incorporating Group Lasso into the context of structural damage identification, we utilize the formulation:

$$\text{Find: } \boldsymbol{\alpha} \in \mathbf{E}^n,\ \alpha_l \le \alpha_i \le \alpha_u,\ i = 1,\ldots,n$$

$$\text{Minimize: } f_1 = \left\| \Delta\mathbf{y} - \mathbf{S}\boldsymbol{\alpha} \right\|_2 \tag{5.7a}$$

$$\text{Minimize: } f_2 = \sum_{g=1}^{G} \sqrt{p_G} \left\| \boldsymbol{\alpha}_{G_g} \right\|_2 \tag{5.7b}$$

For objective $f_1$, the goal is to minimize the admittance change differences between experiment and model prediction, which remains to be the same as Equation (5.6a). In objective $f_2$, the vector $\boldsymbol{\alpha}$ is partitioned into *G* groups, with $p_G$ indicating the size of each group. Based on the principle of Group Lasso, we apply a penalty that is proportional to the $l_2$ norm of the coefficients within each group and then sum these norms with an $l_1$ penalty across groups. This method allows us to enforce sparsity at the group level, effectively detecting which group the damage falls into. Since the group-wise sparse damage detection is still formulated with a bi-objective optimization, multiple solutions will be generated. Therefore, selecting one solution to inform the second step for further refined damage identification becomes a key step, the details of which are presented below.

### 5.3.1. Message passing

In this research, the technique TOPSIS (Greco et al, 2016) is adopted to yield a trade-off choice out of Pareto optimal points because it is efficient in distilling complex optimization outcomes. Meanwhile, the information entropy is employed to derive the weights of the evaluation criteria in this study. The procedure of the combined entropy weight and TOPSIS method is described as follows (Table 5-1).

**Table 5-1.** Algorithm: Message Passing.

| **Algorithm:** Message Passing | |
|---|---|
| 1 | Generate an initial decision matrix $X$ using the values of *m* alternatives and *n* criteria. Here in this study, the number *n* is 2, corresponding to the two objective values and *m* is the number of optimal solutions in the Pareto front solved by the optimizer.<br>$X = [x_{ij}]_{m\times n}$ |
| 2 | Generate the normalization decision matrix *P*. To make the different criteria comparable, the values should be normalized, i.e.,<br>$P = [p_{ij}]_{m\times n} = [\frac{x_{ij}}{\sum_{i=1}^{m} x_{ij}}]_{m\times n}, \quad j = 1,...,n$ |
| 3 | Calculate the entropy weight $\omega_j$ for the *j*th criterion, satisfying $\sum_{j=1}^{n}\omega_j = 1$:<br>$e_j = -\frac{1}{\ln(m)}\sum_{i=1}^{m} p_{ij}\ln(p_{ij}), \quad i\in[1,...,m], j\in[1,...,n]$, $\omega_j = \frac{d_j}{\sum_{j=1}^{n} d_j} = \frac{1-e_j}{\sum_{j=1}^{n}(1-e_j)}, \quad j\in[1,...,n]$<br>where $d_j$ denotes the degree of the diversity of the information, and the amount of decision information is firstly measured by the entropy values $e_j$. |
| 4 | Calculate the weighted normalized decision matrix *T*.<br>$T = [t_{ij}] = [p_{ij}\times\omega_j]_{m\times n}$ |

| | |
|---|---|
| | where, $\omega_j$ is also the normalized weight, i.e., $\omega_j = W_j \Big/ \sum_{j=1}^{n} W_j$ , and $W_j$ is the original weight given to indicator. |
| 5 | Identify the worst alternative $A_\omega$ and the best alternative $A_b$ as follows:<br>$A_\omega = \{(\max(t_{ij})\forall J^-,(\min(t_{ij})\forall J^+)\} \equiv t_{\omega j}, \quad A_b = \{(\min(t_{ij})\forall J^-,(\max(t_{ij})\forall J^+)\} \equiv t_{bj}$<br>where $J^+$ denotes the criteria having a positive impact, and $J^-$ denotes the criteria having a negative impact. |
| 6 | Calculating the distance between the target alternative and the worst, and the best condition, respectively<br>$d_{i\omega} = \sqrt{\sum_{j=1}^{n} (t_{ij} - t_{\omega j})^2}$ , $d_{ib} = \sqrt{\sum_{j=1}^{n} (t_{ij} - t_{bj})^2}$<br>where $d_{i\omega}$ and $d_{ib}$ are norm distances from the target alternative to the worst and best conditions, respectively. |
| 7 | Calculate the similarity to the worst conditions:<br>$S_{i\omega} = \frac{d_{i\omega}}{d_{i\omega} + d_{ib}}, \quad 0 \le S_{i\omega} \le 1$<br>If $S_{i\omega} = 1$ the optimal alternative solution has the best condition; if $S_{i\omega} = 0$, the optimal alternative solution has the worst condition. |
| 8 | Rank the alternative solutions by the values of $S_{i\omega}$. |

In the initial phase, we employ a multi-objective optimization approach, which results in a set of optimal solutions. Typically, the TOPSIS can be utilized to select a solution ranked as 1 for information transferred to the subsequent step. However, due to our adoption of a stochastic optimization algorithm, which will be elaborated on later, the information from a single solution might contain randomness. The information transmitted from the first to the second phase, on the other hand, is crucial; any miscommunication can lead to a failure in identifying the correct damage subsequently. This study adopts a more reliable strategy: 1) Since multi-objective optimization generates multiple solutions along the Pareto front, we start by applying TOPSIS to rank these solutions. 2) Selecting only a single top-ranked solution from the Pareto front could introduce randomness due to the stochastic nature of the algorithm. To mitigate this, we choose the top 20 ranked solutions using TOPSIS. 3) We then conduct statistical analysis on these solutions to determine the frequency with which damage is identified in each group. 4) The algorithm is independently run 10 times, with the same analysis from steps 1 to 3 repeated in each run. This repeated analysis over multiple solutions and iterations helps to reduce random errors, thereby enhancing the reliability of the information used in the second phase of the study.

### 5.3.2. A dual-resolution approach for damage identification

The two-stage optimization method for structural damage detection and localization using experimental measurements and model predictions proposed in this research is outlined in Figure 5-1. The first stage, depicted at the top half of the diagram, is focused on damage detection. It comprises two objectives: the first, Obj 11, is the minimization of the differences between the experimental measurements and the model predictions, represented mathematically as $f_1 = \left\|\Delta\mathbf{y} - \mathbf{S}\boldsymbol{\alpha}\right\|_2$. The second, Obj 12, employs the Group Lasso technique for sparsity enhancement, denoted as $f_2 = \sum_{g=1}^{G} \sqrt{p_G} \left\|\boldsymbol{\alpha}_{G_g}\right\|_2$, which promotes the group sparsity in the parameters by regularization. This is the optimization model in Equation (5.7). The bottom half of Figure 5-1 describes the second stage, which is concerned with damage localization. Similar to the first stage, it includes the minimization of differences between measurements and predictions (Obj 21). The second objective of this stage, Obj 22, seeks to minimize sparsity, specifically reducing the dimensionality of the problem by enforcing that elements of the damage index vector $\boldsymbol{\alpha}$ are zero for all components belonging to the sparse set $G_{\text{sparse}}$, which is formulated as $f_2 = \|\boldsymbol{\alpha}\|_0$, emphasizing the localization of the damage to specific segments of the structure. This is the optimization model shown in Equation (5.6).

This proposed method aims to efficiently identify and localize damage by integrating experimental data with model-based predictions, leveraging optimization techniques to process the sparse nature of structural damages. The process is cyclic, as indicated by the arrows, suggesting iterative refinement between the stages to enhance the accuracy of damage detection and localization.

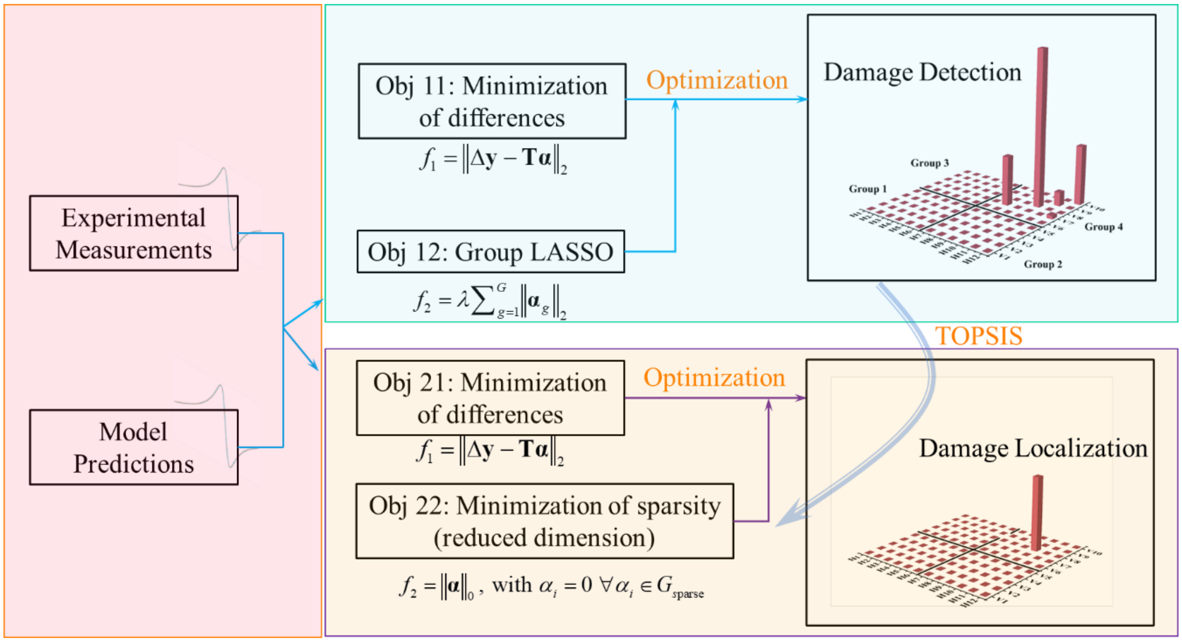

**Figure 5-1.** Flowchart of proposed two-stage damage identification framework.

### 5.3.3. Learning Automata guided swarm optimizer

Addressing the optimization model for pinpointing the exact location and severity of damage presents a significant computational challenge. We aim for a diverse range of solutions to encapsulate the actual damage scenarios while ensuring the solution set remains compact for actionable decision-making insights. Our research utilizes MOPSO for its simplicity, computational efficiency, and small number of control parameters (Kennedy and Eberhart, 1995; Soman, 2024). Building on the recent advancements that integrate LA with single-objective PSO to enhance precision and convergence (Chakraborty et al, 2021), we apply LA strategies to MOPSO, refining our approach to inverse analysis for damage identification.

### 5.3.3.1. 3.3.1 Basics of particle swarm optimization

PSO is an evolutionary algorithm inspired by the behavior of swarms, introduced by Kennedy and Eberhart (1995) and later expanded to multi-objective optimization by Coello et al (2004). As a metaheuristic based on a population, PSO initiates with a randomly generated set of potential solutions, termed particles that navigate a multidimensional search space. The particle moves through a *D* dimensional space as follows,

$$v_i(t+1) = zv_i(t) + c_1r_1(p_{\mathrm{best}i}(t) - x_i(t)) + c_2r_2(g_{\mathrm{best}}(t) - x_i(t)) \tag{5.8a}$$

$$x_i(t+1) = x_i(t) + v_i(t+1) \tag{5.8b}$$

where $x_i(t)$ and $v_i(t)$ represent, respectively, the position and velocity of the $i^{\mathrm{th}}$ particle in the $t^{\mathrm{th}}$ iteration. $p_{\mathrm{best}}$ is the best position visited by particle *i* till the current $t^{\mathrm{th}}$ iteration, and $g_{\mathrm{best}}$ is the global best position amongst all the positions visited by all the particles. *z* is the inertia weight that reflects the tendency of the particles to maintain their previous speed. $c_1$ and $c_2$ are acceleration coefficients. $c_1$ regulates how much the particle trusts its own experience, and $c_2$ represents the trend of particles approaching the best position of the entire swarm. $r_1$ and $r_2$ are two random numbers chosen from uniform distribution over the range (0, 1). In each iteration, each particle’s velocity or position are constrained by the boundary conditions since the particles may exceed the allowed search space and produce invalid solution.

### 5.3.3.2. Learning automata guided search

LA can be conceptualized as abstract decision-making units operating within a stochastic environment to identify optimal actions through iterative interactions. As per Hashemi and Meybodi (2011) and Zhang et al (2020), an automaton is characterized by a limited set of potential actions, each selected according to a predefined probability distribution. The feedback of environment to the selected action serves as a reinforcement signal for the automaton's learning algorithm, which in turn adjusts the action probability distribution. Through repeated cycles of this process, the automaton progressively favors actions that elicit positive environmental feedback.

Mathematically, LA is defined by a quadruple ($a$, $\beta$, $p$, $T$), where $a = (a_1,...,a_r)$ is a set of actions, $\beta = (\beta_1,...,\beta_r)$ is a set of inputs, $p = (p_1,...,p_r)$ is a probability vector that dictates action selection, and $T$ is the learning algorithm used to update $p$. The learning algorithm $T$ is a crucial in affecting the performance of LA. The linear reward-penalty algorithm ($L_{rp}$) is one of the commonly employed learning algorithms presented in literature (Hashemi and Meybodi, 2011). The learning model $T$ for $L_{rp}$ scheme to update the state probability vector $p$ after receiving the reinforcement signal $\beta$ is given as follows,

$$p_j(k+1) = \begin{cases} p_j(k) + c(1 - p_j(k)) & \text{if } i = j \\ p_j(k)(1 - c) & \text{if } i \neq j \end{cases} \tag{5.9a}$$

$$p_j(k+1) = \begin{cases} p_j(k)(1 - b) & \text{if } i = j \\ \dfrac{b}{r-1} + p_j(k)(1 - b) & \text{if } i \neq j \end{cases} \tag{5.9b}$$

where $r$ is the number of actions defined in the automaton; parameters $c$ and $b$ represent reward and penalty step length, respectively. Equation (5.9a) corresponding to the case when $\beta = 0$ (favorable response), and Equation (5.9b) corresponds to the case when $\beta = 1$ (unfavorable response). $a_i$ is thus the action chosen at time $t$ as using the distribution $p(t)$. Figure 5-2 illustrates how the LA interacts with the environment. At each step, an action $a_i$ is selected based on its associated probability $p_i$, and this action is applied to the environment. The environment then provides a feedback signal $\beta$ in response to the action. Based on this feedback, the probability $p_i$ is updated. This process continues iteratively until the search process is terminated.

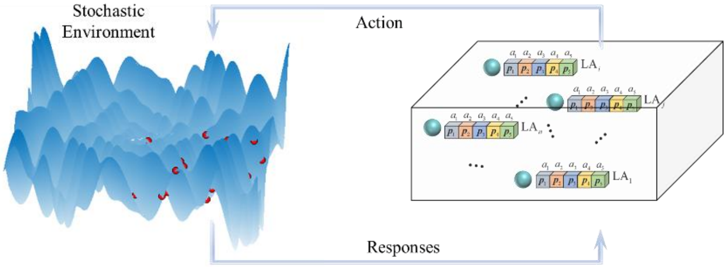

**Figure 5-2.** Illustration of learning automata scheme. Action corresponds to $a$. Stochastic environment means searching space. Response corresponds to $\beta$.

### 5.3.3.3. 3.3.3 Action repository for exploration-exploitation balance

Exploration and exploitation are critical strategies for the advancement of evolutionary algorithms in optimizing solutions or achieving convergence, as noted by Črepinšek et al (2013) and Ding et al (2023). Exploration examines new search space areas, while exploitation conducts an in-depth search near previously explored areas, leading to a conflict between these approaches. Excessive exploration can slow convergence, while excessive exploitation may trap the algorithm in local minima. This issue intensifies in structural damage identification due to high dimensionality and the presence of many local extremes in the multi-modal objective function. To navigate this, we introduce five local search strategies based on MOPSO to balance exploration and exploitation, aimed at promoting particle movement around local extremes and expanding the search for diverse solutions. These strategies, which include two based on coefficient variation and three on mutation, form a repository for particle selection in each iteration, named Time Varying Inertia Weight (TVIW), Time-Varying Acceleration Coefficients (TVAC), Elitist-based Perturbation (EBP), Mutation, and Fine Tuning.

*TVIW*, proposed by Shi and Eberhart (1999), facilitates initial exploration followed by subsequent exploitation. This can be expressed as $z^t = z_{\max} - t(z_{\max} - z_{\min})/t_{\max}$, where $t_{\max}$ is the maximum number of iterations, $t$ is the current iteration, and $z_{\min}$ and $z_{\max}$ are the initial and final values of the inertia weight. Here $z_{\max} = 0.9$ and $z_{\min} = 0.4$ are recommended (Kennedy and Eberhart, 1995). *TVAC*, introduced by Ratnaweera et al (2004), aims to improve early-stage global search capabilities and later-stage convergence to the global optima. This enhancement involves adjustments to the acceleration coefficients $c_1$ and $c_2$ in the following manner, $c_1^t = c_1^{\max} - (c_1^{\max} - c_1^{\min}) t/t_{\max}$ , $c_2^t = c_2^{\max} + (c_2^{\max} - c_2^{\min}) t/t_{\max}$ . Here, $c_1^{\min}$ , $c_2^{\min}$ are the initial values of $c_1$, $c_2$; $c_1^{\max}$ and $c_2^{\max}$ are the final values of the $c_1$ and $c_2$, respectively. *TVAC* modifies the cognitive and social components by reducing $c_1$ and increasing $c_2$ over iterations, balancing social and cognitive experiences to prevent premature convergence of the algorithm.

To address premature convergence in particle swarm optimization, the *EBP* strategy is utilized, enhancing diversity by altering a randomly chosen dimension of the particle's personal best, which aids in avoiding local optima. The modification is made by adding a probabilistic sign to $tempP_{\mathrm{best}i,d} = P_{\mathrm{best}i,d} \pm r_d \cdot (l_{\mathrm{upper},d} - l_{\mathrm{lower},d})$ , taking positive value for random numbers greater than 0.5, and negative otherwise. Here, $P_{\mathrm{best}i,d}$ represents the *d*-th dimension of the personal best of the *i*-th population. $r_d$ is from a normal distribution $N \sim (\mu, R^2)$ with zero mean and standard deviation $R = R_{\max} - (R_{\max} - R_{\min}) \cdot t/t_{\max}$ . Here the maximum and minimum perturbation ranges are taken as $R_{\max} = 1$ and $R_{\min} = 0.1$, as suggested in literature (Lim and Isa, 2013). $l_{\mathrm{upper},d}$ and $l_{\mathrm{lower},d}$ represent the upper and lower bounds for the *d*-th dimension of the *i*-th population, respectively. Concurrently, the *Mutation* action is applied to the global best $g_{\mathrm{best}}$ , utilizing a similar random perturbation to enhance local exploration with the aim of identifying a more advantageous position. The perturbation is based on the same normal distribution used in the *EBP* strategy, $tempg_{\mathrm{best}i,d} = g_{\mathrm{best}i,d} \pm r_d \cdot (l_{\mathrm{upper},d} - l_{\mathrm{lower},d})$ with extensive searching at the start of the algorithm and a more refined search towards the end. In the *Fine Tuning* process, attention is given to each dimension of the personal best by adjusting its velocity. This means particles are expected to move more (positive) towards direction favorable to improve the solution and more slowly (negative) in less beneficial directions: $tempP_{\mathrm{best}i,d} = P_{\mathrm{best}i,d} \pm v_{i,d}$ (Ji et al, 2007; Samma et al, 2016).

Whenever the action is selected and executed, the newly generated solution will be compared to the old one using the non-dominated sorting algorithm, as shown in Equation (5.10) ($\prec$ means dominates and $\sim\prec$ means non-dominated), and the immediate reinforcement signal (0 or 1) will be assigned as

$$\text{if } x_{\text{new}} \prec x_{\text{old}},\ x_{\text{old}} = x_{\text{new}},\ \text{favorable: } \beta{=}0 \tag{5.10a}$$

$$\text{if } x_{\text{new}} \sim\prec x_{\text{old}},\ x_{\text{old}} = x_{\text{old}},\ \text{unfavorable: } \beta{=}1 \tag{5.10b}$$

If the new solution is better than (dominates) the old one, it will replace the old solution and the action that produced it will receive a positive signal. Otherwise, the old solution stays, and the action gets a negative signal. The signal received from environment will be passed into Equation (5.9) to update the probability for the current action selected and executed.

## 5.4. Structural Damage Identification Case Study and Discussion

As outlined in Section 5.2, the piezoelectric admittance-based damage identification is cast into a multi-objective optimization problem. The primary challenge lies in handling such a high-dimensional, multi-modal optimization problem to find a small, yet diverse solution set that can accurately capture the true damage scenarios. To address this, we propose a hierarchical method that mitigates the NP-hard complexity by breaking down the problem into more manageable parts. In the first stage, a coarse damage detection phase identifies potential regions of damage. In the second stage, a detailed assessment phase concentrates on the smaller subset identified in the first stage. This reduction in the number of variables simplifies the combinatorial problem, making it more tractable. In this section, we conduct case studies to examine the proposed algorithm improvements using experimentally acquired piezoelectric admittance measurements.

### 5.4.1. Experimental setup and data acquisition

One significant advantage of piezoelectric impedance/admittance based active interrogation is its simplicity in implementation. Shown in Figure 5-3 is the experimental setup, in which a piezoelectric transducer is bonded to the top surface of a plate using epoxy resin. The plate is hung with 4 thin strings at its corners to emulate the free-free boundary condition. The transducer is connected in series to a resistor (165 Ohm) to facilitate measurement. A Dynamic Signal Analyzer (Agilent 35670A) is employed for applying actuation voltage and measuring the sensing information. Specifically, frequency-sweeping harmonic voltage is applied to the transducer for actuation. Subsequently, the current flowing through the piezoelectric circuit can be obtained by measuring the voltage drop across the resistor. Thus the piezoelectric admittance can be obtained as $Y(\omega) = V_{\text{out}} \big/ RV_{\text{in}}$ where $V_{\text{out}}$ denotes the amplitude of voltage measured across the resistor, and $V_{\text{in}}$ indicates the amplitude of the input/actuation voltage. Here 5 Volts (Vpk) harmonic voltage is applied to the transducer with good signal-to-noise ratio in measurement. For each excitation frequency, 25 cycles are used to reduce the noise effect.

Recall Equation (5.3) that relates structural damage with admittance measurement. In general, the damage effect to admittance measurement is most prominent around the structural resonant frequencies. In this investigation, without loss of generality, we acquire admittance measurements around within two frequency ranges, 3,150 Hz to 3,230 Hz (which covers the 28th natural frequency at 3,194.95 Hz) and 3,650 Hz to 3.730 Hz (which covers the 31st natural frequency at 3,705.8 Hz). In each frequency range we collect admittance measurements at 401 evenly distributed frequency points. Figure 5-4 displays the experimentally acquired admittance curves of the healthy plate structure as baseline. In order to maintain measurement consistency, all data acquisitions are conducted at room temperature of 20ºC with fluctuations within 0.2ºC.

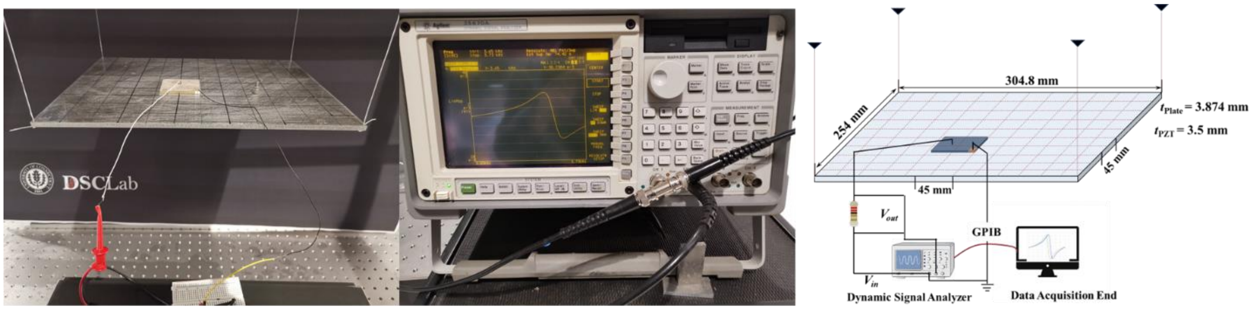

(a) (b)

**Figure 5-3.** Experimental setup (a) testbed; (b) data acquisition.

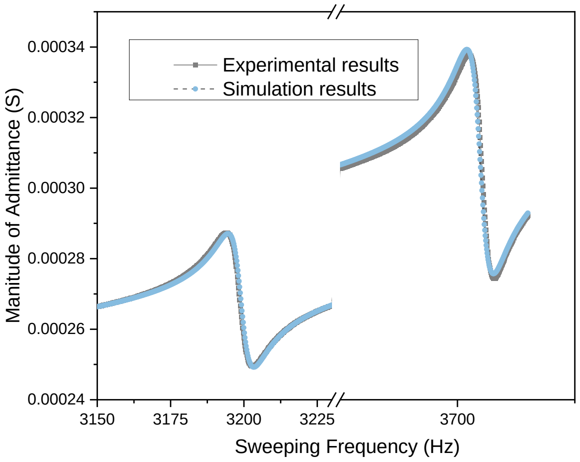

**Figure 5-4.** Admittance curves from experiment and from finite element analysis after model updating.

### 5.4.2. Finite element modeling and model updating

The geometry parameters of the plate and the piezoelectric transducer are shown in Figure 5-3. The plate is made of aluminum alloy with Young's modulus $E_{\mathrm{plate}} = 73\ \mathrm{GPa}$ , mass density $\rho_{\mathrm{plate}} = 2769\ \mathrm{kg}\cdot\mathrm{m}^{-3}$ and Poisson's ratio 0.3. The piezoelectric transducer used is type SM411 supplied by Steiner & Martins, Inc. The nominal material properties of SM411 supplied by the vendor are: Young's moduli $E_{11} = 74\ \mathrm{GPa}$ and $E_{33} = 54\ \mathrm{GPa}$ , mass density $\rho_{\mathrm{PZT}} = 7800\ \mathrm{kg}\cdot\mathrm{m}^{-3}$ , and piezoelectric constants $g_{31} = -10.4\times10^{-3}\ \mathrm{m}^2/\mathrm{C}$ , $g_{33} = 24.2\times10^{-3}\ \mathrm{m}^2/\mathrm{C}$ and $d_{31} = -210\times10^{3}\ \mathrm{m/V}$ . A finite element model is established using an in-house MATLAB code that is verified with ANSYS. The plate and transducer are discretized using 20-node solid elements. The mesh density of 13,766 elements and 290,577 DOFs is determined after convergence analysis in terms of natural frequencies up to 5830.8 Hz, i.e., the 46th natural frequency. The mass and stiffness matrices obtained are then employed in Equation (5.2) to compute the admittance under the healthy condition. The resistance value is 165 Ohm, consistent with the experimental setup. The frequency sweeping points are the same as those used in the experiment. In other words, the numerical simulation matches with the experimental condition exactly, serving as the digital twin of the piezoelectric admittance interrogation.

There is an inevitable discrepancy between experiment and numerical simulation. It is well known that piezoelectric material properties are subject to uncertainties and variances. Additionally, the free-free boundary condition realized with hanging strings is an idealization. Thus, finite element model updating is conducted, aiming at matching the numerical simulation with experimental results by properly adjusting related material constants including the piezoelectric properties and the plate Young's modulus. We formulate a PSO based single objective optimization to minimize the difference between the experimental admittance curve and its numerical counterpart, and obtain the following updated material properties: $E_{\text{plate}} = 72.21 \text{ GPa}$ , $E_{11} = 81.4 \text{ GPa}$ , and $g_{31} = -6.97 \times 10^{-3} \ \text{m}^2/\text{C}$ . The updated admittance curves from finite element analysis are plotted in Figure 5-4, showing excellent matching with respect to the experimental results.

### 5.4.3. Damage identification case setup employing the proposed hierarchical framework

In this subsection we present case studies of piezoelectric admittance-based damage identification employing the proposed two-stage framework solved by improved LAMOPSO optimizer. In order to localize damage, the plate structure being monitored is divided into 120 (12 lengthwise, and 10 widthwise) segments. Damage identification is facilitated through identifying the stiffness reduction at specific damaged segment(s). Therefore, the damage index vector $\boldsymbol{\alpha} = [\alpha_1, ..., \alpha_n]^T$ defined in Section 5.2.1 has 120 unknowns. To ensure the repeatability and to avoid the alteration of boundary conditions, the structural damage is emulated by applying small mass blocks at various locations of the plate. This will induce equivalently the admittance change due to stiffness reduction. For a specific mass block added, the equivalent stiffness reduction is calculated by matching the admittance curve of added mass with that of stiffness reduction. For example, a mass block of 0.6g added to the 75th segment is equivalent to 11.0% stiffness reduction in this segment. Three experimental cases are designed as listed in Table 5-2, 11.0% stiffness reduction in the 75th segment (Case 1), 9.4% stiffness reduction in the 116th segment (Case 2), and 0.734% stiffness reduction in the 49th segment and 0.899% stiffness reduction in the 65th segment (Case 3).

In the first two cases, single damage occurs in different segments. In the third case, smaller stiffness reductions occur in multiple locations. To implement the proposed approach, we divide the damage index vector, consisting of 120 unknown variables, into 4 groups of 30 variables each. These groups are labeled Group A through Group D. Group A contains variables 1 to 30, Group B contains variables 31 to 60, and so on. To validate the effectiveness of the proposed method, we selected two other algorithms for comparison. These two algorithms are MMOPSO (Lin et al, 2015) and CMOQLMT (Ming et al, 2023), chosen for their direct relevance to the algorithm studied in this research. One is a variant of the PSO algorithm, and the other is an evolutionary algorithm reinforced through reinforcement learning.

It is worth emphasizing that the two-step optimization approach proposed aims to divide variables into smaller, more manageable groups so as to reduce the complexity of the optimization process. This addresses the combinatorial challenge of using the $l_0$ norm for damage localization. Especially in structures with many segments, the number of possible damage location combinations is substantial, leading to high computational costs that increase significantly for more complex structures. Therefore, in this study we focus on validating the effectiveness and robustness of this consecutive approach, ranging from coarse damage detection to fine damage identification, rather than directly comparing it to the one-step method.

**Table 5-2.** Damage case settings.

| Cases | Damage Location | Damage Severity |
|---|---|---|
| Case 1 | the 75th segment | 11% stiffness reduction |
| Case 2 | the 116th segment | 9.4% stiffness reduction |
| Case 3 | the 49th segment | 0.734% stiffness reduction |
|  | the 65th segment | 0.899% stiffness reduction |

### 5.4.4. Damage identification results and discussion

For Case 1, the results obtained using the dual damage identification approach are shown in Figure 5-5 and Figure 5-6. As described in Section 5.3.1, To eliminate random errors, we independently run the algorithm 10 times. For each run, the top 20 solutions are selected based on the TOPSIS ranking. A statistical analysis is then conducted on the resulting 200 solutions to determine which group the damage most frequently fall into, indicating the highest likelihood. The same approach and explanation are applied in the subsequent cases, so they will not be repeated further. The violin plot in Figure 5-5 displays the distribution of damage groups identified by different algorithms in the first phase. Figure 5-5(a) shows the group distribution obtained by the LAMOPSO algorithm. We can observe that in 10 runs, the damage mostly falls into Group C and Group D, with the average value of the Group C being higher than the other three groups. This indicates a higher likelihood of the damage falling into the Group C. Since we do not know the number of damages in actual engineering situations, there might be cases where multiple damages span across different groups. Therefore, in this study, we adopt a conservative strategy. That is, we use the information from the two groups with the highest likelihood and pass it on to the second phase. Similarly, Figure 5-5(b) and Figure 5-5(c) respectively show the group distribution identified by the CMOQLMT and MMOPSO algorithms. The damage identified by CMOQLMT is most likely to fall into the Group C. Since we adopt the strategy of using the two groups with high likelihood of damage occurrence, the information from Groups C and D will be passed on to the second phase. Interestingly, the damage identified by MMOPSO falls into Group D, with the next highest likelihood being the Group C. Due to the conservative strategy adopted in this study, information from Group C will also be passed on to the second phase. Otherwise, MMOPSO is not able to identify the actual damage under any circumstances.

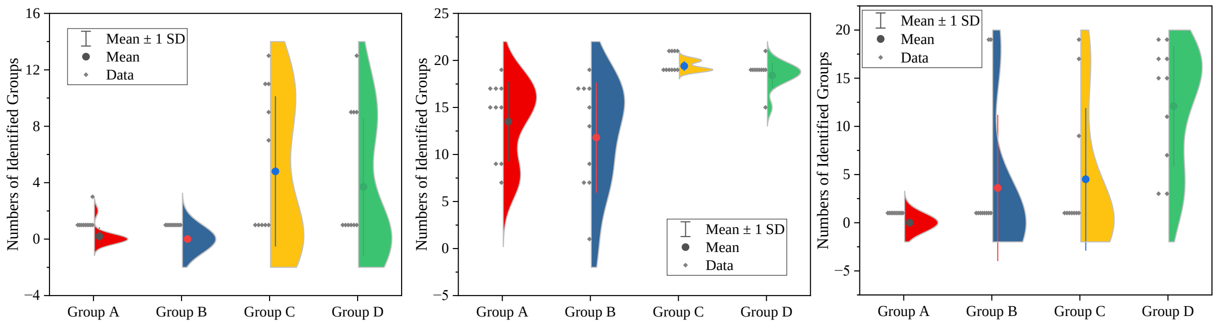

(a) (b) (c)

**Figure 5-5.** Group identification reliability analysis for Case 1, (a) LAMOPSO algorithm, (b) CMOQLMT algorithm and (c) MMOPSO algorithm.

Based on the information from the first phase, the number of variables to be identified in the second phase is reduced from 120 to 60. This reduction substantially alleviates the computational load during the optimization search. The results identified by different algorithms are shown in Figure 5-6. From the identified results, we have two direct observations: 1) Multiple solutions are obtained, which aligns with the nature of the under-determined problem of damage identification; 2) Each solution exhibits good sparsity. For Solution 1, all algorithms pinpoint the actual damage location, with the identified damage severities for LAMOPSO, CMOQLMT, and MMOPSO being 0.10275, 0.10827, and 0.10827, respectively. This is essentially consistent with the actual damage at the 75th segment with an 11% stiffness reduction. In the second solution, besides identifying the actual location, each algorithm also identifies an additional damage location. For LAMOPSO, the additional damage is at the 90th segment with a severity of 0.0168; for CMOQLMT, at the 88th segment with a severity of 0.0397; and for MMOPSO, at the 110th segment with a severity of 0.0594. Furthermore, only CMOQLMT and MMOPSO identifies a third solution. In Solution 3, these two algorithms not only identify the true damage location but also detect two additional damage locations: the 88th and 118th segments for MMOPSO; the 114th and 119th segments for CMOQLMT. Overall, all solutions from all three algorithms capture the true damage scenario. This indicates the proposed approach demonstrates validity in pinpointing damage with high precision. It should be noted, however, that the actual damage location is not known *a priori* in practical engineering scenarios. Therefore, subsequent decision-making or post-analysis techniques should be applied to examine all identified locations, leveraging the sparsity of the results to enhance the efficiency and predictive accuracy of inspections.

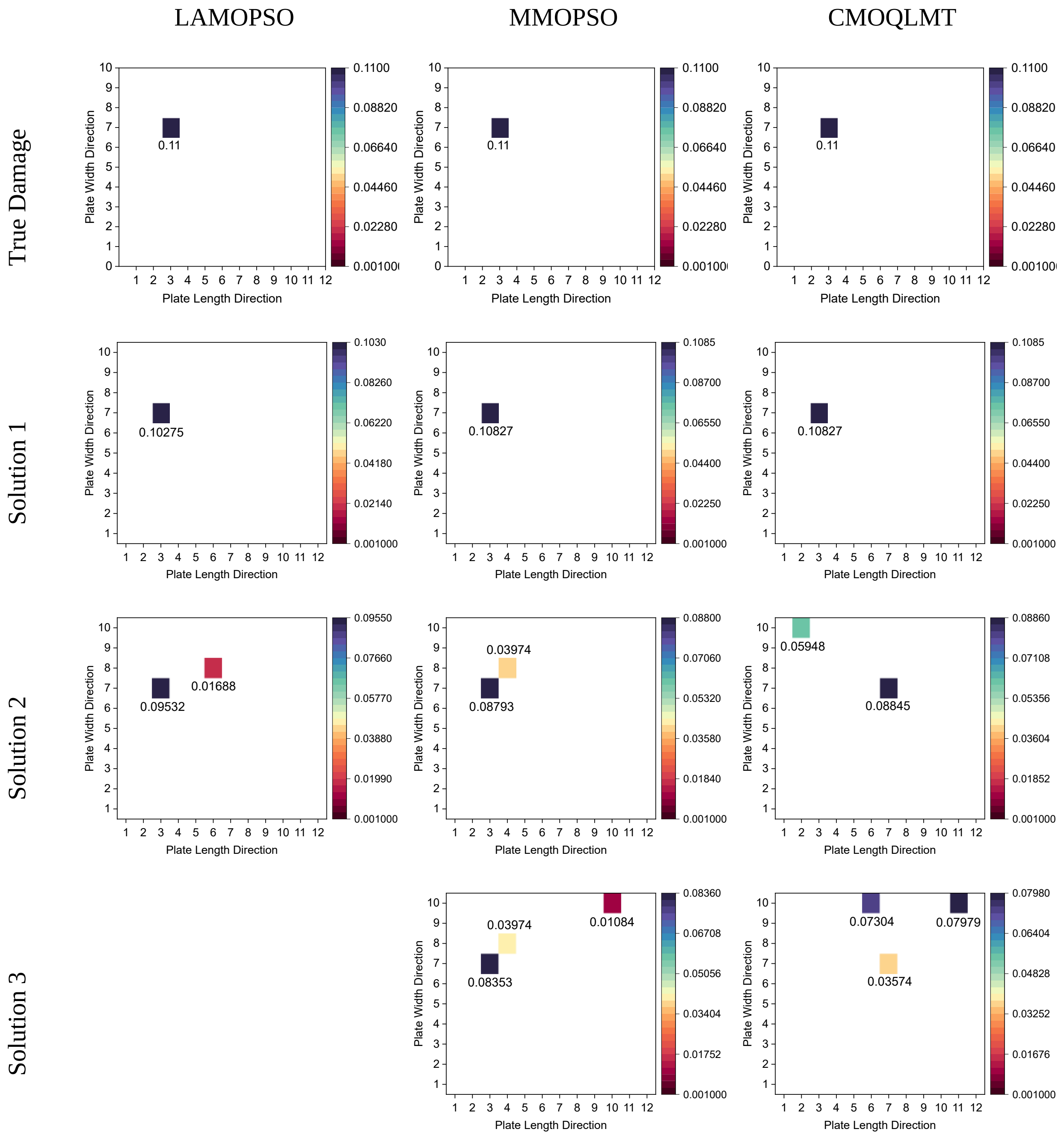

**Figure 5-6.** Multiple solutions from different algorithms for Case 1.

For Case 2, the actual damage is in Group D. The group distributions obtained by different algorithms are shown in Figure 5-7. Clearly, all three algorithms accurately point to Group D, where the actual damage is located. Given the strategy of passing information from the most likely two groups that the damage may fall into to the second phase, for the LAMOPSO algorithm, Groups A and D will be passed to the second phase; for both CMOQLMT and the MMOPSO algorithm, Groups C and D will be passed to the second phase. Therefore, the variables to be identified for Phase 2 becomes 60.

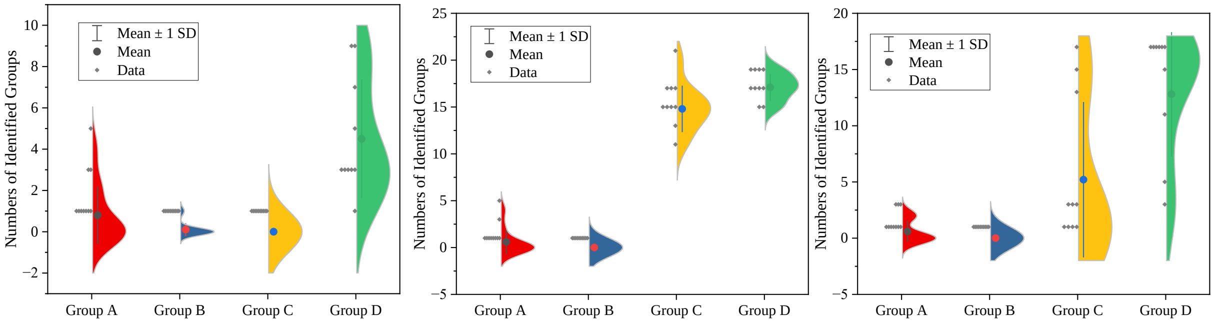

(a) (b) (c)

**Figure 5-7.** Group identification reliability analysis for Case 2, (a) LAMOPSO algorithm, (b) CMOQLMT algorithm and (c) MMOPSO algorithm.

Figure 5-8 shows the results identified by different algorithms for Case 2. Each algorithm produces three solutions with good sparsity. For the LAMOPSO algorithm, the first solution accurately identifies the actual damage location at the 116th segment, with a detected damage severity of 0.09921. In the second solution, an additional damage location is identified at the 106th segment, with a damage size of 1.361e-4, which can be considered negligible compared to the actual damage size. A similar observation is made for the third solution, where two additional locations are identified at the 106th and 111th segments, with damage severity of 1.387e-4 and 2.7126e-7, respectively, both of which are negligible. Therefore, the three solutions obtained by LAMOPSO are almost identical. For the CMOQLMT algorithm, the first solution accurately identifies the true damage scenario. The second solution identifies an additional damage location at the 79th segment with a severity of 0.0149. The third solution identifies two additional damage locations at the 79th and 87th segments, with damage severity of 0.0231 and 0.0293, respectively. Overall, the solutions from LAMOPSO are superior to those from CMOQLMT since the former identifies the additional locations with smaller severities. It is worth noting that the MMOPSO algorithm also identifies three solutions, but none of them can capture the actual damage location. This indicates that, even with reduced search dimensions, MMOPSO still falls into local optima.

For Case 3, the damage is located at the 49th and the 65th segments with 0.734% and 0.899% stiffness reductions, respectively. This case setup aims at examining the capability of the algorithms when damage occurs at multiple locations. In this case, to challenge the algorithms, the damage severities are designed to be quite small. The true damage scenario spans two groups, located in Groups B and C, respectively. Therefore, each algorithm can accurately pass information to the second phase only if it correctly identifies both groups. The first-phase group distributions obtained by the three algorithms are as shown in Figure 5-9. It is evident that apart from the proposed LAMOPSO algorithm, the other two algorithms do not accurately identify the correct groups. The CMOQLMT algorithm identifies the damage as falling into Group C, while MMOPSO identifies the damage as falling into Groups C and D. If we proceed with the information transfer as it stands, neither CMOQLMT nor MMOPSO would be able to identify the actual damage location in the second phase, regardless. To better compare and validate the performance of the proposed algorithm, we artificially chose Group B for CMOQLMT to additionally pass as information to the second phase. The information transfer for MMOPSO remains unchanged, i.e., Groups C and D. The results identified in the second phase are shown in Figure 5-10.

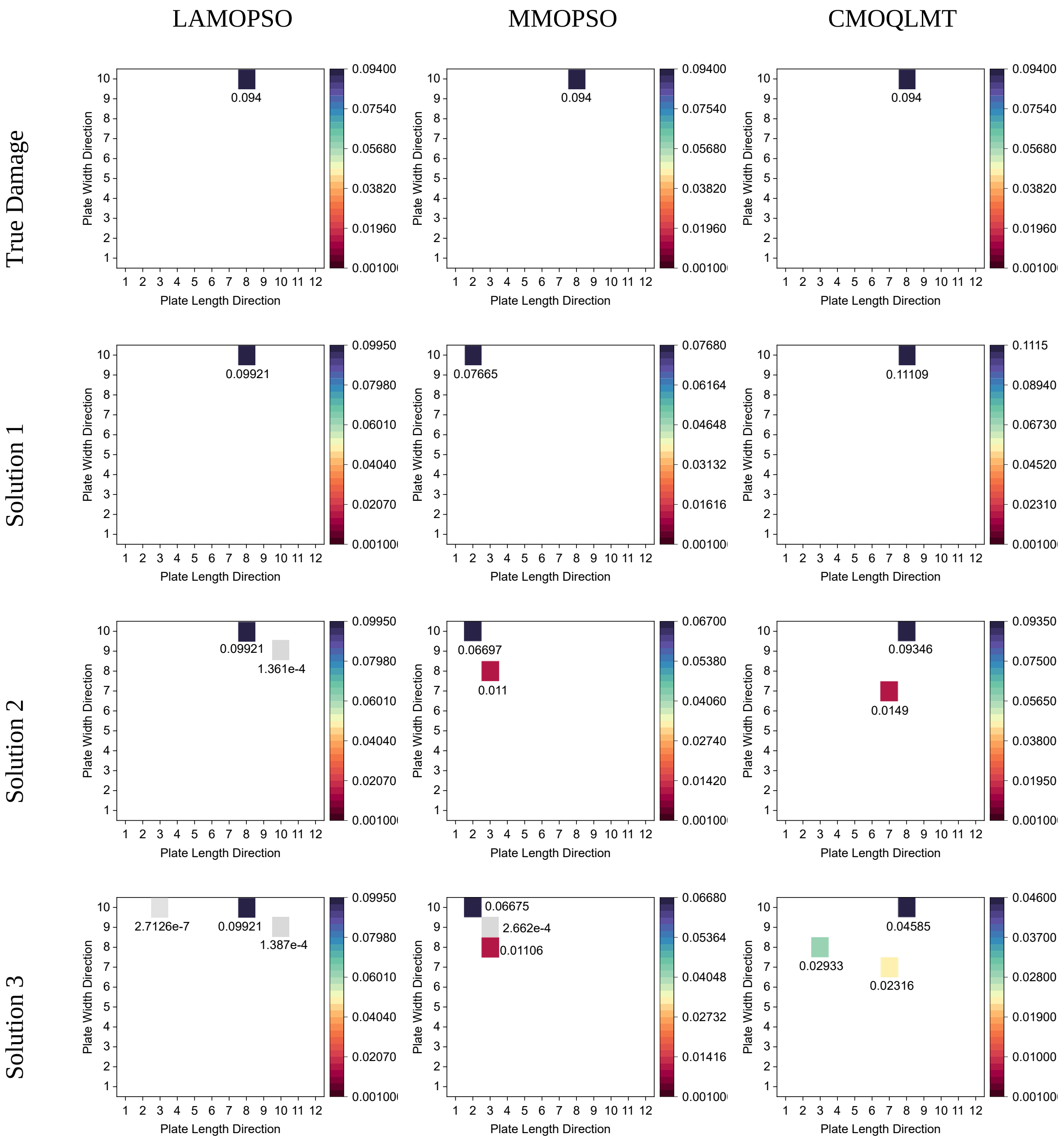

**Figure 5-8.** Multiple solutions from different algorithms for Case 2.

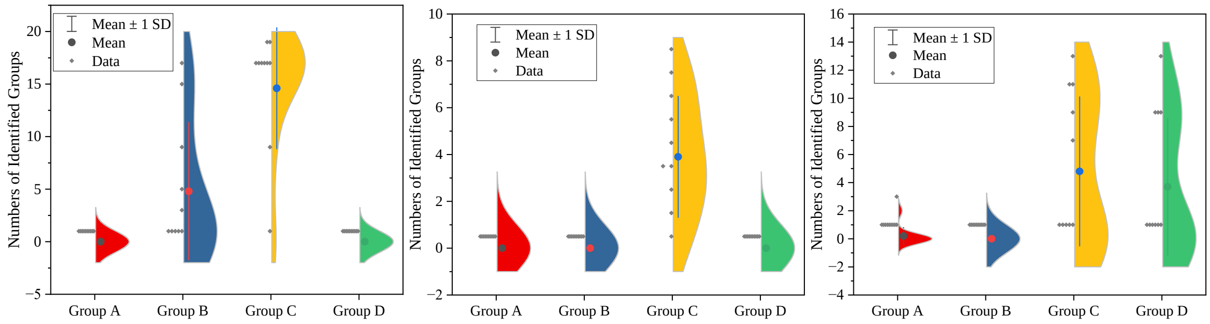

(a) (b) (c)

**Figure 5-9.** Group identification reliability analysis for Case 3, (a) LAMOPSO algorithm, (b) CMOQLMT algorithm and (c) MMOPSO algorithm.

Figure 5-10 displays the solutions identified by different algorithms for Case 3, with each algorithm identifying four solutions. Due to incorrect information passed from the first phase by the MMOPSO algorithm, none of the four solutions accurately captures the real damage scenario. For the proposed LAMOPSO algorithm, the first solution identifies only the first location of the actual damage. Identifying a single damage location is not surprising since the algorithm aims to satisfy the non-dominated sorting algorithm. In the second solution, LAMOPSO accurately identifies two damage locations, precisely indicating the situation of the actual damages. The third solution, besides identifying the actual damage, identifies a third additional location at the 90th segment with a severity of 0.00203. The fourth solution is similar to the third, except for an additional fourth identified damage location at the 56th segment, with a damage severity of 3.916e-6, which is negligible. Additionally, since we artificially choose the second group as the information to be passed for CMOQLMT, in the second phase, CMOQLMT produces four solutions, all of which also point to the actual damage locations. From Case 3, the conclusion is that reducing the dimensionality of the identification problem can indeed help algorithms accurately identify real damages. However, the setting of multiple damage cases poses a significant challenge to the algorithms, especially in the first phase. This makes enhancing the search capability of the algorithm particularly important, which is the aim of this study. In summary, the case study results employing experimental data fully demonstrate the efficacy of the proposed framework.

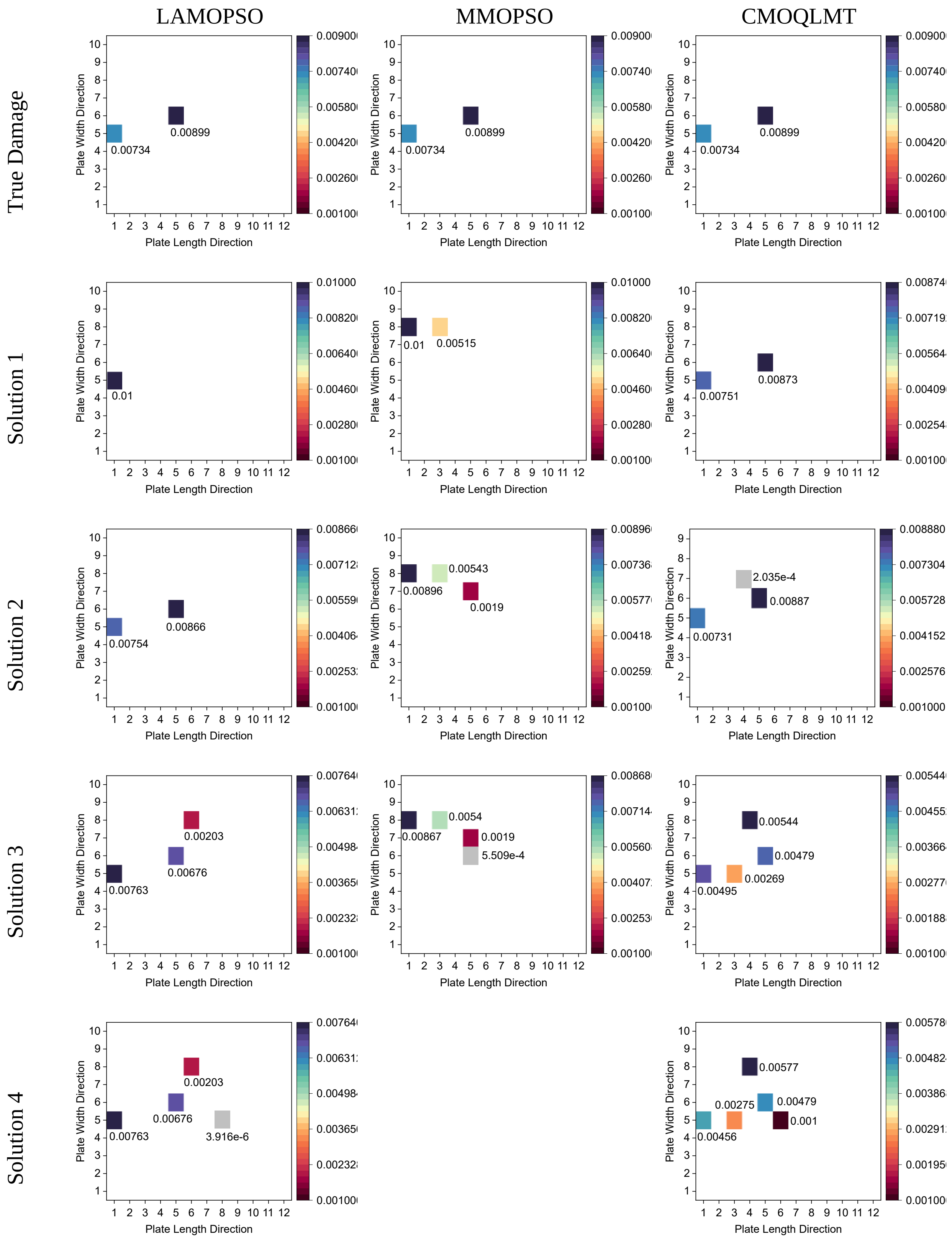

**Figure 5-10.** Multiple solutions from different algorithms for Case 3.

## 5.5. Conclusion

While structural damage detection using piezoelectric admittance has shown promising aspects, the inverse identification of damage location and severity remains to be a hurdle. This study addresses the intricate challenge of structural damage identification using piezoelectric admittance by formulating it as a multi-objective optimization problem. By leveraging the sparsity nature of the damage index and minimizing discrepancies between experimental and model predictions, we present an approach that enhances the efficiency while maintaining accuracy of damage identification processes. The introduction of five distinct local search strategies, tailored for the optimization process, marks an improvement in optimizing solution diversity and convergence accuracy. The employment of Learning Automata as a decision-making tool for strategy selection enables a self-adaptive optimization process that eschews the need for predetermined reward strategies. The introduction of a hierarchical framework that leverages Group Lasso and TOPSIS for effective inter-stage communication has refined the optimization process, as evidenced by the validation on a piezoelectric admittance sensing testbed. Different case studies are designed to examine the capability of the proposed approaches including hierarchical framework and optimizer to identify the true damage scenario using experimental data indicates. The results obtained indicate that the proposed two-stage approach accurately identifies both damage location and severity. Additionally, the enhanced optimizer generates a small solution set while maintaining identification accuracy. This enhanced inverse analysis approach has potential applications in structural damage identification using other types of measurements. Future research could focus on thorough efficiency comparisons between two-stage and one-step methods.

# Chapter 6. Precision Damage Identification in Structural Subsystems Using Reduced-Order Models and Piezoelectric Impedance Sensing

Early detection of small-sized damage is crucial in structural health monitoring to enable timely interventions that minimize safety risks and maintenance costs. To achieve an early detection, the piezoelectric impedance-based active interrogation is increasingly recognized for its promise in structural health monitoring and damage identification. Built upon their self-sensing actuation capability, piezoelectric transducers can be integrated into host structures to acquire the system-level impedance information in high frequency range with small wavelength. High-frequency responses, meanwhile, can reveal small-sized damage but require large-scale finite element models to ensure accurate evaluations. This necessity leads to computationally expensive inverse optimization analyses and results in significantly high-dimensional problems that render the inverse analysis intractable. To address these challenges, we develop a two-stage damage identification scheme that decomposes the complex task into a sequence of manageable steps: coarse damage localization and fine damage identification. Component mode synthesis is firstly applied to develop a reduced-order model of the system. This significantly decreases computational demands while preserving essential dynamic characteristics. The reduced model enables efficient forward analysis to approximate the location of potential damage within specific substructures of the plate. Once the probable damaged substructures are identified, an inverse model updating technique is employed. This step precisely determines the damage location and quantifies its severity within the targeted substructure. By focusing computational resources on smaller regions, the method enhances both accuracy and efficiency. Systematic case studies validate the effectiveness of the proposed approach, demonstrating its capability to accurately identify small-sized damages with reduced computational effort.

## 6.1. Introduction

Structural health monitoring (SHM) involves tracking the condition of structures using sensors to detect, locate, and characterize damage, thereby ensuring integrity and safety (Ren et al, 2017). Early detection of damage, particularly small-scale defects, is essential for enhancing safety, improving reliability, and reducing maintenance costs (Zhang et al, 2024a and 2024c). While identifying the presence of damage is important, effective diagnosis and prognosis require precise information on both the location and severity of the damage, a process known as damage identification. Piezoelectric impedance techniques have proven effective for early identification of small-scale damage due to their ability to generate and measure high-frequency responses (Cao et al, 2018a and 2023a; Fan et al, 2019). In a piezoelectric impedance-based SHM approach, active interrogation is achieved by applying a frequency-sweeping voltage to the transducer, inducing localized high-frequency oscillations. The system's response is captured by measuring the current in the transducer circuitry, which provides the impedance (or its reciprocal, admittance). This sensor-structure interaction can be simulated using finite element analysis. Since impedance measurements reflect harmonic responses, it is feasible to perform an inverse analysis using the finite element (FE) model to detect changes in structural properties, such as local stiffness or mass (Kim and Wang, 2014; Shuai et al, 2017; Fan and Li, 2020). For instance, Shuai et al (2017) employed piezoelectric impedance information to infer structural faults using statistical inference combined with a pre-screening procedure based on evaluated response sensitivity. Ezzat et al (2020) integrated impedance-based fault diagnosis into a statistical calibration framework, including surrogate model construction and bias function usage, substantially enhancing both fault diagnosis capability and computational efficiency. Kim and Wang (2019) utilized bistable and adaptive piezoelectric circuitry to increase impedance measurement reliability, improving the inverse analysis-based structural defect identification. To accurately capture small-scale damage characteristics, high-frequency, model-based inverse analysis requires a baseline FE model with a high mesh density and a detailed damage index (Langer et al, 2017). Conducting the model updating-based damage identification task requires repetitive FE harmonic analyses to collect admittance response curves from the large FE model with varying parameters, which is computationally intractable.

One class of methods designed to reduce computational time for a single analysis run involves sensitivity analysis (Zhou et al, 2016; Cao et al, 2020). However, the accuracy of this approach, which relies on the sensitivity concept, depends significantly on the extent of the damage. As a result, it may not perform satisfactorily when only low-order sensitivity terms are considered. In contrast, surrogate models, once constructed or trained based on data correlations, can efficiently predict the responses of interest (Zhou et al, 2021b; Jin and Jung, 2016). Yet, the reliability of surrogate models is closely tied to the quality and quantity of the dataset used for training. For this research, surrogate models may not be reliable because the response differences, due to the small scale of the damage, are subtle. With advancements in FE analysis, model order reduction has become a critical topic in computational mechanics and dynamics. Over the past few decades, a variety of order-reduction techniques have been developed (Lin et al, 2009; Basselink et al, 2013; Panayirci et al, 2011). Among these, component mode synthesis (CMS) methods stand out as an important and representative branch, demonstrating potential in a wide range of applications (Zhou and Tang, 2016 and 2021a; Masson et al, 2006). Yu et al (2016) developed an element-by-element model updating approach using the component mode synthesis (CMS) method, which significantly enhances computational efficiency in large-scale structural analysis and facilitates accurate damage identification at the element level. Butland and Avitabile (2010) proposed a reduced-order CMS method that incorporates test data into system modeling. This approach combines reduced components to accurately capture dynamic characteristics, even in the presence of typical measurement contaminants. Sarsri and Azrar (2016) presented a stochastic dynamic analysis method for large structures with uncertain parameters, coupling CMS with a second-order perturbation approach to compute the statistical moments of dynamic response efficiently in high-dimensional finite element models. Zhou et al (2016) developed a CMS approach specifically for NURBS finite element models. They introduced an optimized interface construction that preserves geometry consistency during dynamic analysis. This method was validated using case studies on wind turbine blades. Wang et al (2020) proposed a model-updating approach based on CMS and perturbation analysis, enabling efficient reduction in computational cost for large-scale finite element models by capturing higher-order mode effects and applying the method to a wing structure and bolted plate. Additional insights are provided by Chen et al (2014), Wang et al (2018), and Weng et al (2020). However, it is important to note that current CMS methods are typically limited to pure mechanical analyses. In this study, the presence of a piezoelectric transducer embedded in the host structure requires an electromechanical finite element model to capture the coupling between mechanical and electrical domains. Therefore, it is essential to extend standard CMS methods to make them compatible with electromechanical finite element modeling.

Leveraging electromechanical order-reduced modeling indeed facilitates model updating-based damage identification with enhanced computational efficiency. Essentially, such model updating tasks are built upon inverse optimization analysis, in which the structural properties related to the damage are categorized as decision variables. Specifically, each segment of the structure is considered as one decision variable to facilitate the analysis. It is well known that optimization performance is dependent on the number of decision variables. Previous studies have achieved damage identification using model updating by assuming a small number of segments are under possible damage occurrence (Shuai et al, 2017). However, this assumption may not hold when considering small-sized damage. In this context, the goal of this research is to fulfill the mission of small-sized damage identification, where a large number of segments, i.e., decision variables, need to be considered in the optimization analysis. The excessive number of decision variables can substantially degrade optimization performance due to the high-dimensional solution search space. To tackle the issue, the two-stage framework offers an effective solution and has been applied across various contexts. Du et al (2019) introduced a two-phase structure damage assessment method that initially detects potential damage through a modal strain energy index and then quantifies severity using the Jaya algorithm. Perera et al (2020) implemented a two-stage damage identification method for complex structures using the roaming damage method, which identifies damage ranging from large low-damage areas to severely damaged individual beams, enhanced by a multi-objective optimization based on power mode shapes for comprehensive damage detection. Barman et al (2021) applied a two-stage method where the first stage uses mode-shape curvature-based damage indices for rough estimation of damage location, and the second stage refines this using a mixed unified particle swarm algorithm for precise lengthwise and interface location determination in composite structures. The results indicate high accuracy in identifying single and multiple delaminations, showing potential under noisy conditions.

Based on the review, a new multi-level scheme is proposed in this study, aiming to decompose the challenging damage identification task into a set of simpler tasks that can be sequentially undertaken. Instead of directly performing high-dimensional inverse optimization analysis for small-sized damage identification, we adopt multiple consecutive procedures, ranging from coarse-level damage localization to fine-level damage identification. Specifically, in the first phase, we define several metrics, i.e., simultaneously minimizing the differences between the actual damage admittance and the predicted admittance and minimizing the difference between the similarity of the actual damage admittance and the predicted admittance to 1. To preliminarily estimate the damage location, we use a sampling and estimation method. That is, we sample multiple points in a certain interval, then calculate the corresponding objective functions. Through the non-dominated sorting algorithm, we can estimate which locations the Pareto front solutions point to, identifying the coarse damage location. In this phase, the evaluation for each sampling is accelerated by using the order-reduced model. In the second phase, we perform direct inverse optimization iterations. At this stage, we use a multi-objective optimization setup, minimizing the differences between the actual admittance and the predicted admittance, as well as minimizing the L0 norm of the damage index vector. The goal of this second objective is to ensure that the solutions obtained are sparse, which is realistic since damage typically occurs in only a few locations initially. It is worth mentioning that the information available for damage inference is usually limited, while the variables to be identified are numerous. Although one can acquire additional information, there is no guarantee that this information is completely mathematically independent. Thus, damage identification is typically an underdetermined problem. Here, the multi-objective optimization setup can yield multiple solutions, aligning well with the underdetermined nature of the damage identification problem, as underdetermined problems usually have multiple solutions. Since the original dimension of the problem is dramatically reduced via this developed scheme, the desired performance of all involved decomposed tasks can be guaranteed. This establishes a new path toward early-stage damage identification, which is an important aspect of SHM applications.

The rest of this paper is organized as follows. Section 6.2 outlines the new multi-level framework for the small-sized damage identification, where the impedance/admittance information acquired via the efficient electromechanical order-reduced modeling is incorporated. Section 6.3 presents the reduced order modeling for piezoelectric transducer-structure system using component mode synthesis method. Section 6.4 provides comprehensive case studies to demonstrate this new framework with the capability of identifying the small-sized damage. Section 6.5 summarizes the concluding remarks.

## 6.2. Two-stage Damage Identification Via Piezoelectric Admittance Sensing

This section first briefly presents the technique of piezoelectric admittance-based damage identification as well as the finite element model of the integrated system that will serve as the baseline for model-based inverse analysis. We then formulate a multi-objective optimization problem that will be employed to facilitate damage identification inverse analysis.

### 6.2.1. Modeling of piezoelectric admittance

In damage identification, we employ the dynamic response of a structure as an information carrier to infer the damage occurrence. In piezoelectric admittance-based approach, we integrate a piezoelectric transducer into a host structure, and utilize the transducer as actuator and sensor concurrently. The equations of motion of the integrated system can be derived as (Zhang et al, 2024a)

$$\mathbf{M}\ddot{\mathbf{u}} + \mathbf{C}\dot{\mathbf{u}} + \mathbf{K}\mathbf{u} + \mathbf{K}_{12}Q = \mathbf{0} \tag{6.1a}$$

$$R\dot{Q} + k_c Q + \mathbf{K}_{12}^T\mathbf{u} = V_{\text{in}} \tag{6.1b}$$

where **u** is the displacement vector, $k_c$ is the inverse of the capacitance of the piezoelectric transducer; $\mathbf{K}_{12}$ is the electromechanical coupling vector due to the transducer, and **K**, **C**, **M** are the stiffness, damping and mass matrices, respectively. $V_{\text{in}}$ is a frequency-sweeping harmonic voltage excitation, and *Q* is the charge flow. To facilitate the measurement of charge flow, a small resistor *R* is connected in series with the piezoelectric transducer so the voltage across it can be measured. The details of the measurement system will be presented in Section 6.4. We let the excitation frequency be denoted as $\omega$, and use the overbar hereafter to indicate magnitude of the corresponding response variable. The piezoelectric admittance under the healthy structure status can be derived as

$$y_h(\omega) = \frac{\bar{\dot{Q}}}{\bar{V}_{\text{in}}} = \frac{j\omega}{j\omega R + k_c - \mathbf{K}_{12}^T(\mathbf{K} + j\omega\mathbf{C} - \omega^2\mathbf{M})^{-1}\mathbf{K}_{12}} \tag{6.2}$$

where *j* refers to the imaginary unit. Damage may occur in any part of a structure with arbitrary severity. In order to pinpoint damage, we divide the structure into *n* segments where *n* is a relatively large number in order to characterize damage at early stage with small size. Since we conduct damage identification based on the finite element modeling, we assume the damage causes homogenized change of structural properties within a segment. Without loss of generality, in this research we assume the damage results in stiffness reduction only. The stiffness matrix of the healthy structure is expressed as $\mathbf{K} = \sum_{i=1}^{n}\mathbf{K}_h^i$, in which $\mathbf{K}_h^i$ is the stiffness matrix of the *i*th segment under the healthy status and the summation refers to the direct summation in finite element model assemblage. The stiffness of the structure with damage is then expressed as $\mathbf{K}_d = \sum_{i=1}^{n}\mathbf{K}_h^i(1-\alpha_i)$, where $\alpha_i \in [0,1]$ is the damage index to be identified indicating the stiffness loss of the *i*th segment. When damage occurs, the piezoelectric admittance becomes

$$y_d(\omega) = \frac{\bar{\dot{Q}}}{\bar{V}_{\text{in}}} = \frac{j\omega}{j\omega R + k_c - \mathbf{K}_{12}^T(\mathbf{K}_d + j\omega\mathbf{C} - \omega^2\mathbf{M})^{-1}\mathbf{K}_{12}} \tag{6.3}$$

Obviously, damage occurrence is reflected by the change of piezoelectric admittance. In damage identification, we conduct frequency-sweeping measurement of admittances within the frequency range of interest at *m* frequency points $\boldsymbol{\omega} = [\omega_1,...,\omega_m]$. The change of admittance, i.e., $\Delta Y(\boldsymbol{\omega}) = Y_d(\boldsymbol{\omega}) - Y(\boldsymbol{\omega})$ then can be employed to identify above damage index vector, which is the objective of this study. Our research specifically targets the identification of small-sized damage. To capture the characteristics of this type of damage, the number of elements, *n*, must be sufficiently large. Without prior knowledge, any element in the host structure could potentially be damaged. This requirement presents a significant challenge for damage identification methods based on modal updating, as they rely on iterative inverse optimization analysis (Nguyen et al, 2018; Gordan et al, 2020). Including a large number of decision variables, represented by the damage index vector, in the optimization process can significantly impair the identifiability of the final solution. To address this issue, we propose a two-stage damage identification approach in this study. This approach breaks down a high-dimensional, complex problem into a series of manageable, low-dimensional problems, which are detailed in the subsequent section.

### 6.2.2. Overview of two-stage damage identification approach

The proposed approach is summarized in Figure 6-1 and involves two stages: forward analysis to detect the substructure likely containing damage and inverse optimization to locate and quantify the specific damage within the identified substructure. In Stage I, given a structure integrated with a piezoelectric transducer, the structure is divided into substructures based on the characteristics of their connections. Then, CMS analysis is performed to reduce the degrees of freedom (DOFs), yielding a reduced-order model that simplifies the forward analysis by lowering computational complexity. This reduced model enables the estimation of the substructure containing damage using predefined metrics. Based on these metric values, a non-dominated sorting algorithm ranks the substructures, identifying the most likely damaged one. This information is then used in Stage II for inverse model updating, focusing solely on the identified substructure while keeping the others unchanged. The metrics and fitness functions used in each stage are detailed in the following subsections.

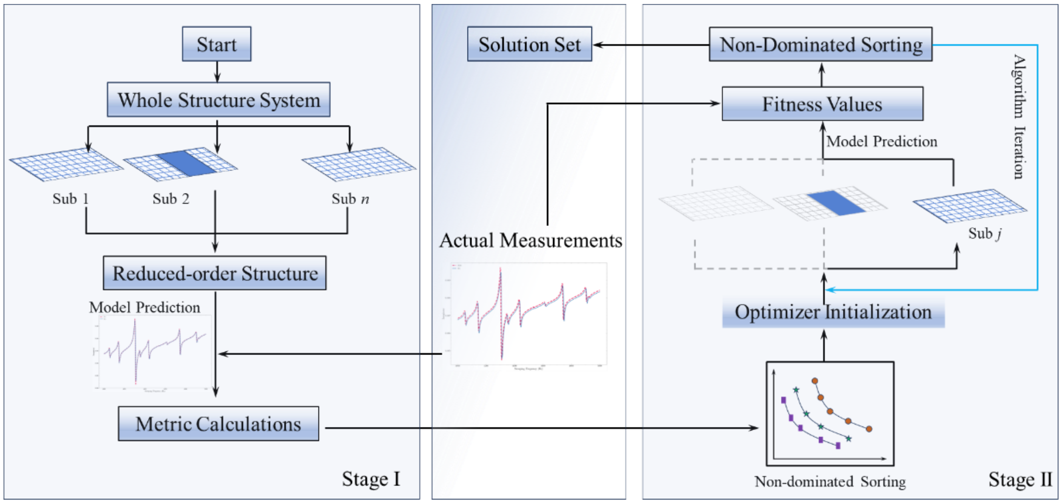

**Figure 6-1.** Two-stage damage identification empowered by reduced order modeling.

#### 6.2.2.1. Forward multi-objective pareto solution domination analysis

In the initial stage, which focuses on damage localization, the host structure is divided into several larger substructures. Each substructure includes multiple elements, which significantly reduces the degrees of freedom compared to analyzing the entire structure. This reduction makes inverse optimization analysis more manageable. Since initial damage is typically sparse, minor damage is likely to appear within only one of these larger substructures. Therefore, it may not be necessary to consider scenarios involving widespread or multiple instances of damage across various substructures. To aid in detecting damage, a forward analysis framework has been developed. This framework leverages Pareto solutions and their dominance relations within a multi-objective optimization setting. The basics of multi-objective optimization and non-dominated sorting are summarized below.

A general multi-objective minimization problem can be represented as

$$\mathbf{y} = \mathbf{f}(\mathbf{x}) = (f_1(\mathbf{x}), f_2(\mathbf{x}), \ldots, f_m(\mathbf{x})) \tag{6.4}$$

where $\mathbf{x} \in \mathbb{R}^n$ is design variable vector with $n$ dimensions and $\mathbf{y} \in \mathbb{R}^m$ is the $m$-dimensional objective vector. $\mathbb{R}^n$ is the feasible domain which is defined by a set of equalities and inequalities of $\mathbf{x}$, and $\mathbb{R}^m$ is the corresponding objective space. Due to potential conflicts among the objectives in such problems, a single solution that optimizes all objectives simultaneously may not exist. Instead, a set of solutions, known as Pareto optimal solutions, can be identified by making trade-offs between the objectives. The concept of Pareto dominance is used to evaluate these solutions. Mathematically, $\mathbf{x}_1$ is said to dominate another solution $\mathbf{x}_2$, denoted as $\mathbf{x}_1 \prec \mathbf{x}_2$, if:

$$f_i(\mathbf{x}_1) \le f_i(\mathbf{x}_2),\ \forall i \in \{1,2,\dots,m\}, \text{ and} \tag{6.5a}$$

$$f_i(\mathbf{x}_1) < f_i(\mathbf{x}_2),\ \exists i \in \{1,2,\dots,m\} \tag{6.5b}$$

When there does not exist another solution that dominates $\mathbf{x}^* \in \mathbb{R}^n$, then it becomes a non-dominated solution, i.e., Pareto optimal and is included in Pareto optimal set.

Building on the principles of the Pareto front and dominance in multi-objective optimization, a forward analysis framework is established to enable coarse-level damage localization (see Figure 6-1). The hypothesis is that each substructure has a certain damage level that produces an admittance response closest to the measured admittance when the substructure contains the actual, small-scale damage. The detailed procedures are summarized as follows:

(1) We produce or parameterize a set of damage level values given certain range $[\widehat{\alpha}_l, \widehat{\alpha}_u]$, where $\widehat{\alpha}_l, \widehat{\alpha}_u \in [0,1]$. Let the number of values is $w$.

(2) We suppose that the number of large substructures in this localization task is $r$ $r \ll n$. As mentioned, only the damage of single substructure is considered due to the sparse nature of initial damage occurrence. We then substitute the previously generated damage level values into each single substructure and conduct the harmonic analysis to collect the admittance response. Consecutively looping over all segments need $w \times r$ runs, resulting in corresponding $w \times r$ admittance response samples.

(3) We establish the multiple design objectives (metrics) to guide the damage localization analysis. When the admittance response curve over one specific frequency range is concerned, we can define the objectives as

$$\text{metric 1:}\begin{cases}\left\|\Delta\mathbf{Y}_{(M)}\right\|_2\\ \left\|\Delta\mathbf{Y}_{(\phi)}\right\|_2\end{cases}\tag{6.6a}$$

$$\text{metric 2:}\begin{cases}\text{1-MAC}(\mathbf{Y}_{(M)},\mathbf{Y}_{d(M)})\\ \text{1-MAC}(\mathbf{Y}_{(\phi)},\mathbf{Y}_{d(\phi)})\end{cases}\tag{6.6b}$$

We employ two different metrics, i.e., $l_2$ norm and modal assurance criteria (MAC) to comprehensively evaluate the quality of solutions. MAC originally is used to correlate and pair the mode shapes (Zhang et al, 2024c), which can be used to assess the similarity of two admittance response vectors in this study. $\mathbf{Y}$ denotes the admittance response curve over specified frequency points. $\Delta\mathbf{Y}$ is admittance difference between healthy and damaged states of the structure. Subscripts $M$ and $\phi$ indicate the magnitude and phase, respectively. $\|\cdot\|$ is the $l_2$ norm operator. $\mathrm{MAC}(\cdot)$ is the operator of modal assurance criteria, which is mathematically defined as $\mathrm{MAC}(\mathbf{A},\mathbf{B})=\dfrac{(\mathbf{A}\mathbf{B}^T)^2}{(\mathbf{A}\mathbf{A}^T)(\mathbf{B}\mathbf{B}^T)}$ ($A$ and $B$ are the row vectors with same length) (Brehm et al, 2010). It is noted that we use 1-MAC instead of MAC because we want to keep the same quality trend with respect to all objectives. Particularly, the smaller the objective is, the better the quality of solution yielded.

(4) Recall we have $w\times r$ admittance samples, and the objectives of each sample can be calculated using Equation (6.6). We thus can generate a solution database with row number $w\times r$ and column number $4\times q$ ($q$ is the number of interested frequency spans, over which the admittance curves are obtained).

(5) We apply the domination analysis of all $w\times r$ solutions in terms of their objectives, yielding the final Pareto optimal set.

(6) We use the pareto optimal set result to point to the most suspicious segment that can be used for the subsequent task in the next level.

#### 6.2.2.2. Inverse model updating for fine damage identification

Since damage is confined to one of the substructures, we narrow our focus to this specific substructure for further damage identification. Given the inherently sparse nature of small-scale damage, sparsity is included as an additional objective, represented mathematically by the $\|\boldsymbol{\alpha}\|_0$ (Cao et al, 2018a). $\|\cdot\|_0$ is $l_0$ norm operator that denotes the number of non-zero elements in the vector. To mitigate the adversarial effects of solutions and streamline the solution post-screening process, we exclude objectives involving the MAC (Modal Assurance Criterion) shown in Equation (6.7). The complete optimization problem with multiple objectives involved is formulated as

$$\text{Find: } \boldsymbol{\alpha} \in \mathbb{R}^n,\ \alpha_l \leq \alpha_i \leq \alpha_u,\ i = 1,...,n \tag{6.7a}$$

$$\text{Minimize: } f_1 = \left\|\Delta \mathbf{Y}_{(M)}\right\|_2,\ f_2 = \left\|\Delta \mathbf{Y}_{(\phi)}\right\|_2 \text{ and } f_3 = \|\boldsymbol{\alpha}\|_0 \tag{6.7b}$$

where $\mathbb{R}^n$ is specified sample space. It is important to note that the data available for inferring damage is generally limited, while there are numerous variables to identify. Although one can acquire additional information, there is no guarantee that this information is completely mathematically independent. Thus, damage identification is typically an underdetermined problem. The multi-objective optimization setup can yield multiple solutions, which align well with the nature of underdetermined damage identification, where multiple solutions are expected. Recall that harmonic analysis, essential for calculating impedance, remains computationally demanding for large-scale full-scale FE models, highlighting the need for a more efficient computational approach.

## 6.3. Reduced-order Modeling for Piezoelectric Transducer-Structure System

In this research, we utilize CMS-based order-reduced modeling to expedite impedance evaluation, which supports the multi-level damage identification process. Conventional CMS methods primarily focus on condensing mechanical degrees of freedom (DOFs). Therefore, adapting these methods to electromechanical systems requires careful consideration. The free interface CMS method is known for its efficiency because it significantly reduces interface DOFs (Zhou and Tang, 2018). However, it does not differentiate between electrical and structural DOFs during the reduction process, which limits its applicability to electromechanical models. The fixed-interface CMS approach, developed by Hurty (1965) and later refined by Craig and Bampton (1968), is more suitable for our needs. This method preserves interface DOFs, allowing us to retain electrical DOFs by incorporating them as part of the interface. As a result, this approach enables the creation of an effective electromechanical order-reduced model that meets the requirements of this study.

The finite element discretized system of equation of motion for the undamped free vibration of a substructure reads (Allen et al, 2020)

$$\mathbf{M}^{(s)}\ddot{\mathbf{u}} + \mathbf{K}^{(s)}\mathbf{u} = \mathbf{f}^{(s)} \tag{6.8}$$

where $\mathbf{M}^{(s)}$ and $\mathbf{K}^{(s)}$ are the mass and stiffness matrices of certain substructure, respectively. $\mathbf{u}^{(s)}$ is the displacement vector, and $\mathbf{f}^{(s)}$ is the forcing vector. The superscript $s$ indicates the $s$-th substructure. In this study, the FE model of certain substructure may include piezoelectric transducer elements if the piezoelectric transducer is occasionally placed at that substructure, as illustrated in Figure 6-2.

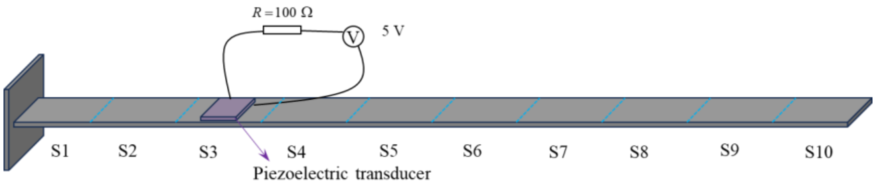

**Figure 6-2.** Structure-piezoelectric transducer system.

Therefore, the generalized coordinates of such substructure consist of interface, interior and piezoelectric transducer coordinates. Equation (6.8) thus can be re-written as

$$\begin{bmatrix} \mathbf{M}_{ii}^{(s)} & \mathbf{M}_{ij}^{(s)} & \mathbf{M}_{ip}^{(s)} \\ \mathbf{M}_{ji}^{(s)} & \mathbf{M}_{jj}^{(s)} & \mathbf{M}_{jp}^{(s)} \\ \mathbf{M}_{pi}^{(s)} & \mathbf{M}_{pj}^{(s)} & \mathbf{M}_{pp}^{(s)} \end{bmatrix} \begin{Bmatrix} \ddot{\mathbf{u}}_i \\ \ddot{\mathbf{u}}_j \\ \ddot{\mathbf{u}}_p \end{Bmatrix} + \begin{bmatrix} \mathbf{K}_{ii}^{(s)} & \mathbf{K}_{ij}^{(s)} & \mathbf{K}_{ip}^{(s)} \\ \mathbf{K}_{ji}^{(s)} & \mathbf{K}_{jj}^{(s)} & \mathbf{K}_{jp}^{(s)} \\ \mathbf{K}_{pi}^{(s)} & \mathbf{K}_{pj}^{(s)} & \mathbf{K}_{pp}^{(s)} \end{bmatrix} \begin{Bmatrix} \mathbf{u}_i \\ \mathbf{u}_j \\ \mathbf{u}_p \end{Bmatrix} = \begin{Bmatrix} \mathbf{0} \\ \mathbf{f}_j^{(s)} \\ \mathbf{0} \end{Bmatrix} \tag{6.9}$$

where subscript $i$, $j$ and $p$ indicate the interior, interface, and piezoelectric transducer coordinates, respectively. As indicated in the Equation (6.3), the piezoelectric transducer elements in the matrices **K**, **M** and **C**, together with vector $\mathbf{K}_{12}$ provide the electromechanical coupling to generate the impedance response, which essentially takes place in the original model space. This implies that entire piezoelectric transducer coordinates should be retained to correctly use that equation for impedance computation. Consistent with the underlying idea of this method, we simply treat piezoelectric transducer coordinates as interface coordinates, which then can be kept. We construct a new set $b$ that is represented as $b = [j \quad p]$, and let it be the new "interface" coordinates, upon which the Equation (6.9) can be simplified as

$$\begin{bmatrix} \mathbf{M}_{ii}^{(s)} & \mathbf{M}_{ib}^{(s)} \\ \mathbf{M}_{bi}^{(s)} & \mathbf{M}_{bb}^{(s)} \end{bmatrix} \begin{Bmatrix} \ddot{\mathbf{u}}_i \\ \ddot{\mathbf{u}}_b \end{Bmatrix} + \begin{bmatrix} \mathbf{K}_{ii}^{(s)} & \mathbf{K}_{ib}^{(s)} \\ \mathbf{K}_{bi}^{(s)} & \mathbf{K}_{bb}^{(s)} \end{bmatrix} \begin{Bmatrix} \ddot{\mathbf{u}}_i \\ \ddot{\mathbf{u}}_b \end{Bmatrix} = \begin{Bmatrix} \mathbf{0} \\ \mathbf{f}_b^{(s)} \end{Bmatrix} \tag{6.10}$$

Starting from here, we can further proceed with the standard derivation of CMS method. The representation modes, commonly, called Component Modes (CMs) in sub-structuring, are formed by computing the static response of the interior of the sub-structure when one interface DOF is given a unit displacement and all the other DOF are held fixed. The CM set for the entire interface is expressed as

$$\mathbf{\Psi}^{(s)} = \begin{bmatrix} -\mathbf{K}_{ii}^{(s)^{-1}} \mathbf{K}_{ib}^{(s)} \\ \mathbf{I} \end{bmatrix} \tag{6.11}$$

The resulting basis is used to statically eliminate all interface DOF from the model, retaining only the boundary DOF. The resulting reduced system is unusually of small size since only boundary DOFs is remaining unknowns. In order to capture the dynamics of the system, the static modes are augmented with a set of dynamic modes which are obtained by fixing the interface DOF and solving the following eigenvalue problem:

$$(\mathbf{K}_{ii}^{(s)} - \omega_r^2 \mathbf{M}_{ii}^{(s)}) \boldsymbol{\varphi}_{ii,r}^{(s)} = 0 \tag{6.12}$$

The eigenvectors obtained from this equation are referred to as fixed-interface modes. A truncated set of m of these mass normalized eigenvectors are collected into a fixed-interface mode matrix

$$\mathbf{\Phi}^{(s)} = \begin{bmatrix} \boldsymbol{\varphi}_{i,1}^{(s)}, \ldots, \boldsymbol{\varphi}_{i,k}^{(s)} \\ \mathbf{0} \end{bmatrix} = \begin{bmatrix} \mathbf{\Phi}_{ik}^{(s)} \\ \mathbf{0} \end{bmatrix} \tag{6.13}$$

Noteworthy, the order reduction process can be carried out by only keeping a small number of modes, i.e., $k$ in the normal modes where $k \ll i$. These modes provide a normal basis for the interior DOF of the substructure. The fixed-interface modes and the CMs are combined to form the reduction matrix as

$$\mathbf{T}^{(s)\mathrm{CMS}} = \begin{bmatrix} \mathbf{\Phi}^{(s)} & \mathbf{\Psi}^{(s)} \end{bmatrix} \tag{6.14}$$

which provides a transformation from the sub-structure physical DOF to the CMS generalized DOF,

$$\begin{bmatrix} \mathbf{u}_i^{(s)} \\ \mathbf{u}_b^{(s)} \end{bmatrix} = \mathbf{T}^{(s)\mathrm{CMS}} \begin{bmatrix} \mathbf{q}_i^{(s)} \\ \mathbf{u}_b^{(s)} \end{bmatrix} \tag{6.15}$$

where **q** represents the modal coordinate vector associated with the fixed-interface modes. The uncoupled substructure-reduced mas and stiffness matrices are now formed by applying the CMS transformation to these matrices as

$$\mathbf{M}^{(s)\mathrm{CM}S} = (\mathbf{T}^{(s)\mathrm{CMS}})^T \mathbf{M}^{(s)} \mathbf{T}^{(s)\mathrm{CMS}}, \ \mathbf{K}^{(s)\mathrm{CM}S} = (\mathbf{T}^{(s)\mathrm{CMS}})^T \mathbf{K}^{(s)} \mathbf{T}^{(s)\mathrm{CMS}} \tag{6.16}$$

Then, we will have

$$\mathbf{M}^{(s)\mathrm{CM}S} = \begin{bmatrix} \mathbf{I} & \tilde{\mathbf{M}}_{ib}^{(s)} \\ \tilde{\mathbf{M}}_{bi}^{(s)} & \tilde{\mathbf{M}}_{bb}^{(s)} \end{bmatrix} \text{ and } \mathbf{K}^{(s)\mathrm{CM}S} = \begin{bmatrix} \mathbf{\Omega}_{kk}^{(s)^2} & \mathbf{0} \\ \mathbf{0} & \tilde{\mathbf{K}}_{bb}^{(s)} \end{bmatrix} \tag{6.17}$$

with $\mathbf{\Omega}$ the diagonal matrix of the eigenfrequencies of the fixed-interface modes and with the full sub-matrices as

$$\tilde{\mathbf{M}}_{kb}^{(s)} = \tilde{\mathbf{M}}_{bk}^{(s)^T} = \mathbf{\Phi}^{(s)^T} (\mathbf{M}_{ib}^{(s)} - \mathbf{M}_{ii}^{(s)} \mathbf{K}_{ii}^{(s)^{-1}} \mathbf{K}_{ib}^{(s)}) \tag{6.18a}$$

$$\tilde{\mathbf{M}}_{bb}^{(s)} = \mathbf{M}_{bb}^{(s)} - \mathbf{M}_{bi}^{(s)} \mathbf{K}_{ii}^{(s)} \mathbf{K}_{ib}^{(s)} - \mathbf{K}_{bi}^{(s)} \mathbf{K}_{ii}^{(s)} \mathbf{M}_{ib}^{(s)} + \mathbf{K}_{bi}^{(s)} \mathbf{K}_{ii}^{(s)} \mathbf{M}_{ii}^{(s)} \mathbf{K}_{ii}^{(s)} \mathbf{K}_{ib}^{(s)} \tag{6.18b}$$

$$\tilde{\mathbf{K}}_{bb}^{(s)} = \mathbf{K}_{bb}^{(s)} - \mathbf{K}_{bi}^{(s)} \mathbf{K}_{bb}^{(s)^{-1}} \mathbf{K}_{bi}^{(s)} \tag{6.18c}$$

It is worth noting that the order-reduced damping matrix can be formulated in the similar way as order-reduced stiffness or mass matrix does. What follows is the assemblage of all order-reduced substructures. The reduced-order models are typically coupled using a primal assembly by defining a transformation between the uncoupled and the coupled DOF that selects the sub-structure boundary DOF from a unique global set of boundary DOFs. The assembled mass and stiffness matrices are formed by adding the coupled contribution from each sub-structure as

$$\mathbf{M}^{\mathrm{CMS}} = \sum_{s=1}^{n} (\mathbf{L}^{(s)\mathrm{CMS}})^{T} \mathbf{M}^{(s)\mathrm{CMS}} \mathbf{L}^{(s)\mathrm{CMS}} \tag{6.19a}$$

$$\mathbf{K}^{\mathrm{CMS}} = \sum_{s=1}^{n} (\mathbf{L}^{(s)\mathrm{CMS}})^{T} \mathbf{K}^{(s)\mathrm{CMS}} \mathbf{L}^{(s)\mathrm{CMS}} \tag{6.19b}$$

where the $s$-th substructure coupling matrix, $\mathbf{L}^{(s)\mathrm{CMS}}$, is formed by extracting the corresponding rows of $\mathbf{L}^{\mathrm{CMS}}$. The coupling matrix $\mathbf{L}^{\mathrm{CMS}}$ can be obtained based on the connections between each sub-structure. Here, a structure with 3 substructures is utilized to explain the formation of coupling matrix, as shown in Figure 6-3. We can have

$$\left\{ \begin{array}{c} \mathbf{q}_{i,1} \\ \mathbf{u}_{\Gamma_1,1} \\ \mathbf{u}_{\Gamma_2,1} \\ \hline \mathbf{q}_{i,2} \\ \mathbf{u}_{\Gamma_1,2} \\ \hline \mathbf{q}_{i,3} \\ \mathbf{u}_{\Gamma_2,3} \end{array} \right\} = \left[ \begin{array}{ccccc} \mathbf{I} & \mathbf{0} & \mathbf{0} & \mathbf{0} & \mathbf{0} \\ \mathbf{0} & \mathbf{0} & \mathbf{0} & \mathbf{I} & \mathbf{0} \\ \mathbf{0} & \mathbf{0} & \mathbf{0} & \mathbf{0} & \mathbf{I} \\ \hline \mathbf{0} & \mathbf{I} & \mathbf{0} & \mathbf{0} & \mathbf{0} \\ \mathbf{0} & \mathbf{0} & \mathbf{0} & \mathbf{I} & \mathbf{0} \\ \hline \mathbf{0} & \mathbf{0} & \mathbf{I} & \mathbf{0} & \mathbf{0} \\ \mathbf{0} & \mathbf{0} & \mathbf{0} & \mathbf{0} & \mathbf{I} \end{array} \right] \left\{ \begin{array}{c} \mathbf{q}_{i,1} \\ \mathbf{q}_{i,2} \\ \mathbf{q}_{i,3} \\ \mathbf{u}_{\Gamma_1} \\ \mathbf{u}_{\Gamma_2} \end{array} \right\} = \mathbf{L}^{\mathrm{CMS}} \left\{ \begin{array}{c} \mathbf{q}_{i,1} \\ \mathbf{q}_{i,2} \\ \mathbf{q}_{i,3} \\ \mathbf{u}_{\Gamma_1} \\ \mathbf{u}_{\Gamma_2} \end{array} \right\} \tag{6.20}$$

where $\mathbf{q}_{i,s}$ represents the interior DOFs of $s$-th substructure with $s = 1,...,3$. $\mathbf{u}_{\Gamma_j,s}$ represents the interface displacement for interface $\Gamma_j$ belonging to the $s$-th substructure with $j = 1,...,2$.

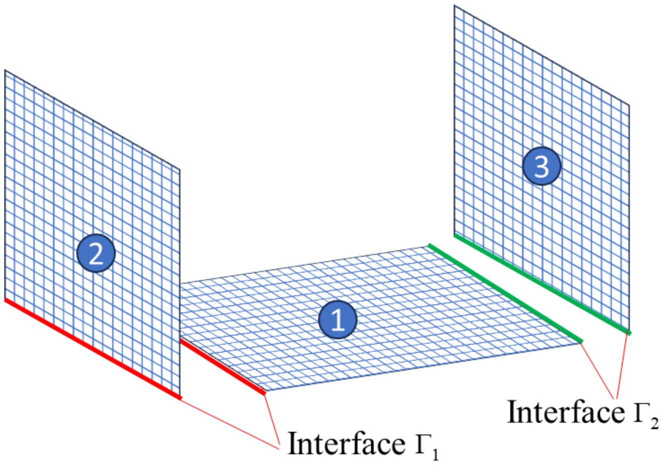

**Figure 6-3.** Illustration of coupling matrix formulation.

The order-reduced stiffness, damping and mass matrices can be identified and substituted into Equation (6.3) to calculate the admittance response, as shown below,

$$\bar{Y}(\omega) = \frac{j\omega}{j\omega R + k_c - \mathbf{K}_{12}^{\mathrm{CMS}\,T}(\mathbf{K}^{\mathrm{CMS}} + j\omega\mathbf{C}^{\mathrm{CMS}} - \omega^2\mathbf{M}^{\mathrm{CMS}})^{-1}\mathbf{K}_{12}^{\mathrm{CMS}}} \tag{6.21}$$

Note, $\mathbf{K}_{12}^{\mathrm{CMS}}$ is a new coupling vector with compatible size with respect to the order-reduced model, which is reorganized in terms of the non-zero values in $\mathbf{K}_{12}^{T}$. Since the sizes of matrices involved are reduced, the computational cost of harmonic FE analysis can be significantly mitigated. It is noted that $\bar{Y}(\omega)$ is the admittance evaluated in the order-reduced space. Since the subsequent identification task relies on the admittance measured from the actual structure, the admittance response in the original space is necessary. This response can be obtained through an additional coordinate transformation step.

## 6.4. Structural Damage Identification Case Study and Discussion

In this section we demonstrate the new framework through case investigations. We illustrate the feasibility of the proposed multi-level scheme which aims at facilitating the identification of small-sized damage with improved identifiability. The fixed interface CMS order-reduction approach is integrated into the framework to significantly reduce the dimension of full-scale electromechanical FE model and meanwhile characterize the high-fidelity impedance information. This enables the substantial improvement of computational efficiency.

### 6.4.1. Problem setup of case investigation

A benchmark cantilever plate structure embedded with a piezoelectric transducer and an electric circuit is investigated and the geometries of both plate and piezoelectric transducer are described in Figure 6-4. The plate is made of aluminum with Young's modulus $68.9\ \mathrm{GPa}$, density $2,700\ \mathrm{kg/m^3}$ and Poisson's ratio 0.33. The Young's moduli of piezoelectric transducer in length and thickness directions are $Y_{11} = 86\ \mathrm{GPa}$ and $Y_{33} = 73\ \mathrm{GPa}$, respectively. The density of piezoelectric transducer is $7,500\ \mathrm{kg/m^3}$. The piezoelectric and permittivity constants of piezoelectric transducer are $h_{31} = -1.0288 \times 10^9\ \mathrm{Vm^{-1}}$ and $\beta_{33} = 1.3832 \times 10^8\ \mathrm{mF^{-1}}$, respectively. A voltage sweep is applied onto the circuit, which is coupled with mechanical host structure (plate) via piezoelectric transducer. The admittance then can be directly measured via the circuit. Specifically, to extract the piezoelectric admittance, a small resistor i.e., $100\,\Omega$ is connected in serial to the transducer to measure the voltage drop across it (Figure 6-4), and the current in the circuit can be obtained which then yields the admittance information. Following such mechanism, the finite element (FE) model is utilized to numerically simulate the admittance data. It is worth noting that, in this research we aim to identify the small-sized damage, which exhibits high sensitivity to the high-frequency impedance information. A large-size FE model with high mesh density hence should be constructed to adequately model the small-sized damage and accurately characterize high-frequency impedance. In this case, we configure the mesh for the target electromechanical system with details shown in Table 6-1. With such high mesh density, the plate and piezoelectric transducer contain 5,000 and 50 elements, respectively, yielding the whole FE model with 89,241 DOFs. The admittance response curve is usually calculated over the selected structural resonant frequency. The relatively dense sweeping frequency points are employed in the harmonic analysis to enable the impedance/admittance response curve with high resolution, from which the resonances can be accurately captured. This requires the repetitive evaluations of the Equation (6.3), and each evaluation based upon the large-size FE model is very costly. The damage identification task implemented through iteratively harmonic analysis naturally will lead to the intractable computational complexity, which is to be addressed by the subsequent order-reduced modeling.

As highlighted, the small-sized damage is of interest, which particularly is of size $10\text{mm} \times 4\text{mm}$ throughout the plate thickness as shown in Figure 6-5. The size of such damage contains 20 solid elements according to above mesh configuration (Table 6-1). Due to the sparse nature of initial damage occurrence, in this study we focus on the investigation of single small-sized damage, in which the stiffness reduction is simply used to represent the type of damage for illustration purpose. A 20% stiffness reduction is particularly employed, upon which the impedance measurement is numerically generated. This problem set-up is capable of providing the ground truth, and thus facilitate the methodology validation. The admittance curves of the healthy and damaged structures are used as useful information to undertake the damage identification analysis, which can be seen in Figure 6-6. The impedance/admittance over more frequency bands will enrich the measurement, which as a result will enhance the damage identifiability. Nevertheless, it meanwhile increases the computational burden. In this study, two frequency bands (i.e., 5,358-5,390 Hz and 8,463-8,514 Hz) with 100 frequency points in between are determined to assess the admittance resonant frequency shift and resonance change as can be seen in Figure 6-6. It is worth mentioning that the frequency selection here is dependent on the element size in the FE model according to the wave propagation principles. Considering the stiffness reduction of such single damage as one model parameter to be identified, the optimization problem formulated for the damage identification includes 250 decision variables, which is challenging to be directly handled by optimization algorithm. This essentially is the major incentive of this research.

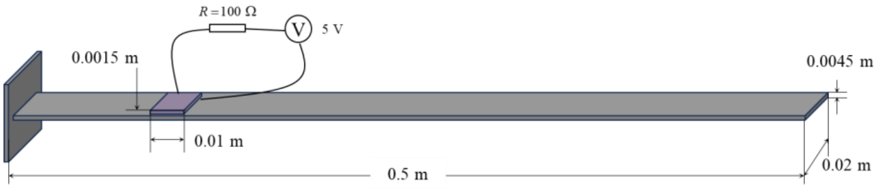

**Figure 6-4.** Layout and geometry of the electromechanical system investigated.

**Table 6-1.** Finite element modeling details.

| | Element type | Mesh configuration (number of elements along directions) | | | Element geometry |
|---|---|---|---|---|---|
| | | Length | Width | Thickness | |
| Plate | 20-node structural solid element | 250 | 10 | 2 | $2 \times 2 \times 2.25$ (mm) |
| Piezoelectric transducer | 20-node PZT solid element | 5 | 10 | 1 | $2 \times 2 \times 1.5$ (mm) |

**Figure 6-5.** Illutration of small-sized damage in the host strucure.

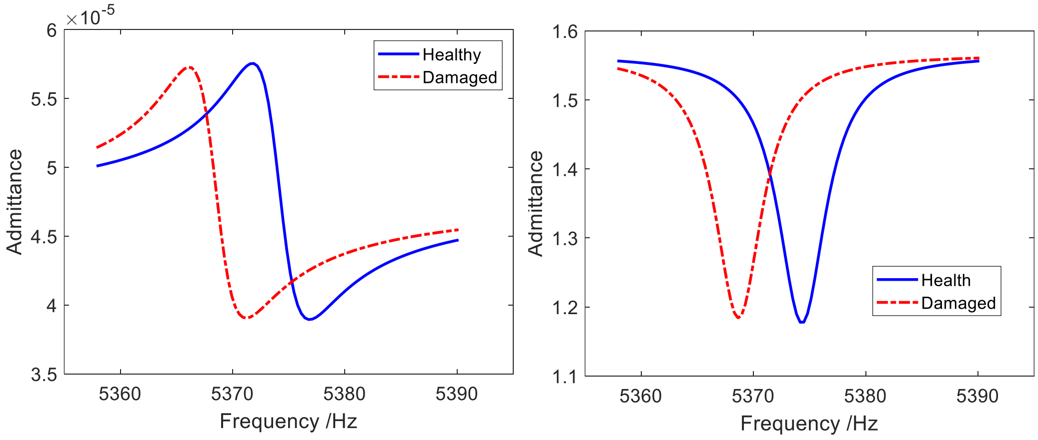

(a) (b)

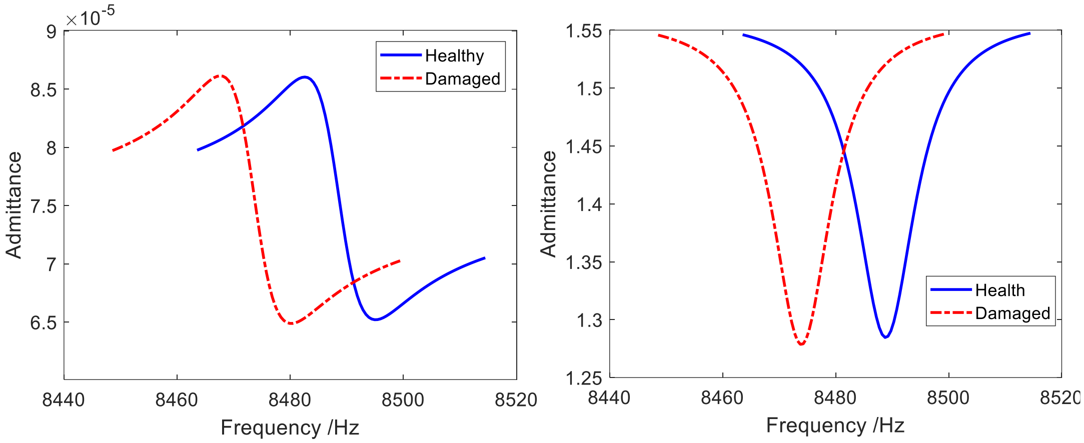

(c) (d)

**Figure 6-6.** Admittances of health and damage scenarios. (a) Magnitude curve over resonant frequency 5,374 Hz; (b) Phase curve over resonant frequency 5,374 Hz; (c) Magnitude curve over resonant frequency 8,484 Hz; (d) Phase curve over resonant frequency 8,484 Hz.

### 6.4.2. Order-reduced model establishment and performance validation

The goal of the order-reduced modeling is to facilitate the damage identification task with enhanced computational efficiency. The fixed interface CMS method is employed in this study, in which the number of kept modes for approximating the interior DOFs of substructures is the key parameter to be determined. The selection of such a parameter should consider both the computational cost and approximation accuracy. To enable the accurate high-frequency response approximation, usually a larger number of kept modes are recommended. In this study, the number of substructures is identical to the segments in the coarse localization, i.e., 10 as will be shown subsequently. The kept number of modes is defined as 50 (i.e., $k$=50 in Equation (6.13)) for all substructures, and then examine the accuracy of order reduced model by comparing its result with that from full-scale FE model (Figure 6-7). The discrepancy of curves slightly increases when the frequency of the admittance becomes higher. Apparently, the overall approximation accuracy is desirable because of the good agreement, indicating the effectiveness of the order-reduced modeling. The order-reduced model developed is adequate for subsequent damage identification analysis.

The most significant advantage of order-reduced modeling is the computational boost obtained from the substantial reduction in degrees of freedom (DOFs) in the model. In this specific case, the model size can be dramatically reduced from 89,241 to 4,334 DOFs under the current setup. Using the same computational platform, an Intel(R) Core (TM) i7-1065G7 CPU @ 1.30GHz, computing the admittance at each frequency point using a full-scale finite element (FE) model (as per Equation (6.3)) takes about 7 seconds, whereas it takes only 1 second with the order-reduced model (as per Equation (6.21)). Although the structural matrix operations in the order-reduction process incur additional computational costs, the harmonic analysis for evaluating the admittance curve remains the primary computational expense. A single run of the FE simulation under the order-reduced model takes approximately 320 seconds. Compared with the original time cost of around 1,400 seconds for the full-scale FE model, a computational acceleration of 4-5 times is indeed achieved, substantially reducing the computational burden. For simulation convenience, both full-scale FE and order-reduced models are established using our in-house MATLAB code.

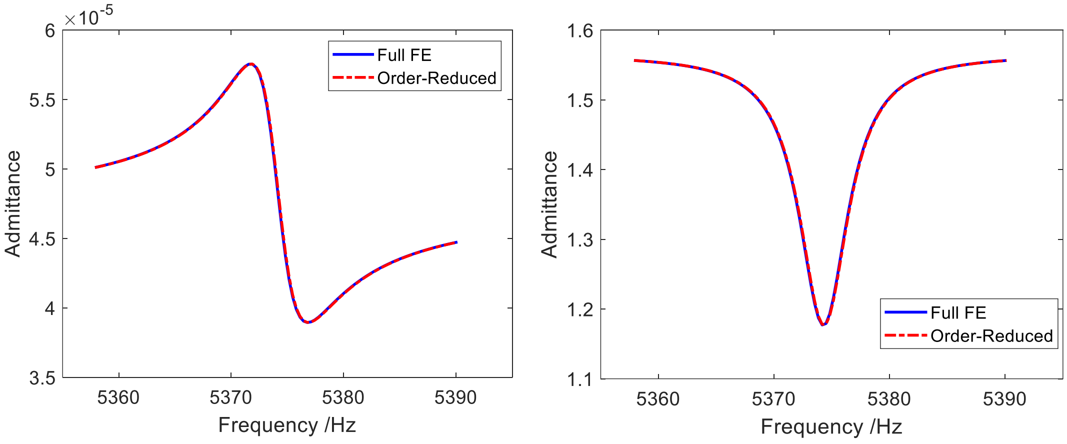

(a) (b)

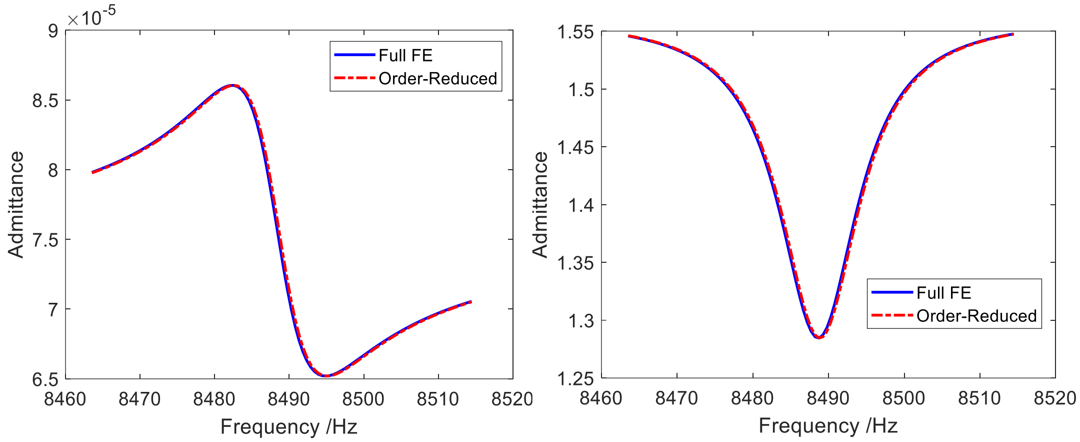

(c) (d)

**Figure 6-7.** Admittances of full-scale FE and order-reduced models. (a) Magnitude curve over resonant frequency 5,374 Hz; (b) Phase curve over resonant frequency 5,374 Hz; (c) Magnitude curve over resonant frequency 8,484 Hz; (d) Phase curve over resonant frequency 8,484 Hz.

### 6.4.3. Coarse-level damage localization

Following the analysis procedures shown in Section 6.2.2.1, we choose the number of divisions as 10 (i.e., $r$=10), which is schematically illustrated in Figure 6-8. For illustration purposes, we assume the damage range for each segment is [0.005,0.2] (i.e., $\widehat{\alpha}_l = 0.005$, $\widehat{\alpha}_u = 0.2$). This range is representative of typical damage that occurs within the structure. Given such range, we evenly generate 100 (i.e., $w$=100) damage level values and collect the corresponding 1,000 (i.e., $w \times r$) admittance response samples via repetitive order-reduced model simulations. The structural properties of different segments exhibit varying degrees of sensitivity with respect to the admittance curve. To illustrate this effect, we compare the envelopes of the admittance curves for the first and second segments under damage conditions, as shown in Figure 6-9. The width of the envelope generally indicates the degree of sensitivity, that is, the wider the envelope, the more sensitive it is to the damage. Clearly, the damage in the first segment is more sensitive than that in the second segment to the admittance response around 5,374 Hz. However, it becomes less sensitive to the admittance response around 8,484 Hz. All envelopes encompass the admittance response corresponding to the actual damage case, making it impossible to directly pinpoint the suspicious segment.

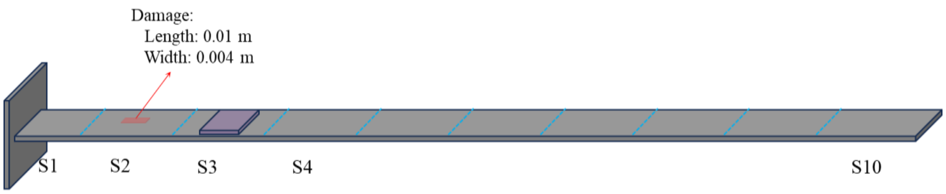

**Figure 6-8.** Segmentation for coarse-level damge localization.

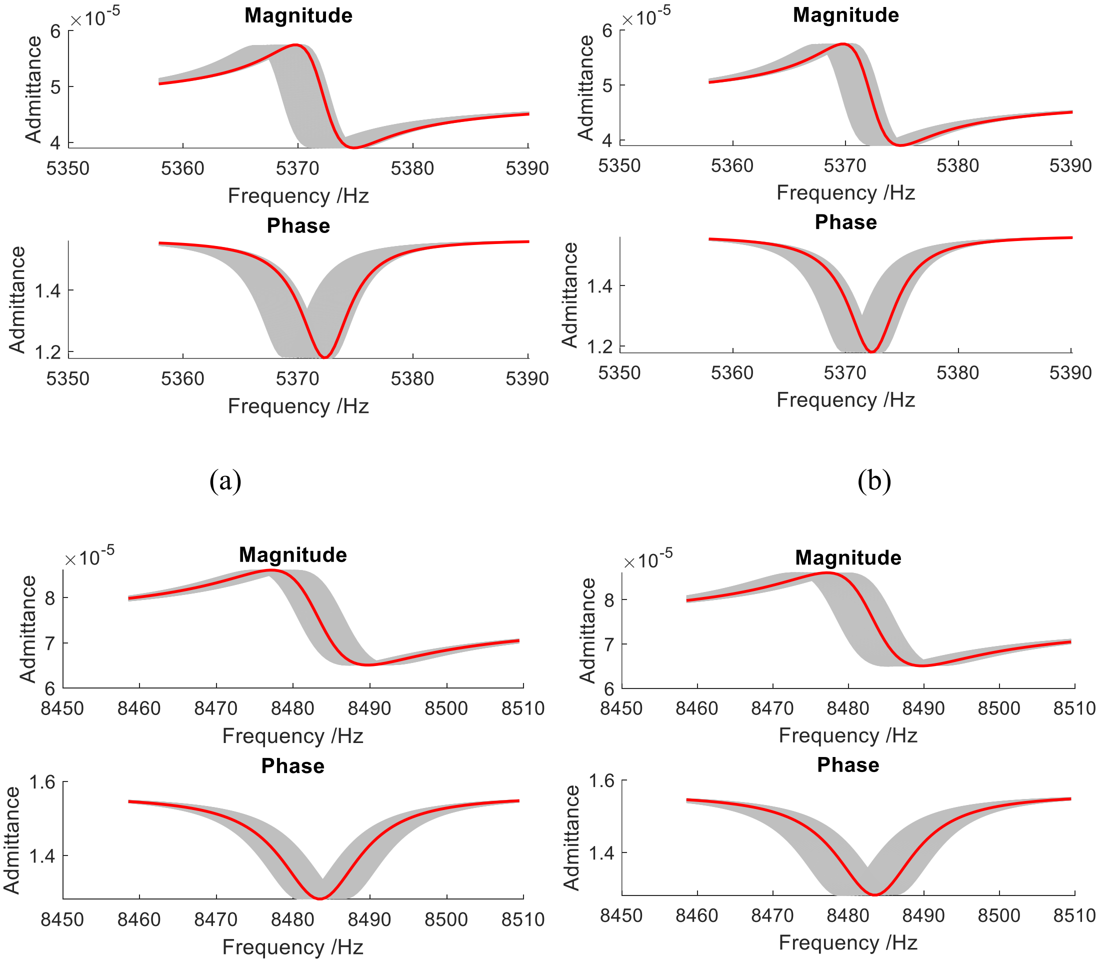

**Figure 6-9.** Envelope comparison among different damaged segments (red curve indicates the curve under actual damage). (a) Admittance under first segment with damage (5,374 Hz); (b) Admittance under second segment with damage (5,374 Hz); (c) Admittance under first segment with damage (8,484 Hz); (d) Admittance under second segment with damage (8,484 Hz).

We conduct the forward Pareto solution domination analysis to assist the suspicious segment identification. According to Equation (6.6), we can calculate the objective values of these 1,000 samples with distributions given in Figure 6-10. In this figure, the horizontal axis represents the two frequency ranges, and the vertical axis represents the objective function values. Since we aim to minimize the objective function, a lower value on the vertical axis indicates a better match. Because two frequency ranges are adopted, 8 objectives are formulated. As can be seen from Figure 6-10, higher-frequency admittance (i.e., 8,484 Hz) appears to be better matched than the lower one. Under certain damage levels, all segments can lead to relatively small objective values, which need to be further differentiated by the following solution domination analysis. The domination analysis is executed upon the entire samples in terms of their objective values, yielding the final 13 Pareto solutions highlighted in red color in Figure 6-10. It is found that all Pareto optimal solutions point to damage occurrence within the second segment. This agrees with the ground truth, which illustrates the feasibility of this particular approach for coarse-level damage localization. To clearly visualize the Pareto solutions and respective Pareto front, we solely plot the objective value trends with respect to the damage level of second segment shown in Figure 6-11. These solutions highlighted with red color indeed can simultaneously minimize all objective values. The effective results provide a solid foundation for implementing the subsequent fine-level damage identification task.

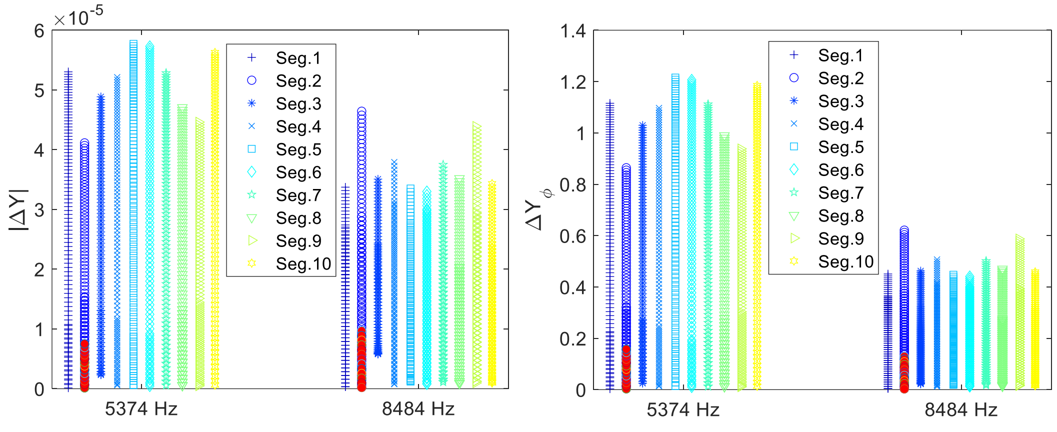

(a) (b)

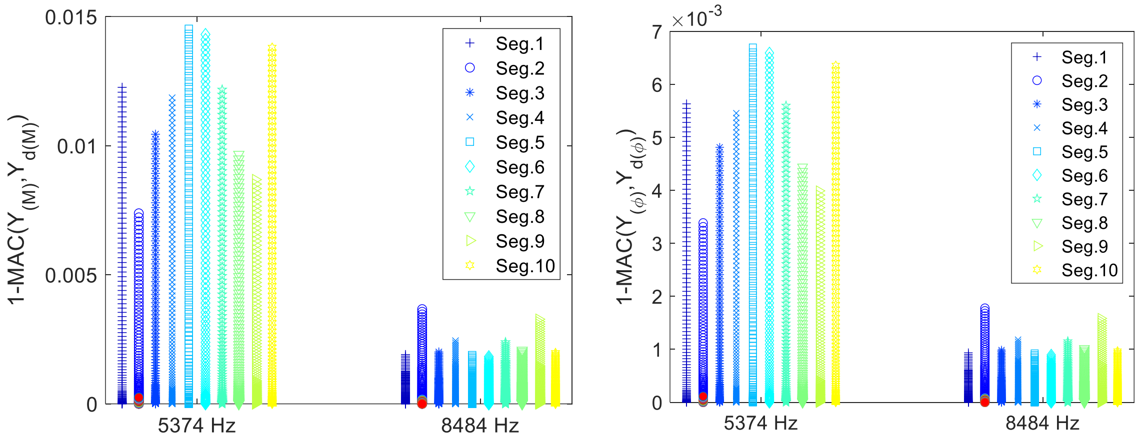

(c)

(d)

**Figure 6-10.** Objective value distribution in original solution database and survived Pareto optimal set (denoted by red color). (a) Magnitude ($\left\|\Delta\mathbf{Y}_{(M)}\right\|_2$); (b) Phase ($\left\|\Delta\mathbf{Y}_{(\phi)}\right\|_2$); (c) $1\text{-MAC}(\mathbf{Y}_{(M)}, \mathbf{Y}_{d(M)})$; (d) $1\text{-MAC}(\mathbf{Y}_{(\phi)}, \mathbf{Y}_{d(\phi)})$.

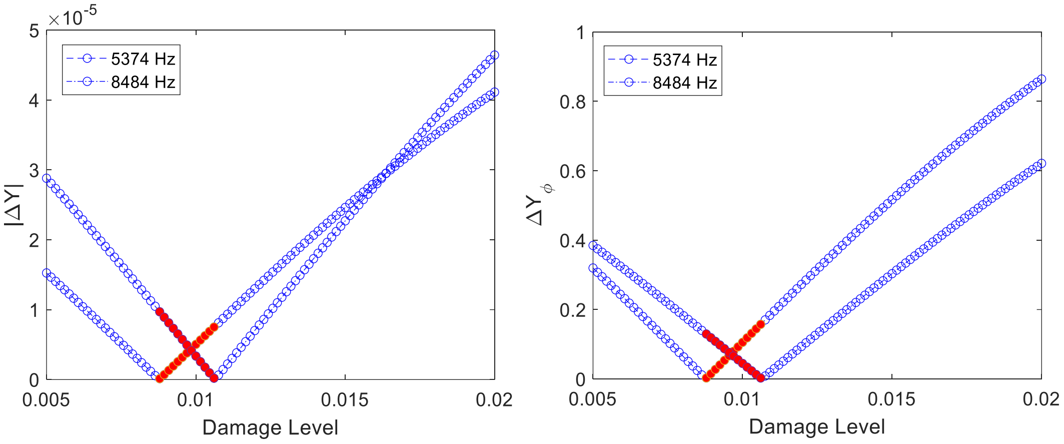

(a)

(b)

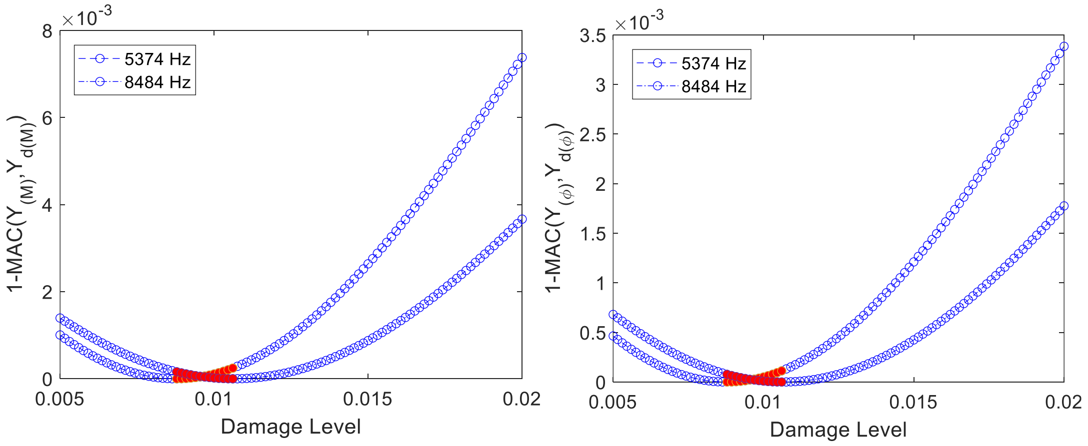

(c) (d)

**Figure 6-11.** Objective value trend with respect to the damage level of the second segment and 13 Pareto optimal solutions (denoted by red color). (a) Magnitude ($\left\|\Delta \mathbf{Y}_{(M)}\right\|_2$); (b) Phase ($\left\|\Delta \mathbf{Y}_{(\phi)}\right\|_2$); (c) 1-MAC($\mathbf{Y}_{(M)}, \mathbf{Y}_{d(M)}$); (d) 1-MAC($\mathbf{Y}_{(\phi)}, \mathbf{Y}_{d(\phi)}$).

### 6.4.4. Fine-level damage identification

Following the results obtained from the previous coarse-level damage localization, we will further conduct the fine-level damage identification detailed in this subsection. The previous results clearly pinpoint that the damage most likely occurs in the second segment. To accurately localize the small-sized damage and identify its severity, we further divide the second segment into 25 small pieces, each containing 20 elements of the same size, i.e., 10 × 4 mm. For validation purposes, the actual small-sized damage is known as piece #12 of the second segment, as shown in Figure 6-12. An inverse optimization problem is formulated to conduct the damage identification, where the stiffness reductions of 25 small pieces ($\boldsymbol{\alpha}$ in Equation (6.7)) represent 25 decision variables. For a problem with a relatively large number of decision variables, a large number of iterations are usually required for the inverse optimization analysis to ensure the high quality of the final solutions. The continuous sample space will cause difficulty in solution search for the optimization problem with such dimension. Instead, owing to the sparse nature of solutions, a discrete sample space is established in advance, upon which sparse sampling is adopted to expedite analysis convergence. As indicated in Section 6.2.2.2, Multi-objective simulated annealing algorithm is used to direct the inverse optimization analysis. The detailed operating parameters are tabulated in Table 6-2. The sparsity is used as an extra metric to evaluate the solution quality. The multiple objectives and entire optimization problem for the fine-level damage identification can be referred to in Equation (6.7).

The Pareto optimal set after optimization solving includes four solutions as illustrated in Figure 6-13. The corresponding Pareto front showing the objective values is given in Table 6-3. Due to the multi-objective optimization setup, we are able to obtain multiple solutions. This is precisely what is needed for structural damage identification. Damage identification is often an under-determined problem, and therefore multiple solutions exist. Thus, the multi-objective setup aligns well with this under-determined problem. Additionally, all solutions yielded are sparse, i.e., only very few non-zero damage level values in the damage vector. Solution 1 essentially represents a healthy structure, as the $l_0$ norm is 0, as shown in Table 6-3. Since we have a multi-objective optimization setup, when $l_0$ is 0, the other objective function values are naturally large. This is true because the impedance of the healthy structure exhibits discrepancy with respect to that of the actual damaged structure. Solution 2 points to the 24th small piece, which clearly deviated from the actual damage location. Solution 3 indicates two damage locations, namely the 12th and 18th small pieces, with damage levels of 0.19 and 0.049, respectively. Clearly, the third solution successfully captures the actual damage location, which is the 12th piece with a damage level of 0.2. Solution 4 identifies the damage location as the 17th small piece, which evidently deviated from the actual damage location. Overall, the entire solution set is small in quantity and has good sparsity. Among them, there is a solution that can capture the actual damage location. In the real world, since we cannot know in advance where the damage is, more post-processing/filtering techniques are needed for damage maintenance and dispatching agents for repair. Because the solution set is small, this will render the post process more efficient.

Overall, the identification result shows good agreement with the ground truth, validating the feasibility of the proposed approach. Once again, while the case investigation in this study illustrates the two-level procedure for damage identification, this framework can be extended into a multi-level scheme if necessary.

This indeed provides a large level of flexibility to pursue solutions with enhanced quality if the two-level procedures don't perform satisfactorily.

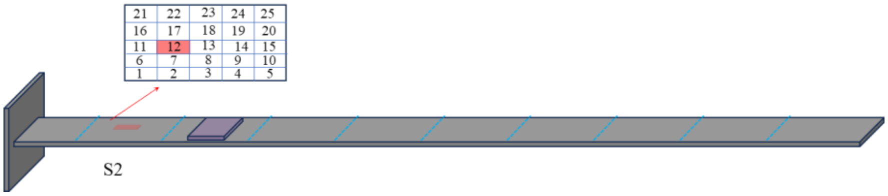

**Figure 6-12.** Further division of the suspicious segment (i.e., second segment) for fine-level damage identification.

**Table 6-2.** Operating parameter set-up of MOSA algorithm.

| | | |
|---|---|---|
| Sparse sampling parameters | Number of increments in sample space | 22 |
| | Sample space range | [0, 1] |
| | Number of solutions in the initial solution pool | 100 |
| | Index of threshold | 5 |
| | Maximum number of non-zero decision variables | 6 |
| SA operating parameters | Initial temperature | 50 |
| | Target temperature | 0.1 |
| | Temperature descent slope | 0.95 |
| | Iteration number at each temperature | 50 |
| | Maximum iteration number | 6,000 |

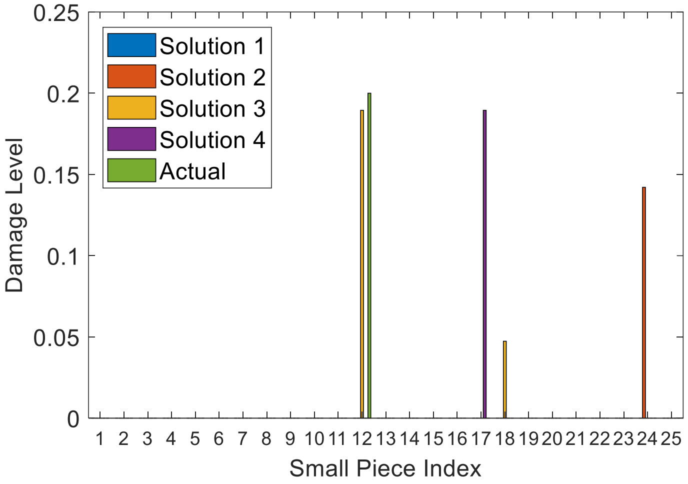

**Figure 6-13.** Pareto optimal solutions that represent the damge vectors identified.

**Table 6-3.** Pareto front (objective values of identified solutions).

| Solution ID | $\left\Vert\Delta\mathbf{Y}_{(M)}\right\Vert_2$ (5374 Hz) | $\left\Vert\Delta\mathbf{Y}_{(\phi)}\right\Vert_2$ (5374 Hz) | $\left\Vert\Delta\mathbf{Y}_{(M)}\right\Vert_2$ (8384 Hz) | $\left\Vert\Delta\mathbf{Y}_{(\phi)}\right\Vert_2$ (8384 Hz) | $\left\Vert\boldsymbol{\alpha}\right\Vert_0$ |
|---|---|---|---|---|---|
| 1 | $3.3499\times10^{-5}$ | 0.7028 | $5.0969\times10^{-5}$ | 0.6814 | 0 |
| 2 | $3.9706\times10^{-7}$ | 0.0086 | $3.1220\times10^{-5}$ | 0.4171 | 1 |
| 3 | $1.3799\times10^{-5}$ | 0.2895 | $6.2344\times10^{-7}$ | 0.0082 | 2 |
| 4 | $9.4922\times10^{-7}$ | 0.0198 | $1.4582\times10^{-6}$ | 0.0194 | 1 |

## 6.5. Conclusion

While structural damage detection using piezoelectric admittance has shown promising aspects, the inverse identification of damage location and severity remains to be a hurdle. This study addresses the intricate challenge of structural damage identification using piezoelectric admittance by formulating it as a multi-objective optimization problem. By leveraging the sparsity nature of the damage index and minimizing discrepancies between experimental and model predictions, we present an approach that enhances the efficiency while maintaining accuracy of damage identification processes. The introduction of five distinct local search strategies, tailored for the optimization process, marks an improvement in optimizing solution diversity and convergence accuracy. The employment of Learning Automata as a decision-making tool for strategy selection enables a self-adaptive optimization process that eschews the need for predetermined reward strategies. The introduction of a hierarchical framework that leverages Group Lasso and TOPSIS for effective inter-stage communication has refined the optimization process, as evidenced by the validation on a piezoelectric admittance sensing testbed. Different case studies are designed to examine the capability of the proposed approaches including hierarchical framework and optimizer to identify the true damage scenario using experimental data indicates. The results obtained indicate that the proposed two-stage approach accurately identifies both damage location and severity. Additionally, the enhanced optimizer generates a small solution set while maintaining identification accuracy. This enhanced inverse analysis approach has potential applications in structural damage identification using other types of measurements. Future research could focus on thorough efficiency comparisons between two-stage and one-step methods.

# Chapter 7. Concluding Remarks

In this research, early damage identification is conducted by fully unleashing the capability of piezoelectric impedance measurement measured in high-frequency range. While promising, the measurement information of piezoelectric impedance change is generally limited, oftentimes leading to an under-determined problem for damage identification. Early-stage damage typically affects only small areas, allowing us to frame the problem as a multi-objective optimization that minimizes the difference between model predictions and physical measurements while enforcing sparsity in damaged locations. This setup often produces multiple solutions, a natural fit for structural damage identification. To effectively solve the inverse problem while addressing challenges such as underdetermination, sparsity, high dimensionality, and multimodality, several interconnected studies are conducted. The main contributions are highlighted as follows:

1) A Sparsity-Aware Metaheuristic Algorithm is developed to handle the $l_0$ norm directly, guiding the search toward sparse solutions that prioritize limited regions for structural maintenance. This approach is further strengthened by 2) Enhanced Optimization with Local Search and Reinforcement Learning, where various local search strategies and adaptive reinforcement learning techniques, such as Q-learning and learning automata, are employed to improve optimization through accumulated search experience and interactions with the environment. Additionally, 3) Tunable Circuitry for Measurement Enrichment is integrated into the piezoelectric transducer system, adjusting inductance values to enrich measurements and mitigate underdetermination by generating diverse datasets for each damage profile. 4) A Hierarchical Damage Identification Framework is also introduced, segmenting the structure into groups and using group Lasso to achieve damage identification in stages: the first stage promotes sparsity at the group level, and the second stage pinpoints the specific group with potential damage. 5) Model Order Reduction is then applied using Component Mode Synthesis to develop reduced-order models of the PZT-enhanced plate structure, enabling efficient forward analysis to approximate damage locations within substructures, followed by inverse model updating to determine damage location and severity. These approaches are

validated through experimental piezoelectric impedance data, consistently yielding compact, diverse solution sets that include the true damage scenarios.

The methodologies and findings from this dissertation open numerous possibilities for applications across various fields, extending the impact of this work beyond its original scope. In structural engineering, the approaches developed here, such as sparsity generation, reinforcement learning guided metaheuristics, can enhance structural optimal design by addressing large-scale, sparse, multi-objective optimization challenges with improved precision and efficiency. The mechatronics integration, i.e., the tunable inductor circuitry, also offer contributions to mechanical metamaterial design, particularly for creating wave-guiding structures, and can support data enrichment processes critical for deep learning applications by generating diverse and enriched datasets. Beyond these areas, the reinforcement learning enhanced metaheuristics established in this research provide new pathways for dynamic optimization, facilitating advancements in path planning, multi-swarm tasks, obstacle avoidance and traffic prediction, where real-time optimization is essential. The work also presents potential benefits for optimizing neural network architectures and structural designs through innovative applications in surrogate modeling and sparse representation like dictionary learning etc. Collectively, these possibilities demonstrate the broader relevance of this dissertation's contributions, highlighting its value as a resource for future exploration and adaptation in emerging fields.

Building on the insights gained in this dissertation, several related topics present exciting opportunities for future research in structural health monitoring (SHM). One promising avenue is the integration of agent-in-the-loop optimization frameworks, where agents can dynamically guide optimization processes, enabling adaptive and efficient solutions for complex structural problems. Another area of exploration is the application of graph neural networks (GNNs) for structural modeling, which could pave the way for digital twin technologies to enable real-time monitoring and predictive capabilities. Additionally, advanced methods such as dictionary learning, physics-informed neural networks (PINNs), and operator learning offer significant potential for uncertainty quantification and data-driven system identification, especially in scenarios with limited or sparse measurements. These directions, grounded in the current understanding of SHM, could contribute to the development of robust, scalable, and intelligent monitoring frameworks for the future.

# References

Ai, D., Luo, H., Wang, C. and Zhu, H., Monitoring of the load-induced RC beam structural tension/compression stress and damage using piezoelectric transducers. Engineering Structures, 154 (2018), 38-51.

Ai, D., Mo, F., Han, Y. and Wen, J., Automated identification of compressive stress and damage in concrete specimen using convolutional neural network learned electromechanical admittance. Engineering Structures, 259 (2022), 114176.

Ai, D. and Zhang, R., Deep learning of electromechanical admittance data augmented by generative adversarial networks for flexural performance evaluation of RC beam structure. Engineering Structures, 296 (2023), 116891.

Alkayem, N.F., Cao, M., Zhang, Y., Bayat, M. and Su, Z., Structural damage detection using finite element model updating with evolutionary algorithms: a survey. Neural Computing and Applications, 30 (2018), 389-411.

Allen, M.S., Rixen, D., Van der Seijs, M., Tiso, P., Abrahamsson, T. and Mayes, R.L., Substructuring in engineering dynamics. Springer International Publishing, (2020).

Aller, B., Pellegrino, S., Kinkaid, N., Mejia-Ariza, J., Chan, P. and Pena, F., Health monitoring of high strain composites using embedded fiber bragg grating sensors. In AIAA SciTech 2022 Forum, (2022) (p. 1622).

Avci, O., Abdeljaber, O., Kiranyaz, S., Hussein, M., Gabbouj, M. and Inman, D.J., A review of vibration-based damage detection in civil structures: from traditional methods to machine learning and deep learning applications. Mechanical Systems and Signal Processing, 147 (2021), 107077.

Butland, A. and Avitabile, P., A reduced order, test verified component mode synthesis approach for system modeling applications. Mechanical Systems and Signal Processing, 24(4) (2010), 904-921.

Brehm, M., Zabel, V. and Bucher, C., An automatic mode pairing strategy using an enhanced modal assurance criterion based on modal strain energies. Journal of Sound and Vibration, 329 (2010), 5375-5392.

Besselink, B., Tabak, U., Lutowska, A., Van De Wouw, N., Nijmeijer, H., Rixen, D.J., Hochstenbach, M.E. and Schilders, W.H.A., A comparison of model reduction techniques from structural dynamics, numerical mathematics and systems and control. Journal of Sound and Vibration, 332 (2013), 4403-4422.

Bertero, M., Boccacci, P. and De Mol, C., Introduction to inverse problems in imaging. CRC Press, (2021).

Barman, S.K., Maiti, D.K. and Maity, D., Vibration-based delamination detection in composite structures employing mixed unified particle swarm optimization. AIAA Journal, 59(1) (2021), 386-399.

Boukabache, H., Escriba, C., Zedek, S., Medale, D., Rolet, S. and Fourniols, J.Y., System-on-chip integration of a new electromechanical impedance calculation method for aircraft structure health monitoring. Sensors, 12(10) (2012), 13617-13635.

Craig, R.R. Jr. and Bampton, M.C.C., Coupling of substructures for dynamic analyses. AIAA Journal, 6 (1968), 1313-1319.

Chakraborty, A., Ghosh, K.K., De, R., Cuevas, E. and Sarkar, R., Learning automata based particle swarm optimization for solving class imbalance problem. Applied Soft Computing, 113 (2021), 107959.

Coello, C.A.C., Pulido, G.T. and Lechuga, M.S., Handling multiple objectives with particle swarm optimization. IEEE Transactions on Evolutionary Computation, 8(3) (2004), 256-279.

Črepinšek, M., Liu, S.H. and Mernik, M., Exploration and exploitation in evolutionary algorithms: a survey. ACM Computing Surveys (CSUR), 45(3) (2013), 1-33.

Chen, S., Lin, W., Yu, J. and Qi, A., Free-interface modal synthesis based substructural damage detection method. Shock and Vibration, 2014(1) (2014), 741697.

Cao, P., Shuai, Q. and Tang, J., Structural damage identification using piezoelectric impedance measurement with sparse inverse analysis. Smart Materials and Structures, 27(3) (2018a), 035020.

Cao, P., Shuai, Q. and Tang, J., A multi-objective DIRECT algorithm toward structural damage identification with limited dynamic response information. Journal of Nondestructive Evaluation, Diagnostics and Prognostics of Engineering Systems, 1(2) (2018b), 021004.

Cao, Z., Fei, Q., Jiang, D., Zhang, D., Jin, H. and Zhu, R., Dynamic sensitivity-based finite element model updating for nonlinear structures using time-domain responses. International Journal of Mechanical Sciences, 184 (2020).

Cao, P., Zhang, Y., Zhou, K. and Tang, J., A reinforcement learning hyper-heuristic in multi-objective optimization with application to structural damage identification. Structural and Multidisciplinary Optimization, 66(1) (2023a), 16.

Cao, P., Zhang, S., Wang, Z. and Zhou, K., Damage identification using piezoelectric electromechanical impedance: a brief review from a numerical framework perspective. Structures, 50 (2023b), 1906-1921.

Chen, Z. and Sun, H., Sparse representation for damage identification of structural systems. Structural Health Monitoring, 20(4) (2021), 1644-1656.

Cha, Y.J. and Buyukozturk, O., Structural damage detection using modal strain energy and hybrid multiobjective optimization. Computer-Aided Civil and Infrastructure Engineering, 30(5) (2015), 347-358.

Challapalli, A., Patel, D. and Li, G., Inverse machine learning framework for optimizing lightweight metamaterials. Materials & Design, 208 (2021), 109937.

Davenport, M.A., Duarte, M.F., Eldar, Y.C. and Kutyniok, G., Introduction to compressed sensing. (2012), 1-64.

Ding, Z., Li, J. and Hao, H., Structural damage identification using improved Jaya algorithm based on sparse regularization and Bayesian inference. Mechanical Systems and Signal Processing, 132 (2019), 211-231.

Ding, Z., Li, J. and Hao, H., Non-probabilistic method to consider uncertainties in structural damage identification based on Hybrid Jaya and Tree Seeds Algorithm. Engineering Structures, 220 (2020), 110925.

Ding, Z., Hou, R. and Xia, Y., Structural damage identification considering uncertainties based on a Jaya algorithm with a local pattern search strategy and L0.5 sparse regularization. Engineering Structures, 261 (2022), 114312.

Ding, Z., Li, L., Wang, X., Yu, T. and Xia, Y., Vibration-based FRP debonding detection using a Q-learning evolutionary algorithm. Engineering Structures, 275 (2023), 115254.

Deb, K., Agrawal, S., Pratap, A. and Meyarivan, T., A fast elitist non-dominated sorting genetic algorithm for multi-objective optimization: NSGA-II. In *Parallel Problem Solving from Nature PPSN VI: 6th International Conference Paris, France, September 18–20, 2000 Proceedings 6* (pp. 849-858). Springer Berlin Heidelberg.

Dash, M. and Liu, H., Feature selection for classification. Intelligent Data Analysis, 1(1-4) (1997), 131-156.

Dinh-Cong, D., Vo-Duy, T., Ho-Huu, V. and Nguyen-Thoi, T., Damage assessment in plate-like structures using a two-stage method based on modal strain energy change and Jaya algorithm. Inverse Problems in Science and Engineering, 27(2) (2019), 166-189.

Du, Dinh-Cong and Nguyen-Thoi, T., An effective damage identification procedure using model updating technique and multi-objective optimization algorithm for structures made of functionally graded materials. Engineering with Computers, 39 (2023), 1229-1247.

Dimopoulos, V., Desmet, W. and Deckers, E., Sparse damage detection with complex group lasso and adaptive complex group lasso. Sensors, 22(8) (2022), 2978.

Dutta, A., McKay, M.E., Kopsaftopoulos, F. and Gandhi, F., Multicopter fault detection and identification via data-driven statistical learning methods. AIAA Journal, 60(1) (2022), 160-175.

Ezzat, A.A., Tang, J. and Ding, Y., A model-based calibration approach for structural fault diagnosis using piezoelectric impedance measurements and a finite element model. Structural Health Monitoring, 19(6) (2020), 1839-1855.

Foucart, S. and Rauhut, H., A mathematical introduction to compressive sensing. Birkhäuser Basel, (2013).

Fu, H., Khodaei, Z.S. and Aliabadi, M.F., An event-triggered energy-efficient wireless structural health monitoring system for impact detection in composite airframes. IEEE Internet of Things Journal, 6(1) (2018), 1183-1192.

Friedrich, T., Horoba, C. and Neumann, F., Multiplicative approximations and the hypervolume indicator. In Proceedings of the 11th Annual Conference on Genetic and Evolutionary Computation, (2009), 571-578.

Fan, X., Li, J. and Hao, H., Impedance resonant frequency sensitivity based structural damage identification with sparse regularization: experimental studies. Smart Materials and Structures, 28(1) (2019), 015003.

Fan, X. and Li, J., Damage identification in plate structures using sparse regularization based electromechanical impedance technique. Sensors, 20(24) (2020), 7069.

Gad, A.G., Particle swarm optimization algorithm and its applications: a systematic review. Archives of Computational Methods in Engineering, 29(5) (2022), 2531-2561.

Greś, S., Döhler, M. and Mevel, L., Statistical model-based optimization for damage extent quantification. Mechanical Systems and Signal Processing, 160 (2021), 107894.

Gomes, G.F., Mendéz, Y.A.D., da Cunha, S.S. and Ancelotti, A.C., A numerical–experimental study for structural damage detection in CFRP plates using remote vibration measurements. Journal of Civil Structural Health Monitoring, 8 (2018), 33-47.

Greco, S., Ehrgott, M. and Figueira, J.R. (eds), Multiple Criteria Decision Analysis: State of the Art Surveys. *International Series in Operations Research & Management Science*, vol. 233, Springer New York, New York, NY, (2016).

Gao, F., Shao, Y., Hua, J., Zeng, L. and Lin, J., Enhanced wavefield imaging method for impact damage detection in composite laminates via laser-generated Lamb waves. Measurement, 173 (2021), 108639.

Gordan, M., Ismail, Z., Abdul Razak, H., Ghaedi, K., Ibrahim, Z., Tan, Z.X. and Ghayeb, H.H., Data mining-based damage identification of a slab-on-girder bridge using inverse analysis. Measurement, 151 (2020), 107175.

Hurty, W.C., Dynamic analysis of structural systems using component modes. AIAA Journal, 3 (1965), 678-685.

Hadamard, J., Sur les problèmes aux dérivées partielles et leur signification physique. Princeton University Bulletin, (1902), 49-52.

Hoshyarmanesh, H. and Abbasi, A., Structural health monitoring of rotary aerospace structures based on electromechanical impedance of integrated piezoelectric transducers. Journal of Intelligent Material Systems and Structures, 29(9) (2018), 1799-1817.

Hashemi, A.B. and Meybodi, M.R., A note on the learning automata based algorithms for adaptive parameter selection in PSO. Applied Soft Computing, 11(1) (2011), 689-705.

Hou, R. and Xia, Y., Review on the new development of vibration-based damage identification for civil engineering structures: 2010–2019. Journal of Sound and Vibration, 491 (2021), 115741.

Ishibuchi, H., Imada, R., Setoguchi, Y. and Nojima, Y., Reference point specification in inverted generational distance for triangular linear Pareto front. IEEE Transactions on Evolutionary Computation, 22(6) (2018), 961-975.

Inman, D.J. and Grisso, B.L., Adaptive structures for structural health monitoring. In *Adaptive Structures: Engineering Applications*, edited by D. Wagg, I. Bond, P. Weaver, and M. Friswell, 1-22. John Wiley & Sons, Chichester, UK, (2007).

Jiang, L.J., Tang, J. and Wang, K.W., An enhanced frequency-shift-based damage identification method using tunable piezoelectric transducer circuitry. Smart Materials and Structures, 15(3) (2006), 799.

Jiang, L.J., Tang, J. and Wang, K.W., An optimal sensitivity-enhancing feedback control approach via eigenstructure assignment for structural damage identification. Journal of Vibration and Acoustics, 129(6) (2007), 771-783.

Jiang, L.J., Tang, J. and Wang, K.W., On the tuning of variable piezoelectric transducer circuitry network for structural damage identification. Journal of Sound and Vibration, 309(3-5) (2008), 695-717.

Ji, Z., Liao, H., Wang, Y. and Wu, Q.H., A novel intelligent particle optimizer for global optimization of multimodal functions. 2007 IEEE Congress on Evolutionary Computation, Singapore, (2007), 3272-3275.

Jin, S.S., Cho, S., Jung, H.J., Lee, J.J. and Yun, C.B., A new multi-objective approach to finite element model updating. Journal of Sound and Vibration, 333(11) (2014), 2323-2338.

Jin, S.S. and Jung, H.J., Sequential surrogate modeling for efficient finite element model updating. Computers and Structures, 168 (2016), 30-45.

Kennedy, J. and Eberhart, R., Particle swarm optimization. In *Proceedings of ICNN'95 International Conference on Neural Networks*, 4 (1995), 1942-1948. IEEE.

Kim, J. and Wang, K.W., An enhanced impedance-based damage identification method using adaptive piezoelectric circuitry. Smart Materials and Structures, 23(9) (2014), 095041.

Kim, J., Harne, R.L. and Wang, K.W., Enhancing structural damage identification robustness to noise and damping with integrated bistable and adaptive piezoelectric circuitry. Journal of Vibration and Acoustics, 137(1) (2015), 011003.

Kim, J. and Wang, K.W., Electromechanical impedance-based damage identification enhancement using bistable and adaptive piezoelectric circuitry. Structural Health Monitoring, 18(4) (2019), 1268-1281.

Kumar, S. and Sunny, M.R., Data-driven Lamb-wave-based approach to detect multiple structural damages. AIAA Journal, 59(6) (2021), 2339-2345.

Langer, P., Maeder, M., Guist, C., Krause, M. and Marburg, S., More than six elements per wavelength: the practical use of structural finite element models and their accuracy in comparison with experimental results. Journal of Computational Acoustics, 25 (2017), 1-23.

Liu, Y. and Chattopadhyay, A., Low-velocity impact damage monitoring of a sandwich composite wing. Journal of Intelligent Material Systems and Structures, 24(17) (2013), 2074-2083.

Lim, W.H. and Isa, N.A.M., Two-layer particle swarm optimization with intelligent division of labor. Engineering Applications of Artificial Intelligence, 26(10) (2013), 2327-2348.

Li, H., Ai, D., Zhu, H. and Luo, H., An orthogonal matching pursuit based signal compression and reconstruction approach for electromechanical admittance based structural health monitoring. Mechanical Systems and Signal Processing, 133 (2019), 106276.

Lin, T.Y., Tao, J. and Huang, H.H., A multiobjective perspective to optimal sensor placement by using a decomposition-based evolutionary algorithm in structural health monitoring. Applied Sciences, 10(21) (2020), 7710.

Li, X., Niu, S., Bao, H. and Hu, N., Improved adaptive multi-objective particle swarm optimization of sensor layout for shape sensing with inverse finite element method. Sensors, 22(14) (2022), 5203.

Lin, Q., Li, J., Du, Z., Chen, J. and Ming, Z., A novel multi-objective particle swarm optimization with multiple search strategies. European Journal of Operational Research, 247(3) (2015), 732-744.

Lin, Q., Liu, S., Zhu, Q., Tang, C., Song, R., Chen, J., Coello, C.A.C., Wong, K.C. and Zhang, J., Particle swarm optimization with a balanceable fitness estimation for many-objective optimization problems. IEEE Transactions on Evolutionary Computation, 22(1) (2018), 32-46.

Livani, M.A., Khaji, N. and Zakian, P., Identification of multiple flaws in 2D structures using dynamic extended spectral finite element method with a universally enhanced meta-heuristic optimizer. Structural and Multidisciplinary Optimization, 57 (2018), 605-623.

Li, Y.F., Minh, H.L., Khatir, S., Sang-To, T., Cuong-Le, T., MaoSen, C. and Wahab, M.A., Structure damage identification in dams using sparse polynomial chaos expansion combined with hybrid K-means clustering optimizer and genetic algorithm. Engineering Structures, 283 (2023), 115891.

Lin, Y., Theiler, J. and Wohlberg, B., Physics-guided data-driven seismic inversion: recent progress and future opportunities in full-waveform inversion. IEEE Signal Processing Magazine, 40(1) (2023), 115-133.

Lin, Y., Bao, L. and Wei, Y., Order reduction of bilinear MIMO dynamical systems using new block Krylov subspaces. Computers and Mathematics with Applications, 58 (2009), 1093-1102.

Masson, G., Ait Brik, B., Cogan, S. and Bouhaddi, N., Component mode synthesis (CMS) based on an enriched Ritz approach for efficient structural optimization. Journal of Sound and Vibration, 296 (2006), 845-860.

Min, J., Park, S., Yun, C.B., Lee, C.G. and Lee, C., Impedance-based structural health monitoring incorporating neural network technique for identification of damage type and severity. Engineering Structures, 39 (2012), 210-220.

Ming, F., Gong, W. and Gao, L., Adaptive auxiliary task selection for multitasking-assisted constrained multi-objective optimization. IEEE Computational Intelligence Magazine, 18(2) (2023), 18-30.

Meerza, S.I.A., Islam, M. and Uzzal, M.M., Q-learning based particle swarm optimization algorithm for optimal path planning of swarm of mobile robots. In *2019 1st International Conference on Advances in Science, Engineering and Robotics Technology (ICASERT)* (2019), 1-5. IEEE.

Minh, H.L., Khatir, S., Wahab, M.A. and Cuong-Le, T., An enhancing particle swarm optimization algorithm (EHVPSO) for damage identification in 3D transmission tower. Engineering Structures, 242 (2021), 112412.

Noel, M.M., A new gradient-based particle swarm optimization algorithm for accurate computation of global minimum. Applied Soft Computing, 12(1) (2012), 353-359.

Nguyen-Tuan, L. and Könke, C., Lahmer, T., Damage identification using inverse analysis for 3D coupled thermo-hydro-mechanical problems. Computers and Structures, 196 (2018), 146-156.

Panayirci, H.M., Pradlwarter, H.J. and Schuëller, G.I., Efficient stochastic structural analysis using Guyan reduction. Advances in Engineering Software, 42 (2011), 187-196.

Perera, R., Sandercock, S. and Carnicero, A., Civil structure condition assessment by a two-stage FE model update based on neural network enhanced power mode shapes and an adaptive roaming damage method. Engineering Structures, 207 (2020), 110234.

Pereira, J.L.J., Francisco, M.B., de Oliveira, L.A., Chaves, J.A.S., Cunha Jr, S.S. and Gomes, G.F., Multi-objective sensor placement optimization of helicopter rotor blade based on feature selection. Mechanical Systems and Signal Processing, 180 (2022), 109466.

Park, G., Sohn, H., Farrar, C.R. and Inman, D.J., Overview of piezoelectric impedance-based health monitoring and path forward. Shock and Vibration Digest, 35(6) (2003), 451-464.

Qian, C., Yu, Y. and Zhou, Z.H., Subset selection by Pareto optimization. Advances in Neural Information Processing Systems, 28 (2015).

Ratnaweera, A., Halgamuge, S.K. and Watson, H.C., Self-organizing hierarchical particle swarm optimizer with time-varying acceleration coefficients. IEEE Transactions on Evolutionary Computation, 8(3) (2004), 240-255.

Ren, H., Chen, X. and Chen, Y., Structural health monitoring and influence on current maintenance. In *Aerospace Engineering*, edited by H. Ren and X. Chen, Academic Press, (2017), 173-184.

Sarsri, D. and Azrar, L., Dynamic analysis of large structures with uncertain parameters based on coupling component mode synthesis and perturbation method. Ain Shams Engineering Journal, 7(1) (2016), 371-381.

Sung, H., Chang, S. and Cho, M., Efficient model updating method for system identification using a convolutional neural network. AIAA Journal, 59(9) (2021), 3480-3489.

Shuai, Q., Zhou, K., Zhou, S. and Tang, J., Fault identification using piezoelectric impedance measurement and model-based intelligent inference with pre-screening. Smart Materials and Structures, 26(4) (2017), 045007.

Selva, P., Cherrier, O., Budinger, V., Lachaud, F. and Morlier, J., Smart monitoring of aeronautical composites plates based on electromechanical impedance measurements and artificial neural networks. Engineering Structures, 56 (2013), 794-804.

Samma, H., Lim, C.P. and Saleh, J.M., A new reinforcement learning-based memetic particle swarm optimizer. Applied Soft Computing, 43 (2016), 276-297.

Soman, R., Sequential niching particle swarm optimization algorithm for localization of multiple damage locations using fiber Bragg grating sensors. NDT & E International, 143 (2024), 103069.

Shi, Y. and Eberhart, R.C., Empirical study of particle swarm optimization. In *Proceedings of the 1999 Congress on Evolutionary Computation (CEC)*, 3 (1999), 1945-1950.

Shi, B., Cao, M., Wang, Z. and Ostachowicz, W., A directional continuous wavelet transform of mode shape for line-type damage detection in plate-type structures. Mechanical Systems and Signal Processing, 167 (2022), 108510.

Sang-To, T., Le-Minh, H., Mirjalili, S., Wahab, M.A. and Cuong-Le, T., A new movement strategy of grey wolf optimizer for optimization problems and structural damage identification. Advances in Engineering Software, 173 (2022), 103276.

Tian, Y., Cheng, R., Zhang, X. and Jin, Y., PlatEMO: A MATLAB platform for evolutionary multi-objective optimization [educational forum]. IEEE Computational Intelligence Magazine, 12(4) (2017), 73-87.

Tian, Y., Zhang, X., Wang, C. and Jin, Y., An evolutionary algorithm for large-scale sparse multiobjective optimization problems. IEEE Transactions on Evolutionary Computation, 24(2) (2019a), 380-393.

Tian, Y., Cheng, R., Zhang, X., Li, M. and Jin, Y., Diversity assessment of multi-objective evolutionary algorithms: performance metric and benchmark problems [research frontier]. IEEE Computational Intelligence Magazine, 14(3) (2019b), 61-74.

Tian, Y., Li, X., Ma, H., Zhang, X., Tan, K.C. and Jin, Y., Deep reinforcement learning based adaptive operator selection for evolutionary multi-objective optimization. IEEE Transactions on Emerging Topics in Computational Intelligence, 7(4) (2023), 1051-1064.

Tiachacht, S., Bouazzouni, A., Khatir, S., Wahab, M.A., Behtani, A. and Capozucca, R., Damage assessment in structures using combination of a modified Cornwell indicator and genetic algorithm. Engineering Structures, 177 (2018), 421-430.

Vogel, C.R., Computational methods for inverse problems. SIAM, (2002).

Ventresca, M., Harrison, K.R. and Ombuki-Berman, B.M., The bi-objective critical node detection problem. European Journal of Operational Research, 265(3) (2018), 895-908.

Voutetaki, M.E., Papadopoulos, N.A., Angeli, G.M. and Providakis, C.P., Investigation of a new experimental method for damage assessment of RC beams failing in shear using piezoelectric transducers. Engineering Structures, 114 (2016), 226-240.

Wang, X. and Tang, J., Damage identification using piezoelectric impedance approach and spectral element method. Journal of Intelligent Material Systems and Structures, 20(8) (2009), 907-921.

Wang, T., He, J., Hou, S., Deng, X., Xi, C. and He, H., Complex component mode synthesis method using hybrid coordinates for generally damped systems with local nonlinearities. Journal of Sound and Vibration, 476 (2020), 115299.

Watkins, C.J. and Dayan, P., Q-learning. Machine Learning, 8 (1992), 279-292.

Wang, X. and Tang, J., An enhanced piezoelectric impedance approach for damage detection with circuitry integration. Smart Materials and Structures, 19(4) (2010a), 045001.

Wang, X. and Tang, J., Damage detection using piezoelectric admittance approach with inductive circuitry. Journal of Intelligent Material Systems and Structures, 21(7) (2010b), 667-676.

Weng, S., Zhu, H., Xia, Y., Li, J. and Tian, W., A review on dynamic substructuring methods for model updating and damage detection of large-scale structures. Advances in Structural Engineering, 23(3) (2020), 584-600.

Wang, T., He, H., Yan, W. and Chen, G.P., A model-updating approach based on the component mode synthesis method and perturbation analysis. Journal of Sound and Vibration, 433 (2018), 349-365.

Xu, C. and Deng, M., Lamb wave imaging based on multi-frequency sparse decomposition. Mechanical Systems and Signal Processing, 174 (2022), 109076.

Xue, B., Zhang, M. and Browne, W.N., Particle swarm optimization for feature selection in classification: a multi-objective approach. IEEE Transactions on Cybernetics, 43(6) (2012), 1656-1671.

Xu, Y., Ding, O., Qu, R. and Li, K., Hybrid multi-objective evolutionary algorithms based on decomposition for wireless sensor network coverage optimization. Applied Soft Computing, 68 (2018), 268-282.

Yao, R., Pakzad, S.N. and Venkitasubramaniam, P., Compressive sensing based structural damage detection and localization using theoretical and metaheuristic statistics. Structural Control and Health Monitoring, 24(4) (2017), e1881.

Yue, C., Qu, B. and Liang, J., A multiobjective particle swarm optimizer using ring topology for solving multimodal multiobjective problems. IEEE Transactions on Evolutionary Computation, 22(5) (2018), 805-817.

Yuan, S., Ren, Y., Qiu, L. and Mei, H., A multi-response-based wireless impact monitoring network for aircraft composite structures. IEEE Transactions on Industrial Electronics, 63(12) (2016), 7712-7722.

Yu, J.X., Xia, Y., Lin, W. and Zhou, X.Q., Element-by-element model updating of large-scale structures based on component mode synthesis method. Journal of Sound and Vibration, 362 (2016), 72-84.

Zhao, J., Tang, J. and Wang, K.W., Enhanced statistical damage identification using frequency-shift information with tunable piezoelectric transducer circuitry. Smart Materials and Structures, 17(6) (2008), 065003.

Zhao, S., Fan, S. and Chen, J., Quantitative assessment of the concrete gravity dam damage under earthquake excitation using electro-mechanical impedance measurements. Engineering Structures, 191 (2019), 162-178.

Zitzler, E., Deb, K. and Thiele, L., Comparison of multiobjective evolutionary algorithms: empirical results. Evolutionary Computation, 8(2) (2000), 173-195.

Zhang, Q., Zhou, A., Zhao, S., Suganthan, P.N., Liu, W. and Tiwari, S., Multiobjective optimization test instances for the CEC 2009 special session and competition. University of Essex, Colchester, UK and Nanyang Technological University, Singapore, special session on performance assessment of multi-objective optimization algorithms, technical report, (2008), 264.

Zhang, Z. and Sun, C., Structural damage identification via physics-guided machine learning: a methodology integrating pattern recognition with finite element model updating. Structural Health Monitoring, 20(4) (2021), 1675-1688.

Zhu, J., Qing, X., Liu, X. and Wang, Y., Electromechanical impedance-based damage localization with novel signatures extraction methodology and modified probability-weighted algorithm. Mechanical Systems and Signal Processing, 146 (2021), 107001.

Zheng, T., Luo, W., Liang, X. and Tong, H., Damage identification for functionally graded materials using improved experience-based learning algorithm based on sparse regularization. Engineering Optimization, (2022), 1-20.

Zhang, Q. and Li, H., MOEA/D: A multiobjective evolutionary algorithm based on decomposition. IEEE Transactions on Evolutionary Computation, 11(6) (2007), 712-731.

Zhang, Y., Zhou, K. and Tang, J., Piezoelectric impedance-based high-accuracy damage identification using sparsity conscious multi-objective optimization inverse analysis. Mechanical Systems and Signal Processing, 209 (2024a), 111093.

Zhang, G., Kang, J., Wan, C., Xie, L. and Xue, S., Output-only structural damage identification based on Q-learning hybrid evolutionary algorithm and response reconstruction technique. Measurement, 224 (2024b), 113951.

Zhang, Y., Zhou, K. and Tang, J., Harnessing collaborative learning automata to guide multi-objective optimization based inverse analysis for structural damage identification. Applied Soft Computing, 160 (2024c), 111697.

Zhang, X., Wang, H., Hou, B., Xu, J. and Yan, R., 1D-CNN-based damage identification method based on piezoelectric impedance using adjustable inductive shunt circuitry for data enrichment. Structural Health Monitoring, 21(5) (2022a), 1992-2009.

Zhang, L., Liang, Y. and Yu, L., Moving force identification based on group lasso and compressed sensing. International Journal of Structural Stability and Dynamics, 22(15) (2022b), 2250170.

Zhang, Z., Wang, D. and Gao, J., Learning automata-based multiagent reinforcement learning for optimization of cooperative tasks. IEEE Transactions on Neural Networks and Learning Systems, 32(10) (2020), 4639-4652.

Zhou, K., Liang, G. and Tang, J., Component mode synthesis order-reduction for dynamic analysis of structure modeled with NURBS finite element. Journal of Vibration and Acoustics, 138(2) (2016), 021016.

Zhou, K. and Tang, J., Uncertainty quantification in structural dynamic analysis using two-level Gaussian processes and Bayesian inference. Journal of Sound and Vibration, 412 (2018), 95-115.

Zhou, K. and Tang, J., Efficient characterization of dynamic response variation using multi-fidelity data fusion through composite neural network. Engineering Structures, 232 (2021a), 111878.

Zhou, K. and Tang, J., Structural model updating using adaptive multi-response Gaussian process meta-modeling. Mechanical Systems and Signal Processing, 147 (2021b), 107121.